THE UNIVERSITY OF CHICAGO

INORGANIC BIOINTERFACES FOR MODULATING CELL SIGNALING

A DISSERTATION SUBMITTED TO

THE FACULTY OF THE PRITZKER SCHOOL OF MOLECULAR ENGINEERING

IN CANDIDACY FOR THE DEGREE OF

DOCTOR OF PHILOSOPHY

BY

LINGYUAN MENG

CHICAGO, ILLINOIS

AUGUST 2022

Dedication

To my beloved family members and friends.

Table of Contents

List of Figures

List of Tables

Acknowledgment

In retrospect, my time at UChicago was filled with excitement, passion, trust, and fulfillment shared among my peers and me as we faced and tackled lab and life challenges together. The doctoral thesis I am presenting here is the product of dedication and hard work from many people. I was fortunate to work alongside several gifted scientists in a collective undertaking. Developing a deep friendship with these people has been one of the most meaningful achievements.

The most important person to thank first is my research advisor, Dr. Bozhi Tian; without his support and valuable guidance, I could not achieve the work in this thesis. Bozhi has always been helpful and supportive throughout my Ph.D. journey, and he provided many insightful suggestions for research. He has been one of the nicest advisors I have ever met, and Bozhi has been a mentor and a life coach. In 2017, I contacted Dr. Tian due to my research interest in the multidisciplinary field across biology, material science, and chemistry. Luckily, the field of biointerfaces has gradually been developed since then, and we have together built foundations for the field. I enjoyed my experience here in the lab. I learned a lot, from the chemical vapor deposition (CVD) of silicon nanowires to device fabrication and animal experiments to super-resolution imaging and other state-of-the-art technologies. The great enthusiasm, dedication, and positive attitude of Dr. Bozhi Tian in the field and emerging topics always give us energy and shape our way of research. He created a lab with a comfortable, collaborative, and challenging working environment.

I am also fortunate to have my thesis committee members, Dr. Bozhi Tian, Dr. Jun Huang, and Dr. Aaron Esser-Kahn, who provided valuable and constructive comments to improve this thesis. Among them, Dr. Jun Huang, my academic advisor, and Dr. Bozhi Tian, my research

advisor, guided the early stage of my candidacy exam and continuously offered tremendous experimental support for advising the T cell signaling work. I am honored to have them review the research.

My gratitude further extends to my colleagues at the University of Chicago. I would like to thank Dr. Yuanwen Jiang, Dr. Yin Fang, Dr. Yin Fang, Dr. Xiang Gao, Dr. Xiaodan Huang, Dr. Youjin Lee, Dr. Yiliang Lin, Bernadette Miao, Dr. Vishnu Nair, Ellie Ostroff, Dr. Aleksander Prominski, Dr. Jihun Park, Jiuyun Shi, Dr. Chuanwang Yang, Dr. Jiping Yue, and Dr. Jing Zhang for their accompany and shared enjoyable moments with me throughout my time in the lab and beyond.

Finally, I would like to thank my beloved family members and friends for their love and care. Special thanks to Dr. Zhaodi Pan, Dylan Meng Pan, my parents and parents-in-law. They are the most substantial support in my life. Also, thanks to my friends, Yifan Zhang, Yanjing Li, Yang Song, and many others.

Abstract

Biointerfaces have emerged as an exciting and rapidly expanding field. The highly versatile biointerfaces and tunable platforms have improved our understanding of biological problems and developed better therapeutic approaches for diseases. By designing functional materials-cell biointerfaces and utilizing fabrication techniques and physics, existing tools for cell stimulation have been extended to study cellular responses to external factors, including electrical signals, forces, and biochemical signals. In recent years, there has been remarkable growth in the field, allowing for a deeper understanding of biological complexity and more rigorous development of methods.

This thesis focuses on electrochemical cell modulation, bioelectrically augmented exosome production, and molecular and magnetically triggered T-cell signaling by employing carbon-based devices, interdigitated gold electrodes, and inorganic heterostructures, respectively.

The first part of this dissertation (**Chapter 1**) discusses multiple biointerfaces in biological applications. We showed that synthetic materials and devices are excellent platforms to sense and modulate cardiac, nervous, and microbial systems.

The second part of this dissertation (**Chapter 2 and Chapter 3**) focuses on electrical modulation using planar devices. First, we developed a new synthetic route for fabricating carbon-based flexible devices from a bottom-up approach using micelles and silica nanoparticles as templates, which generate hierarchical carbon porosity to enable softening biointerfaces while maintaining excellent conductivity for cell and tissue *in vitro, ex vivo*, and *in vivo* bioelectrical stimulation. Furthermore, we investigated cellular changes upon bioelectrical stimulation from the nanoscale. Spontaneous super-resolution imaging during the bioelectrical stimulation allowed us

to observe real-time electrical-induced exosome releases using interdigitated gold electrodes fabricated on glass substrates. Extracellular vesicles (EVs) play essential roles in intercellular communication and are promising drug delivery vehicles for biomedical engineering. We engineered scalable bioelectrical production of exosomes as microRNA carriers for *in vivo* tissue repair. Given the acute recovery in myocardial infarction (MI) mice model using electrically produced EVs loaded with therapeutical mRNA, we demonstrated the translation of bioelectronic-generated exosome into clinical practice.

The third part of this dissertation further demonstrates the application of structurally unique inorganic heterostructures to investigate T cell sensitivity. Existing synthetic materials approaches to T-cell research generally focus on ensembles or individual cells. However, the subsequent significant advances in our understanding of immune cell biology are likely to come from data obtained at the molecular and nanometer scales. Studies of T-cell receptors (TCRs) and chimeric antigen receptors (CARs) recognition at the single-molecule level requires precise manipulation of the biointerfaces, which is beyond the capabilities of most synthetic tools. Moreover, it is very difficult to use existing antigen-presenting systems to accurately assess T-cell mechanosensitivity because that immobilization can change the cells' physiological environment and how they respond to force. It is essential to introduce new modulation approaches to study suspension/floating T cells physiologically and with single-molecule resolution. Therefore, we developed a bi-functional hematite-silica hexapod heterostructure for biomimetic antigen-presenting. Nanostructured silica branches on the hexapod allow bioconjugation of ligands and spatial confinement of the biointerfaces. In proof-of-principle studies, we apply the hexapod heterostructures to interrogate the signaling and biochemical/mechanical dual sensitivity of T cells. Our study demonstrates that

T cells can be sensitized/activated by a single agonist peptide-MHC ligand. TCRs can discriminate peptides that differ only by one amino acid, and TCR antigen recognition is significantly superior to CARs **(Chapter 4)**.

Furthermore, magnetic field-induced piconewton forces on the hexapods enhance activation in floating T and CAR-T cells **(Chapter 5)**. In this way, the multimodal hexapods antigen-presenting system provides a unique nanotechnology-based strategy for investigating recognition, signaling, and the dual sensitivity of immune cells. This novel biochemical and biophysical investigative approach may facilitate the future development of cancer immunotherapies and rational vaccine design.

We have demonstrated some of our efforts in applying function biointerfaces for probing biological responses. In the future, we believe that improved stimulation profiles and experimental setups may contribute to a greater understanding of cellular mechanics and regenerative medicine through an interdisciplinary approach that spans the fields of biointerfaces, nanomaterials synthesis, engineering, biological modulation, and immunotherapy.

Chapter 1. Introduction

1.1 Overview of Biointerfaces

Recent decades have witnessed a growing interest in precisely integrating biological systems with synthetic material components at the cellular and subcellular levels. The development of such hybrid systems, taking advantage of optimized functions of material components and active biological behaviors, provides us with advanced recording devices to monitor cellular behavior and modulation techniques for manipulating biological activities.

Cells sense and interact with their external environments through various cellular components, including ion channels, membrane receptors, organelles, and extracellular matrix. These components provide the cell with cues such as mechanical, thermal, and electrical information and further regulate various cell functions. These functions include but are not limited to apoptosis, proliferation, and phenotype change. A complete understanding of the sensation and interaction mechanism and the development of techniques to control them are essential to advancing multiple fields. Over the last few decades, researchers have begun to reveal the material candidates that are suitable for biological interrogation. By precisely integrating biological systems with these materials at the cellular and subcellular levels, most naturally occurring biological processes become observable and can be leveraged through tunable properties of synthetic materials. Such hybrid systems allow us to understand how cells sense and respond to multiple environmental cues. On the other hand, functional materials can also introduce localized biophysical and biochemical signals to manipulate physiological processes.

1.2 Bioelectrical Interfaces

The electrical potential is the most common biophysical link that establishes communication between biological systems and inorganic materials. Ions and charged molecules in cytoplasm and intercellular space can interact with electrons and holes in materials and electronic devices via charge interactions and electrical potentials. In recording mode, the dynamic flow of ions in biological tissues yields spatially defined bioelectric fields, such as extracellular field potentials or intracellular action potentials, which can be sensed and converted into a current or voltage output by electrically active materials. Conversely, in stimulation mode, the electrical signal produced by the materials is translated to cells through induced movements and redistribution of ions and biomolecules around and across a plasma membrane. While electrical signals unravel the electrophysiological activity within the biological system, electrical inputs also work as biological stimuli to control cellular processes underlying sensation, movements, and neurological disorders. Currently, electrical stimulation is clinically approved to treat Parkinson's disease and neuropathic pain, and it is a candidate for restoring lost motor function.

Bioelectrical interfaces connect materials and biological systems across various length scales, from subcellular dimensions to tissue and organ levels. The development of interfaces has significantly grown in the last few decades. So far, research has been utilizing nanoscale conductive materials with rational device structures and efficient fabrication methods to develop new applications in neuroscience, cardiovascular disease research, microbial-related energy systems, and many other expanding areas[1–5]. Semiconductors, carbon, metals, and their composites and oxides are materials used in interfaces to catalyze profound progress in developing deep-brain stimulators, retinal protheses, implantable artificial pacemakers, and microbial fuel cells, as well as the exploration of personalized medicine[6–10]. These developments increase the ability to better

understand complex electrophysiological biological processes within and between cells, tissues, and organ systems.

Historically, challenges to developing efficient and effective bioelectrical interfaces include improving the signal-to-noise ratio, optimizing stability, dealing with a mechanical mismatch, refining spatiotemporal resolution, and achieving translatability to the clinical setting[11,12]. Currently, most researchers are pursuing stable, seamless material-biology interfaces of minimal foreign-body response that operate for chronic time scales and remain functional for large-scale high-resolution investigation.

Temporally, bioelectrical interfaces can reach a sub-microsecond resolution for recording a single-unit action potential with a recording span of up to hours, as in monitors of hormones, neurotransmission, and local field potential fluctuation[13]. Some biocompatible interfaces can last for months without severe immune responses. Spatially, bioelectrical interfaces enable organelle-level local precision and can also be globally extended to work as whole organ patches[14,15]. High-density distributions of thousands of interfacing sites can be achieved by complementary metal-oxide-semiconductor (CMOS) techniques and microelectrode arrays[16].

1.2.1 Development of Electrical Biointerfaces

The first example of a functional material-biology interface is widely credited to Luigi Galvani, an eighteenth-century physicist who discovered bioelectricity, a phenomenon that biological systems can generate and respond to electrical signals. In his experiment, dissected legs of a dead frog were twitched into the upward position when contacted with electrically charged metal implements as if the frog was alivea[17]. This electrophysiological phenomenon turned out to

be a fundamental process involved in many vital biological functions, such as sensing and moving, across all species.

Understanding that the impetus behind muscle movement was electrical energy, scientists have developed numerous tools to utilize bioelectricity. Since the early 2000s, the field has advanced from patch clamps, microelectrode arrays (MEAs), and field-effect-transistors (FETs) to include minimally invasive, ultrasmall, and biocompatible nanomaterials-based sensing and modulation techniques[18–20]. Driven by the need for intracellular signal recordings, German biophysicists Bert Sakmann and Erwin Neher developed the patch-clamp technique in the late 1970s[21], which was later rewarded the Nobel Prize in Physiology or Medicine in 1991. With the patch-clamp method, ionic currents either passing through single ion channels or an entire cell membrane are directly measurable. By the 1980s, silicon-based multielectrode arrays (MEA) for recording and modulating cortical circuits were developed with microfabrication techniques[22]. MEA can non-invasively depolarize cell membranes at the formed material biointerfaces.

More recently, sophisticated probes, inspired by the Utah arrays[23] and the Michigan probes[24], are developed with expanded modulation functionalities and pave the way for selective cell modulations with cellular specificity. For example, bidirectional neural probes, engineered with optical fibers to MEA for optogenetics research or integrated with microfluidic channels to deliver chemical stimuli and biological agents[25–27]. The refined spatial resolution is achieved via light-sensitive ion channels, called opsins, or neuromodulators, respectively. In the past decade, there is also accelerating development of neural prostheses, a series of devices that replace or improve impaired neurons. Examples as cochlear implants already exist in clinical use, with more than 300,000 implanted worldwide[28]. The remarkable progress of the electrical stimulation has successfully helped people with spinal-cord injuries to regain control over their leg muscles and

improve their walking[29]. In the late 2000s, advances in nanotechnology-enabled various elaborated constructions of functional minimally invasive nano-bio-materials interfaces for single cells intracellular recording, including but not limited to micrometer-sized gold mushrooms[30], silicon nanowires[31], gold-nanopillar electrodes[32], and nanowire field-effect transistors (NWFETs) bioprobe[33]. NWFETs exhibit exquisite sensitivity in signal detections and can strongly couple electrical devices with cellular components. Advances in flexible electronics now make it possible to integrate circuits with tissues.

The development of biological stimulation has shown a staggering potential for restoring lost sensory or motor functions. For example, restorative prostheses have corrected visual processing disorders and limb dysfunctions[34]. Notably, epidural electrical stimulation has helped patients with spinal-cord injuries regain control over their leg muscles, and their walking ability was retained even after the stimulation had stopped. Neural stimulation, especially deep brain stimulation, is also a candidate for treating Parkinson's disease, epilepsy, and tremor and alleviating major depression, dystonia, and neuropathic pain symptoms. Besides the neural prostheses, advances in flexible electrodes also facilitated the beginning of the "cyborg" era by forming "cyborg" tissues composed of living cells and electronic junctions. To date, cyborg tissues have helped monitor brains, neurons, and muscles electronically. Currently, seamlessly integrated flexible electrodes in the forms of flexible meshes and tissue-like probes have offered new approaches for large-scale (large spatial span), long-term recordings (great temporal span) of brain circuits, or large numbers of neurons with single-neuron single-spike (high spatiotemporal resolution) recording and multiplexed capability. The development of such intimate material-biology interfaces enables a more in-depth investigation of brain dynamics and functions that span orders of magnitude in time and length scales.

Currently, these techniques are still limited by the number and possible location of electrodes-biointerfaces. For example, they cannot stimulate target cells at arbitrary sites *in vivo*, such as in the deep brain region[5]. Although it has already been shown to treat several neurological diseases, the stimulation electrodes are often limited by their need to be tethered to external electrical wiring. Moreover, these electrodes can induce severe inflammation in target tissue by inducing foreign body reactions, which is deleterious for the long-term implantation of the materials[35,36]. Therefore, wireless modulation methods with minimal tissue damage have recently attracted more attention.

1.2.2 Inorganic Electrical Biointerfaces

Blurring the boundaries between biotic and abiotic systems, inorganic materials catalyze profound progress in neuroscience research and neurotechnology for recording electrophysiology and neuromodulations. Advancements in material-based neural interfaces are essential for developing a scientific understanding of brain functions and treatments for various neurological disorders. While conductive inorganic materials establish neural interfaces for recording neural electrical signals, multifunctional electrodes and functional transducers allow for controlling spatiotemporal neural activities via delivering a variety of biophysical stimuli in a targeted way.

Inorganic materials are routinely used for bioelectrical interfaces because of their unique features, including but not limited to tunable size to ultrasmall scale, excellent electrical properties (e.g., conductivities), and diverse signal transduction mechanisms for energy conversion[37–39]. Additionally, they can be processed via highly scalable fabrication technologies into a broad spectrum of functional devices. There is also an extensive toolbox for various choices and possibilities of material composition. Inorganic nanomaterials are used in bioelectrical interfaces;

they serve as essential abiotic-biotic ties, bridging gaps and enabling connections between biological and synthetic systems.

Metals and carbon-based conducting materials have intrinsic electrical properties suitable for interfacing with cells and tissues for recording and stimulation purposes (**Table 1-1**). Inorganic material-based electronic devices have several advantages compared to their organic counterparts. Inorganic dry-state devices allow for easier passivation in physiological fluids, generally require lower operation voltages, and are easier to fabricate at nanoscale dimensions. As such, inorganic materials are readily applied as biointerfaces. They are essential for designing high-performance devices with desirable applications such as electronic sensing, signal amplification, and transduction.

Table 1-1. Merits of common electrical biointerface materials.

Materials	Characteristics
Pt, Au, and Pt-Ir	○ Most widely used bioelectronic probes ○ Excellent electrical conductivity, stability, and biocompatibility ○ Nano fabrication and surface processing methods ○ Gold nanostructures exhibit plasmonic properties
Liquid metal (e.g., EGaIn)	○ Low melting point for fabricating soft and self-healing circuits
Silver	○ Excellent conductivity and antimicrobial properties
Stainless steel	○ Cheap alternative to noble metals ○ Great chemical stability
Copper	○ Nonmagnetic and MRI safe ○ Alternative to gold with excellent conductivity
Carbon	○ High chemical stability ○ Can be mechanically flexible ○ Large surface area
Silicon	○ Established industrial processing techniques ○ Surface modification and device fabrication methods ○ Tunable electrical and optical properties ○ Multiple length scales ○ Photovoltaic or photoelectrochemical effect ○ Bioresorbable
Oxides, nitride, carbides	○ Wide range of physical and chemical properties ○ Emerging opportunities for future bioelectronics

Table 1-1, continued.

Materials	Characteristics
PEDOT/PSS	○ The most studied conductive polymer ○ Solution processable ○ Printable ○ Flexible and stretchable ○ Excellent electrochemical stability ○ High volumetric capacitance ○ High ionic mobility ○ Biocompatibility
PPy	○ pH-sensitive and tunable conductivity ○ Flexible and stretchable ○ Mechanoelectrical properties ○ Can be synthesized through photopolymerizationa
PANI	○ Low-cost precursor and synthesis ○ pH-sensitive and tunable conductivity ○ Flexible and stretchable ○ *In situ* synthesis onto biological structures

Inorganic semiconductors are widely utilized in electronic and photonic bio-interface research. In particular, semiconducting Si has attracted interest due to its biocompatibility and well-developed microfabrication methods[40]. The well-established and precisely controlled synthesis of Si makes it easy to fabricate various architectures from nano- to macroscopic scale. Such multiscale material control matches the multi-scale application for different biological components and enables integration with various biological systems.

Si reacts with water via hydrolysis to form silicic acid $Si(OH)_4$: $Si + 4H_2O \rightarrow Si(OH)_4 + 2H_2$, where the $Si(OH)_4$ departs the Si surface through diffusion. The chemical processes of Si degradation have already opened a new way toward transient electronics[41,42]. For long-term applications of Si-based bioelectronics, degradation needs to be minimized. One technique for accomplishing this employs a thermal oxide thin layer directly grown on the surface, which can prevent biodegradation in phosphate-buffered saline solution[43]. Several efficient passivation coating materials also work well to inhibit Si degradations, including stable Al_2O_3[44], TiO_2[45], and

$SrTiO_3$[46]. As demonstrated by Hu *et al.*, atomic layer deposition (ALD) of the TiO_2 layer (4 to 143 nm thick) significantly improves the stability of Si photoanodes under basic water oxidation conditions[47]. More generally, TiO_2 stabilizes many semiconductors during oxidative photochemical processes by engineering the band structures and the defect states.

1.2.3 Organic Electrical Biointerfaces

Common biocompatible conductive polymers for biointerfaces include polypyrrole (PPy), poly(3,4-ethylene dioxythiophene) (PEDOT), polythiophene (PT), polyaniline (PANI), their doped forms with poly(styrene sulfonate) (PSS) or para toluene sulfonate (pTS), chemically modified or biologically functionalized derivatives, and blends with hydrogels, elastomers, nanomaterials, and biomolecules. Critical characteristics of PPy, PEDOT: PSS, and PANI are summarized in **Table 1-1**. The inherent conjugated molecular double bonds in the polymer chain and charge carriers from dopants provide these polymers with a tunable electrical conductivity that spans more than ten orders of magnitude. The function of these polymers is highly versatile in offering conductivity, serving as substrate or insulation packing, providing mechanical flexibility, and improving biocompatibility. For example, PEDOT: PSS was found to downregulate glial reaction and progressively reduce glial cell density without compromising the neuronal viability and synaptic function[48]. Coating with PEDOT: PSS also prevent electroactive materials (for example, Si, metal, and carbon) from direct contact with the ionic solution[49], and further prevent delamination and corrosion of the electrode. These organic materials have been used for bioelectrical interfaces, especially in flexible electronics or electronic skin, stretchable hydrogel electronics, and 3D hydrogel scaffolds[50–52].

Conductive organic materials, including conjugated polymers and hydrogels, are generally more biocompatible and easier to fabricate than most inorganic materials. For hydrogels, in particular, their Young's moduli and water content are much closer to those of biological tissues, allowing them to form more compliant biointerfaces while at the same time providing satisfactory electrical performance via ionic conduction[52,53]. Most organic biointerface devices need inorganic nanomaterial components, such as highly conductive metal and carbon, as interconnects because conductive polymers generally have higher operating voltages than conductive inorganic materials[54,55]. Typically, conductive polymers of tailorable structures, thickness, and chemistry are patterned directly onto the electrodes through chemical polymerization, improving the electrochemical and mechanical properties of the electrodes[56,57]. Additionally, organic bioelectrical interfaces can be constructed with inorganic nanostructured surfaces to promote tighter adhesion and thus better signal transduction at interfaces and enable higher spatial resolution[58].

Organic semiconductors have become excellent candidates for flexible and stretchable bioelectronic applications because of their low-temperature solution-phase processability, good mechanical deformability, and applicable charge transport properties. When in contact with skin or implanted into tissues, mechanically compliant organic bioelectronics can minimize discomfort and adverse effects due to the mechanical mismatch[8]. Moreover, some self-healable and biodegradable organic semiconductors are ideal for wearable and injectable bioelectronics[60,61]. The balance between mechanical deformability, long-term stability under physiological conditions, stretching, and bending durability are factors for developing the next generation of organic bioelectronics.

1.2.4 Composite Electrical Biointerfaces

Since the electrodes must directly contact the wet and chemically dynamic biological environment, which can corrode or degrade electrode materials and decrease signal sensitivity, an encapsulation is preferred to prevent biofluid penetration and minimize biofouling effects. The encapsulation layers tolerate solvents, such as cerebrospinal fluid, and they have a relatively low thermal expansion and a stable dielectric constant. These polymers are available in various geometries (e.g., thin-film, thin-tube, coating layers, *etc*.) and can offer sufficient flexibility and distribute stress so that the device does not fail under mechanical strain. Polymers are also featured with mechanical compliance of young's modulus from a few gigapascals (GPa) down to a few megapascals (MPa), while those of inorganic materials (semiconductors and metals) are around a few hundred gigapascals. For example, Young's modulus of silicon-based Utah arrays is about 150 GPa, and that of tungsten microwire arrays is ~200 GPa, while plastic polyimide arrays are of ~ 5GPa softness and the e-dura is only ~ 1 MPa. The encapsulation can also help to avoid leakage of potentially toxic components.

Parylene-C, polyimide (PI)[62], SU-8[63], polydimethylsiloxane (PDMS), silicone, benzocyclobutene (BCB) [64], poly(p-xylylene)[65], and polyethylene glycol (PEG) are widely used at biointerfaces as probe encapsulation. For example, SU-8 supported NeuE[66], parylene-C coated Pt-graphene fiber[67], polyimide-insulated stainless steel and Neurotassels[68], and silicone-based e-dura[69]. PEG displays excellent biocompatibility for *in vivo* applications and is commonly used as an anti-biofouling polymer. It can be functionalized with chemical functional groups and cargo-releasing structures, which holds potential for bio-conjugation and integration of drug-delivery modality. Besides chronically stable polymers, poly(vinyl alcohol) (PVA) and poly(lactic-coglycolic acid) (PLGA) are widely used as biodegradable or bioresorbable shuttles for transient

biointerfaces[70–72]. Both Utah arrays and Michigan probes use the low elastic modulus polyimide or parylene C for insulation to lessen tissue damages[73,74]. These polymers are also flexible and stretchable, enabling the fabrication of bioelectronics and electrode arrays desired for mechanically active biological systems, for instance, the spinal cord. As demonstrated by Zhang *et al*., transparent SU-8/CNTs/PDMS electrode array signals retained excellent electrochemical performance during cyclic stretching[75]. These transparent, stretchable electrodes combined electrical, optical, and mechanical modalities, holding potential for real-time monitoring of local circuit dynamics of traumatic brain injury and other mechanically active conditions.

While optimizing geometries, hydrophilicity, crosslink density, and dopants can improve the performance of polymers, combinational strategies using both polymers and inorganic materials make the best use of the advantages of each component while bypassing their disadvantages. Therefore, composites could perform well on all electrical, mechanical, and biological properties and are consistently applied in high-quality chronic neural interfaces. One example is the Au-TiO_2-PDMS-based high-density stretchable electrode for chronic neural recording reported by Tybrandt *et al.*[76]. Due to the flexible and stretchable nature, the developed electrode grids were successfully inserted into the brain of rats through a craniotomy window that was 30% smaller than the device itself. They successfully resolved high spatiotemporal neural signals from the surface of the cortex in freely moving rats and demonstrated continuous recording of the brain activity for three months. In another case, polydopamine-coated gold-polycaprolactone (PDA-gold-PCL) nanocomposites showed great potential in peripheral nerve regeneration *in vivo*[77]. As conductive nerve guidance, the composite scaffold improved myelin sheath growth, angiogenesis, and functional recovery of sciatic nerves. Nanostructured carbon materials are also widely used in composites by mixing with metals (e.g., IrO_x-graphene and Au-CNT),

semiconductors (e.g., the Si/SiO2 nanorods-CNTs)[78], or polymers (e.g., PEDOT-CNT and PPy-CNT)[79] to boost conductivity and biocompatibility for electroactive neural interfaces.

Natural and bioengineered biological polymers, for instance, ECM-based/mimic proteins (e.g., collagen, laminin, silk fibroin, gelatin, *etc*.), transmembrane proteins (e.g., L1CAM), neurotrophic factors, Arg-Gly-Asp peptides (RGD), and poly-l-lysine, have been immobilized on the surface of the device as biological cues to encourage adhesion and growth of cells, which in turn reduce inflammation and improve the performance of biointerfaces. Generally, functional groups like carboxylic acid are modified onto the electrode surface to incorporate these polymers through covalent bonds. In addition to these neural adhesion polymers, internalization-promoting biomolecules also help the development of intimate electrode-tissue interfaces. For example, phospholipid bilayers coating on various nanostructured inorganic materials fuse the neural cell membrane and enable the robust use of intracellular probes[80–83]. Similarly, trans-activating transcriptional activator (TAT), a type of cell-penetrating peptide, promoted the spontaneous internalization of SiNWs into nonphagocytic cells, such as primary DRG neuron cells and mouse hippocampal neurons[84].

1.3 Nano-transducers Enabled Biointerfaces

The application of electricity in the monitoring and modulation of biological activities has paved the way for understanding bioelectric phenomena. However, there is still a concomitant pursuit to instigate cellular behavior in a wireless, minimally invasive, highly targeted way. Biological systems also generate and respond to a few other physical signals besides electricity. For example, light, heat, mechanical forces, and substrate stiffness offer advantages in cell modulations. Towards this direction, stimulus-transducing nanomaterials that can transduce

primary physical stimuli (e.g., light, magnetic field, and ultrasound) to secondary biological cues (e.g., electricity, heat, forces) are promising tools that have attracted considerable attention in wireless precise biological modulation. These transducers are highly versatile and operate via various mechanisms that can benefit specific biological events. For example, the nanoscale featured sizes enable precise modulation of cellular activities down to subcellular dimensions, and the use of light (in particular, near-infrared or NIR light), acoustic and magnetic stimuli extend the signal penetration depth. So far, photo-electric, photo-thermal, photon upconversion, acousto-mechanical, acoustoelectric, magento-electric, magneto-thermal, and magneto-mechanical transducing mechanisms have been demonstrated to sense and modulate neurons via various proteins and regulating pathways by directly altering the biophysical properties of microenvironments[85,86]. These functional inorganic materials have been invaluable for deciphering the physiological roles of cells.

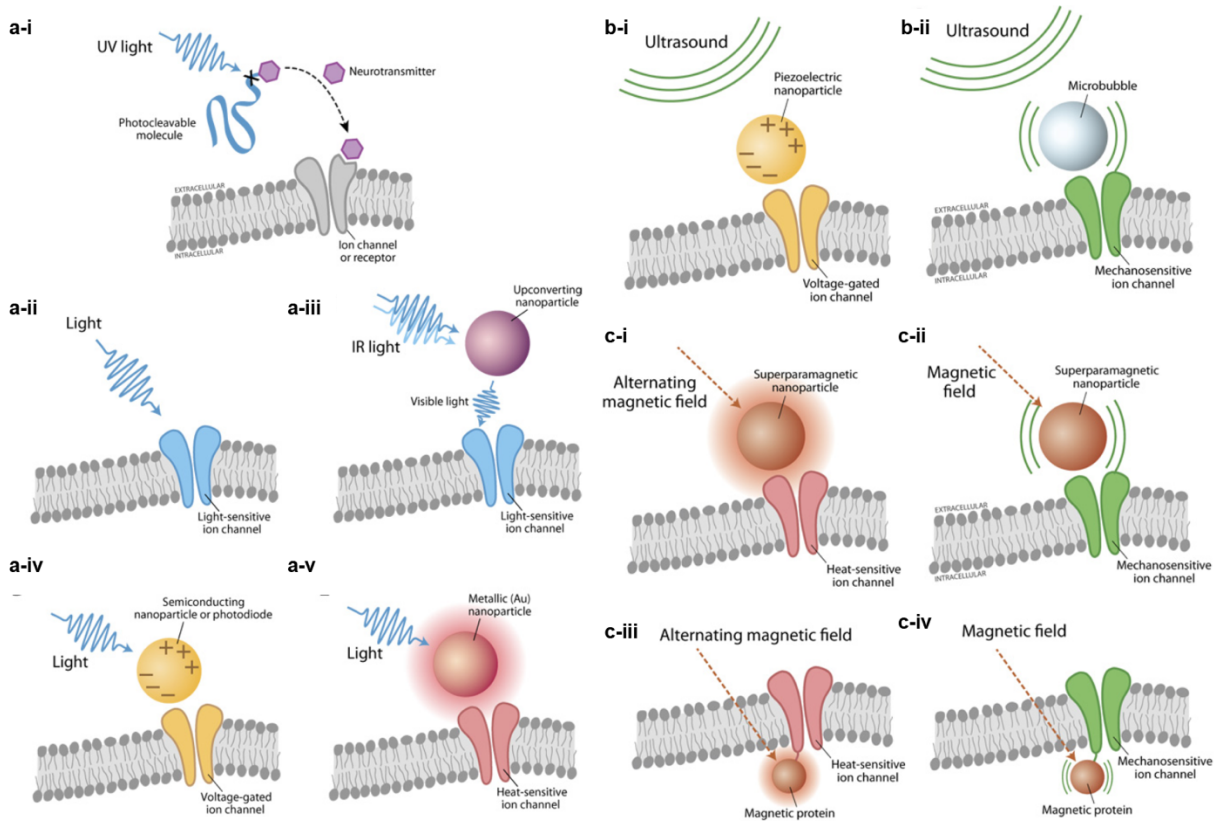

Figure 1-1. Cell-specific biophysical stimulation methods and related biointerfaces. a. Optical stimulation methods. (a-i) Receptor activation via Two-photon uncaging of caged biologically inert neurotransmitter. (a-ii) Optogenetic techniques. (a-iii) NIR optogenetic using upconversion nanoparticles acting on light-sensitive ion channels. (a-iv) Photoelectric stimulation via semiconducting materials acting on voltage-sensitive ion channels. (a-v) Photothermal stimulation with metallic nanoparticles acting on the cell membrane or heat-sensitive channels. **b.** Ultrasonic stimulation methods. (b-i) Ultrasonic stimulation via piezoelectric nanoparticles acting on voltage-sensitive channels. (b-ii) Ultrasonic stimulation via microbubbles acting on mechanosensitive ion channels. **c.** Magnetic stimulation methods. (c-i) Magnetothermal stimulation via superparamagnetic nanoparticles acting on a heat-sensitive channel (for example, TRPV1). (c-ii) Magnetomechanical stimulation via magnetic nanoparticles acting on a mechanosensitive channel.

Figure 1-1, continued. (c-iii) Magnetothermal stimulation via magnetic proteins acting on a heat-sensitive channel. (c-iv) Magnetomechanical stimulation via magnetic proteins acting on a mechanosensitive channel. Figure adapted with permission from Ref. 86 (CC BY 4.0).

1.3.1 Optically Controlled Biointerfaces

Light can directly induce chemical or conformational changes in light-responsive proteins, such as a neurotransmitter, photoreceptors, and some ion channels. For example, caged biologically inert neurotransmitters, like the glutamate caged methoxy-nitroindolino (MNI-glutamate), can be uncaged and activated using light from a 720-nm, two-photon laser and then become available for receptor binding[87] (**Fig. 1-1. a-i**). This method gives researchers the ability to control receptor activation temporally and anatomically. The limitations to this two-photon approach are the limited number of compounds available to be caged, the need to know the precise location of specific receptors, and the delivery of the caged compound. Another example of light direct modulation is the optogenetic (**Fig. 1-1. a-ii**), a method that stimulates neurons by shining light of the correct wavelength to light-sensitive ion channels, such as channelrhodopsin-2 (ChR2) and Halorhodopsin from Natronomonas (NpHR)[88–91]. However, these proteins are only reactive to visible light, which cannot penetrate deep tissue regions without implanted optical fibers[89,92]. On the other hand, optogenetics-based therapy is currently limited to use in humans due to the need for genetic engineering. The near-infrared (NIR) light (650-1450 nm) has better tissue penetration and, therefore, it facilitates the recently developed NIR optogenetics technique based on up-conversion lanthanide-doped nanoparticles (LNPs)[93] (**Fig. 1-1. a-iii**). The LNPs absorb low-energy NIR light and act as luminous bodies to emit high-energy visible light that further activates the nearby light-sensitive ion channels. The NIR optogenetics thus can allow distant light (several

millimeters) outside the skull to modulate deep brain neurons and evoke dopamine release in the deep brain region, extending the penetration depth of the photo-stimulation technique[86,94,95].

Material-based photo-electric and photo-thermal platforms have recently been studied as new tools for optically controlled biointerface and light-based cell modulations to overcome the aforementioned challenges. Semiconducting materials, such as poly(3-hexylthiophene)[96,97] and silicon of multiple length scales[15,98], are shown to stimulate cells by light-induced electric signals (**Fig. 1-1.a-iv**), and gold nanoparticles[99,100] and mesoporous silicon particles[101] are shown to stimulate cells by light-induced heat (**Fig. 1-1. a-v**).

Semiconductors have unique optical and electrical properties and, therefore, have long been the material choice for electronic and photonic devices[102]. Semiconductors show variable light absorption and energy emission depending on the bandgap structures. In direct bandgap semiconductors, a light source of sufficient intensity gives rise to photoluminescence, emitted from the radiative recombination of photo-excited electrons and holes. Indirect bandgap semiconductors convert photon energy (lattice vibrations) via both photothermal (light-induced heat) and photovoltaic (light-induced current or voltage) pathways. As an indirect bandgap semiconductor, silicon of various dimensions and doping profiles transduce light into other forms of energy, such as heat, electricity, chemical energy, and mechanical perturbation through photothermal, photoelectrical, photoelectrochemical, and photoacoustic processes, respectively[15,103]. The transduced energies further affect interfacing biological components, for example, depolarizing the plasma membrane and eliciting neural action potentials.

Given the enhanced light absorption and reduced heat dissipation of mesostructured silicon, which had multi-scale structural and chemical heterogeneities, Jiang *et al.* first exploited a nongenetic subcellular photothermal modulation of live dorsal root ganglia (DRG) neurons[101]. The

silicon was placed on live-cell phospholipid bilayers. Irradiating with a 532 nm laser to the membrane-supported Si yielded a rapid photothermal effect, which produced a quick local temperature increase. This fast heat further triggered a transient capacitive current in phospholipid bilayers and the depolarization process, eliciting single action potentials in targeted individual cells. Light pulses were able to excite DRG neurons in a one-pulse-one-spike manner wirelessly repeatedly. In this study, the mesoporous silicon was deformable and mechanically soft with Young's modulus of ~0.4 GPa, comparable to collagen fibers. Therefore, the heterogeneous silicon is not mechanically invasive to cellular components. Si nanowires (SiNWs) were also reported for high-resolution photothermal neuromodulation, with surface nanoscale Au textures to improve the photothermal responses[104]. Photothermal neuromodulation does not rely on tight silicon-neuron interfaces because of the ~100 μm effective heat distance. As such, photothermal neuromodulations are ideal for stimulating neurons with thick extracellular matrix or other cellular barriers, for example, peripheral nerves.

In addition to the photothermal effect, SiNWs containing diode junctions photoelectrochemically modulate neurons with electrons and holes generated by light. As proposed by Parameswaran et al., coaxial p-type/intrinsic/n-type (p-i-n) SiNWs induced a cathodic photoelectrochemical current while generating minimal heat[105]. Upon light illumination, holes move towards the p-type core of these p-i-n SiNWs, while electrons move to the n-type nanowire shell. With a tight silicon-neuron interface, negative charge carriers at the nanowire shell could reduce local the potential in the extracellular region and cause localized membrane depolarization as well as action potentials (APs) firing. Unlike photothermal methods, photoelectrochemical stimulations require a tight interface between the silicon material and the target neuron to leverage the local negative potential on the SiNW shell efficiently. Surface modification with peptides or

macromolecules can be readily applied to silicon to form high-affinity bindings to specific biocomponents.

SiNWs were also found to convert light to mechanical perturbation of the cells when internalized into cells[15]. In this photoacoustic process, even intracellular calcium dynamics in non-excitable cells, for example, human umbilical vein endothelial cells (HUVECs), can be modulated. Upon illuminating, the surrounding and entangling microtubule around the nanowires was repelled, and a shockwave was generated because of produced local heat. In this case, intracellular calcium ion release was triggered, which originates from the mitochondria and the endoplasmic reticulum instead of membrane-integrated ion channels. This realization prompted a study using nanowires to track protein-microtubule interactions. Using SiNWs to modulate calcium dynamics at the subcellular level could also enable the directional transportation of intracellular cargo along the calcium wavefront.

Freestanding nanostructured silicon is advantageous to perform target optical modulation at subcellular scales, the high spatial specificity of which is currently challenging for electrode-based electrophysiology. By controlling the duration and pulse frequency of light illumination, silicon performs optical modulation in a temporally transient way with high temporal resolution. Silicon nanostructures are also biocompatible and can form robust intracellular biointerfaces without cell membrane disruptions.

In contrast to freestanding SiNWs, silicon can be fabricated into large-scale meshes and devices for tissue and organ stimulations. At the organ level, Jiang and co-workers utilized a flexible silicon-membrane-SU-8 mesh with gold decoration to modulate forelimb movements by interfacing the material with a mouse brain[15]. Optical stimulation of the mesh on the right forelimb motor context evoked the up-and-down movements of the contralateral left forelimb of the

anesthetized mouse. The silicon membrane stimulation involves a photoelectric process with light-induced capacitive and Faradaic effects but minimal photothermal effect. Such techniques influence brain activities and simple animal behaviors wirelessly. The photovoltaic nature of silicon also enables its application as a retinal prosthesis for vision restoration. Demonstrated by Palanker and co-workers as a pioneering example, silicon-based photodiode microarrays were implanted into the subretinal region in a rat eye with damaged photoreceptors[106]. Using pulsed illumination-yield photocurrents, silicon photodiodes electrically burst spikes in the retinal ganglion cells. A camera can capture the original images after image processing, which indicates a successful resumption of the vision of the rat with the help of the silicon subretinal prosthesis. This silicon-based retinal prosthesis is wire-free, miniaturized, and fully integrated with high pixel density, whereas most electronic retinal prostheses are coil-rich and require complicated implantation surgery. Assembling single freestanding SiNW into meshes with the help of polymer gels also can stimulate organs optically. For example, Parameswaran and Koehler *et al.* recently reported a p-i-n SiNW-fibronectin-SU-8 mesh to optically train an *ex vivo* heart to a target beating frequency by applying precise optical pulse[107].

Chemical vapor deposition (CVD) is a commonly used strategy to produce Si-based materials[108]. In a CVD system (**Fig. 1-2**), Si nanowires (SiNWs) are typically synthesized through the vapor–liquid–solid (VLS) growth mechanism[108]. Metal catalysts (*e.g.*, Au) act as energetically preferential sites for the absorption and decomposition of gas-phase Si precursors (*e.g.*, silane (SiH_4), disilane (Si_2H_6), or silicon tetrachloride ($SiCl_4$)), when operated above the eutectic temperatures. The continuously fed gas reactants establish supersaturated metal/Si alloy droplets, followed by the nucleation and precipitation of SiNWs. Besides producing nanowires, CVD is also helpful in the scalable synthesis of various other nanostructures, such as 0D nanoparticles, 2D

multilayered membranes[40], and 3D mesoporous structures[101]. In particular, the Si mesoporous structures were synthesized from a nano-casting method using mesoporous silica (*e.g.,* SBA-15) as a template, in which SiH_4 was decomposed inside the mesopores in a CVD system. Precision Si synthesis in a CVD system is essential since the doping profile, morphology, and crystal structure can determine their physical properties and the corresponding bioelectronic applications[40].

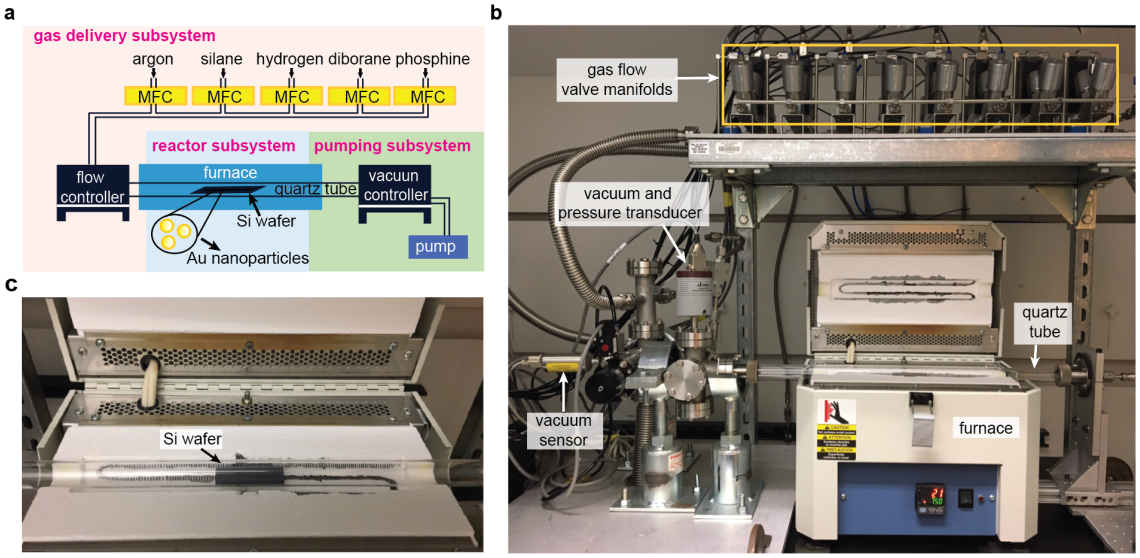

Figure 1-2. Experimental setup for the CVD growth of Si nanowires. Figure adapted from Ref. 110.

Doping, surface chemistry, and dimensions of silicon promote specific photoresponses and physicochemical processes. For example, metal-free p-i-n silicon membranes produced enhanced capacitive current spikes compared to the p-type silicon, and Au-coated p-i-n silicon membranes demonstrated an even more significant light-induced capacitive effect. The Au decoration also enhanced the Faradaic current of p-i-n silicon membranes. In freestanding SiNWs configuration, the presence of surface atomic gold catalyzes the photoelectrochemical reaction and plays a vital role in reducing the kinetic barrier for the current generation.

Silicon materials of varying structures form biointerfaces that are exceptionally efficient for precise spatial and temporal optical control of neurons at subcellular (nanowires and mesostructured silicon), cellular, or tissue (multilayered silicon membranes), and organ levels (silicon meshes). So far, silicon-based optical modulations have achieved control over subcellular Ca^{2+} signals, cytoskeletal organization and transport, neuronal excitability, and simple animal movements. Notably, the application of silicon mentioned above does not rely on gene delivery to express light-sensitive ion channels in mammalian cells, unlike optogenetics, which was challenged in terms of therapeutic applications because of necessary genetic modifications to introduce light-sensitive opsins. Therefore, silicon is a nongenetic variant of optogenetics, using light-induced energies to control electrophysiological dynamics in targeted neurons remotely[110].

Besides silicon, there are other materials-based transducers for optical neural interrogation with subcellular resolution, for example, semiconductor quantum dots (QDs)-based photo-electrical[111], nano-gold-based photothermal[112–114], and upconversion particles-based platforms[94,95,115] have emerged in the field of light-based wire-free neuron photo-stimulation. For photo-electrical modulation, optically excited QDs-films generate localized electric fields that enough to activate nearby voltage-gated ion channels on the interfaced neuron, which elicit the neural action potential. Vice versa, QDs can shift their emission profile in response to local electric potentials, enabling QDs-based voltage sensors, which correlate intensity changes at specified wavelengths with electric potential changes caused by local neuron electrical activity[116,117]. Active molecules (antibodies or peptides) bioconjugations construct tight QD-neuron interfaces via ligand-receptor binding that immobilize QDs on a neuron culture substrate. Generally, QDs applied at neural interfaces consist of different group elements in core-shell structure with a size of 5-10 nm, for example, CdSe/ZnS QDs. These QDs are toxic to the cells because of the potential

release of toxic Cd^{2+} ions. Therefore, many studies have focused on developing cadmium (Cd)-free QDs, for example, InP/ZnO and InP/ZnS core/shell QDs[118,119]. QDs are also widely applied in μLED-based optogenetics[120] and fluorescent-labeled subcellular tracking because of their size-dependent photoluminescence. Organic semiconductor P3HT or poly(3-hexylthiophene) was also reported to trigger nerve cells firing upon illumination photoelectrically through the activation of photoelectrochemical reactions and the formation of a localized electric dipole[121]. The establishment of P3HT light transducers can amplify the function of primitive photoreceptors and restore light sensitivity in rat retinas with damaged photoreceptors[97]. Photoactive P3HT-induced electrical stimulation also promoted the neurogenesis of neural stem cells (NSCs) [96].

For photothermal modulation, nano-gold, such as gold nanorods (AuNRs) and gold nanoparticles (AuNPs), are promising candidates because of their localized surface plasmon resonance and absorption of light of specific wavelength the range of NIR light[114,122]. Upon irradiation by a laser at the resonant wavelength, electrons in nano-Au oscillate and collide, generating rapid plasmonic heating that further stimulates neurons by influencing cell membrane capacitance or heat-sensitive channels[123] (**Fig. 1-1. a-v**). The photothermal approach needs lower optical power densities than those required for activating light-sensitive ion channels, such as channelrhodopsin-2 (ChR2). As the surface plasmons are also sensitive to local electric fields, gold nanomaterials, in principle, can be developed into voltage sensors, which are similar to quantum dots. Synthetically, organic quinacridone nanocrystals were also reported to stimulate single cells optically, through both photocapacitive and photothermal effects, with the help of tight nanoscale needle-cell interfaces[124].

1.3.2 Cell-Specific Acoustic and Magnetic Biointerfaces

Besides light, ultrasound and magnetic field also work as primary stimuli; compared to light, they have better penetration[125]. Ultrasound can be transduced via piezoelectric materials (**Fig. 1-1. b-i**) into electrical signals, acting on voltage-sensitive channels. These piezoelectric materials include boron nitride nanotubes (BNNTs), $BaTiO_3$ nanoparticles[126], poly(vinylidene fluoride) (PVDF) films, lead zirconate titanate or $Pb[Zr_{(x)}Ti_{(1-x)}]O_3$ (PZT) ceramic arrays[127], and ZnO nanowires, etc. BNNTs were reported to promote axonal sprouting and Ca^{2+} influx in neuronal-like PC12 cells upon ultrasound stimulation[128], and $BaTiO_3$ nanoparticles were demonstrated to evoke Ca^{2+} and Na^{+} voltage-sensitive channels[129]. When applied mechanical vibrations, PVDF substrates enhanced the number and length of neural branching of rat spinal cord neurons[130], and polyvinylidene fluoride trifluoroethylene (PVDF-TrFE) fibers-based piezoelectric scaffolds promoted *in vitro* neural differentiation of human neural stem/progenitor cells[131,132]. Although ultrasound can be directly used for nervous systems stimulations without material media, the energy efficiency and mechanistic specificity are limited[133,134]. The ability to be focalized to where piezoelectric materials are located and penetrate deep enable remote acoustic stimulations with high spatial resolution in the magnitude of the material sizes, which is generally a few nanometers to sub-micrometers in cases of piezoelectric nanoparticles. Besides, ultrasound-induced deformations can be amplified by gas-filled microbubbles[135–137] (**Fig. 1-1. b-ii**) to excite neurons by acting on genetically encoded mechanosensitive channels, the transient receptor potential channels-4 (TRP-4)[135], or inducing drug release from carriers[138,139]. However, more *in vivo* evidence of biological responses following acoustic stimulations is needed to confirm the observations, mechanism, and biocompatibility prior to clinical trials.

Similarly, magnetic fields also penetrate deep into soft tissues with minimal tissue damage and field attenuation. Applications of magnetic fields in ion channel opening, cell fate regulation, and *in vivo* deep-brain wireless stimulation were widely studied, based on magnetic nanoparticles (MNPs)-dissipated heat, MNPs-converted electrical potential, MNPs-triggered small-molecule release, and MNPs-transduced forces or torques[140–142]. Superparamagnetic MFe_2O_4 (M=Fe, Co, Zn, Mn, and Ni) nanoparticles convert the alternating magnetic field (AMF) into localized heat generated by hysteresis. The induced heat, in turn, activated genetically modified heat-sensitive receptors, for example, the transient receptor potential vanilloid one receptor (TRPV1), and evoked evoke excitation in the targeted deep brain *in vivo*[142] (**Fig. 1-1.c-i**). Interfacing with ferroelectric $BaTiO_3$, a core-shell $CoFe_2O_4$-$BaTiO_3$ nanoparticle may directly couple the intrinsic electrical neural activity with external magnetic fields, albeit the underlying mechanisms of magnetoelectric effect are still needed to be determined by further investigations[143,144]. MNPs can also transduce mechanical forces and induce torque in stationary field gradients. Tay and colleagues have discussed several possible modulation mechanisms via mechanosensitive ion channels (**Fig. 1-1.c-ii**), including PIEZO1, PIEZO2, TRPV4, and N-type Ca^{2+}. In their several attempts, they showed that MNPs-generated mechanical forces of various strengths, ranging from 0.1 nano newtons (nN) to 1 nN and from 0.15 micron-newtons (μN) to 1 μN, induced significant increments in Ca^{2+} signals in both DRG neurons and fragile X syndrome (FXS) neural networks upon acute magneto-mechanical treatments with ferromagnetic nanoparticles. Besides, they found that periodic modulations for four days could reduce endogenous ion channel expression in neural circuits, which, if true, can be adopted for mediating ion channel equilibrium and treating diseases like hypersensitivity to pain or epilepsy, where such mechanosensitive channels are usually overexpressed. Tay *et al.* also reported coating-decided interfaces for allocating subcellular

interfaces at varying positions. While starch-coated MNPs showed preferential location at the cell membrane, chitosan-coated MNPs were internalized into the cortical neurons. Besides, the magnetic field can influence magnetic proteins (**Fig. 1-1.c-iii and c-iv**), such as MagR or ferritin-coexpressed ion channels[86,145], to induce channel opening, cation entry, and further cellular activation. These techniques currently suffer from several limitations, including heat-induced cytotoxicity, and rely on gene transfection for overexpressing ion channels and other binding proteins, limiting their clinical translation.

In summary, techniques for stimulating cells with light-, ultrasound-, and magnetic-induced secondary stimuli are versatile and operate via various mechanisms that can be beneficial in specific contexts. There is still a need for gene transfection to overexpress stimulus-sensitive receptors, the safety of which must be surmounted. And more rigorous statistical studies are still needed to confirm the stimulation precision, reliability, and feasibility of using these inorganic materials before implementing them in humans. However, the development of minimal invasive transducers-based tools represents a highly critical step towards remotely activating cellular activities with high spatial resolution and wireless targetability by directly delivering physiological and pathological signals.

1.4 Biology-Guided Bioelectrical Interfaces

Bioelectrical interfaces that bridge biotic and abiotic systems have heightened the ability to monitor and manipulate target biological systems to understand their physiological behaviors and are catalyzing profound progress in neuroscience research, treatments for heart failure, and microbial energy systems (**Fig. 1-3**). With advances in nanotechnology, bifunctional and high-density devices with tailored structural designs are developed to enable multiplexed recording or

stimulation across multiple length and temporal scales with resolution down to millisecond-nanometer interfaces, enabling efficient and effective communication with intracellular electrical activities in a relatively noninvasive and biocompatible manner. Biological systems guide the design, engineering, and implementation of bioelectrical interfaces for applications in nervous, cardiac, and microbial systems. Many state-of-the-art biology-guided bioelectrical interfaces have high biocompatibility, extended long-term stability, and integrated system functionality for potential clinical usage.

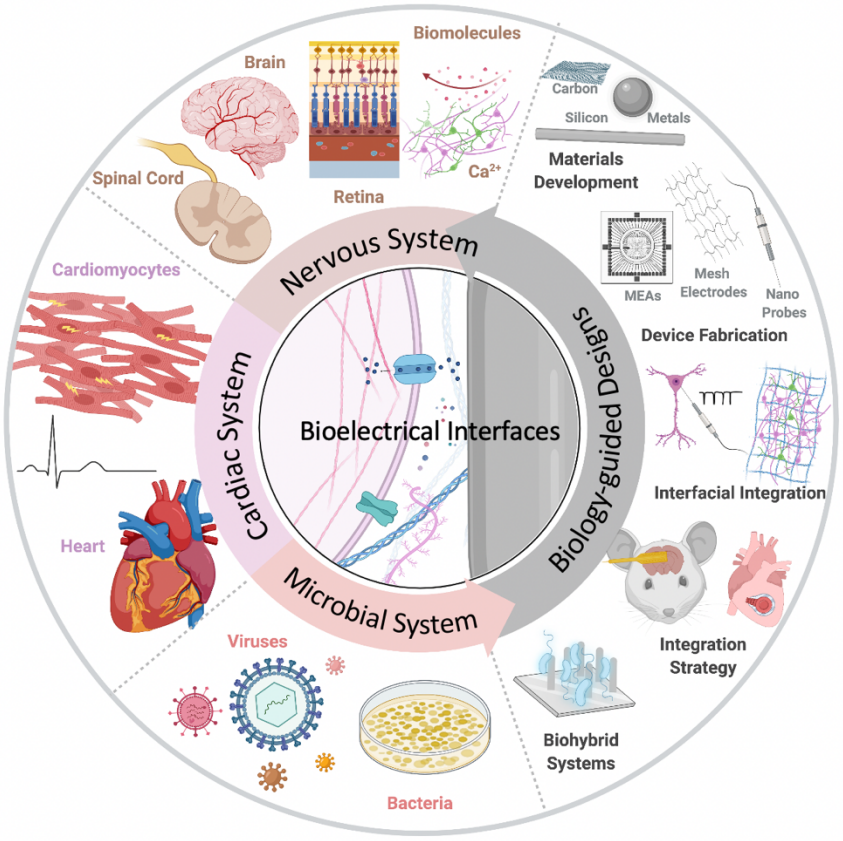

Figure 1-3. Biology-guided bioelectrical interfaces in nervous, cardiac, and microbial systems. Figure adapted from Ref. 146 with images created with BioRender.com.

1.4.1 Biology-Guided Biointerfaces in Nervous Systems

Neural control circuits exist throughout the body and are essential for everyday physiological functions. Notably, the human brain contains billions of neurons, which communicate through quadrillions of synapses to control thoughts, memories, speech, body movements, and organ function throughout the body. There are thousands of genetically and structurally defined neuron subtypes and neural networks, and their organization and distinct functions remain an active area of research. Neurotechnology to record and modulate activities of many neurons is of fundamental importance in understanding the organization and physiological processes of the neural networks and the brain, helping the treatment of related physiological dysfunctions.

Neurons and the whole neuro-muscular system, including the brain, spinal cord, sensory neurons, and motor neurons, deploy endogenous electric fields in the cytoplasm and extracellular space to transmit electrical signals or impulses. These fields vary in magnitude from a few to hundreds of mV/mm. Recent studies have shown that the electrical potential, once regarded as a homogeneous resistive medium with a constant conductivity, is dynamic and substantially influenced by capacitive effects created by electrically active membranes and local ion flow. Notably, each ion channel can open and close within a millisecond and transport between 1-100 million ions per second (10^{-10} to 10^{-12} amperes). Ion transport plays a remarkable role in many physiological processes and accounts for bioelectricity, the electrophysiological phenomenon through which biological systems generate and respond to electrical signals.

Using electrical signals generated from static electricity generators, Italian biologist Luigi Galvani was the first to discover that neuron electrical stimulation caused muscle twitching and the activation of dissected frog legs[147]. This observation of bioelectricity in the late 18th century

is now known to be a result of action potentials (APs) being excited and propagating through neurons and muscle cells. APs and electric fields are now understood to be fundamentally involved in many vital biological processes, from embryogenesis to the growth of organisms and animal movements[148].

Action potentials are sub-microsecond ~100 mV voltage, serving as signatures of neural activities. At the negative resting potential of a neuron, the phospholipid bilayer and selective ion pumps act as the dielectric of a capacitor, creating a separation of charges and a membrane polarization where the intracellular potential is 70 mV below the extracellular fluid. When stimulated by synaptic inputs, direct current inputs, or possible external signals such as pressure and temperature that correspond to the switching of specific receptors, voltage-gated ion channels open and allow a sodium ions influx. The changes in the electrochemical gradient, in turn, produce a further rise in the membrane potential and cause more channels to open, having a higher electric current across the plasma membrane and depolarizing the membrane to reach the threshold potential at around –55 mV, which initiates an action potential. An action potential further opens adjacent channels and results in a nerve impulse traveling along the axon. At repolarization, the declining phase of the action potential, Na^+ channels become inactivated, and potassium channels open, moving K^+ out of the axon, and returning the electrochemical gradient to the resting state. APs propagate across neuronal membranes, assisted by voltage-sensitive ion channels and myelin sheaths around axons, and further trigger the release of neurotransmitters from presynaptic terminals into the synaptic cleft. Partner dendrites are activated when neurotransmitters bind to receptors on postsynaptic cells, and signal transductions proceed. These neurotransmitters have either excitatory or inhibitory functions on the downstream neuron. As these processes run and repeat, stimulation information, for example, electrical, thermal, and mechanical signals, is

translated into chemical signals and then electrical signals. This signal transduction cycle both propagates and modifies the initial signal.

At a larger scale, where multiple neurons within a spatial region connect and assemble into networks, action potentials combine to create rhythms that generate slow-varying local field potentials (LFPs). APs and LFPs further coordinate activity across the brain and the peripheral nervous system, a web of neurons of around 180,000 km, giving rise to and influencing behavior across the entire body. Time function (temporal signals) of either APs or LFPs can be decomposed by Fourier transformation into a distinguishable spectrogram (signals vary over time), which can be separated by applying digital filters or analog methods. Generally, LFPs from population activities produce signals up to 350 Hz, while APs or spiking activities of individual neurons are of a few kHz. Detection and perturbation of APs and LFPs serve as the primary mode of material-neuron communications and play an indispensable role in neural recording and neural modulation technologies. Further, this is essential for restoring and correcting neural dysfunctions and disorders in some neurological diseases, such as essential tremors and Parkinson's disease.

The measured potentials at a recoding site depend on the magnitude of the nearby events, their polarity, and the distance from the recording sites. In the extracellular space, endogenous bioelectric field potentials produced by dynamic ion flows can be understood qualitatively by Poisson's equation, $\varphi(x', y', z') = \frac{1}{4\pi\sigma} \int \frac{I_v(x,y,z)}{r(x,y,z,x',y',z')} dx\, dy\, dz$. The potential $\varphi(x', y', z')$ at a recoding site (x', y', z') depends on the volumetric current density, $I_v(x, y, z)$, around the recorded neuron cell, (x, y, z), the distance between recording electrode, the nearby neurons, $r(x, y, z, x', y', z')$, and the electrical conductivity of the medium, σ. Therefore, to ensure accurate recording, the recording sites should be around neurological activities with large magnitudes and

polarity and close enough to the cell membrane through either engineering the electrodes with optimized topography and flexibility for seamless integration or mechanical pressing.

The development of rational material-neuron interfaces is critical for understanding the basis of brain organization and function and creating novel applications for neuromodulation as it applies to diagnoses, therapy, and prosthetics[149–151]. Rapid progress in material-based neural interfaces has allowed for a more in-depth understanding of neural activity and the role neural circuits play in physiological events and cognitive behaviors. However, there are still uncharted territories and challenges in neuroscience. For example, when relatively simple neurons assemble into a network, tissue, or organ, the overall behavior of the assembly becomes unpredictable, and the connection patterns between neurons are not yet fully understood. Additionally, our ability to manipulate nervous system dynamics remains insufficient for restoring lost neural functions at impaired nerve sites and reversing neurodegenerative disorders such as Alzheimer's[152] and Parkinson's disease[153]. The drive to answer such puzzles and assist people with neurological diseases inspires advanced material-enabled functional neural interfaces for neural recording and modulation.

Inorganic materials are routinely used for functional neural interfaces because of their relevant physical properties, such as conductivity, and their diverse signal transduction mechanisms[39]. Additionally, they can be processed via highly scalable fabrication technologies into a broad spectrum of functional devices. Engineered inorganic materials serve as essential abiotic-biotic transducers that bridge biological nervous systems with synthetic ones. Such hybrid material-neural interfaces, which leverage both active biological components and the tunable properties of synthetic materials, have provided us with advanced neurotechnology to sense and record neuronal signals and modulate and manipulate neuronal activity. So far, high-performance

biocompatible inorganic materials have been precisely fabricated into various architectures and interfaced with neurons at distinct length scales, ranging from subcellular or organelle levels to entire organs. However, it is still challenging to build a stable seamless material-neuron interface with minimal foreign-body responses that operate for a chronic time scale and are functional for large-scale high-resolution investigations[5,12].

Ideal neural interface devices or stimulators should perform reliably for chronic timescales while creating seamless large-scale integration into the neurobiological system with minimal tissue damage but high spatiotemporal resolution. While sophisticated neural probes have been advanced by leaps and bounds in recent decades, electrode-based neural recording and stimulation technologies remain immature in aspects of unsatisfied long-term stability, inconvenience caused by linked transmission lines, inability to achieve subcellular spatial resolution, and limited action sites for functional neural interfaces. For example, foreign-body response[154,155], inflammatory, and neural degeneration induced by materials with unmatched stiffness and biochemical properties would diminish the interface quality over time and fail the long-term functioning. Multiple tethered external electrical wires for electrode inputs and readouts are also problematic regards highly invasive surgical procedures and risks of infection. Even though wireless power and data transmission could eliminate the need for wire connections, the wireless circuit would generate a significant amount of heat from powering and high data rates, causing severe tissue heat-up.

Moreover, the electrode-based approach can barely stimulate target cells at subcellular or organelle levels or at arbitrary deep locations *in vivo*. While nanomaterial-based neurotechnology becomes promising alternatives to electrode-based methods for wireless modulation, subcellular dimensions interfaces, and remote stimulation, the widespread application of neural electrodes in biomedical therapeutics is still hindered by the failure in chronic settings and large-scale interplay.

The overall performance of material-neuron interfaces depends on the biological rationality for long-term stability (biochemical properties, mechanical properties, and stability) and engineered functionality (architecture, electrical properties, and functionalities). Several design principles to tailor materials to achieve long-lasting functioning and improve probe efficacy and functionality are discussed in the preceding section.

Nowadays, investigations of nervous systems and the basic neuron structures have advanced our understanding of neuronal functions and their physiological phenomena. By this point, functional neural interfaces have attracted a research population of different backgrounds and developed diverse multidisciplinary approaches. Engineering of conductive inorganic materials by advanced fabrication techniques and implantation protocols has enabled interrogation with prolonged stability and enhanced signal quality. Besides, biocompatible and mechanically soft neural probes with diversified functions also created new prospects in neuroscience research. Considerable efforts to find a proper balance between physical size, mechanical softness, tissue-friendly biochemical properties, and signal transduction efficiency will further nourish the development of seamless interfaces for continuous sensing or manipulating neural signals over an extended time. It is expected that the future material-neuron interfaces will be smaller, sites-rich, autonomous, wireless, chronically stable, and widely accessible, with each methodology having its strengths and limitations in specific aspects. A dramatic revolution beyond electricity usage has also brought neural interfaces into a new stage, where other physical modalities, such as light and magnetic fields, are explored for neural recording and modulation.

Thanks to the launch of several worldwide large neurotechnology initiatives, for example, the Brain Research through Advancing Innovative Neurotechnologies (BRAIN) in the United States[156], the European Human Brain Project (HBP), the Brain Mapping by Integrated

Neurotechnologies for Disease Studies (Brain/MINDS) project in Japan and the China Brain Project, more creative and scalable approaches with multiple modes, such as those using nanomaterials with projects focused on understanding dynamic actions of the brain, fundamental principles, and origins of disease through ethical scientific research, computing analysis, and worldwide collaboration, are expected to advance bioelectrical interfaces for medical applications. For electrical interfaces, smart designed high-density neural probes with high spatial-temporal resolution and multi-function across various length scales (from subcellular dimensions up to tissue level) will likely promote the translation of cutting-edge neural interfaces from laboratory samples into diagnostics and biomedical treatments of neurological diseases, future commercialized consumer electronics and even entertainment industry. Types of wireless neuromodulation, such as optical, magnetic, or acoustic-based transducers, and interfaces across multiple modalities and multiple biological length scales are also expected to enable target activation or inhibition of neurons and pave the way for addressing unanswered questions in neuroscience and develop future therapeutics for neurological dysfunctions. Exploring synthetic biology and materials science in relation to neural recording and stimulation also offers unique and promising perspectives. Additionally, various advances in micro- and nanostructured materials highlight the expanding frontiers of this field and the vast potential of leveraging machine intelligence and semiconductor technology.

1.4.2 Biology-Guided Biointerfaces in Cardiac Systems

The heart reliably and rhythmically forms electrical pulses that yield contractions to circulate blood throughout the body. However, misfunction in the heart and circulatory system could lead to adverse cardiovascular disease, a leading cause of death. According to an American

Heart Association report, nearly 18 million deaths worldwide were related to cardiovascular disease in 2017[157].

Bioelectrical research applies to the cardiac system because cardiac disease processes and characteristics that necessitate treatment often relate to electrical functionality. For example, heart contractions originate from depolarization at the sinoatrial node and subsequent electrical conduction signaling activity[158]. Currently, treatments are being developed by monitoring and modulating electrical activity *in vitro*, *in vivo*, and *ex vivo*. Biology-guided biointerfaces in Cardiac Systems focus on developments for treating conduction abnormalities and regeneration of injured tissue as these are ways to correct and fix damage from cardiac disease.

In the cardiac system, biology has significantly influenced research developments and targets. Translation to the clinical setting is hindered by rigid designs that cannot conform with heart tissue and incredibly soft structures that cannot maintain functionality. A conventional approach would design a material for cardiac recording to withstand dynamic movements of the heart and maintain biocompatibility. On the contrary, a biology-guided approach might seek to create materials that synergistically interact with cardiac tissue and correct beating abnormalities, yielding a result that supports and amplifies natural processes.

Biology-guided designs include stretchable and flexible materials to withstand the dynamic environment of the heart[159] and some that are soft and rubbery to closely match the modulus of heart tissue and deform and stretch with beating[14]. Biology has also influenced design integration, such as heart implantation through organogenesis to achieve dimensional and spatial resolution with increased conformability[160], formulation of tissue scaffolds to match natural properties[161], and resorbable cardiac pacemakers without leads or batteries[42].

Cardiovascular disease often disrupts proper conduction activity and leads to beating abnormalities that require correction, which is typically assisted with electronic pacemakers. Although electronic pacemakers effectively correct beating, they are generally invasive with biocompatibility issues and have limited resolution. These challenges are being conquered with developments in the extracellular and intracellular recording. For example, vertical plasmonic nanoelectrodes[162] and Pt nanopillars that form a heart-on-a-chip can be used for action potential recording[163]. The idea of a heart-on-a-chip has also been explored in its use as a biosensor array to determine electrical-based cell signaling communication in the development of cardiac spheroids[164]. High-resolution investigation of cardiac systems improves understanding of fundamental functionality and can also be used to screen and treat disease. One development that has enabled high-precision recording is complementary metal-oxide-semiconductor (CMOS) circuits, such as the CMOS nanoelectrode array by Abbott *et al.* that enables single-cell level investigation and stimulation with 1,024 pixels[165]. Another newly developed recording method follows attempts to reduce cytotoxicity and inadvertent cell responses by noninvasive monitoring of mirror charges. Barbaglia *et al.* demonstrate optical-based recording of cardiomyocytes using a device that mirrors ionic currents in a microfluidic chamber[166]. This advancement enables future *in vivo* devices and reliable determination of cardiac cell activities.

Intracellular investigation of electrical activity has been done with structural designs, beginning with silicon nanowires (SiNWs) since they are of a high surface-to-volume ratio and enable electrical readouts with their one-dimensionality. Although SiNWs have enabled intracellular investigation, *in vivo* studies present challenges. Nevertheless, a nongenetic method was demonstrated to investigate intracellular electrical processes *in vivo* using SiNWs hybridized with cells. This wireless process relies on laser stimulation and is of high specificity[167]. The use of

SiNWs has been expanded with other morphological configurations, such as using a mesh composed of polymer and SiNWs to optically modulate cardiac systems, including primary cultured cardiomyocytes and *ex vivo* rat hearts[107]. This composite mesh can also enable modulation in targeted cardiac cells, making it a promising alternative to bulky, invasive, and wire-tethered electrical pacemakers. This approach for regulating heart beating frequency is guided by biological principles behind cardiac conduction disorders that are often characterized by abnormal heart beating.

Other materials have been used for cardiac interfaces. Rastogi *et al.* discussed the use of a graphene-based electrical platform for investigating intracellular and intercellular signaling and communication of human embryonic stem cell-derived cardiomyocytes[168]. The authors synthesized graphene using vapor deposition and gold and graphene microelectrode arrays. This biocompatible and transparent platform is guided by the need to provide an alternative to fluorescent indicators to monitor electrophysiology to better study intracellular and intercellular communication involved in cardiac arrhythmia and neurological disease. Graphene that has been fabricated in other forms has also been used. Dipalo and colleagues demonstrated how a 3D fuzzy graphene microelectrode platform could be used to intracellularly record cardiomyocyte action potentials with high sensitivity[169]. This approach relies on optoporation of the cell membrane, which guided the authors to design out-of-plane graphene flakes to enable tight interfacial interactions between the electrodes and plasma membrane. Recently, Bruno *et al.* reported an optical, nongenetic approach to modulate cardiomyocytes and neurons with plasmonic porous metamaterials[170]. This method enabled optical and label-free stimulation using pulses from a near-infrared laser that is suitable for tissue penetration in biological systems. Furthermore, Nair *et al.* developed flexible electrodes for heart modulation using laser ablation to synthesize silicon

carbide (SiC) from polydimethylsiloxane (PDMS), where a graphite layer forms between the SiC and PDMS[171]. Additionally, carbon-based materials have been used for both *in vivo* and *ex vivo* heart modulation, as demonstrated by Fang *et al.* using monolithic carbon devices with self-assembled hierarchical porosity via a bottom-up approach[172]. As these developments show, achieving cardiac interfaces remains challenging but is advancing. The future of pacemakers likely involves the evolution of electronic pacemakers, including smaller and longer-lasting designs, and the introduction of biological pacemakers, such as those based on cell and gene transfer and transplantation. These developments increase the ability to treat individual patients' needs in a way that will advance medicine.

1.4.3 Biology-Guided Biointerfaces in Microbial Systems

Research has recently focused on ways to investigate microbial systems with a medical-related focus due to discovered links between microbes and biological systems, such as the influence of the microbiome on the human body, development of viral and bacterial infections, and health connections with clean energy to address climate change. Better understanding and formation of interfaces with microbial systems will enable the field of bioelectronics to harness favorable genetic characteristics, evolutionary adaptability, and unique biological processes of microbial systems. Similarly, functionalities of microbes can be enhanced with nanostructured materials, such as gold nanoclusters, to introduce photosynthetic properties to non-photosynthetic bacteria[173].

To investigate microbial systems, methods that are precise and direct are necessary. One way that enables targeted and controlled study is optical stimulation, specifically with Si-based materials. Similar to neural and cardiac interfaces, forming interfaces with bacteria presents

challenges due to variation in length scale and morphology. Approaches that account for microbe morphology and length scale highlight how biology guides microbial system research. Gao *et al.* reported that multiscale and structured silicon materials could modulate bacterial cells and biofilms[174]. This nongenetic method of high spatial and temporal resolution can be used to investigate functions of microbial systems, such as calcium dynamics and biofilm mechanics. Nanowires and microplates were shown to manipulate these bacterial communities and interface with different length scales. For individual planktonic cells of the micrometer length scale, SiNWs were used due to their one-dimensionality and sub-micrometer length that matches tubular bacteria. In contrast, Si microplates, two-dimensional disc structures, were used to interface with the aggregation of cells in biofilms. Improved interfaces can be achieved with mesostructured SiNWs.

Interfacing with microbial systems can also be addressed with biohybrid systems for energy applications. Photosynthetic biohybrid systems can be used in CO_2 reduction and N_2 fixation[175,176]. Su *et al.* reported microbe-guided solar-to-chemical conversion supported by electron transfer[175]. To apply this research to biomedicine, it is possible to use these biosynthetic pathways of bacteria with inorganic light-harvesting processes as alternative activators and energy sources in medical applications in a way that combines living systems with previously nonbiological areas of research. For example, the method to efficiently drive CO_2 fixation with solar energy via close-packed nanowire-bacteria hybrids could potentially be adapted to biological modulation, such as in the ability to use microbes to guide chemical synthesis by using genetically engineered *E. coli* for acetate conversion into biofuels, polymers, and pharmaceuticals[177]. Such an approach draws from and is guided by the symbiotic principles of biology, such as mutualism and commensalism. In this case, microbes help facilitate critical processes while growing in a directed and viable manner.

Understanding the relationship microbes have on other cells has also been of interest. For example, Cervera *et al.* presented theoretical information about how bacteria and non-excitable cells can be synchronized through oscillatory actions[178]. They focus on the properties of single cells relevant to the behavior of multiple cells and the properties at the multicellular level that enable the synchronization of bioelectrical oscillations. These oscillatory dynamics are prevalent in various cell types, such as glioma cells, bacteria, pancreatic islets, and the developmental stages of chicken embryos. This research was motivated by the biological occurrence of oscillations in cell populations and relied on the biological principles of ion channel proteins that control the transmembrane electrical potential in the cell membrane. This model shows the possibility of controlling electrical potential and current to manipulate both excitable and non-excitable cells. The applications of work are diverse and quite relevant to current trends, especially those in regenerative medicine and synthetic biology[179].

1.5 Rational Design of Biointerfaces

The exact causes of progressive biointerface failures are multifaceted and complex, and they can result from any combination of various factors, including mechanical breakdown (e.g., fracture of electrode shank), chemical degradation (e.g., electrode delamination and corrosion), device micromotion, and, most importantly, a cascade of biological events, which also called foreign-body responses.

Immediately after material insertion into the neuron tissue, microglia and astrocytes respond to the foreign bodies by changing their morphology and upregulating neuroinflammatory responses[180–183]. Microglial proliferate and migrate toward the foreign bodies to form cellular encapsulation, which is further enriched by activated astrocytes and cellular debris. The buildup

of the cellular sheath would gradually lead to the separation of functioning sites from nearby neurons and eventually insulation that significantly limits the ion diffusion, making it physically and electrically challenging to sense or modulate any activity. Over time, the activated microglial cells also create an inhibitory environment for neurite extension and accumulate necrotic substances in the immediate vicinity. Upon acute vessel rupture, the breach of the blood-brain barrier (BBB) and blood-nerve barrier (BNB), initiation of macrophages and phagocytosis, activation of the caspase-1 enzyme and pro-inflammatory cytokines, and the release of reactive oxygen intermediates are all dominant factors limiting the longevity of neuronal recordings. Besides, associated enzymatic dissolution and saline or acid-caused surface corrosion of materials also contribute to probe failures by increasing the impedance at the interfaces. The complex array of foreign-body responses is present in all implanted materials to a varying degree. The progressive function deterioration of implanted materials ranges from days to months.

Previous studies have suggested that the interplaying biochemical properties, mechanical properties, and physical stability of the electrode-tissue interfaces are all crucial factors for alleviating neuroinflammatory responses (for example, the responses of glial cells) and tissue level failures (such as reduced neuronal activity and fibrosis or astrogliosis-caused tissue impedance increase).

Research has been working towards utilizing suitable materials with rational design strategies to achieve long-lasting functional materials in biointerface study and treatments of physiological disorders, and it is crucial to balance biological rationalities in the first place and satisfy the following requirements.

1.5.1 Biosafety

Safety is one of the most paramount neuroethical concerns that requires all material-based interfaces to consider and address responsibly[184]. Materials employed to construct any part of the implant, including a substrate, encapsulation or passive layer, and recording sites, should be biologically safe, not toxic, allergenic, or harmful to adjacent tissue. For example, none of the materials should release chemical byproducts, such as reactive oxidative species (ROS), which may cause DNA or RNA damage, induce necrotic response and cell death, and also contribute to material corrosion and degradation. Materials like silver, cobalt, and copper should be avoided as they provoke adverse health effects, such as severe immune response and induced biochemical reactions during operation. Three main integration strategies to support the normal function of both the implants and surrounding tissues are chemically inert surface coatings or alloys to prevent delamination and corrosion, biomimetic polymer-based coating layers to provide biochemical similarities and improve cell adhesion, and controlled drug release systems or passive immunosuppressant-diffusion coating to minimize the activated neuroinflammatory pathways.

1.5.2 Tissue-Like Mechanical Properties

Thick and rigid materials are highly invasive and not well tolerated by the nervous tissue. Rigidity upregulates molecular determinants of inflammation in glia through several signaling molecules, such as IL-1β and TNFα[185]. Mechanical dissimilarities from their neuron targets always lead to excessive foreign body response, for example, neuronal loss and neuroinflammation, which disables interfaces within a short period and further causes measurement instabilities. The Young's modulus of neural tissue ranges from a few hundred pascals (Pa) to a few thousand pascals (kPa); for example, brain ECM is around 300–3,000 kPa [186], which is similar to jelly and varies based on

specific tissue content and orientations. To establish a physiological interface bridging stiff electronics and soft neural tissue, intelligent design strategies and appropriate material engineering, for example, micropatterning of ultrathin materials into flexible fibers or meshes, need to be considered to achieve body compliance[187–189]. Materials should be soft enough to allow seamless integration and withstand small displacement between pulsating tissue and static materials, especially when applied *in vivo* chronically. However, the materials should also be strong enough to avoid buckling during the implant procedure and maintain the mechanical integrity following implantation.

1.5.3 Physical Stability

The material must be acceptably stable for surgical procedures and the duration of use. The structures, interconnections, electrical impedance, conductivity, and corrosion-protecting insulation must remain intact. Any delamination, breakage, corrosion, or degradation may significantly lose unit amplitudes or signal-to-noise ratio (SNR) that hinders the signal interpretation. Shifting of impedance value would risk the restriction of charge injection. Pure capacitive (double-layer charging) transfer can no longer be maintained once the voltage at the electrode-electrolyte interface breaches the safe charge injection limits. Irreversible Faradic reactions (electrochemical reduction or oxidation reactions) will then occur and cause electrolysis of water, pH changes, production of reactive species, further tissue damage, and material corrosion or degradation. In a vicious circle, tissue damage and material failure could further increase the impedance by neuroinflammation or production of oxidative or toxic species, respectively.

Physical stability, mechanical properties, and biosafety or biocompatibility involve a high level of interplay; combinatorial strategies must be applied to bridge the soft, molecular-rich,

evolving tissue with the stiff and static materials. This complexity necessitates the development of stable and biocompatible materials of tissue-like mechanical properties to provide a robust and long-term interface for faithfully recording and stimulating biological activities.

1.5.4 Engineered Functionality

While a material-driven pursuit emphasizes recapitulating biochemical and mechanical properties of tissues to reduce neuroinflammatory responses and ensure chronic functionality, the design and engineering of inorganic materials is the prerequisite for functional biointerfaces that allow efficacious readout and control. Current efforts to tailor materials, regarding their electrical properties (e.g., impendence and charge injection capacity), architectures (e.g., engineered structures and dimensions), and function modalities (e.g., incorporated drug delivery or wireless functional transductions), hold the key to improving the probe faithfulness, efficacy, and functionality and moving beyond the limitations, for example, large-scale interrogation with high spatiotemporal resolution and wireless non-genetic modulation.

Electrical properties are the most essential and fundamental considerations for building a bioelectronic interface. The carrier mobility, dopant, bandgap structure, Fermi level, impedance, and charge injection capacity all determine the efficacy of a material. For electrical recording, appropriate conductivity is crucial to obtain a high signal-to-noise ratio of recording signals. For electrical stimulation, an adequately low impedance is a vital parameter for suppressing tissue damage. Materials with low impedance, thus high charge injection limit, deliver charges to the interfaced tissue through pure capacitive mechanisms via double-layer charging. As sufficient charge is required to elicit action potentials or activate target neurons, a large charge injection

capacity is preferred. However, materials with high impedance have limited charge storage capacities.

Moreover, the intrinsic charge injection limit restricts the magnitude of the voltage that the surface could hold. Beyond this safety level, also known as the water window, faradaic reactions occur and electrochemically change the surrounding biological fluids and induce cytotoxicity and electrode degradation. On the other hand, high impedance also weakens the electrical recording of bioelectrical activities because of the high resistance of the current flow. Charge injection capacity can be improved by either increasing surface area or texturing materials with low electrochemical impedance. The electrochemical stability of materials should also be considered.

1.5.5 Architecture

Depending on the interfacing sites, materials of suitable sizes and geometries in 0D particles, 1D wires/fibers, 2D planar probes, or 3D-distributed interfaces have been developed for interfacing neurons from the subcellular organelle level to the tissue/organ level. Besides microscale electrodes and probes, which include silicon-based rigid electrodes (such as the Michigan probe and Utah array) and polymer-based multifunctional fibers and stretchable elastomeric planar electrodes (for example, the e-dura), new probe architectures have been developed for neural interfaces, for instance, nanostructured arrays, ultrathin sheet-like electrodes, syringe-injectable freestanding meshes, bioinspired-biomimetic neural-like electronics (NeuE), and nanosized FET-based bioelectronics. Traditional large and rigid single-site probe or planar electrodes evolve towards thin, compliant, multi-site geometrically different ones to improve interface quality, resolution, and efficiency and combat neuroinflammation. The state-of-the-art architecture designs focusing on miniaturizing implant footprints ensure high-resolution biointerfaces and reduced tissue damage. Structure engineering to incorporate compliance by

applying soft materials or ultrathin wave-like geometries enables long-lasting conformal devices. Ongoing research using the proximity of multiple electrodes for multiplexed parallel recordings or stimulation provides large-scale integration, helps simultaneous signal collections, and reduces the use of animals and their maintenance cost. The integration of secondary structure modifications further enables high-performance biointerfaces[190]. These modifications include but are not limited to the surface coating and texturing, porosity, flexible encapsulations and subtracts, incorporation of transparency, stretchability, bio-resorbability, high-density patterns, and channels for drug delivery.

1.5.6 Functionalities

As a concomitant upgrade in electrode performance and scalability, the development of functionalities other than electricity was factored in and assembled into the integrated probes intended for a more sophisticated investigation of biological activities, for example, drug delivery, optogenetics, MRI or acoustic imaging, and wireless signal transductions. Controlled release systems via either bio-conjugated polymer coating or engineered microfluidic channels offer local administration of anti-inflammatory drugs, neurotransmitters, and chemo-genetic molecules, providing a more physiological environment and improving chronic tissue integration and signal sensitivity. Engineering with optogenetics using micro-light-emitting devices (μLEDs)[120] or optical fibers[191] enables simultaneous light modulation and electrical readouts/input because no interplay exists between electrical signals and optical ones, achieving precise and selective recording upon genetically defined light-sensitive populations. MRI-compatible neural probes fabricated with nonferromagnetic materials that have no susceptibility to magnetic fields, such as titanium, copper, graphene, or CNT, make it possible to combine global MRI mapping of

bioelectrical activity with high-resolution electrophysiological recordings without interference. Last but not least, freestanding nano-transducers achieve new biointerfaces suitable for wireless single-cell or subcellular-level modulation via various mechanisms across multiple primary-to-secondary modalities, for example, photo-thermal and magneto-mechanical stimulations, and the usage of ultrasonic transducers can incorporate ultrasonic beam-mediated neuromodulation with simultaneous tissue images. Unique diversified functionalities using appropriate materials with innovative design strategies and integrated fabrication approaches will further catalyze a broader expansion of the functional material toolkit for biointerfaces and a more comprehensive platform for simultaneous stimulation, electrophysiological recording, and tissue imaging.

1.6 Bibliography

1. Pavlov, V. A. & Tracey, K. J. Bioelectronic medicine: updates, challenges and paths forward. *Bioelectron. Med.* **5**, 1 (2019).
2. Sanjuan-Alberte, P. & Rawson, F. J. Engineering the spark into bioelectronic medicine. *Ther. Deliv.* **10**, 139–142 (2019).
3. McLaughlin, K. A. & Levin, M. Bioelectric signaling in regeneration: mechanisms of ionic controls of growth and form. *Dev. Biol.* **433**, 177–189 (2018).
4. Sanjuan-Alberte, P., Alexander, M. R., Hague, R. J. M. & Rawson, F. J. Electrochemically stimulating developments in bioelectronic medicine. *Bioelectron. Med.* **4**, 1 (2018).
5. Chen, R., Canales, A. & Anikeeva, P. Neural recording and modulation technologies. *Nat. Rev. Mater.* **2**, 16093 (2017).
6. Rotenberg, M. Y. & Tian, B. Talking to cells: semiconductor nanomaterials at the cellular interface. *Adv. Biosyst.* **2**, 1700242 (2018).
7. Rastogi, S. K., Kalmykov, A., Johnson, N. & Cohen-Karni, T. Bioelectronics with nanocarbons. *J. Mater. Chem. B* **6**, 7159–7178 (2018).
8. Wellman, S. M. *et al.* A materials roadmap to functional neural interface design. *Adv. Funct. Mater.* **28**, 1701269 (2018).
9. Ma, Y. *et al.* Mammalian near-infrared image vision through injectable and self-powered retinal nanoantennae. *Cell* **177**, 243-255.e15 (2019).
10. Maya-Vetencourt, J. F. *et al.* Subretinally injected semiconducting polymer nanoparticles rescue vision in a rat model of retinal dystrophy. *Nat. Nanotechnol.* **15**, 698–708 (2020).
11. Sung, C. *et al.* Multimaterial and multifunctional neural interfaces: from surface-type and implantable electrodes to fiber-based devices. *J. Mater. Chem. B* **8**, 6624–6666 (2020).
162. Hong, G. & Lieber, C. M. Novel electrode technologies for neural recordings. *Nat. Rev. Neurosci.* (2019).
13. Frank, J. A., Antonini, M.-J. & Anikeeva, P. Next-generation interfaces for studying neural function. *Nat. Biotechnol.* (2019)
14. Sim, K. *et al.* An epicardial bioelectronic patch made from soft rubbery materials and capable of spatiotemporal mapping of electrophysiological activity. *Nat. Electron.* **3**, 775–784 (2020).
15. Jiang, Y. *et al.* Rational design of silicon structures for optically controlled multiscale biointerfaces. *Nat. Biomed. Eng.* **2**, 508–521 (2018).
16. Abbott, J. *et al.* A nanoelectrode array for obtaining intracellular recordings from thousands of connected neurons. *Nat. Biomed. Eng.* **4**, 232–241 (2020).
17. Piccolino, M. Animal electricity and the birth of electrophysiology: the legacy of Luigi Galvani. *Brain Res. Bull.* **46**, 381–407 (1998).
18. Zhang, A. & Lieber, C. M. Nano-bioelectronics. *Chem. Rev.* **116**, 215–257 (2016).
19. Kornreich, B. G. The patch clamp technique: principles and technical considerations. *J. Vet. Cardiol.* **9**, 25–37 (2007).
20. Spira, M. E. & Hai, A. Multi-electrode array technologies for neuroscience and cardiology. *Nat. Nanotechnol.* **8**, 83–94 (2013).
21. Sakmann, B. & Neher, E. Patch clamp techniques for studying ionic channels in excitable membranes. *Annu Rev Physiol* **46**, 455–472 (1984).
22. Obien, M. E. J., Deligkaris, K., Bullmann, T., Bakkum, D. J. & Frey, U. Revealing neuronal function through microelectrode array recordings. *Front. Neurosci.* **8**, (2015).

23. Campbell, P. K., Jones, K. E., Huber, R. J., Horch, K. W. & Normann, R. A. A silicon-based, three-dimensional neural interface: manufacturing processes for an intracortical electrode array. *Ieee Trans Biomed Eng* **38**, 758–768 (1991).
24. Drake, K. L., Wise, K. D., Farraye, J., Anderson, D. J. & BeMent, S. L. Performance of planar multisite microprobes in recording extracellular single-unit intracortical activity. *Ieee Trans Biomed Eng* **35**, 719–732 (1988).
25. Bruegmann, T. Optogenetic control of heart muscle *in vitro* and *in vivo*. *Nat Methods* **7**, 897–900 (2010).
26. Magown, P. Direct optical activation of skeletal muscle fibres efficiently controls muscle contraction and attenuates denervation atrophy. *Nat Commun* **6**, 8506 (2015).
27. Montgomery, K. L. Beyond the brain: optogenetic control in the spinal cord and peripheral nervous system. *Sci Transl Med* **8**, 337rv5 (2016).
28. Macherey, O. & Carlyon, R. P. Cochlear implants. *Curr. Biol.* **24**, R878–R884 (2014).
29. Wagner, F. B. *et al.* Targeted neurotechnology restores walking in humans with spinal cord injury. *Nature* **563**, 65 (2018).
30. Shmoel, N. Multisite electrophysiological recordings by self-assembled loose-patch-like junctions between cultured hippocampal neurons and mushroom-shaped microelectrodes. *Sci Rep* **6**, 27110 (2016).
31. Robinson, J. T. Vertical nanowire electrode arrays as a scalable platform for intracellular interfacing to neuronal circuits. *Nat Nanotechnol* **7**, 180–184 (2012).
32. Xie, C. Intracellular recording of action potentials by nanopillar electroporation. *Nat Nanotechnol* **7**, 185–190 (2012).
33. Tian, B. Three-dimensional, flexible nanoscale field-effect transistors as localized bioprobes. *Science* **329**, 830–834 (2010).
34. Formento, E. *et al.* Electrical spinal cord stimulation must preserve proprioception to enable locomotion in humans with spinal cord injury. *Nat. Neurosci.* **21**, 1728–1741 (2018).
35. Tracey, K. J. Reflex control of immunity. *Nat Rev Immunol* **9**, 418–428 (2009).
36. Polikov, V. S., Tresco, P. A. & Reichert, W. M. Response of brain tissue to chronically implanted neural electrodes. *J Neurosci Methods* **148**, 1–18 (2005).
37. Schaumann, E. N. & Tian, B. Biological interfaces, modulation, and sensing with inorganic nano-bioelectronic materials. *Small Methods* **4**, 1900868 (2020).
38. Acarón Ledesma, H. *et al.* An atlas of nano-enabled neural interfaces. *Nat. Nanotechnol.* **14**, 645–657 (2019).
39. Fattahi, P., Yang, G., Kim, G. & Abidian, M. R. A review of organic and inorganic biomaterials for neural interfaces. *Adv. Mater.* **26**, 1846–1885 (2014).
40. Jiang, Y. & Tian, B. Inorganic semiconductor biointerfaces. *Nat. Rev. Mater.* **3**, 473–490 (2018).
41. Bai, W. *et al.* Bioresorbable photonic devices for the spectroscopic characterization of physiological status and neural activity. *Nat. Biomed. Eng.* **3**, 644–654 (2019).
42. Choi, Y. S. *et al.* Fully implantable and bioresorbable cardiac pacemakers without leads or batteries. *Nat. Biotechnol.* **39**, 1228–1238 (2021).
43. Fang, H. *et al.* Capacitively coupled arrays of multiplexed flexible silicon transistors for long-term cardiac electrophysiology. *Nat. Biomed. Eng.* **1**, 0038 (2017).
44. Peled, A., Pevzner, A., Peretz Soroka, H. & Patolsky, F. Morphological and chemical stability of silicon nanostructures and their molecular overlayers under physiological conditions: towards long-term implantable nanoelectronic biosensors. *J. Nanobiotechnology* **12**, 7 (2014).

45. Chen, Y. W. *et al.* Atomic layer-deposited tunnel oxide stabilizes silicon photoanodes for water oxidation. *Nat. Mater.* **10**, 539–544 (2011).
46. Ji, L. *et al.* A silicon-based photocathode for water reduction with an epitaxial SrTiO3 protection layer and a nanostructured catalyst. *Nat. Nanotechnol.* **10**, 84–90 (2015).
47. Hu, S. *et al.* Amorphous TiO2 coatings stabilize Si, GaAs, and GaP photoanodes for efficient water oxidation. *Science* **344**, 1005–1009 (2014).
48. Cellot, G. *et al.* PEDOT:PSS interfaces support the development of neuronal synaptic networks with reduced neuroglia response *in vitro*. *Front. Neurosci.* **9**, (2016).
49. Sandu, G. *et al.* Mechanochemical synthesis of PEDOT:PSS hydrogels for aqueous formulation of Li-ion battery electrodes. *ACS Appl. Mater. Interfaces* **9**, 34865–34874 (2017).
50. Feiner, R. & Dvir, T. Tissue–electronics interfaces: from implantable devices to engineered tissues. *Nat. Rev. Mater.* **3**, 17076 (2017).
51. Bettinger, C. J. & Bao, Z. Biomaterials-based organic electronic devices. *Polym. Int.* **59**, 563–567 (2010).
52. Yuk, H., Lu, B. & Zhao, X. Hydrogel bioelectronics. *Chem. Soc. Rev.* **48**, 1642–1667 (2019).
53. Yang, C. & Suo, Z. Hydrogel ionotronics. *Nat. Rev. Mater.* **3**, 125–142 (2018).
54. Simon, D. T., Gabrielsson, E. O., Tybrandt, K. & Berggren, M. Organic bioelectronics: bridging the signaling gap between biology and technology. *Chem. Rev.* **116**, 13009–13041 (2016).
55. Fang, Y. *et al.* Recent advances in bioelectronics chemistry. *Chem. Soc. Rev.* **49**, 7978–8035 (2020).
56. Charkhkar, H. Chronic intracortical neural recordings using microelectrode arrays coated with PEDOT–TFB. *Acta Biomater* **32**, (2016).
57. Ryu, M. *et al.* Enhancement of interface characteristics of neural probe based on graphene, ZnO nanowires, and conducting polymer PEDOT. *ACS Appl. Mater. Interfaces* **9**, 10577–10586 (2017).
58. Higgins, S. G. *et al.* High-aspect-ratio nanostructured surfaces as biological metamaterials. *Adv. Mater.* **32**, 1903862 (2020).
59. Someya, T., Bao, Z. & Malliaras, G. G. The rise of plastic bioelectronics. *Nature* **540**, 379–385 (2016).
60. Boutry, C. M. *et al.* Biodegradable and flexible arterial-pulse sensor for the wireless monitoring of blood flow. *Nat. Biomed. Eng.* **3**, 47–57 (2019).
61. Oh, J. Y. *et al.* Stretchable self-healable semiconducting polymer film for active-matrix strain-sensing array. *Sci. Adv.* **5**, eaav3097 (2019).
62. Heo, D. N. *et al.* Flexible and highly biocompatible nanofiber-based electrodes for neural surface interfacing. *ACS Nano* **11**, 2961–2971 (2017).
63. Xie, C. *et al.* Three-dimensional macroporous nanoelectronic networks as minimally invasive brain probes. *Nat. Mater.* **14**, 1286–1292 (2015).
64. Lee, K., Massia, S. & He, J. Biocompatible benzocyclobutene-based intracortical neural implant with surface modification. *J. Micromechanics Microengineering* **15**, 2149–2155 (2005).
65. Kozai, T. D. Y. Ultrasmall implantable composite microelectrodes with bioactive surfaces for chronic neural interfaces. *Nat Mater* **11**, (2012).
66. Yang, X. *et al.* Bioinspired neuron-like electronics. *Nat. Mater.* **18**, 510–517 (2019).
67. Wang, K. *et al.* High-performance graphene-fiber-based neural recording microelectrodes. *Adv. Mater.* **31**, 1805867 (2019).

68. Guan, S. *et al.* Elastocapillary self-assembled neurotassels for stable neural activity recordings. *Sci. Adv.* **5**, eaav2842 (2019).
69. Minev, I. R. *et al.* Electronic dura mater for long-term multimodal neural interfaces. *Science* **347**, 159–163 (2015).
70. Yu, K. J. *et al.* Bioresorbable silicon electronics for transient spatiotemporal mapping of electrical activity from the cerebral cortex. *Nat. Mater.* **15**, 782–791 (2016).
71. Kang, S.-K. *et al.* Bioresorbable silicon electronic sensors for the brain. *Nature* **530**, 71–76 (2016).
72. Pas, J. *et al.* A bilayered PVA/PLGA-bioresorbable shuttle to improve the implantation of flexible neural probes. *J. Neural Eng.* **15**, 065001 (2018).
73. Yoo, J.-M., Song, J.-I., Tathireddy, P., Solzbacher, F. & Rieth, L. W. Hybrid laser and reactive ion etching of Parylene-C for deinsulation of a Utah electrode array. *J. Micromechanics Microengineering* **22**, 105036 (2012).
74. Cheung, K. C., Renaud, P., Tanila, H. & Djupsund, K. Flexible polyimide microelectrode array for *in vivo* recordings and current source density analysis. *Biosens. Bioelectron.* **22**, 1783–1790 (2007).
75. Zhang, J. *et al.* Stretchable transparent electrode arrays for simultaneous electrical and optical interrogation of neural circuits *in vivo*. *Nano Lett.* **18**, 2903–2911 (2018).
76. Tybrandt, K. *et al.* High-density stretchable electrode grids for chronic neural recording. *Adv. Mater.* **30**, 1706520 (2018).
77. Qian, Y. *et al.* 3D manufacture of gold nanocomposite channels facilitates neural differentiation and regeneration. *Adv. Funct. Mater.* **28**, 1707077 (2018).
78. Bareket, L. *et al.* Semiconductor nanorod–carbon nanotube biomimetic films for wire-free photostimulation of blind retinas. *Nano Lett.* **14**, 6685–6692 (2014).
79. Kozai, T. D. Y. *et al.* Chronic *in vivo* evaluation of PEDOT/CNT for stable neural recordings. *IEEE Trans. Biomed. Eng.* **63**, 111–119 (2016).
80. Chernomordik, L. V. & Kozlov, M. M. Mechanics of membrane fusion. *Nat. Struct. Mol. Biol.* **15**, 675–683 (2008).
81. Misra, N. *et al.* Bioelectronic silicon nanowire devices using functional membrane proteins. *Proc. Natl. Acad. Sci.* **106**, 13780–13784 (2009).
82. Zhou, X., Moran-Mirabal, J. M., Craighead, H. G. & McEuen, P. L. Supported lipid bilayer/carbon nanotube hybrids. *Nat. Nanotechnol.* **2**, 185–190 (2007).
83. Tian, B. *et al.* Three-dimensional, flexible nanoscale field-effect transistors as localized bioprobes. *Science* **329**, 830–834 (2010).
84. Lee, J.-H., Zhang, A., You, S. S. & Lieber, C. M. Spontaneous internalization of cell penetrating peptide-modified nanowires into primary neurons. *Nano Lett.* **16**, 1509–1513 (2016).
85. Wang, Y. & Guo, L. Nanomaterial-enabled neural stimulation. *Front. Neurosci.* **10**, (2016).
86. Rivnay, J., Wang, H., Fenno, L., Deisseroth, K. & Malliaras, G. G. Next-generation probes, particles, and proteins for neural interfacing. *Sci. Adv.* **3**, e1601649 (2017).
87. Ellis-Davies, G. C. R. Basics of photoactivation. *Cold Spring Harb. Protoc.* **2009**, pdb.top55 (2009).
88. Anikeeva, P. Optetrode: a multichannel readout for optogenetic control in freely moving mice. *Nat Neurosci* **15**, 163–170 (2011).
89. Yizhar, O. Optogenetics in neural systems. *Neuron* **71**, 9–34 (2011).

90. Wu, F. Monolithically integrated μLEDs on silicon neural probes for high-resolution optogenetic studies in behaving animals. *Neuron* **88**, 1136–1148 (2015).
91. Nagel, G. Channelrhodopsin 2, a directly light-gated cation-selective membrane channel. *Proc Natl Acad Sci Usa* **100**, 13940–13945 (2003).
92. Horton, N. G. *In vivo* three-photon microscopy of subcortical structures within an intact mouse brain. *Nat Photonics* **7**, 205–209 (2013).
93. He, L. Near-infrared photoactivatable control of Ca^{2+} signaling and optogenetic immunomodulation. *E Life* **4**, e10024 (2015).
94. Chen, S. *et al.* Near-infrared deep brain stimulation via upconversion nanoparticle–mediated optogenetics. *Science* **359**, 679–684 (2018).
95. Lin, X. *et al.* Multiplexed optogenetic stimulation of neurons with spectrum-selective upconversion nanoparticles. *Adv. Healthc. Mater.* **6**, 1700446 (2017).
96. Yang, K. *et al.* Photoactive poly(3-hexylthiophene) nanoweb for optoelectrical stimulation to enhance neurogenesis of human stem cells. *Theranostics* **7**, 4591–4604 (2017).
97. Ghezzi, D. *et al.* A polymer optoelectronic interface restores light sensitivity in blind rat retinas. *Nat. Photonics* **7**, 400–406 (2013).
98. Parameswaran, R. & Tian, B. Rational design of semiconductor nanostructures for functional subcellular interfaces. *Acc. Chem. Res.* **51**, 1014–1022 (2018).
99. Murphy, C. J. Gold nanoparticles in biology: beyond toxicity to cellular imaging. *Acc Chem Res* **41**, 1721–1730 (2008).
100. Yoo, S. Photothermal inhibition of neural activity with near-infrared-sensitive nanotransducers. *Acs Nano* **8**, 8040–8049 (2014).
101. Jiang, Y. *et al.* Heterogeneous silicon mesostructures for lipid-supported bioelectric interfaces. *Nat. Mater.* **15**, 1023–1030 (2016).
102. Priolo, F., Gregorkiewicz, T., Galli, M. & Krauss, T. F. Silicon nanostructures for photonics and photovoltaics. *Nat. Nanotechnol.* **9**, 19–32 (2014).
110. Lee, Y. V. & Tian, B. Learning from solar energy conversion: biointerfaces for artificial photosynthesis and biological modulation. *Nano Lett.* (2019).
104. Fang, Y. *et al.* Texturing silicon nanowires for highly localized optical modulation of cellular dynamics. *Nano Lett.* **18**, 4487–4492 (2018).
105. Parameswaran, R. *et al.* Photoelectrochemical modulation of neuronal activity with free-standing coaxial silicon nanowires. *Nat. Nanotechnol.* **13**, 260–266 (2018).
106. Mathieson, K. *et al.* Photovoltaic retinal prosthesis with high pixel density. *Nat. Photonics* **6**, 391–397 (2012).
107. Parameswaran, R. *et al.* Optical stimulation of cardiac cells with a polymer-supported silicon nanowire matrix. *Proc. Natl. Acad. Sci.* **116**, 413 (2019).
108. Patolsky, F., Zheng, G. & Lieber, C. M. Fabrication of silicon nanowire devices for ultrasensitive, label-free, real-time detection of biological and chemical species. *Nat. Protoc.* **1**, 1711–1724 (2006).
109. Luo, Z. *et al.* Atomic gold-enabled three-dimensional lithography for silicon mesostructures. *Science* **348**, 1451–1455 (2015).
118. Jiang, Y. *et al.* Nongenetic optical neuromodulation with silicon-based materials. *Nat. Protoc.* (2019).
111. Efros, A. L. *et al.* Evaluating the potential of using quantum dots for monitoring electrical signals in neurons. *Nat. Nanotechnol.* **13**, 278–288 (2018).

112. Yoo, S., Hong, S., Choi, Y., Park, J.-H. & Nam, Y. Photothermal inhibition of neural activity with near-infrared-sensitive nanotransducers. *ACS Nano* **8**, 8040–8049 (2014).
121. Yadid, M., Feiner, R. & Dvir, T. Gold Nanoparticle-integrated scaffolds for tissue engineering and regenerative medicine. *Nano Lett.* (2019).
114. Paviolo, C. & Stoddart, P. Gold nanoparticles for modulating neuronal behavior. *Nanomaterials* **7**, 92 (2017).
115. Ding, H. *et al.* Microscale optoelectronic infrared-to-visible upconversion devices and their use as injectable light sources. *Proc. Natl. Acad. Sci.* **115**, 6632–6637 (2018).
116. Marshall, J. D. & Schnitzer, M. J. Optical strategies for sensing neuronal voltage using quantum dots and other semiconductor nanocrystals. *ACS Nano* **7**, 4601–4609 (2013).
117. Nag, O. K. *et al.* Quantum dot–peptide–fullerene bioconjugates for visualization of *in vitro* and *in vivo* cellular membrane potential. *ACS Nano* **11**, 5598–5613 (2017).
118. Bahmani Jalali, H. *et al.* Effective neural photostimulation using indium-based type-ii quantum dots. *ACS Nano* **12**, 8104–8114 (2018).
127. Bahmani Jalali, H. *et al.* Biocompatible quantum funnels for neural photostimulation. *Nano Lett.* (2019).
120. Kim, T. -i. *et al.* Injectable, Cellular-scale optoelectronics with applications for wireless optogenetics. *Science* **340**, 211–216 (2013).
121. Tortiglione, C. *et al.* Semiconducting polymers are light nanotransducers in eyeless animals. *Sci. Adv.* **3**, e1601699 (2017).
122. Yoo, S., Park, J.-H. & Nam, Y. Single-cell photothermal neuromodulation for functional mapping of neural networks. *ACS Nano* **13**, 544–551 (2019).
123. Carvalho-de-Souza, J. L. *et al.* Photosensitivity of neurons enabled by cell-targeted gold nanoparticles. *Neuron* **86**, 207–217 (2015).
124. Sytnyk, M. *et al.* Cellular interfaces with hydrogen-bonded organic semiconductor hierarchical nanocrystals. *Nat. Commun.* **8**, (2017).
125. Colombo, E., Feyen, P., Antognazza, M. R., Lanzani, G. & Benfenati, F. Nanoparticles: a challenging vehicle for neural stimulation. *Front. Neurosci.* **10**, (2016).
126. Marino, A. Piezoelectric nanoparticle-assisted wireless neuronal stimulation. *Acs Nano* **9**, 7678–7689 (2015).
127. Gougheri, H. S., Dangi, A., Kothapalli, S.-R. & Kiani, M. A Comprehensive study of ultrasound transducer characteristics in microscopic ultrasound neuromodulation. *IEEE Trans. Biomed. Circuits Syst.* **13**, 835–847 (2019).
128. Ciofani, G. *et al.* Enhancement of neurite outgrowth in neuronal-like cells following boron nitride nanotube-mediated stimulation. *ACS Nano* **4**, 6267–6277 (2010).
129. Marino, A. *et al.* Piezoelectric nanoparticle-assisted wireless neuronal stimulation. *ACS Nano* **9**, 7678–7689 (2015).
130. Royo-Gascon, N., Wininger, M., Scheinbeim, J. I., Firestein, B. L. & Craelius, W. Piezoelectric substrates promote neurite growth in rat spinal cord neurons. *Ann. Biomed. Eng.* **41**, 112–122 (2013).
131. Wu, S. *et al.* Aligned fibrous PVDF-TrFE scaffolds with Schwann cells support neurite extension and myelination *in vitro*. *J. Neural Eng.* **15**, 056010 (2018).
132. Li, Liao, & Tjong. Electrospun polyvinylidene fluoride-based fibrous scaffolds with piezoelectric characteristics for bone and neural tissue engineering. *Nanomaterials* **9**, 952 (2019).

133. Lee, W. *et al.* Transcranial focused ultrasound stimulation of human primary visual cortex. *Sci. Rep.* **6**, (2016).
134. Ye, P. P., Brown, J. R. & Pauly, K. B. Frequency dependence of ultrasound neurostimulation in the mouse brain. *Ultrasound Med. Biol.* **42**, 1512–1530 (2016).
135. Ibsen, S., Tong, A., Schutt, C., Esener, S. & Chalasani, S. H. Sonogenetics is a non-invasive approach to activating neurons in *Caenorhabditis elegans*. *Nat. Commun.* **6**, 8264 (2015).
136. Maresca, D. *et al.* Biomolecular ultrasound and sonogenetics. *Annu. Rev. Chem. Biomol. Eng.* **9**, 229–252 (2018).
137. Wu, X. *et al.* Sono-optogenetics facilitated by a circulation-delivered rechargeable light source for minimally invasive optogenetics. *Proc. Natl. Acad. Sci.* **116**, 26332–26342 (2019).
148. Rapoport, N. Drug-loaded perfluorocarbon nanodroplets for ultrasound-mediated drug delivery. in *Therapeutic Ultrasound* (eds. Escoffre, J.-M. & Bouakaz, A.) vol. 880 221–241 (2016).
139. Airan, R. D. *et al.* Noninvasive targeted transcranial neuromodulation via focused ultrasound gated drug release from nanoemulsions. *Nano Lett.* **17**, 652–659 (2017).
140. Wu, C. *et al.* Recent advances in magnetic-nanomaterial-based mechanotransduction for cell fate regulation. *Adv. Mater.* **30**, 1705673 (2018).
141. Rao, S. *et al.* Remotely controlled chemomagnetic modulation of targeted neural circuits. *Nat. Nanotechnol.* (2019).
142. Chen, R., Romero, G., Christiansen, M. G., Mohr, A. & Anikeeva, P. Wireless magnetothermal deep brain stimulation. *Science* **347**, 1477–1480 (2015).
143. Fiebig, M. Revival of the magnetoelectric effect. *J. Phys. Appl. Phys.* **38**, R123–R152 (2005).
144. Guduru, R. *et al.* Magnetoelectric 'spin' on stimulating the brain. *Nanomed.* **10**, 2051–2061 (2015).
145. Tosha, T. *et al.* Ferritin protein nanocage ion channels. *J. Biol. Chem.* **287**, 13016–13025 (2012).
146. Miao, B. A., Meng, L. & Tian, B. Biology-guided engineering of bioelectrical interfaces. *Nanoscale Horiz.* **7**, 94–111 (2022).
147. Cajavilca, C., Varon, J. & Sternbach, G. L. Luigi Galvani and the foundations of electrophysiology. *Resuscitation* **80**, 159–162 (2009).
148. Thrivikraman, G., Boda, S. K. & Basu, B. Unraveling the mechanistic effects of electric field stimulation towards directing stem cell fate and function: a tissue engineering perspective. *Biomaterials* **150**, 60–86 (2018).
149. Lacour, S. P., Courtine, G. & Guck, J. Materials and technologies for soft implantable neuroprostheses. *Nat. Rev. Mater.* **1**, (2016).
150. Hochberg, L. R. *et al.* Neuronal ensemble control of prosthetic devices by a human with tetraplegia. *Nature* **442**, 164–171 (2006).
159. Smalley, E. The business of brain–computer interfaces. *Nat. Biotechnol.* (2019).
152. Aron, L. & Yankner, B. A. Neural synchronization in Alzheimer's disease. *Nature* **540**, 207–208 (2016).
153. Bronstein, J. M. *et al.* Deep brain stimulation for parkinson disease: an expert consensus and review of key issues. *Arch. Neurol.* **68**, (2011).
154. Lotti, F., Ranieri, F., Vadalà, G., Zollo, L. & Di Pino, G. invasive intraneural interfaces: foreign body reaction issues. *Front. Neurosci.* **11**, (2017).

155. Moshayedi, P. *et al.* The relationship between glial cell mechanosensitivity and foreign body reactions in the central nervous system. *Biomaterials* **35**, 3919–3925 (2014).
156. Jorgenson, L. A. *et al.* The BRAIN Initiative: developing technology to catalyse neuroscience discovery. *Philos. Trans. R. Soc. B Biol. Sci.* **370**, 20140164–20140164 (2015).
157. Virani, S. S. *et al.* Heart disease and Stroke statistics—2020 update: a report from the American Heart Association. *Circulation* **141**, e139–e596 (2020).
158. Cingolani, E., Goldhaber, J. I. & Marbán, E. Next-generation pacemakers: from small devices to biological pacemakers. *Nat. Rev. Cardiol.* **15**, 139–150 (2018).
159. Feiner, R. *et al.* A stretchable and flexible cardiac tissue–electronics hybrid enabling multiple drug release, sensing, and stimulation. *Small* **15**, 1805526 (2019).
160. Li, Q. *et al.* Cyborg organoids: implantation of nanoelectronics via organogenesis for tissue-wide electrophysiology. *Nano Lett.* **19**, 5781–5789 (2019).
161. Li, X.-P. *et al.* Electrical stimulation of neonatal rat cardiomyocytes using conductive polydopamine-reduced graphene oxide-hybrid hydrogels for constructing cardiac microtissues. *Colloids Surf. B Biointerfaces* **205**, 111844 (2021).
162. Dipalo, M. *et al.* Intracellular and extracellular recording of spontaneous action potentials in mammalian neurons and cardiac cells with 3D plasmonic nanoelectrodes. *Nano Lett.* **17**, 3932–3939 (2017).
163. Liu, H. *et al.* Heart-on-a-chip model with integrated extra- and intracellular bioelectronics for monitoring cardiac electrophysiology under acute hypoxia. *Nano Lett.* **20**, 2585–2593 (2020).
164. Kalmykov, A. *et al.* Organ-on-e-chip: three-dimensional self-rolled biosensor array for electrical interrogations of human electrogenic spheroids. *Sci. Adv.* **5**, eaax0729 (2019).
165. Abbott, J. *et al.* CMOS nanoelectrode array for all-electrical intracellular electrophysiological imaging. *Nat. Nanotechnol.* **12**, 460–466 (2017).
166. Barbaglia, A. *et al.* Mirroring action potentials: label-free, accurate, and noninvasive electrophysiological recordings of human-derived cardiomyocytes. *Adv. Mater.* **33**, 2004234 (2021).
167. Rotenberg, M. Y. *et al.* Living myofibroblast–silicon composites for probing electrical coupling in cardiac systems. *Proc. Natl. Acad. Sci.* **116**, 22531 (2019).
168. Rastogi, S. K. *et al.* Graphene microelectrode arrays for electrical and optical measurements of human stem cell-derived cardiomyocytes. *Cell. Mol. Bioeng.* **11**, 407–418 (2018).
169. Dipalo, M. *et al.* Intracellular action potential recordings from cardiomyocytes by ultrafast pulsed laser irradiation of fuzzy graphene microelectrodes. *Sci. Adv.* **7**, eabd5175 (2021).
170. Bruno, G. *et al.* All-optical and label-free stimulation of action potentials in neurons and cardiomyocytes by plasmonic porous metamaterials. *Adv. Sci.* **8**, 2100627 (2021).
171. Nair, V. *et al.* Laser writing of nitrogen-doped silicon carbide for biological modulation. *Sci. Adv.* **6**, eaaz2743 (2020).
172. Fang, Y. *et al.* Micelle-enabled self-assembly of porous and monolithic carbon membranes for bioelectronic interfaces. *Nat. Nanotechnol.* **16**, 206–213 (2021).
173. Zhang, H. *et al.* Bacteria photosensitized by intracellular gold nanoclusters for solar fuel production. *Nat. Nanotechnol.* **13**, 900–905 (2018).
174. Gao, X. *et al.* Structured silicon for revealing transient and integrated signal transductions in microbial systems. *Sci. Adv.* **6**, eaay2760 (2020).

175. Su, Y. *et al.* Close-packed nanowire-bacteria hybrids for efficient solar-driven CO_2 fixation. *Joule* **4**, 800–811 (2020).
176. Sakimoto, K. K., Kornienko, N. & Yang, P. Cyborgian material design for solar fuel production: the emerging photosynthetic biohybrid systems. *Acc. Chem. Res.* **50**, 476–481 (2017).
177. Cestellos-Blanco, S., Zhang, H., Kim, J. M., Shen, Y. & Yang, P. Photosynthetic semiconductor biohybrids for solar-driven biocatalysis. *Nat. Catal.* **3**, 245–255 (2020).
178. Cervera, J., Manzanares, J. A., Mafe, S. & Levin, M. Synchronization of bioelectric oscillations in networks of nonexcitable cells: from single-cell to multicellular states. *J. Phys. Chem. B* **123**, 3924–3934 (2019).
179. Selberg, J., Gomez, M. & Rolandi, M. The potential for convergence between synthetic biology and bioelectronics. *Cell Syst.* **7**, 231–244 (2018).
180. Marin, C. Biocompatibility of intracortical microelectrodes: current status and future prospects. *Front. Neuroengineering* **3**, (2010).
181. Kozai, T. D. Y., Jaquins-Gerstl, A. S., Vazquez, A. L., Michael, A. C. & Cui, X. T. Brain tissue responses to neural implants impact signal sensitivity and intervention strategies. *ACS Chem. Neurosci.* **6**, 48–67 (2015).
182. Salatino, J. W., Ludwig, K. A., Kozai, T. D. Y. & Purcell, E. K. Glial responses to implanted electrodes in the brain. *Nat. Biomed. Eng.* **1**, 862–877 (2017).
183. Wellman, S. M. & Kozai, T. D. Y. *In vivo* spatiotemporal dynamics of NG2 glia activity caused by neural electrode implantation. *Biomaterials* **164**, 121–133 (2018).
195. Cabrera, L., Sadle, C. & Purcell, E. Neuroethical considerations of high-density electrode arrays. *Nat. Biomed. Eng.* (2019).
185. Ereifej, E. S., Cheng, M. M.-C., Mao, G. & VandeVord, P. J. Examining the inflammatory response to nanopatterned polydimethylsiloxane using organotypic brain slice methods. *J. Neurosci. Methods* **217**, 17–25 (2013).
186. Miller, K., Chinzei, K., Orssengo, G. & Bednarz, P. Mechanical properties of brain tissue in-vivo: experiment and computer simulation. *J. Biomech.* **33**, 1369–1376 (2000).
198. Park, S., Loke, G., Fink, Y. & Anikeeva, P. Flexible fiber-based optoelectronics for neural interfaces. *Chem. Soc. Rev.* (2019).
199. Wang, L. *et al.* Application challenges in fiber and textile electronics. *Adv. Mater.* 1901971 (2019).
189. Shi, J. & Fang, Y. Flexible and implantable microelectrodes for chronically stable neural interfaces. *Adv. Mater.* **31**, 1804895 (2019).
190. Kim, Y. *et al.* Nano-architectural approaches for improved intracortical interface technologies. *Front. Neurosci.* **12**, (2018).
191. Canales, A. Multifunctional fibers for simultaneous optical, electrical and chemical interrogation of neural circuits *in vivo*. *Nat Biotechnol* **33**, (2015)

Chapter 2. Porous and Monolithic Carbon Bioelectronic Interfaces: New Self-Assembly Bottom-Up Fabrication

2.1 Introduction

Contributing to our modern understanding of biological dynamics and function by allowing macro-scale modulation of biological activity, most applications in bioelectronics, including medicinal delivery, biosensing, and electrical regulation of tissues and organs, require macro-level interfaces[1–4]. Moreover, they hold great therapeutic potential for treating many biological disorders, including Parkinson's disease, congenital heart defects, and paralysis. However, macro-scale bioelectronic devices usually require high charge injections to biological systems, yielding deep-penetrating electrical fields that produce unintended side effects in surrounding tissues and organs. Besides, a faradaic reaction can also occur at the biointerfaces and generate harmful reactive species, corrode electrodes, and permanently damage adjacent tissues[5]. On the other hand, macro-scale bioelectronic devices always exhibit inefficient architectures with poor spatial resolution at biointerfaces.

Typically, reducing the size of electrodes for minimally invasive biointerfaces and spatially confined electric fields compromises the charge injection limit of the device. To combat this, functional coating layers with carbon materials, such as graphene and carbon nanotubes (CNTs), are widely used in traditional electrodes to reduce the impedance at the electrode junctions and increase the charge transfer rate[6–8]. However, during carbon coatings procedures, the required polymer binding process can result in problematic 'dead' volumes or surfaces, increased total device thickness, and reduced flexibility or bendability at the biointerfaces[9]. Moreover, the potential production of freestanding carbon nanostructures can result in cytotoxicity *in vivo*[10,11].

Nevertheless, carbon materials have been advancing modern electronics in multiple areas, such as supercapacitor power sources[12,13] and stretchable microelectrodes for biointerfaces[14–16], due to their excellent charge storage and low power consumption[17]. Thus, carbon is still a great candidate for modern high-performance electronics.

The use of conducting polymers in bioelectronics for biological modulation is also widespread because of their excellent electronic conductivity and mechanical softness[18,19]. However, unlike inorganic devices, conductive hydrogels are not as electrochemically stable as inorganic devices, particularly in terms of degradation during repetitive charge injections and swelling during long-term soaks in liquid solutions[20,21].

We rationally developed porous and monolithic carbon membranes for bioelectronic interfaces according to the above reasons. The porosity enables a tight and mechanical compliant biointerface by increasing surface roughness and reducing young's modulus. A micelle-enabled self-assembly bottom-up fabrication route was exploited to produce an adhesive-free, carbon-based, large-scale micro-supercapacitor device. Micelle-enabled preparation of porous monolithic carbon does not produce isolated CNTs, which eliminates the risk of *in vivo* toxicity associated with free carbon nanostructures. This device can modulate the rate of contraction of primary cardiomyocytes (CMs) to the target frequency *in vitro*, the electrophysiological control of the isolated cardiac and retinal tissue *ex vivo*, and the capacitive modulation of sciatic nerves *in vivo*. Overall, the micro-supercapacitor device is flexible, biocompatible, and capable of low current bioelectric modulation. We extended the use of carbon from functional coating to the complete electrode in bioelectronics devices and led the way to expand platforms used in energy research to new applications in bioelectronics and biological interfaces.

2.2 Results and Discussion

2.2.1 Carbon Membrane Synthesis and Characterization

We adopted a bottom-up approach to directly prepare monolithic (*i.e.*, binder-free) and hierarchical carbon membranes. Nanoscale micelles were prepared through biphasic interaction between triblock copolymer Pluronic F127 (template) and resin (precursor) in ethanol. Following solvent evaporation-induced self-assembly, the micelles were carbonized into mesoporous carbon membranes (**Fig. 2-1a**). This led to highly ordered mesostructures with a uniform pore size of 7 nm. The addition of ~200 nm-sized silica (SiO_2) spheres into the Pluronic F127 and resin mixture during the membrane preparation introduced macroporous (*i.e.*, pore size >50 nm) structures (**Fig. 2-1b**). The fabrication scheme permitted the layer-by-layer assembly of mesoporous carbon by spin coating, where the thickness and porosity of individual layers could be controlled (**Fig. 2-1c**). While the mesoporous film had Young's modulus and hardness of 25.30 GPa and 3.82 GPa, respectively, the addition of ~700 nm of the macroporous layer reduced these values to 4.20 GPa (modulus) and 0.69 GPa (hardness) (**Fig. 2-2**). The large surface area of the hierarchical membrane leads us to hypothesize that efficient ion transport during charging and discharging can occur, making the device suitable for biological modulation when biointerfaces are formed.

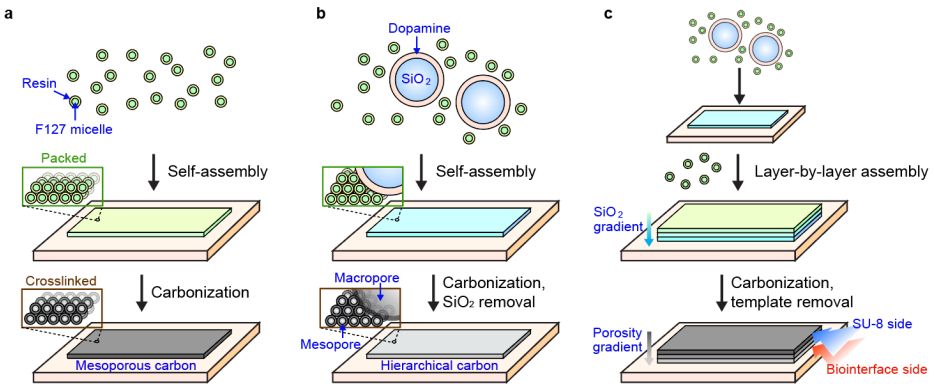

Figure 2-1. Preparation route of the hierarchical porous carbon. a. Synthesis of mesoporous

Figure 2-1, continued. carbon. **b.** Synthesis of hierarchical carbon containing both mesopores and macropores. **c.** Layer-by-layer assembly of carbon layers creating a porosity gradient. The bottom layer of the carbon membranes will become the side for biointerface formation after the device fabrication is completed. Figure reproduced from Ref. 22.

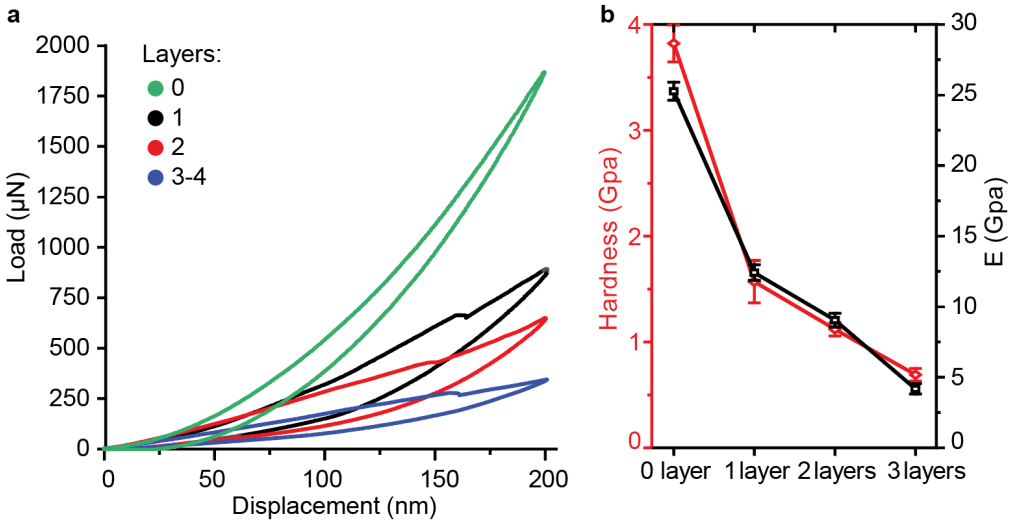

Figure 2-2. Mechanical properties of the hierarchical porous carbon film. a. Load versus displacement plots of the hierarchical porous carbon film measured with a nano-indenter. Each sample has 0, 1, 2, or 3–4 macropore layers. The experiment was repeated four times at various locations on each sample. **b.** Calculated hardness and Young's modulus from the load versus displacement plots (mean ± s.e.m.). As the number of layers increases, the Young's modulus and hardness decrease, indicating that the film becomes softer. Figure reproduced from Ref. 22.

2.2.2 Micro-Supercapacitor Fabrication and Characterization

We designed and fabricated a micro-supercapacitor-like device to achieve rapid ion modulation. Photo-patternable, mechanically flexible, and chemically stable SU-8 film was used

as the substrate (**Fig. 2-3**). The device was designed such that the microfabricated porous carbon electrodes created an interdigitated pattern on top of a ~10 µm-thick SU-8 mesh substrate. The SU-8 mesh substrate has holes to facilitate the passage of liquids. Since SU-8 is incompatible with the carbonization conditions under high temperature, all photolithography processes must be performed on the fully carbonized membrane. To avoid difficult substrate transfer steps, we followed an 'upside-down' fabrication method, where the last step releases the device from the substrate and exposes the side for potential biointerfaces. This fabrication technique requires the softer biointerface layer on the bottom of the as-made membrane; hence the layer-by-layer assembly has to start from the layer that yields macropores (**Fig. 2-4**).

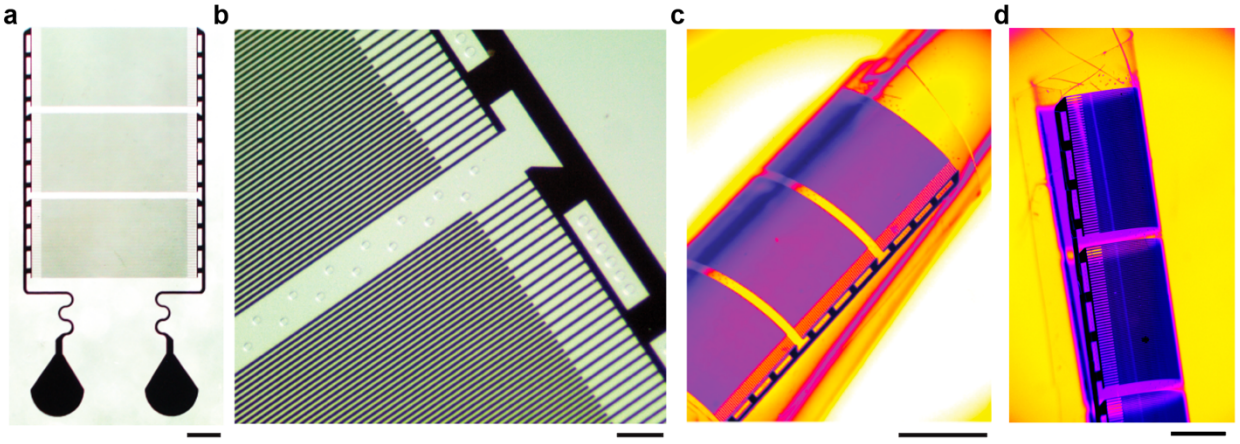

Figure 2-3. Photographs of the micro-supercapacitor-like device. a. An optical image of the hierarchical porous carbon micro-supercapacitor device. Scale bar, 1 mm. **b.** A close-up view of the hierarchical porous carbon micro-supercapacitor device. The SU-8 mesh substrate has holes to facilitate the passage of liquids. Scale bar, 200 µm. **c.** A micro-supercapacitor-like device conforms around a cylindrical holder, demonstrating its mechanical compliance. Scale bar, 2 mm. **d.** A curved free-standing micro-supercapacitor-like device, showing its mechanical compliance. Scale bar, 1 mm. Figure reproduced from Ref. 22.

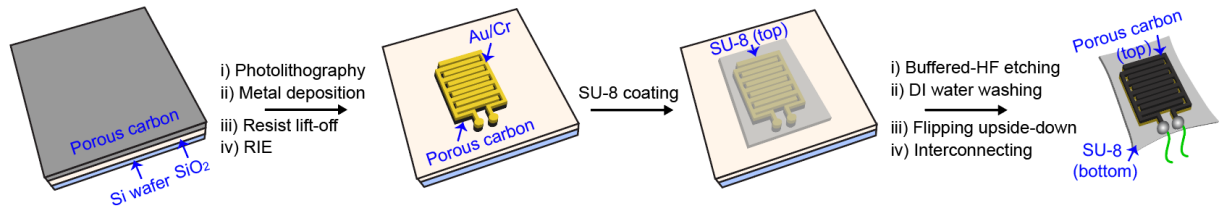

Figure 2-4. Overview of the flexible device fabrication workflow. RIE, reactive ion etching; HF, hydrofluoric acid. Figure reproduced from Ref. 22.

Finite element simulations of the electrolyte potentials between two comb-like electrodes revealed ion transport gradients (**Fig. 2-5**). The electric field distribution at the cross-section of the interdigitated comb-like structure was compared with a simple two-electrode model of the same electrode area (**Fig. 2-6**). A smaller field distribution height on the z-axis for the micro-supercapacitor signified a more localized and refined electrical field with much less penetration depth than the simple two-electrode model (**Fig. 2-6**).

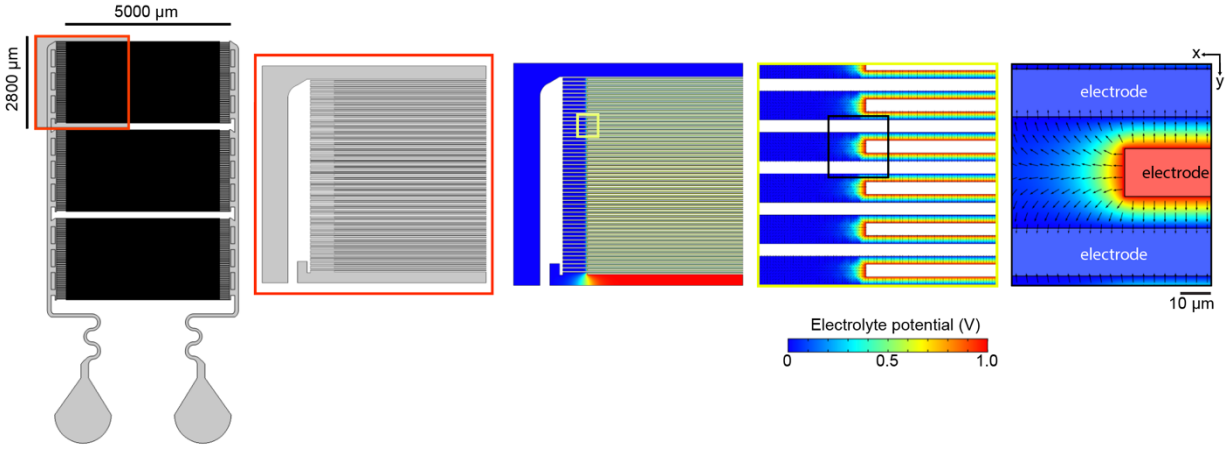

Figure 2-5. COMSOL simulation of the 2D electrolyte potential. The color indicates the electrolyte potentials in the gap between the two comb-like electrodes, where a relative voltage of 1 V was applied. Figure reproduced from Ref. 22.

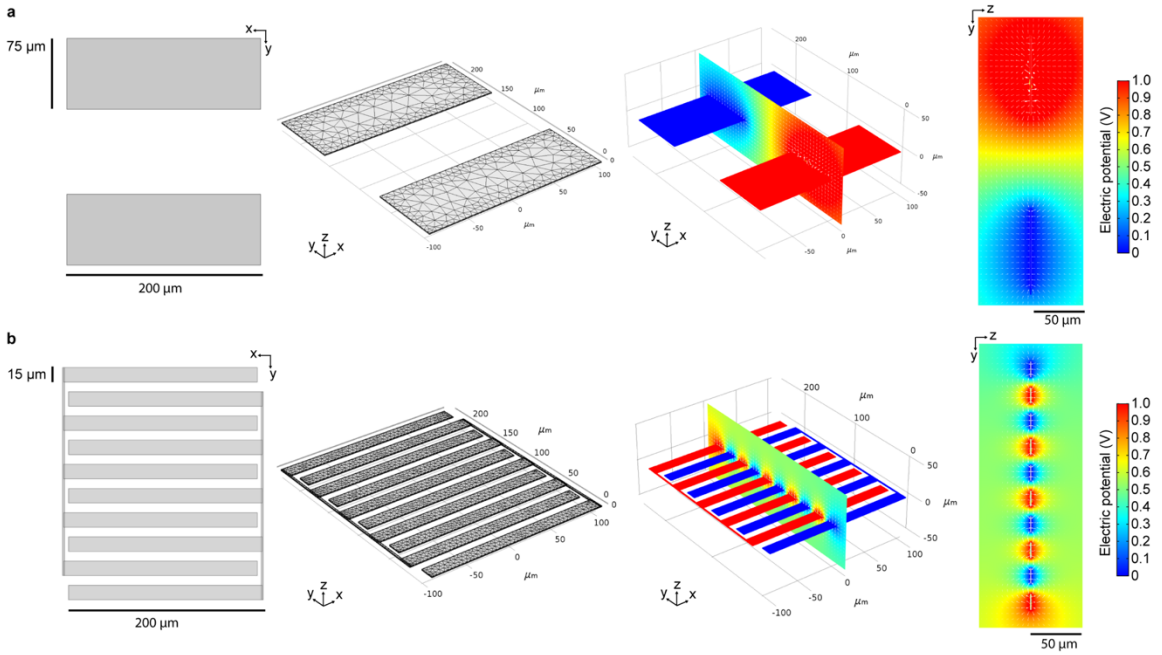

Figure 2-6. COMSOL simulation for 3D electric potential distribution. a. 3D electric potential distribution of a simplified two planar electrode system. The electric potential at the cross-section spreads up to more than 50 µm space. **b.** 3D electric potential distribution of a micro-supercapacitor model with a pair of five-prong comb-like electrodes. The electric potential at the cross-section shows a much refined and localized field. Figure reproduced from Ref. 22.

The micro-supercapacitor was then used directly in electrochemical tests using culture media as electrolyte without any binder or additives. The electrochemical performance of the micro-supercapacitor was calculated by cyclic voltammogram (CV) analysis using three-electrode measurements. The capacitive behavior of the micro-supercapacitor was also measured by the galvanostatic charge/discharge method at varied current densities and time (**Fig. 2-7**). CV was performed over a wide range of scan rates (2-100 mV/s) in multiple electrolytes, including HEPES-buffered Tyrode's solution, PBS, DMEM, Na_2SO_4 solution, and ACSF solution (**Fig. 2-8**). In Na_2SO_4 electrolyte solution, the micro-supercapacitor showed rectangular CV profiles up to a scan rate of 100 mV/s, indicating that the device acted as an electrostatic double-layer capacitor.

Notably, the micro-supercapacitor also showed a near-rectangular CV profile in DMEM up to a scan rate of 100 mV/s, demonstrating that the capacitor behavior is maintained even in a cell culture medium. Stack volumetric capacitances calculated from the CV profiles (**Fig. 2-9**) were comparable to those of other micro-supercapacitors[23–25], indicating a low ion transport resistance at the interfaces. Device stability was tested by submerging the device in 37°C PBS solution for one month, during which no noticeable change in capacitance rate was observed (**Fig. 2-10a**). The device also showed good cycling stability; after 10,000 cycles, the device capacity maintained its initial rate (**Fig. 2-10b**). Together, these results demonstrate that the device is promising for biological modulations.

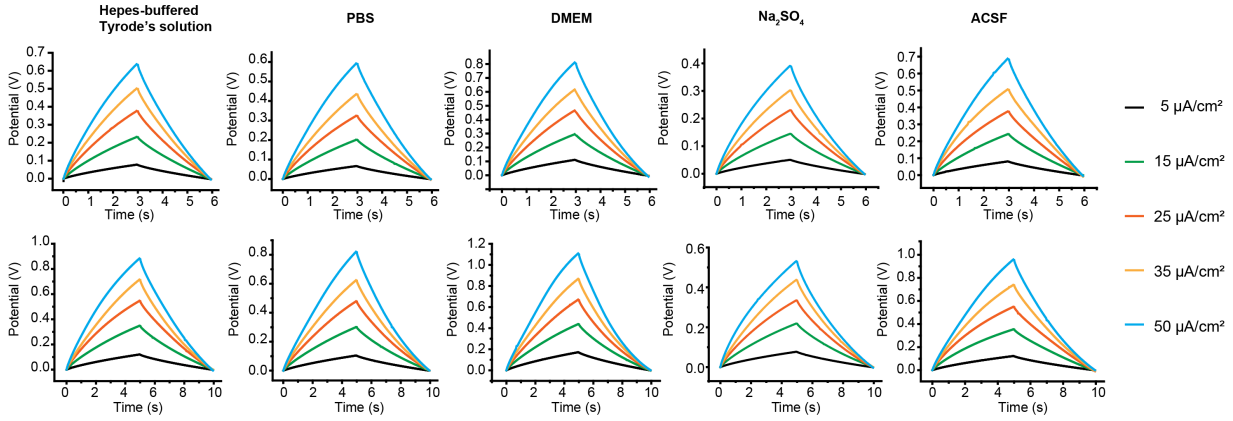

Figure 2-7. Representative charge/discharge curves of the micro-supercapacitor device. Charge/discharge curves in various testing solutions at different current densities of the time window of 6 s and 10 s were shown. Figure reproduced from Ref. 22.

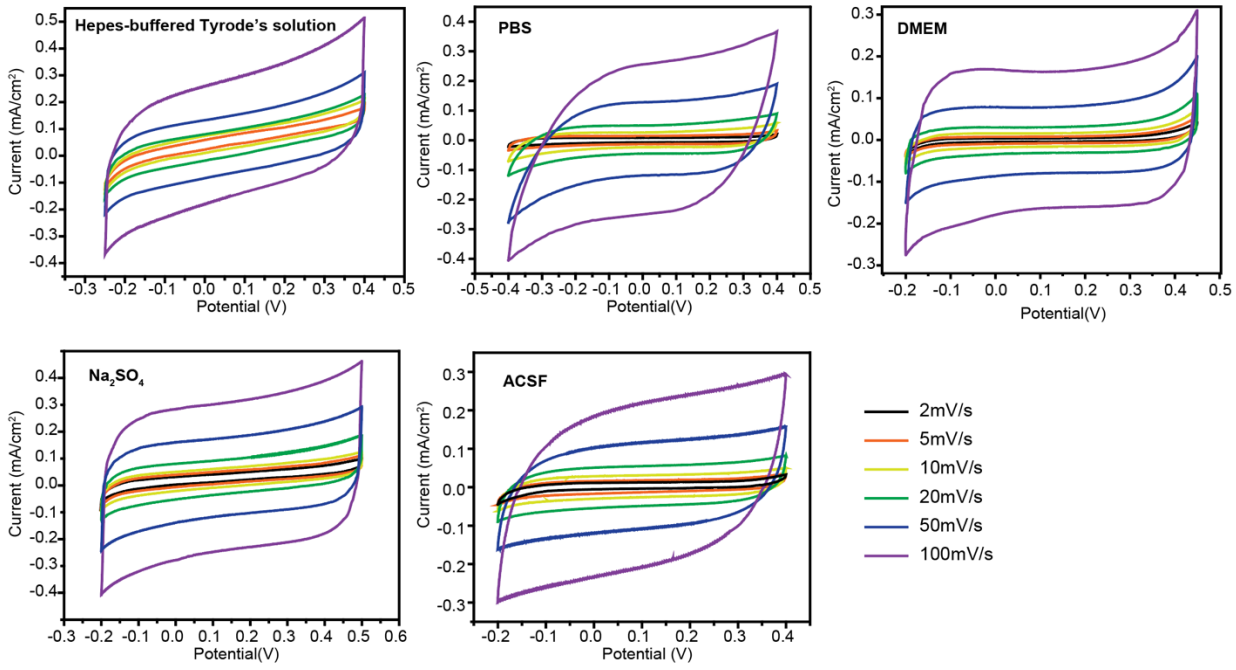

Figure 2-8. CV profiles of the micro-supercapacitor in different solutions and scan rates. Figure reproduced from Ref. 22.

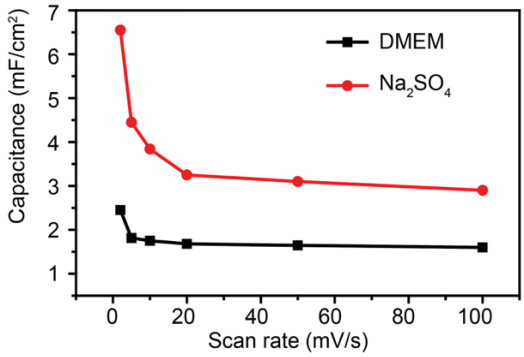

Figure 2-9. The stack volumetric capacitance in DMEM and Na_2SO_4 electrolytes. Figure reproduced from Ref. 22.

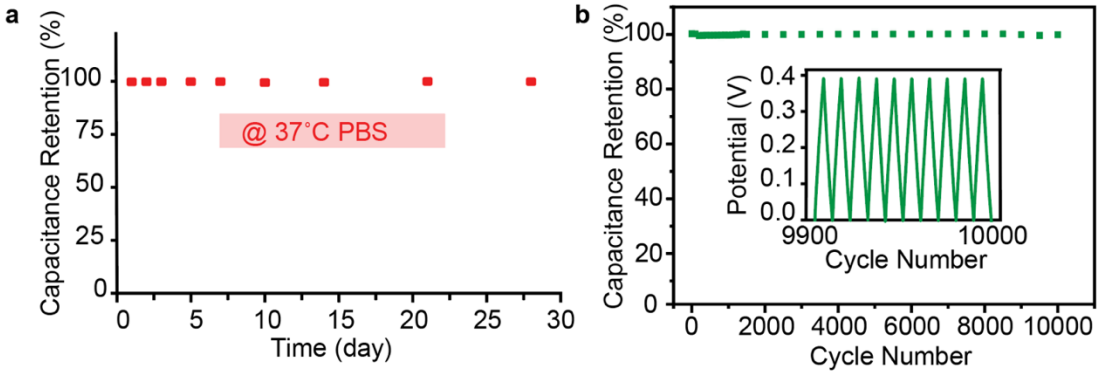

Figure 2-10. Cycling stability of the device. a. Cycling stability of the device in PBS solution over one month at 37°C. **b.** The cycling stability of the device was tested over 10,000 cycles, and the charge-discharge curve during the last 10 cycles is shown in the insert. Figure reproduced from Ref. 22.

2.2.3 Biological Training *In Vitro*

To study the ability of the micro-supercapacitor to modify signal transduction, we established a biointerface between the device and CMs. We first seeded CMs on the device and verified cell adhesion and expression of typical cardiac markers, such as cardiac troponin and connexin-43 (**Fig. 2-11**). To evaluate how the charging/discharging cycles from the micro-supercapacitor-like device affect the CM electrophysiology, we applied the stimulation current to the CM-interfacing devices and performed simultaneous calcium imaging to monitor cellular electrical activity. Each side of the inter- digitated electrodes acts as a lead, and a square current waveform is applied between them. Prior to stimulation, CMs were synchronized with a baseline beating rate of ~0.67Hz. Upon application of an input electric current waveform, overdrive pacing was achieved, and the contraction rate immediately synchronized to the pacing frequency (**Fig. 2-12**). It is noteworthy that the pacing rate doubles that of the stimulation rate (*i.e.,* the applied current frequency). This is expected as both the anodic and the cathodic phases of the electrochemical

stimulation (from the same finger electrode area) can excite the CMs, although the action potentials (APs) may be initiated at different subcellular locations. One advantage of the electrical stimulation from the interdigitated layout is that it can achieve direct cell modulation uniformly across the entire device area. Also, the confined electrical potential around the finger electrodes may help improve stimulation efficiency as CM cultures are typically monolayer, and it may be unnecessary to deliver an electric field far above the cell surface.

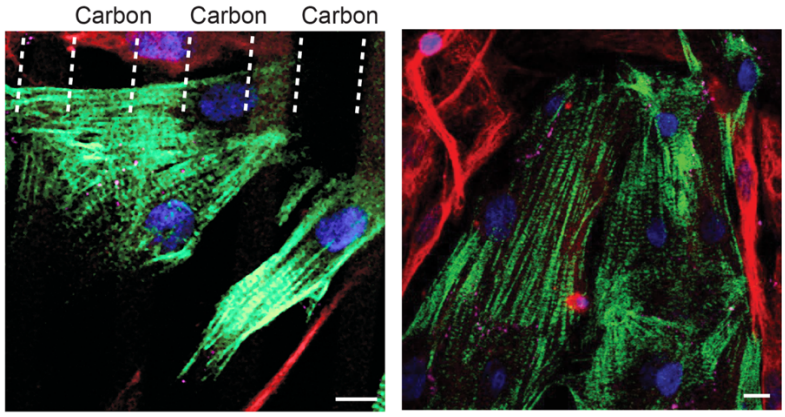

Figure 2-11. Immunohistochemistry images. Cardiac cells cultured on the micro-supercapacitor device were stained for cardiac troponin (CMs, green), connexin-43 (magenta), vimentin (fibroblasts, red), and 4′,6-diamidino-2-phenylindole (DAPI; nuclei, blue). Dashed lines, the edges of the interdigitated carbon electrodes. Scale bars, 10 μm. Figure reproduced from Ref. 22.

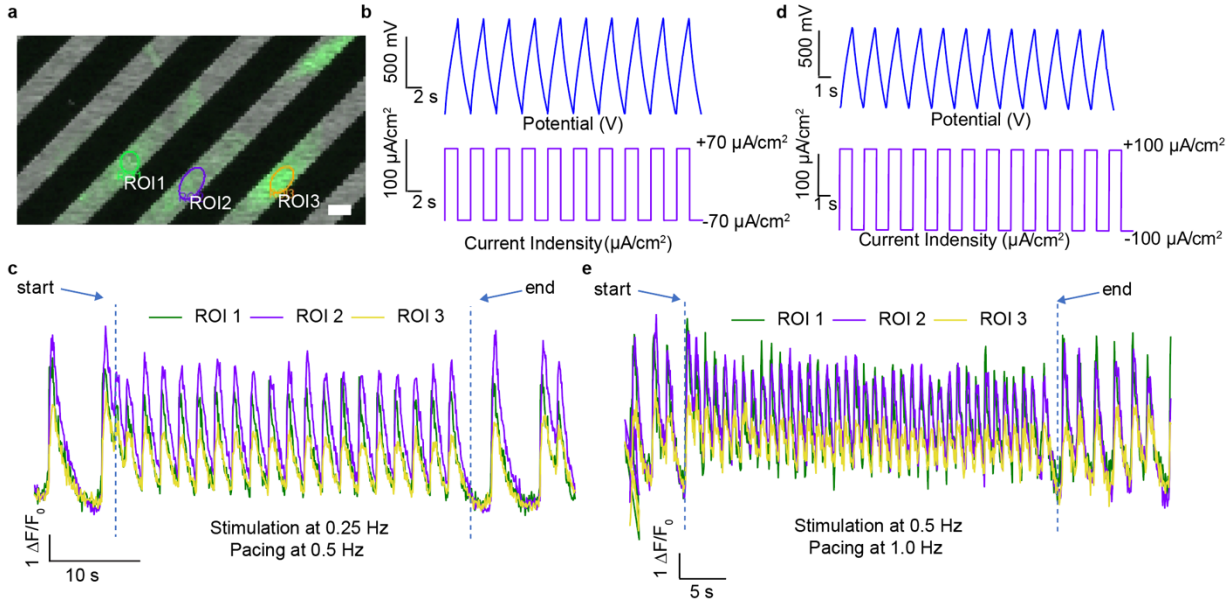

Figure 2-12. ***In vitro*** **cardiomyocytes training and calcium imaging. a.** Image of CMs loaded with calcium-sensitive dye. The micro-supercapacitor appears in black. Regions of interest (ROI) were labeled. Scale bar, 10 μm. **b.** Device voltage (top) and input current density (bottom) during the 0.25 Hz stimulation. **c**. Cell contraction illustrated by the intensity profile of the ROI (highlighted in panel **a**) is reached 0.5 Hz. **d.** Device voltage (top) and input current density (bottom) during the 0.5 Hz stimulation. **c**. Cell contraction illustrated by the intensity profile of the ROI (highlighted in panel **a**) is reached 1.0 Hz. Figure reproduced from Ref. 22.

This ability to perform overdrive pacing of CMs may have promising therapeutic applications. However, we also wanted to demonstrate the utility of the device for *in vitro* cellular manipulation that would allow for basic mechanistic investigations. To this end, we applied ionic manipulation with subthreshold amplitude, which did not elicit a direct overdrive pacing response. Before stimulation, CMs illustrate low spontaneous activity with ~0.2 Hz and 0 Hz at two regions of interest (ROI 1 and ROI2, **Fig. 2-13** pre-training traces). When low amplitude charge/discharge

cycles were applied (0-0.23 V, 1 Hz, ~4 times lower than for overdrive pacing), the CMs did not show an immediate response. However, a gradual increase in contraction was observed when the stimulation was applied for a longer duration. After ~1500 s of stimulation, the cells were 'trained' by the ionic manipulation and their contraction rate increased to the target stimulation rate of 1 Hz (**Fig. 2-13**). These results resemble the gradual increase in the rate of electrical activity previously observed in CMs upon subthreshold optical stimulation[26]. We postulate that repetitive stimulation alters the resting membrane potential of the CMs to the point that they are sufficiently depolarized to elicit action potentials (APs), reminiscent of the 'memory effect' (referring to how pacing history alters the excitability of a cell)[27]. Because the micro-supercapacitor operates via capacitive charge injection, we could pace or train the CMs in a biocompatible way without generating faradaic reactions on the surface of the micro-supercapacitor. The lack of anodic and cathodic reactions will also prevent complications due to electrode hydrolysis, which would result in an increased resistance over time, and in severe cases, device failure.

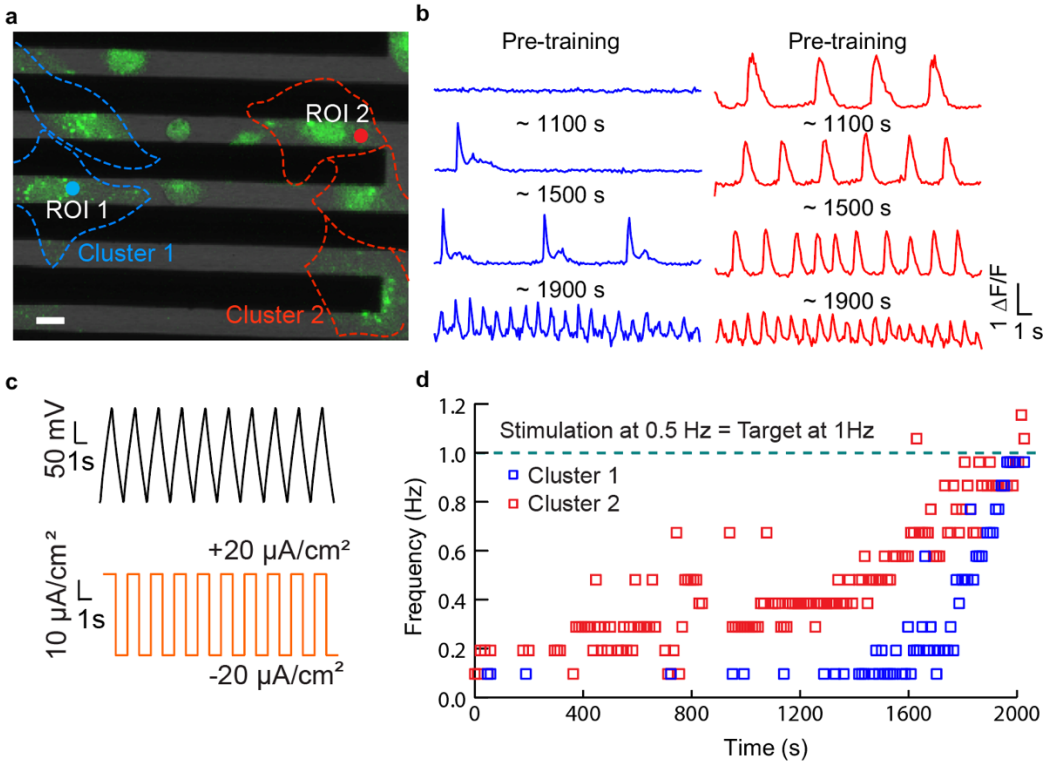

Figure 2-13. Subthreshold stimulation and contraction frequency analysis. a. Representative calcium image of CMs labeled with fluo-4 AM calcium indicator during subthreshold stimulation. Scale bar, 10 μm. Overlay dash lines show approximate positions of CMs clusters (blue, cluster 1; red, cluster 2). **b.** Representative traces of fluorescence intensities at the ROIs (dots in panel a) at the beginning of the experiment and at 1,100, 1,500, and 1,900 s of stimulation. **c.** Voltage (top) and the input current density (bottom) waveforms during the training process. **d.** The contraction rate gradual increases and eventually reached the target training frequency of 1 Hz. Figure reproduced from Ref. 22.

2.2.4 Biological Modulation at the Tissue and Organ Level

We tested the efficacy of our device as a bio-modulator in both intact excitable tissues and *ex vivo* organs. For *ex vivo* whole heart experiments, a micro-supercapacitor was placed below the apex, and another was placed on the left ventricular (LV) wall of a rat heart (**Fig. 2-14**). The

flexibility of our device allowed it to conform around the heart, minimizing the mechanical mismatch. The rat heart contained ~75 μm thick epicardium separating the CMs and the device[28]. Therefore, a single micro-supercapacitor with just 10 μm spacing between the leads was insufficient to accumulate the depolarizing charge. The thickness of the epicardium, which is much larger than the distance between the leads, would prevent the CMs from sensing the electrical input with our initial device dimensions due to the cancellation between the positive and negative prongs, resulting in a zero charge at the CMs. Therefore, we used two micro-supercapacitors, one on the apex or the right ventricular (RV) wall and the other on the LV wall, to deliver different current waveforms. Electrocardiogram (ECG) electrodes were placed on the aorta and the LV, and the pacing can be easily observed with an LVP balloon (**Fig. 2-14a**).

The two porous carbon device configuration is highly efficient as both flexible devices form good contacts with the heart surface (**Fig. 2-14b and 2-14c**). By separating the charge/discharge cycles, we could perform overdrive pacing of the heart. It is essential to mention that every cycle contained charging and discharging inputs from each device; each input gave rise to an AP, the result being a pacing frequency double that of the device frequency. To stimulate the isolated heart, we applied anodic/cathodic current square waves (1 Hz, ±0.5 mA/cm^2, **Fig. 2-15**). Upon stimulation, the heart immediately contracted at double the stimulation rate as expected, *i.e.,* 1 and 1.67 Hz stimulation frequencies corresponded to 2 and 3.33 Hz pacing frequencies, respectively. This is similar to the observed *in vitro* pacing with a micro-supercapacitor device configuration, suggesting that both the anodic and cathodic stimulations from the working electrode can achieve a pacing effect. Due to the capacitive nature of our device and lack of faradaic charge injection, we believe that the mechanism governing the electrical stimulation of our device is similar to field coupling[29,30].

The ECG recording of the heart gave insight by showing the artifacts associated with the charge/discharge cycle. While no artifact was associated with the spontaneous contraction, we observed a positive/negative ECG artifact during the stimulation (**Fig. 2-15,** green and blue arrowheads, respectively). As the ECG was recorded from the aorta and the LV wall, the observed artifact may be attributed to the stimulating micro-supercapacitor positioned on the LV. The artifact shapes and the positions are dependent on the device/ECG configurations, so they vary in different settings. Overall, the stable, flexible, and successful modulation of the heart activity *ex vivo* could be implemented for the long-term *in vivo* heart pacing.

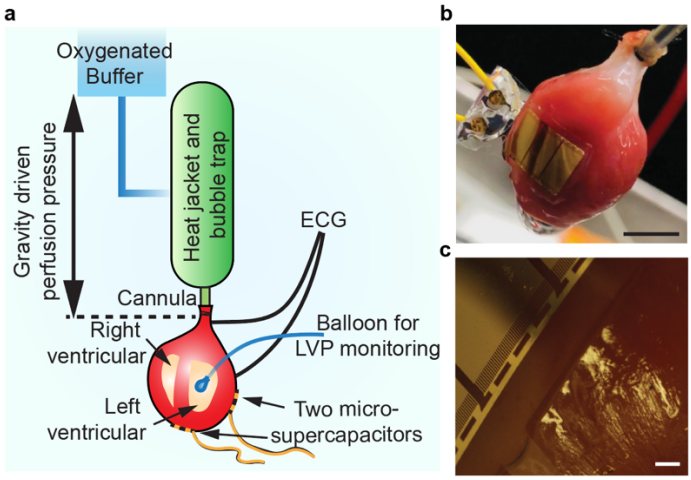

Figure 2-14. Ex vivo heart modulation experiment. a. Schematic of the experimental setup and the Langendorff perfusion system. ECG and left ventricular pressure (LVP) were monitored to show the effect of stimulation on the heart beating rate. **b.** Image of a micro-supercapacitor-like device conforming around the curvilinear and contractile cardiac tissue. Scale bar, 5 mm. c. A close-up view. Scale bar, 500 µm. Figure reproduced from Ref. 22.

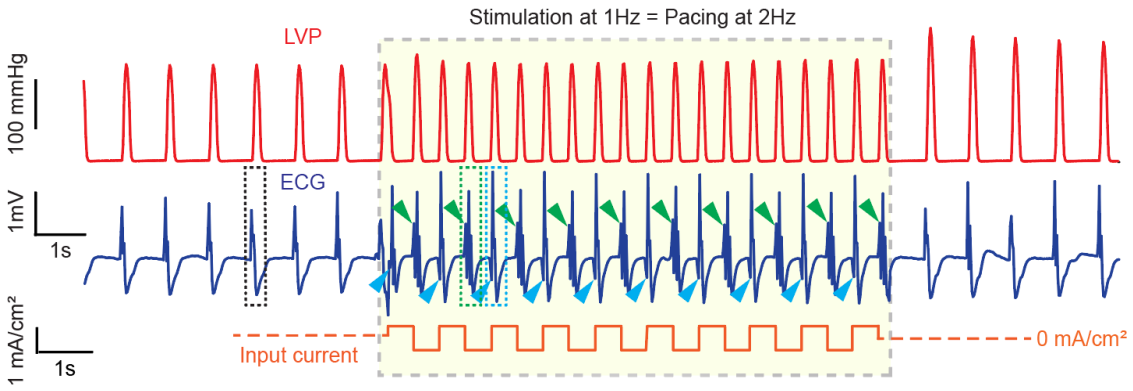

Figure 2-15. LVP profiles and ECG recordings of the isolated heart. Stimulation performed at a frequency of 1 Hz and a current density of ±0.5 mA/cm^2. The LVP and ECG recordings were synchronized to the corresponding portions of the input current. Dashed boxes and arrows are spontaneous APs (black) and APs that follow positive (green) and negative (blue) artifacts. Figure reproduced from Ref. 22.

We interfaced the micro-supercapacitor with sciatic nerves to demonstrate its utility for *in vivo* neuro-modulation applications. We used an acute setting where the micro-supercapacitor was interfaced with the exposed nerve (**Fig. 2-16a**). When one device was interfaced with the sciatic nerve, and the other was with the rat's body, we observed that the associated limb was moving with every cathodic phase of the current injection. This was further validated by electromyography (EMG) recordings from the rat foot, which showed an AP synchronized to the discharge cycle **(Fig. 2-16b**). After that, we exposed the second sciatic nerve and connected the two devices to the two nerves. As every discharge in one device corresponded to the charge of the other device, the two limbs were alternatingly stimulated with a discharge. Consequently, the limbs moved in turn, triggered by each discharge portion of the cycle, resulting in the nerve's depolarization. Overall, we show that our micro-supercapacitor device can be employed for *in vivo* applications. It can

allow precise control of neuronal modulation, which will open many avenues for the long-term, non-faradaic electrical modulation.

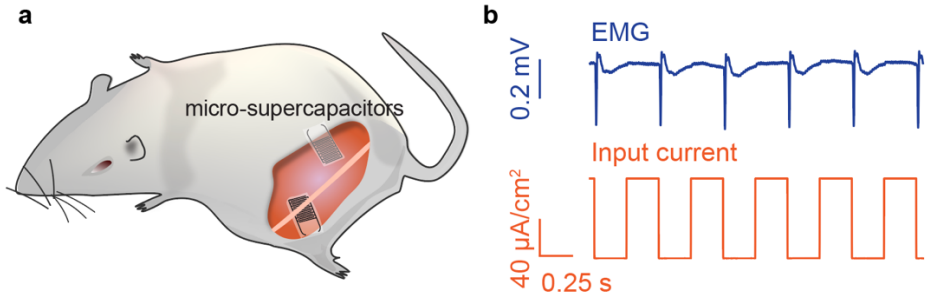

Figure 2-16. *In the Vivo* nerve stimulation experiment. Figure reproduced from Ref. 22.

2.3 Conclusion

In summary, we have developed a bottom-up route, using micelles building blocks and SiO_2 templates, to fabricate carbon-based micro-supercapacitor devices capable of *in vitro, ex vivo,* and *in vivo* bioelectrical modulations. The hierarchical carbon membrane composition allows control over ion flow via electrical inputs. The micro-supercapacitor device shows long-term stability and good biocompatibility, enabling potential use in clinical settings. We have shown that this device can modulate the contraction of primary CMs from a slow beating rate to a specified target beating frequency in a minimally invasive manner via a cell training process. This system also successfully modulated electrical activity at the tissue and organ scale. The experiments expand available toolkits for investigating fundamental biological modulation mechanisms.

2.4 Experimental

2.4.1 Materials Preparation and Device Fabrication

Hierarchical mesoporous carbon films were synthesized by carbonizing layer-by-layer assembled micelles. Resol precursors (low-molecular) were prepared by crosslinking phenol and formaldehyde following methods from the literature[31]. Pluronic block copolymer F127 (template) and phenolic resol (carbon source) were mixed at a ratio of 1:2 into an ethanol solution. The solution was stirred for 1 hour before use (Solution A).

Vesicle structures were constructed using silica nanosphere templates. 200 nm-diameter silica nanospheres (NanoComposix, 10 mg/ml) were surface modified with a dopamine layer, according to a literature method[32]. The modified nanospheres were then added to Solution A and mixed until a homogeneous mixture formed. This new solution was named Solution B.

Silicon wafer (Nova Electronic Materials, p-type, 600 nm thermal oxide SiO_2) was cut into small pieces of suitable sizes (e.g., 2 cm × 4 cm) and cleaned by O_2 plasma (Plasma Etcher, PE100) at 100 w for 2 minutes. Solution B was spin-coated (Laurell, WS-650 spin coater) onto the surface-cleaned silicon at 1500 rpm for 45 s. Multiple layers were formed by leaving the silicon wafer at room temperature for 10 minutes and then repeating the spin-coating. Then Solution A was spin-coated onto the substrate at 3000 rpm for 45 s. The wafers were kept immobile for 4-6 h at 25°C, then baked in an oven for 24 h at 100°C. After baking, the wafers were transferred into an inert argon atmosphere and heated at 500°C (temperature rise rate at 5°C/min) for 30 min. The wafers were cooled to room temperature and then spin-coated in a thin protective layer of polymethyl methacrylate. The thin film was etched off the silicon wafer, and nanospheres were etched by submerging the wafers in buffered hydrofluoric acid (HF) for 8 h. The thin film was rinsed with deionized (DI) water 3-4 times, then carefully transferred onto a new silicon wafer and dried slowly

at room temperature. The wafers were transferred into an inert argon atmosphere and calcined at 700°C for 30 minutes.

After cooling, a standard photolithography procedure was applied to make the desired pattern on the hierarchical mesoporous carbon. An 80 nm thick Au layer was evaporated on the pattern surface using an e-beam evaporator (AJA, ATC-Orion), and extra carbon parts were removed by reactive-ion etching (Oxford Instruments PlasmaPro, NGP80) in O_2 flow (100 sccm, 4 mins). The supporting SU-8 layer with designed mesh patterns was made following a standard photolithography procedure using a double-side mask aligner (EVG, EVG620). The pattern on the SU-8 layer was etched from the substrate by buffered HF and transferred into DI water for one day. After washing the device with DI water six times, the patterns on SU-8 were carefully transferred onto the cover glasses or culture dishes. Wire bonding on the desired pattern led to final device fabrication.

2.4.2 Nano-Indentation Mechanical Tests

Indentation modulus and hardness were measured by performing nanoindentation using a Hysitron 950 Tribolndenter in an ambient environment with a Berkovich indenter (three-sided pyramid-shaped diamond tip, tip radius ∼100 nm). All measurements were kept at a constant displacement of 200 nm. The data were analyzed using standard Oliver and Pharr (1) analysis to extract the reduced modulus (E_r) and hardness by selecting upper fit at 95% and lower fit at 20%. The Young's modulus E of the samples was extracted based on Eq. (1)[33], a general relation that applies to any axisymmetric indenter. The diamond tip has Young's modulus E_i = 1141 GPa and a Poisson's ratio ν_i = 0.07[34]. Here, we assume the Poisson's ratio of the samples ν = 0.25, widely used for amorphous carbon[35].

$$\frac{1}{E_r} = \frac{1-\nu^2}{E} + \frac{1-\nu_i^2}{E_i} \qquad (1)$$

2.4.3 Primary Cardiomyocytes Isolation and Culture

All animal procedures were conducted in complete compliance with and approval from the University of Chicago Institutional Animal Care and Use Committee (IACUC) Animal Care and Use Protocol. Hearts were excised from P0-5 neonatal rats into ice-cold HBSS (without Ca^{2+} or Mg^{2+}). The hearts were cut into small <1 mm pieces and then rinsed with HBSS to remove blood. Pierce™ primary cardiomyocyte isolation kit (Thermo Fisher Scientific) was used for digesting the tissue according to manufacturer protocol.

After isolation, the suspended cells (mainly cardiomyocytes contaminated with cardiac fibroblasts) were pre-plated for 2 h in 37 °C and 5% CO_2, allowing fibroblasts to adhere to the tissue culture plate. Then the enriched cardiomyocytes population was seeded onto the micro-supercapacitor device pre-treated with fibronectin (Sigma). The cells were allowed to sit in culture media (DMEM high glucose + 10% FBS, 1% Glutamax, and 1% penicillin-streptomycin) for 24 h in an environment of 37 °C and 5% CO_2, then the media was changed to CM-specific media (DMEM high glucose + 10% FBS, 1% penicillin-streptomycin, and 0.1% growth supplement from isolation kit). This media prevented fibroblasts from proliferating and taking over the culture.

2.4.4 Calcium Imaging and Immunocytochemistry

Cardiomyocytes were labeled with calcium-sensitive dye (2 μM fluo-4, AM, Thermo Fisher Scientific) for 30 min at 37 °C. Cells were rinsed and incubated for 30 min to allow complete de-esterification. The treated cells were then visualized with a Leica SP5, STED-CW Super-resolution Laser Scanning Confocal.

For immunocytochemistry imaging, primary cardiac cells were cultured onto devices for three days and were fixed (4% paraformaldehyde), permeabilized (0.2% Triton X), and then blocked (2% bovine serum albumin (BSA) solution) for an hour to prevent nonspecific binding. Cells were incubated overnight at 4 °C with rabbit anti-cardiac troponin I antibody (1:400 in 2% BSA), chicken anti-vimentin antibody (1:500 in 2% BSA) and mouse Anti-Connexin-43 antibody (1:100 in 2% BSA). Cells were rinsed and subsequently stained for one hour with Alexa Fluor 488 anti-rabbit, Alexa Fluor 594 anti-chicken and Alexa Fluor 647 anti-mouse secondary antibodies (1:250). DAPI (Invitrogen, P36931) was used to label the nuclei. Stained cells were imaged using the Leica SP5 Confocal and analyzed using ImageJ.

2.4.5 COMSOL Simulation of The Electric Field Distribution

The finite element analysis of the electric field distribution through electrodes was performed using AC/DC Module of COMSOL Multiphysics software. For 2D electrolyte potential, the device geometry was uploaded from an autoCAD file and was consistent with the experimental setup. Each electrode had a length of 5000 μm and a width of 15 μm. A relative voltage of 1 V was applied between the two combs in one micro-supercapacitor. A heat map was colored according to the electrolyte potentials (V) with arrows indicating the electrolyte current density vectors. The boundaries were defined as $\emptyset_I = \emptyset_{I,bnd}$, while the insulations were defined as $-n \cdot i_I = 0$ and $-n \cdot i_s = 0$, and the electrolyte was defined with $\nabla \cdot i_I = Q_I$ and $i_I = -\sigma_I \nabla \emptyset_I$. Secondary current distributions were also considered in simulating the electric field potential. For 3D electric field distribution at the cross-section of the micro-supercapacitor, the electric scalar potential, V, satisfies Poisson's equation, $-\nabla \cdot (\varepsilon_0 \varepsilon_r \nabla V) = \rho$, where ε_0 is the permittivity of free space, ε_r is the relative permittivity, and ρ is the space charge density. The electric fields are

obtained from the gradient of V: $\mathbf{E} = -\nabla V$, and the displacement is defined as $\mathbf{D} = \varepsilon_0\varepsilon_r\mathbf{E}$. To simplify the simulation (versus actual device with three hundred prongs), a five-prong comb-like electrode model pair was built with a gap of 10 μm and prongs of 200 μm length and 15μm width. Prong width and gap width were consistent with the experimental setup. A relative voltage of 1 V was applied. The electric field distribution of two planar electrodes was also calculated for comparison. The area of each electrode was equal to the total area of a single comb, and the gap width between the two planar electrodes was equal to the summation of the gaps in each comb-like electrode; as such, each electrode was of 75 μm width and 200 μm length with a gap of 50 μm between the two. A heat map was colored according to the surface electric potentials (V) with arrows indicating the electric field direction and strength.

2.4.6 Electrochemical Measurements

Galvanic charge/discharge measurements were tested using two symmetric devices in a two-electrode configuration using a source meter (Keithley 2636A, Tektronix) controlled by a LabVIEW program (National Instruments). The voltage shown was the potential between the two symmetric devices. CV was performed over a wide range of scan rates at room temperature or 37 °C in various electrolytes. A potentiostat (SP-200, BioLogic) controlled with EC-Lab software with the three-electrode cell was used. A platinum wire was used as the counter electrode, a Ag/AgCl electrode (1 M KCl) as the reference electrode, and a micro-supercapacitor device as the working electrode. In general, the electrochemical tests were performed without pre-treatment or pre-soak. Capacitance (C) was calculated from the cathodic phase of CV by $\mathrm{C} = (\int \mathrm{I}\,\mathrm{dV})/(\mathrm{s}\Delta\mathrm{VA})$, where I is the current, V is the potential, ΔV is the potential window, s is the scan rate, and A is the area of the electrode.

2.4.7 *In Vitro* Cardiomyocytes Stimulation

Devices were generally connected in a two-electrode (*i.e.,* working electrode and counter electrode) configuration, and the counter electrode was connected to the ground. Square current waveforms were delivered using a source meter (Keithley 2636A) controlled using a LabVIEW program. Current pulses were delivered using a potentiostat (SP-200, BioLogic) using EC-Lab Express software. The electric potential was reported as the potential between the two electrodes. In the *in vitro* cardiomyocytes training, the square current waveforms were applied to the two interdigitated electrodes within the same carbon micro-supercapacitor-like device, where one interdigitated electrode as the working electrode and the other interdigitated electrode as the grounded counter electrode.

2.4.8 *Ex Vivo* Isolated Rat Heart Stimulation

An adult rat was heparinized (1,000 IU/kg IP) and anesthetized using open-drop exposure of isoflurane in a bell jar configuration. The heart was removed and placed in ice-cold HBSS buffer, and the aorta was cannulated in preparation for use in a Langendorff setup. Oxygenated Hepes-buffered Tyrode's solution (containing, in mM, NaCl 126, KCl 5.4, Glucose 10, Hepes 10, $MgCl_2$ 1, $CaCl_2$ 2, $MgSO_4$ 1.2, NaH_2PO_4 0.39; bubbled with 99.5% O_2; pH 7.3) was perfused through the cannulated aorta. The perfusion was passed through a heating coil and bubble trap (Radnoti), and the heart was placed in a water-jacketed beaker (Fisher Scientific) to maintain a temperature of 37°C. The perfusion pressure was maintained at 80–100 mmHg by adjusting the height of the IV bag containing the perfusion buffer. The perfusion and left ventricular pressures (LVP) were monitored using a BP-100 probe (iWorx) connected to the perfusion line and a water-filled balloon inserted into the LV, respectively. For ECG recordings, needle electrodes were

positioned on the apex and aorta and connected to a C-ISO-256 preamplifier (iWorx). All signals (perfusion, LVP, and ECG) were amplified using an IA-400D amplifier (iWorx) and interfaced with a PC using a DigiData 1550 digitizer with pClamp software (Molecular Devices). Two devices were placed on the heart: one below the heart's apex and the other covering the LV wall. Charge/discharge cycles were applied to the devices, while the clear ECG artifacts were used to time the stimulation with the recording. To avoid the electrical noise introduced by the devices, we recorded the LVP to monitor the contraction rate of the heart during stimulation.

2.4.9 *In Vivo* Rat Nerve Stimulation

Seven-week-old rats were deeply anesthetized with ketamine (100 mg/kg) and xylazine (10 mg/kg) via intraperitoneal injection. The fur was removed from the hindquarters using a surgical clippers and hair removal cream. A semi-circular incision across the midline was made in the skin, and the fascial plane was opened between the gluteus maximus and the anterior head of the biceps femoris, thereby exposing the sciatic nerve. In this setting, two devices were used. One device was placed under the sciatic nerve and the other under the rat's skin. For intermittent limb stimulation, the two devices were paced under the two sciatic nerves. All animals were housed under pathogen-free conditions, and all animal procedures were approved by the Institutional Animal Care and Use Committees of the University of Chicago (IACUC).

2.5 Bibliography

1. Someya, T., Bao, Z. & Malliaras, G. G. The rise of plastic bioelectronics. *Nature* **540**, 379–385 (2016).
2. Xie, Z., Avila, R., Huang, Y. & Rogers, J. A. Flexible and stretchable antennas for biointegrated electronics. *Adv. Mater.* 1902767 (2019).
3. Wang, L. *et al.* Functionalized helical fibre bundles of carbon nanotubes as electrochemical sensors for long-term *in vivo* monitoring of multiple disease biomarkers. *Nat. Biomed. Eng.* (2019).
4. Huang, Z. *et al.* Three-dimensional integrated stretchable electronics. *Nat. Electron.* **1**, 473–480 (2018).
5. Zhirnov, V. V. & Cavin, R. K. *Microsystems for bioelectronics: scaling and performance limits*. (William Andrew, 2015).
6. Chen, N. *et al.* Neural interfaces engineered via micro- and nanostructured coatings. *Nano Today* **14**, 59–83 (2017).
7. Rastogi, S. K., Kalmykov, A., Johnson, N. & Cohen-Karni, T. Bioelectronics with nanocarbons. *J. Mater. Chem. B* **6**, 7159–7178 (2018).
8. Yang, W., Thordarson, P., Gooding, J. J., Ringer, S. P. & Braet, F. Carbon nanotubes for biological and biomedical applications. *Nanotechnology* **18**, 412001 (2007).
9. Alkire, R. C., Bartlett, P. N. & Lipkowski, J. *Electrochemistry of carbon electrodes*. (Wiley, 2015).
10. Hansen, S. F. & Lennquist, A. Carbon nanotubes added to the SIN List as a nanomaterial of Very High Concern. *Nat. Nanotechnol.* **15**, 3–4 (2020).
11. Zhu, W. *et al.* Nanomechanical mechanism for lipid bilayer damage induced by carbon nanotubes confined in intracellular vesicles. *Proc. Natl. Acad. Sci.* **113**, 12374–12379 (2016).
12. Hwang, J. Y., Li, M., El-Kady, M. F. & Kaner, R. B. Next-generation activated carbon supercapacitors: a simple step in electrode processing leads to remarkable gains in energy density. *Adv. Funct. Mater.* **27**, 1605745 (2017).
13. Zhu, Y. *et al.* Carbon-based supercapacitors produced by activation of graphene. *Science* **332**, 1537–1541 (2011).
14. Guo, Y. *et al.* Polymer composite with carbon nanofibers aligned during thermal drawing as a microelectrode for chronic neural interfaces. *ACS Nano* **11**, 6574–6585 (2017).
15. Yin, R. *et al.* Soft transparent graphene contact lens electrodes for conformal full-cornea recording of electroretinogram. *Nat. Commun.* **9**, (2018).
16. Chen, X. *et al.* Stretchable supercapacitors as emergent energy storage units for health monitoring bioelectronics. *Adv. Energy Mater.* 1902769 (2019).
17. Chmiola, J., Largeot, C., Taberna, P. L., Simon, P. & Gogotsi, Y. Monolithic carbide-derived carbon films for micro-supercapacitors. *Science* **328**, 480–483 (2010).
18. Pan, L. *et al.* Hierarchical nanostructured conducting polymer hydrogel with high electrochemical activity. *Proc. Natl. Acad. Sci.* **109**, 9287–9292 (2012).
19. Lee, Y. *et al.* Stretchable organic optoelectronic sensorimotor synapse. *Sci. Adv.* **4**, eaat7387 (2018).
20. Lyu, S. & Untereker, D. Degradability of polymers for implantable biomedical devices. *Int. J. Mol. Sci.* **10**, 4033–4065 (2009).
21. Ratner, B. D., Hoffman, A., Schoen, F. & Lemons, J. *Biomaterials science: an introduction to materials in medicine*. (Elsevier/Acad. Press, 2013).

22. Fang, Y. *et al.* Micelle-enabled self-assembly of porous and monolithic carbon membranes for bioelectronic interfaces. *Nat. Nanotechnol.* **16**, 206–213 (2021).
23. Song, B. *et al.* Solution-processed flexible solid-state micro-supercapacitors for on-chip energy storage devices. in *2015 IEEE 65th Electronic Components and Technology Conference (ECTC)* 1483–1487 (IEEE, 2015).
24. Lee, G. *et al.* High-performance all-solid-state flexible micro-supercapacitor arrays with layer-by-layer assembled MWNT/MnO_x nanocomposite electrodes. *Nanoscale* **6**, 9655–9664 (2014).
25. Pech, D. *et al.* Ultrahigh-power micrometre-sized supercapacitors based on onion-like carbon. *Nat. Nanotechnol.* **5**, 651–654 (2010).
26. Parameswaran, R. *et al.* Optical stimulation of cardiac cells with a polymer-supported silicon nanowire matrix. *Proc. Natl. Acad. Sci.* **116**, 413–421 (2019).
27. Hund, T. J. & Rudy, Y. Determinants of excitability in cardiac myocytes: mechanistic investigation of memory effect. *Biophys. J.* **79**, 3095–3104 (2000).
28. Jenkins, M. W. *et al.* Optical pacing of the adult rabbit heart. *Biomed. Opt. Express* **4**, 1626 (2013).
29. Copene, E. D. & Keener, J. P. Ephaptic coupling of cardiac cells through the junctional electric potential. *J. Math. Biol.* **57**, 265–284 (2008).
30. Sperelakis, N. & McConnell, K. Electric field interactions between closely abutting excitable cells. *IEEE Eng. Med. Biol. Mag.* **21**, 77–89 (2002).
31. Meng, Y. *et al.* Ordered mesoporous polymers and homologous carbon frameworks: amphiphilic surfactant templating and direct transformation. *Angew. Chem. Int. Ed.* **44**, 7053–7059 (2005).
32. Liu, R. *et al.* Dopamine as a carbon source: the controlled synthesis of hollow carbon spheres and yolk-structured carbon nanocomposites. *Angew. Chem. Int. Ed.* **50**, 6799–6802 (2011).
33. Oliver, W. C. & Pharr, G. M. Measurement of hardness and elastic modulus by instrumented indentation: Advances in understanding and refinements to methodology. *J. Mater. Res.* **19**, 3–20 (2004).
34. Li, X. & Bhushan, B. A review of nanoindentation continuous stiffness measurement technique and its applications. *Mater. Charact.* **48**, 11–36 (2002).
35. Suk, J. W., Murali, S., An, J. & Ruoff, R. S. Mechanical measurements of ultra-thin amorphous carbon membranes using scanning atomic force microscopy. *Carbon* **50**, 2220–2225 (2012).

Chapter 3. Bioelectrical Production of Extracellular Vesicles for Cardiac Tissue Repair

3.1 Introduction

3.1.1 Extracellular Vesicles

Extracellular vesicles (EVs) are membranous particles secreted by nearly all types of cells. Based on their biogenesis and sizes, EVs can be divided into ectosomes (microvesicles, microparticles, or large vesicles in the size range of 100 nm to 1 μm in diameter)1 that generated via outward budding from the plasma membrane and exosomes, the nanoscale vesicles (diameter: 30 to 200 nm) that generated with an endosomal origin2 via the formation of intracellular multivesicular bodies (MVB), which are later released through MVB fusion to the plasma membrane (i.e., exocytosis).

Sequential invagination of the plasma membrane ultimately results in the formation of multivesicular bodies, which can intersect with other intracellular vesicles and organelles, contributing to diversity in the constituents of exosomes[3]. Depending on the biogenesis, exosomes can contain many components of a cell, including DNA, RNA, lipids, metabolites, cytosolic proteins, and membrane proteins. EVs with highly heterogeneous constituent are playing an essential role in intercellular communication, transporting biomolecules to regulate cellular processes, and supporting normal physiology[2–4]. The heterogeneity also makes EVs an ideal candidate for disease diagnostics[4]. For example, in neuroscience, most research focus on the roles that EVs play in neural disease mechanism and neuron-to-neuron/glial communication[5–8]. EVs mediate cellular communication in a feedback loop-like manner[9,10]. Neurotransmitters stimulate oligodendrocytes to secrete vesicles, which are internalized by recipient neurons. Once

internalized, the oligodendrocyte-derived cargo induces downstream neural responses, for instance, greater stress tolerance and increased viability. Therefore, neuron-derived EVs have been studied extensively to identify potential biomarkers for neuropsychological diseases, and analysis of the EVs profile and changes can benefit the studies of synaptic plasticity, neuronal stress response, and neurogenesis[11]. Studies have suggested that exosomes may have a role in regulating intercellular communication based on the targeted accumulation of specific cellular components. Exosomes also ensure cellular homeostasis by removing excess and unnecessary cells components[4] and influence the development of metabolic diseases as well as cardiovascular fitness. For example, exosomes and exosomal microRNAs promote cardiovascular health, possibly by promoting mitochondrial function, limiting cardiomyocyte apoptosis, and maintaining cardiac contractility[12–14].

EVs are also promising drug-delivery vehicles possessing favorable pharmacokinetics and immunological properties for biomedical engineering[15–17]. EVs carry biomolecules and regulate many cellular processes by transporting biomolecules, such as proteins and genetic materials. Meanwhile, compared to other synthetic drug-delivery vehicles, exosomes, the smallest class of EVs, can penetrate physiological barriers almost impermeably (e.g., the blood-brain barrier), making exosomes widely used for targeted, localized delivery of chemical drugs to treat neural dysfunction[18]. Particularly, EVs are considered to have potential as ribonucleic acid (RNA) carriers, especially for microRNA (miRNA) and small interfering RNA (siRNA), due to excellent biocompatibility, bioavailability, minimal immunogenicity, structural proximity with cellular components, and various loading techniques, resulting in significantly high efficiency and stability of RNAs[19–23].

3.1.2 Production of Extracellular Vesicles

To apply EVs as clinically relevant therapeutic tools, EVs should contain bioactive ingredients necessary for therapeutic action. In addition to the quality of the content, EVs should be mass-produced to reach enough quantity. Since the composition of natural EVs is limited, EVs are mainly be used as therapeutical carriers. However, until now, accumulating enough therapeutic EVs *in vitro* has proven difficult due to the limited number of EVs can be generated per cell[24]. Currently, mass production of EVs involves isolating EVs from biological fluids, such as blood, urine, and saliva, which ends up collecting heterogenous EVs from multiple cell origin[25]. It is still challenging and of significant concerns to create EV carriers with constant characteristics and properties on a large scale for encoding biopharmaceutical cargos. Therefore, new strategies to produce sufficient EVs carriers from sole cell sources on a large scale are still required.

A few strategies have been explored to solve the mass production challenge for EVs-based *in vivo* application, including applying external stimulation (such as serum deprivation[26], inducing hypoxia[27,28], cellular nanoporation[29], mechanical forces[30], and high frequency acoustic[31] or electrical[32] stimulation), adjusting cell culture microenvironments by introducing cytokines[33], growth factors[32] or altering calcium levels[29,31,34], and modifying the EVs biogenesis machinery, for example the knockdown of Rab27a, 27b, 35[35,36], or inhibition of acid sphingomyelinase decreased EVs production[37] while the overexpression of cortactin (an actin cytoskeletal regulatory protein) promotes exosomal secretion without altering the EVs cargo content[38] and the application of a production booster can achieve 15 to 20-fold increase in EVs production[39].

3.1.3 Bioelectrical Production of EVs

External electrical fields regulate cellular activities, such as calcium ion flow, action potentials firing, and synaptic communication. However, while many bioelectronic and electrical biointerfaces have been extensively applied in biomodulation to induce controllable biosignals, the impact of electrical field stimulation on widespread EVs signaling remains undetermined. As such, profiling real-time changes of EVs in live cell cultures under electrical stimulation remains interesting. Besides, the next wave of refinements in our understanding of bioelectronic interactions is likely to come from data at the subcellular or nanoscale level. As electric field can induce calcium influx during modulations, in principle, the profiles of EVs – their content, size, and amount – will change under electrical signals as EVs release is highly dependent on calcium influx[31,34,40,41], and electrical stimulation can alter the calcium profile of cells. However, no previous research has revealed the real-time impact of bioelectric modulations on EVs biogenesis.

The recently reported cellular nanoporation method using a biochip made up of 500 nm nanochannels generated 50-fold EVs amount and simultaneously increased (10^3-fold) mRNA loading compared with bulk electroporation and other EVs production techniques (i.e., hypoxia, starvation, and heat stress). For the electroporation methods, membrane poration plays an important role, and it requires high voltages (100-220V) across the nanochannels for inducing exosome releases[29]. There is still a need for additional research to better understand the role of electrical signals in modulating the formation of EVs.

3.2 Results and Discussion

3.2.1 Bioelectrical Stimulation and Real-time Observation of Exosomal Release

With the help of pHluorin-tagged CD63 exosome markers[42,43], the MVB-PM fusion events (i.e., exosome release events) can be visualized, appearing as a burst of fluorescent intensity generated from the pHluorin tag when experience a shift from the intra-vesicular region (pH = 5.5) to the extracellular region (pH = 7.4) as a corollary of the exosome release **(Fig. 3-1a)**. To evaluate the real-time impact of bioelectrical modulations on EVs biogenesis dynamics in live cells, we developed transparent electronic devices **(Fig. 3-1b)** to deliver spatially controlled electrical signals **(Fig. 3-1)** and observed the cells super-resolution microscope upon electrical stimulation.

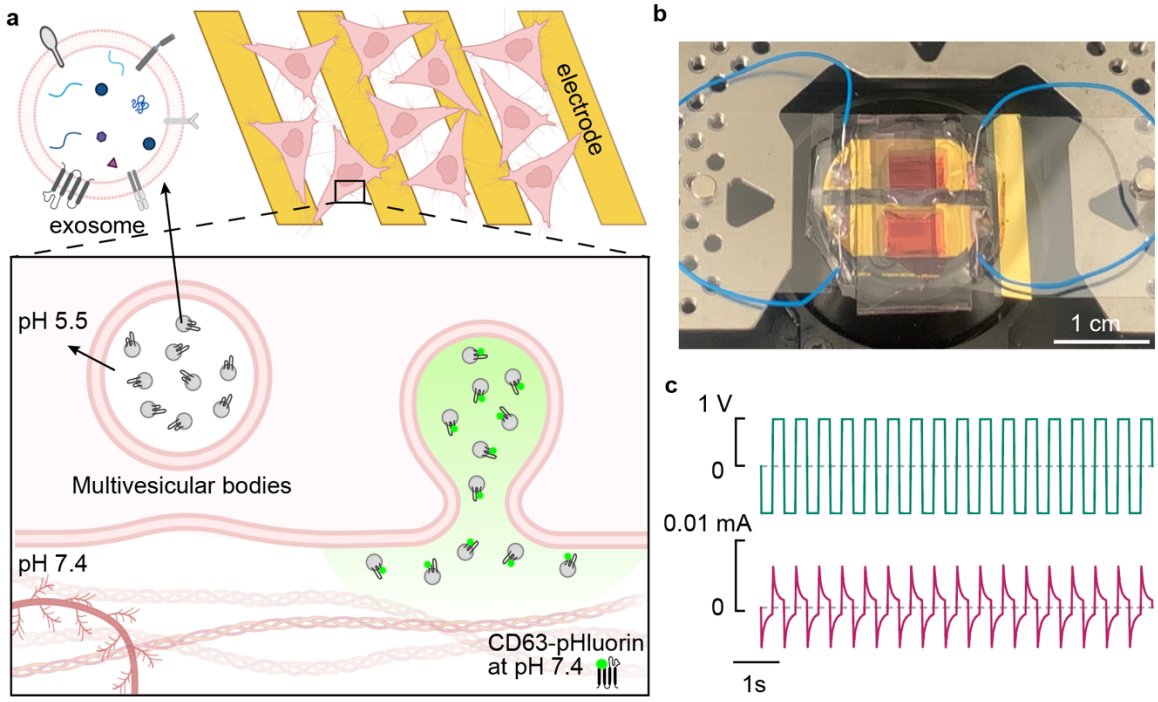

Figure 3-1. Experimental setup and design. a. Schematics of the working mechanism of pHluorin, the MVB-PM fusion reporter. **b.** A picture of the device on super-resolution microscope. **c.** Delivered electrical waveforms (biphasic ±1V, 2Hz) for the bioelectrical stimulation. Voltages are the input signals between the two interdigitated comb-shaped electrodes.

3.2.2 Preparation and Characterization of the Stimulation Device

We used lithography to fabricate planer interdigitated electrodes for extracellular electrical cellular stimulation on glass slides (#1.5 or 0.17-mm thickness) so that spontaneous super-resolution imaging is applicable. Interdigitated gold electrodes on silicon substrates were also fabricated according to traditional photolithography for non-imaging experiment. The devices were wired, and a well on the slide was fabricated using PDMS, where the cell can be cultured. The electric potential of stimulation devices was evaluated via finite element analysis using COMSOL Multiphysics simulations **(Fig. 3-3)**.

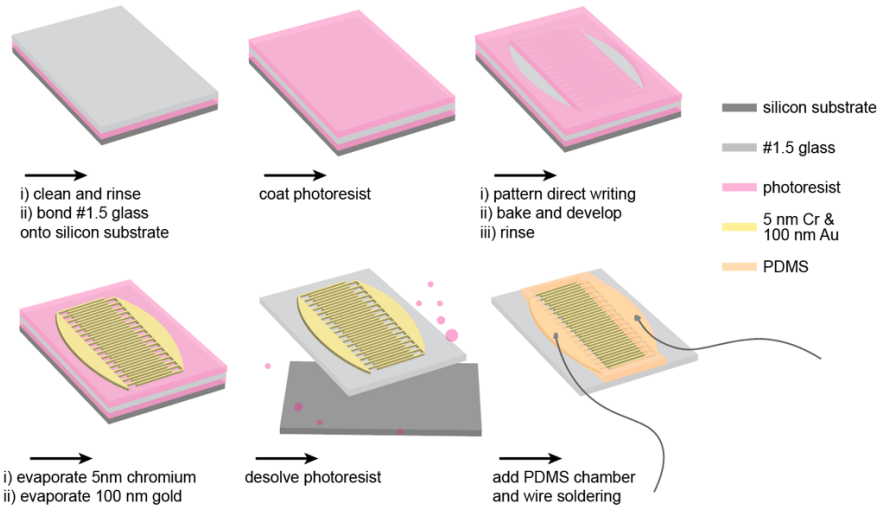

Figure 3-2. Overview of the transparent device fabrication workflow.

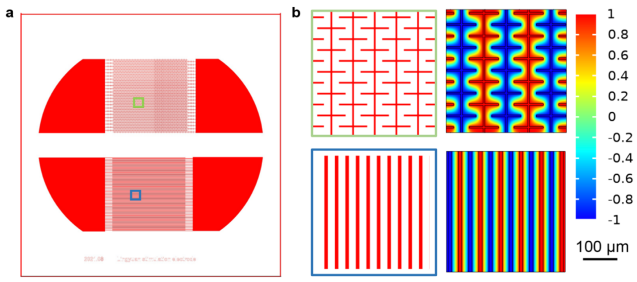

Figure 3-3. Bioelectronic stimulation device. a. Electrode design. Two comb-like electrodes are interdigitated placed. The upper plane electrode has branches to increase spatial heterogeneity. **b.**

Figure 3-3, continued. Zoom-in view of the device design (left) and COMSOL Multiphysics finite element analysis of the electrical potential distribution between the gap of two interdigitated electrodes (right).

HeLa cells were cultured on the devices, and we performed electrochemical tests using three-electrode setup, where a platinum wire was used as the counter electrode, a Ag/AgCl electrode was used as the reference electrode, and a pair of gold interdigitated electrodes on silicon substrate (silicon size: 2 cm x 2 cm) was used as a working electrode. The altered cyclic voltammetry (CV) and impedance profiles (**Fig. 3-4**) on the device with cells indicated that the cultured HeLa cells formed tight interfaces onto the gold electrodes.

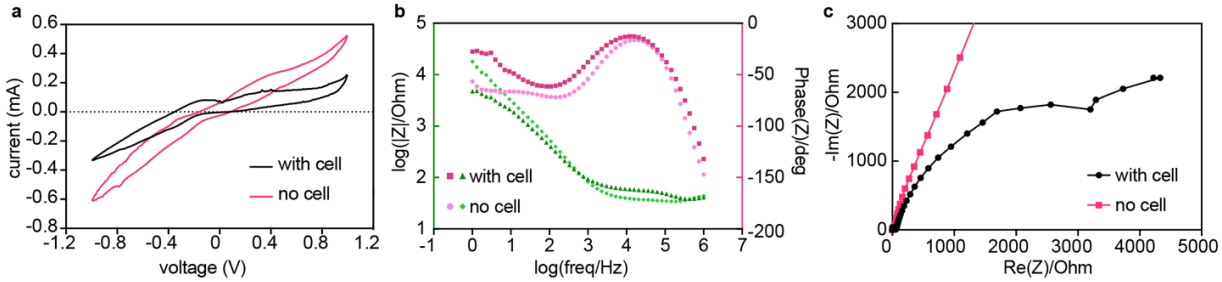

Figure 3-4. Electrochemical characterization. a. CV profiles for the gold interdigitated device in PBS with or without cell culture. **b.** The Bode plot of the measured impedance with or without cell culture. **c.** Nyquist Diagram of the measured impedance with or without cell culture.

3.2.3 Bioelectrical Stimulations Amplified Exosomal Release

We used HeLa cells as an exploratory step to study the EVs dynamics in live cells under an electrical field. HeLa cells were cultured on gold interdigitated devices on #1.5 glass substrate and transfected with plasmids expressing pHluorin-tagged CD63. Upon bioelectrical stimulation of 1V for 0.25 s and -1V for 0.25 s (i.e., ±1V, 2Hz signals) for 50 s, the HeLa cell across the two interdigitated comb-shaped gold electrodes showed boosted exosomal secretion (**Fig. 3-5**) under

super-resolution total internal reflection fluorescence (TIRF) imaging. We adjusted the voltage and the frequency of alternating fields and identified ±1V, 2Hz as optimized bioelectrical stimulation conditions. Stimulation with ± 2V, 2Hz induces cell death (**Fig. 3-5d**), which is due to the membrane leakage, indicated by the large area of pHluorin signal (**Fig. 3-5c**; normal exosome secretion events show fluorescence spots with a diameter of <10 pixels or 1.17 μm like **Fig. 3-5a and 3-5b**) and elevated calcium levels in non-excitable cells (**Fig. 3-6**). Therefore, to activate the MVB–PM fusion machinery and induce exosome release with minimal cell death, we applied ±1V, 2Hz in future experiments.

To quantitatively assess exosomal release dynamics upon electrical stimulation in real-time, we counted individual release events before and during electrical stimulation (±1V, 2Hz) in the same recording duration. Electrical stimulation along is able to significantly boost the exosomal release in tens of seconds (**Fig. 3-7**), as shown in the pHluorin fluorescence signal burst (**Fig. 3-8**). This discovery would be crucial for understanding the stimulation-induced exosome biogenesis and biological roles of EVs under biophysical stimulation.

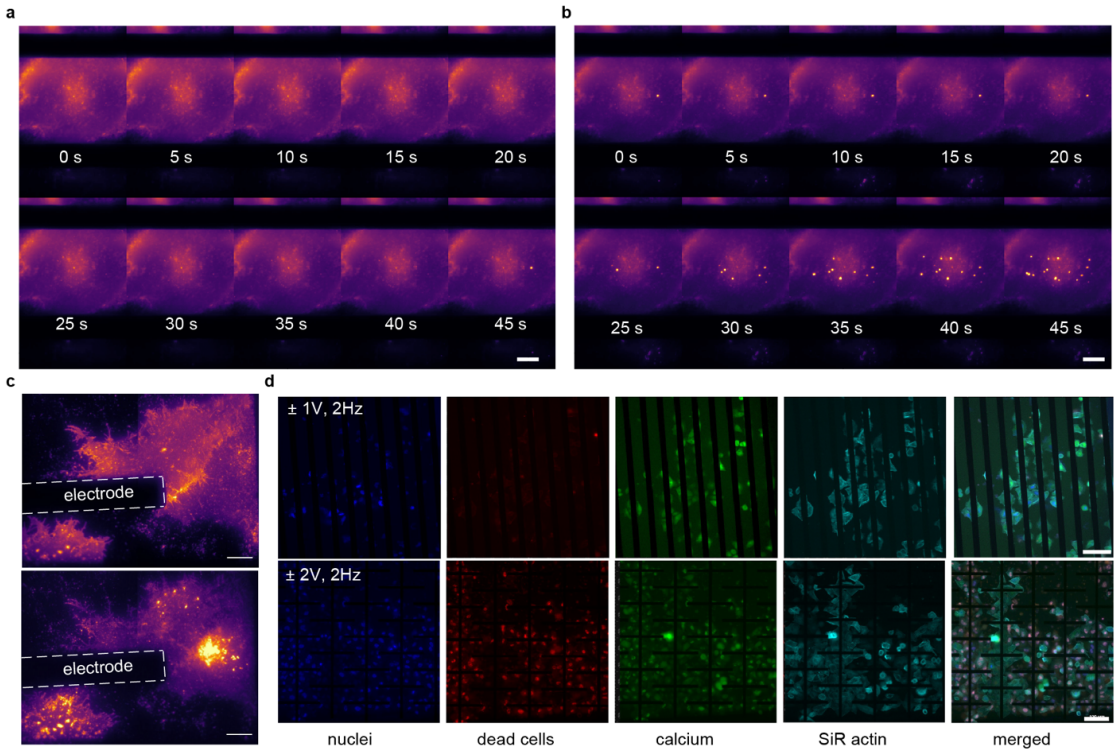

Figure 3-5. Bioelectrical stimulation induced exosomal release. a. A montage of super-resolution TIRF images of a HeLa cell cultured across the interdigitated gold electrodes (on #1.5 glass substrate). No bioelectrical stimulation was performed. **b.** Upon bioelectrical stimulation of 1V for 0.25 s and -1V for 0.25 s (i.e., ± 1V, 2Hz signals) for 50 s, the HeLa cell across the interdigitated gold electrodes showed boosted exosomal secretion. **c.** Top: the transfected HeLa on a gold electrode edge before bioelectrical stimulation. Bottom: the same transfected HeLa on the gold electrode edge after ± 2V, 2Hz bioelectrical stimulation for 1 min. The large area of pHluorin signal after ± 2V, 2Hz stimulation indicated cell membrane leakage. **d.** Live/dead analysis after applied bioelectrical stimulations.

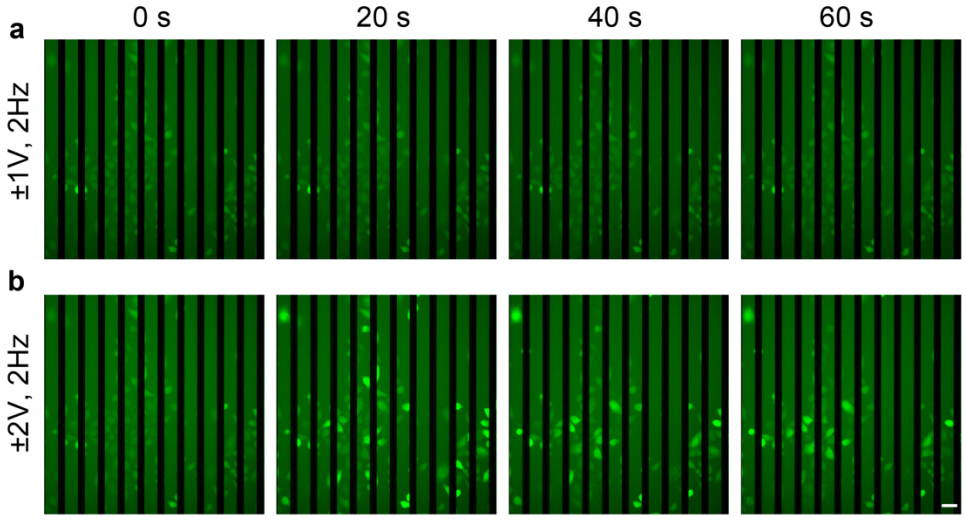

Figure 3-6. Calcium signals in electrical-stimulated HeLa cells. a. During ± 1V, 2Hz electrical stimulation, HeLa calcium levels remain stable, indicating intact membrane. **b.** During ± 2V, 2Hz electrical stimulation, HeLa cells quickly demonstrated elevated calcium, indicating membrane leakage. Scale bar, 20 µm.

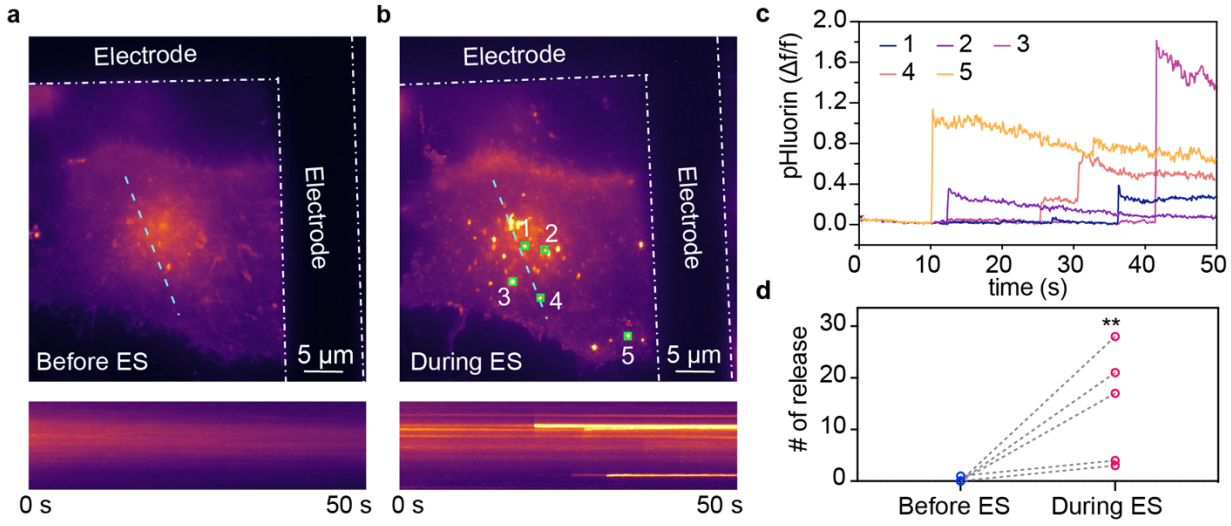

Figure 3-7. Bioelectrical stimulation-boosted exosomal release. a. Before electrical stimulation, no exosomal release was observed. **b.** During ± 1V, 2Hz electrical stimulation, 17 exosomal release events were observed in 50 s recording window. **c.** Representative individual intensity profiles

Figure 3-7, continued. shows the bioelectrical stimulation-induced exosomal releases. **d.** Quantification of the exosomal release observed in electrical-stimulated (± 1V, 2Hz) HeLa cells indicates that electrical stimulation can amplify exosomal production. The statistical analysis was performed using paired two-tailed t-tests; ** for $P < 0.01$.

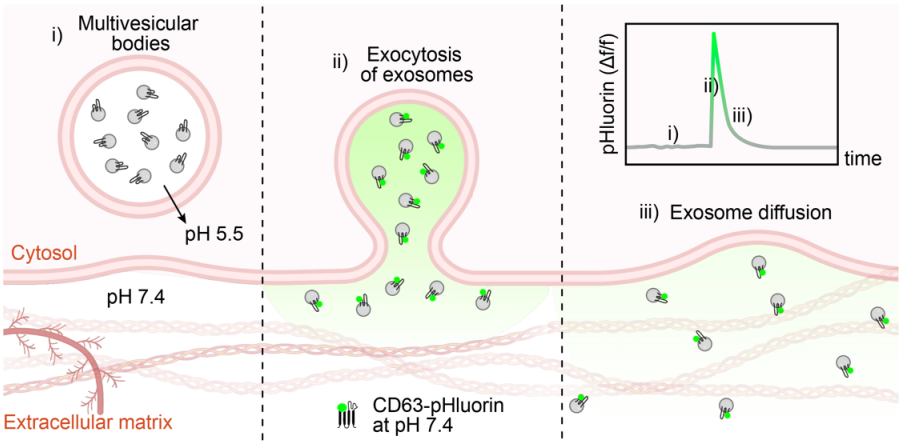

Figure 3-8. Signal of pHluorin during exosomal secretion. i) pHluorin is not fluorescent inside the multivesicular bodies, where has a neutral pH. ii) the MVB-PM fusion events (i.e., exosome release events) lead to a burst of pHluorin fluorescent intensity with the pH shift from the intra-vesicular region (pH = 5.5) to the extracellular region (pH = 7.4); iii) the pHluorin signal decays due to diffusion in extracellular region.

To further study the mechanisms that regulate exosome secretion, we used live-cell imaging and fixed-cell imaging to study actin cytoskeleton (**Fig. 3-9**), which is crucial for the study of many fundamental biological processes. We used Lifeact, a 17-amino-acid peptide that stained filamentous actin (F-actin) structures to visualize the actin dynamics together with pHluorin-CD63 exosomal secretion monitor. We also used AF647-phalloidin to label F-actin and antiCD63 antibodies (AF555) to label EVs marker CD63 in fixed HeLa cells. Here, we show that actin cytoskeleton may control the trafficking of multivesicular endosomes (MVEs).

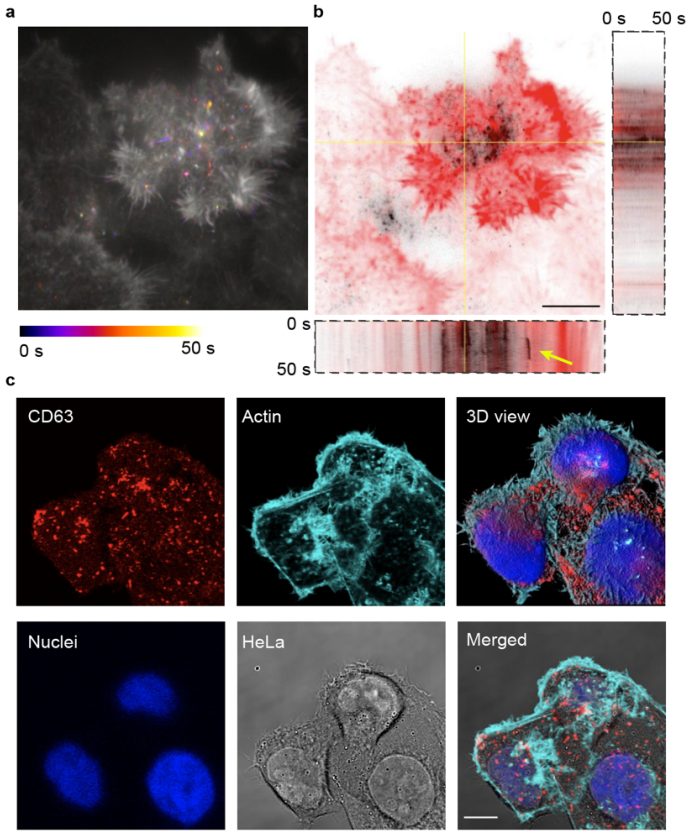

Figure 3-9. Actin may control the trafficking of multivesicular endosomes (MVEs). a. Live-cell imaging of the actin (white) and pHluorin-CD63 (temporal color) shows the trafficking of multivesicular endosomes. **b.** Orthogonal View (depth is the timescale) of the actin (red) and pHluorin-CD63 (black) in live HeLa cells shows the alignment of the traveling multivesicular body with the actin filament. Scale bar, 10 µm. **c.** Confocal microscopic imaging shows the distribution of actin (AF647-phalloidin) and CD63 (AF555-antiCD63). Scale bar, 10 µm.

3.2.4 EVs characterization

Transmission electron microscopy (TEM) has been the standard imaging technique in characterizing the nanoscale EVs. TEM revealed an approximately 3-fold increase in the exosome production and an approximately 1.5-fold increase in EVs sizes in term of diameter after electrical

stimulation for 12 hours (**Fig. 3-10**). The increased size of EVs would further help EVs engineering such as therapeutical cargo loading by allowing for a higher capacity.

We also characterized isolated EVs at the molecular scale by resolving subcellular structures via super-resolution direct stochastic optical reconstruction microscopy (dSTORM, **Fig. 3-11**). The multi-color dSTORM images verified the presentation and spatial distribution of representative exosomal markers (i.e., tetraspanins CD9, CD63, and CD81).

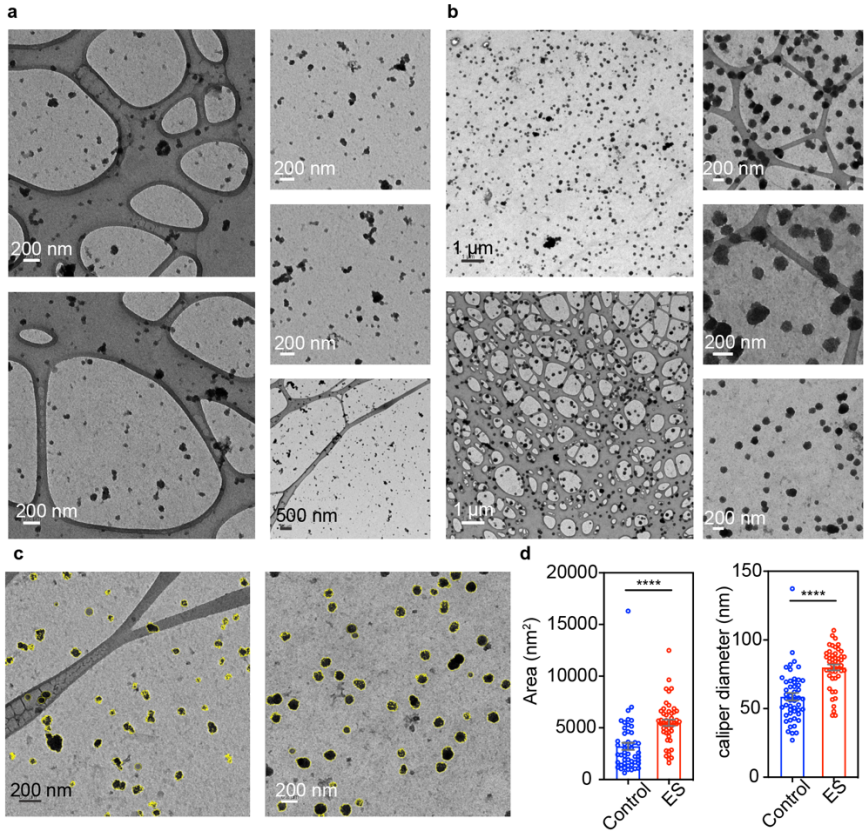

Figure 3-10. TEM images of isolated EVs. a. TEM images of isolated EVs from HeLa without bioelectrical stimulation. Cells were cultured 12 hours on silicon in DMEM medium with 10% exosome-depleted FBS. **b.** TEM images of isolated EVs from HeLa after 12-hour bioelectrical stimulation (± 1V, 2Hz) in DMEM medium with 10% exosome-depleted FBS. Experiment **a** and **b** were operated at the same time with the same procedures and there are more EVs from bioelectrical-stimulated HeLa compared to the non-stimulated HeLa-generated EVs. **c.** Selected

Figure 3-10, continued. regions of interest (ROIs) for EVs analysis. Left, isolated EVs from non-stimulated HeLa in **a;** Right, isolated EVs from bioelectrical-stimulated HeLa (± 1V, 2Hz, 12 hours) in **b. d.** Analyzed 2D area and diameter of the EVs in the ROIs in **c.** EVs from bioelectrical-stimulated HeLa show larger size compared to the non-stimulated HeLa-generated EVs. The statistical analysis was performed using unpaired two-tailed t-tests; mean value ± S.E.M with individual data points were showed in the bar chart. **** for $P < 0.0001$.

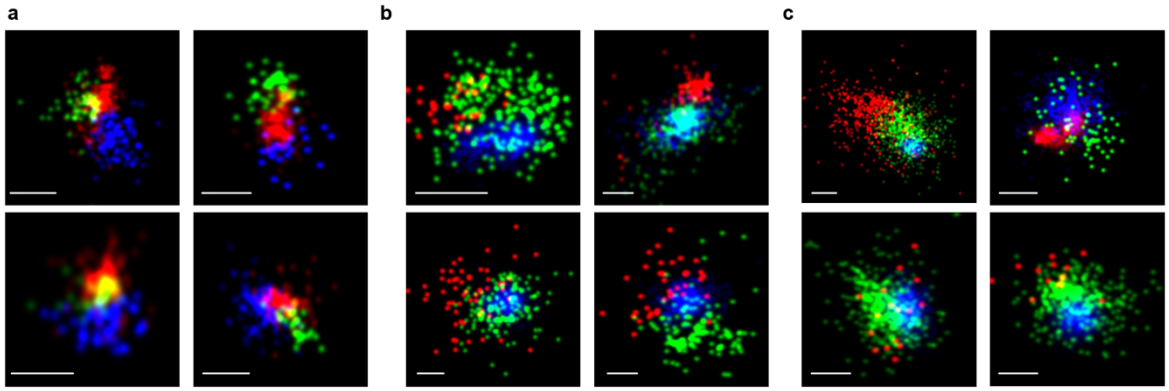

Figure 3-11. Representative super-resolution dSTORM micrographs of isolated EVs. a. EVs standards obtained from HCT116 human colorectal cell line. **b.** EVs isolated from non-stimulated HeLa cells (no stimulation, 2-hour culture in DMEM medium with 10% exosome-depleted FBS). **c.** EVs isolated from electrical-stimulated HeLa cells (± 1V, 2Hz, 2-hour stimulation in DMEM medium with 10% exosome-depleted FBS). Colors are tetraspanins CD9 (blue), CD81(red), and CD63(green) extracellular vesicles biomarkers. Scale bar, 100 nm.

3.2.5 Engineering Electrical Generated EVs for Cardiac Tissue Repair

Proliferation of cardiomyocytes after damage show potential in promoting cardiac repair[44–46]. Several microRNAs that are responsible for cardiomyocyte proliferation are of increasing interest to prompt cardioprotective strategies[47–51], for example, a miR-199a was shown to stimulate adult mouse cardiomyocytes to enter the cell cycle and proliferate following myocardial infarction

(MI)[47,52–54]. MiR-199a regulates critical pathways in cardiomyocytes glucose metabolism, hypertrophy, apoptosis, and autophagy[55–57], and induce pathological fibrosis in fibroblasts[52,58]. Other studies have identified that miR210[59,60] promotes angiogenesis in acute myocardial infarction.

Using EVs as microRNA carriers is minimally invasive to biological systems as EVs are endogenous biological signals. Besides, EV membranes enable stable preservation of the cargo microRNAs to avoid degradation and digestion in biofluidic.

As a proof-of-concept study to demonstrate the usage of electrical stimulation produced EVs (E-EVs) as shuttle for therapeutical microRNAs delivery, we first scaled up the bioelectrical stimulation devices on large piece silicon wafer to produce sufficient homogeneous quantities of EVs as the therapeutical drug delivery building block (**Fig. 3-12**).

We isolated the EVs from electrically stimulated (12-hour) HeLa supernatant (DMEM with 10% exosome-depleted FBS) and the therapeutical miR199a-3p and miR210 (1:1 mixture) were then loaded into the isolated E-EVs (miRNAs-E-EVs, **Fig. 3-13**) using transfection method (**Fig. 3-13a)**. We hypothesize that miRNAs-E-EVs treatment can empower the endogenous capacity of cardiac repair after damage by promoting regeneration of lost contractile tissue.

To ensure the loading was successful, we first used SYTO nucleic acid stain to label the miRNAs-E-EVs and obtained a fluorescence image of the EVs. loaded E-EVs with Texas Red-labeled siRNA as positive loading control EVs. These EVs were then added to HeLa cells and cultured for 24 hours. Fluorescence of the recipient HeLa cells indicated that the Texas Red-labeled siRNA cargo was successfully delivered using the E-EVs as carriers **(Fig. 3-13c).**

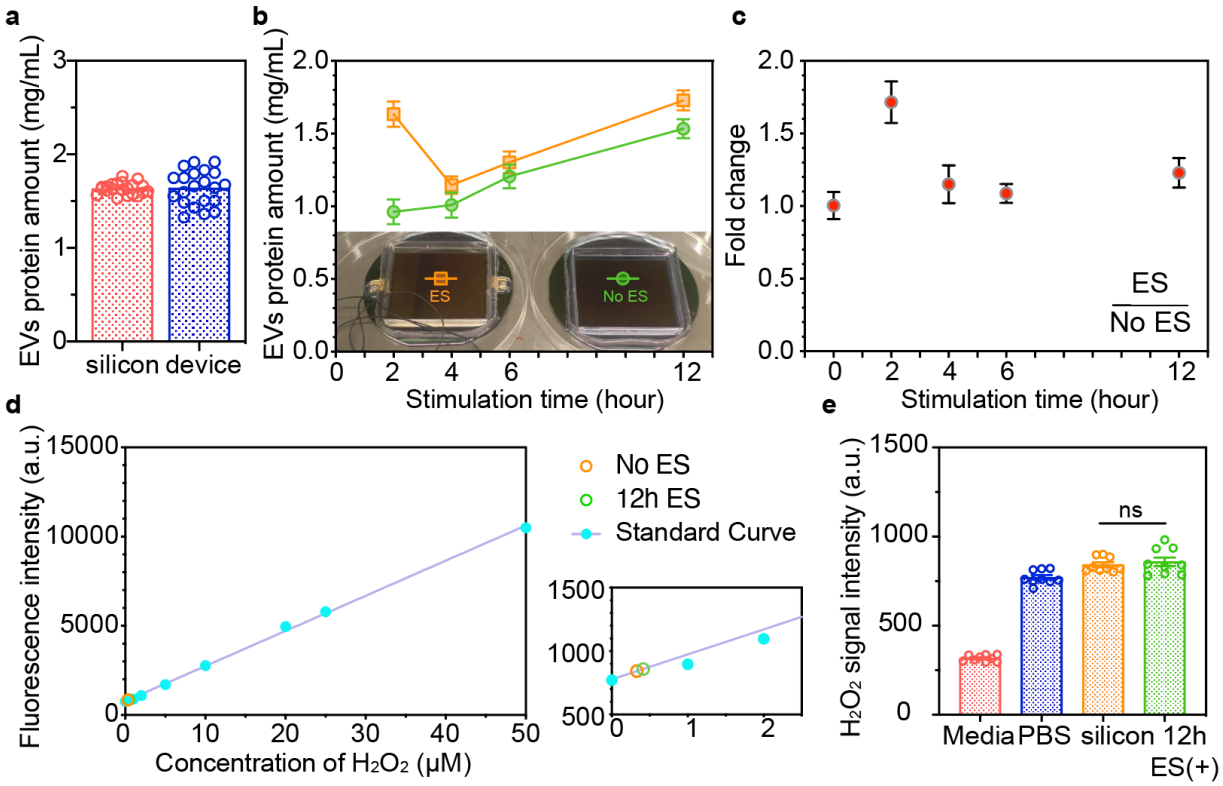

Figure 3-12. Scalable E-EVs production using large silicon device. a. HeLa cells were seeded onto silicon control wafer or device wafer with the same density and the medium was changed to DMEM with 10% exosome-depleted FBS after cell adhesion and HeLa were cultured for 12 hours on the substrate, after which the media were collected and EVs was isolated for protein quantification using BCA assay. No obvious difference on different substrates was observed. **b.** EVs protein amount was quantified using BCA assay after 2-, 4-, 6-, or 12-hour culture on silicon without electrical stimulation or on device with electrical stimulation. EVs in media were then isolated and quantified. Picture shows the 4-in wafer scale devices (left) and silicon wafer control (right). **c.** The fold change comparing electrical stimulation (ES) generated EVs amount with EVs amount in no ES culture on silicon. **d.** Standard curve and quantification of H_2O_2, an indicator of reactive oxygen species (ROS), shows minimal induced ROS after the 12-h electrical stimulation on device or 12-h culture on silicon**. e.** No significant production was observed in electrical

stimulated (12-h) culture. Statistical analysis was performed using unpaired two-tailed t-tests. The bar chart shows individual data points and the mean value ± S.E.M of multiple measurements. Ns for not significant or $p \geq 0.05$.

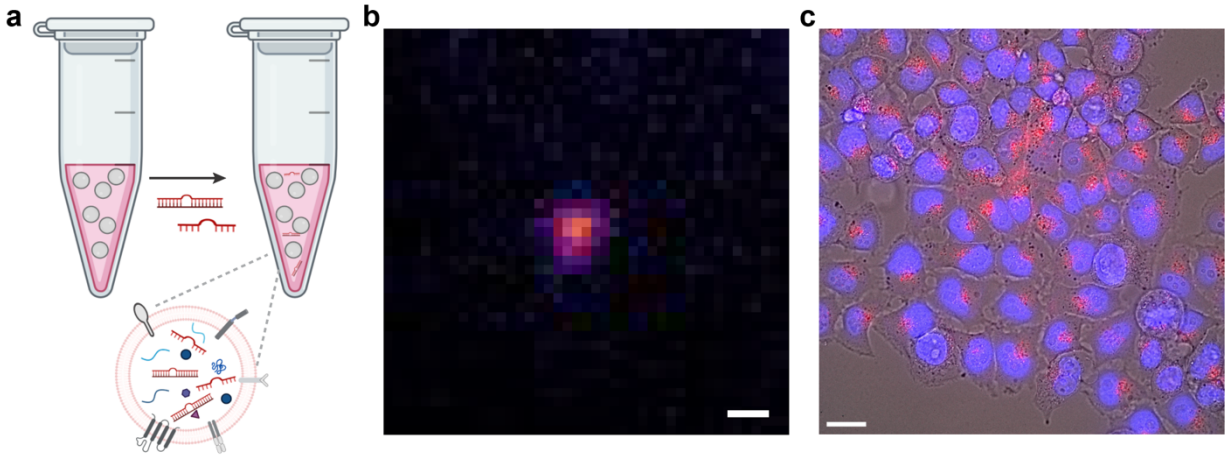

Figure 3-13. Engineering E-EVs with microRNA cargoes. a. To further evaluate the therapeutic potential of using electrical stimulation produced EVs (E-EVs) as microRNAs carriers, we loaded the isolated (E-EVs) with miR199a-3p and miR210 microRNA mimics using Exo-Fect™ miRNA Transfection Kit. **b.** A representative super-resolution image shows a miRNAs-E-EVs labelled with SYTO™ nucleic acid stain. Scale bar, 500 nm. **c.** Fluorescence imaging shows the recipient HeLa cells cultured with E-EVs that contained Texas Red-labelled siRNA cargo as positive loading control. Blue, nuclei; red, Texas Red-labelled siRNA. Scale bar, 20 µm.

3.2.6 Myocardial Infarction Treatment with miRNAs-E-EVs

Cardiac function repair was evaluated in rodent models of myocardial infraction (MI) using wild-type C57BI6 mice (6-8 weeks of age, male, weight > 20 g). During the MI surgery, the left anterior descending coronary artery (LAD) was ligated for 45 minutes. The cardiac specific miRNAs-E-EVs were delivered by four intramyocardial injections in four locations (10 µL each) to peri-infarct area within 5 minutes after reperfusion into each mouse. In this experimental setting,

the delivery of the EVs directly following MI surgery avoids a second surgery, which would importantly increase animal mortality. PBS injection was used as a negative control.

Heart function assessment was performed using echocardiography (Echo, **Fig. 3-14**). We conducted pre-surgery echo, and 1, 3, 7, 30 days after MI. To identify the anatomical structures and evaluate the heart functions, we collected parasternal long-axis view (PLAX) and parasternal short-axis view (PSAX) using both brightness mode (B-mode) setting and motion mode (M-mode) setting. We evaluated regional cardiac function using M-mode images, where the left ventricular (LV) ejection fraction (EF), fraction shortening (FS), and cardiac output (CO) were calculated.

$$EF = (1 - Systolic\ volume/Diastolic\ volume) \times 100\%$$

$$FS = (1 - Siastolic\ internal\ diameter/Diastolic\ internal\ diameter) \times 100\%$$

$$CO = (Diastolic\ volume - Systolic\ volume) \times Heart\ rate\ /\ 1000\ \ (mL/min)$$

Besides, we collected Pulsed-Wave (PW) Doppler Mode and Tissue Doppler Mode waveforms to assess mitral valve flow and annulus in the apical four chamber view, where we measured the mitral valve E wave, A wave, E' velocity, and A' velocity to evaluate the systolic and diastolic function and myocardium health (**Fig. 3-14**).

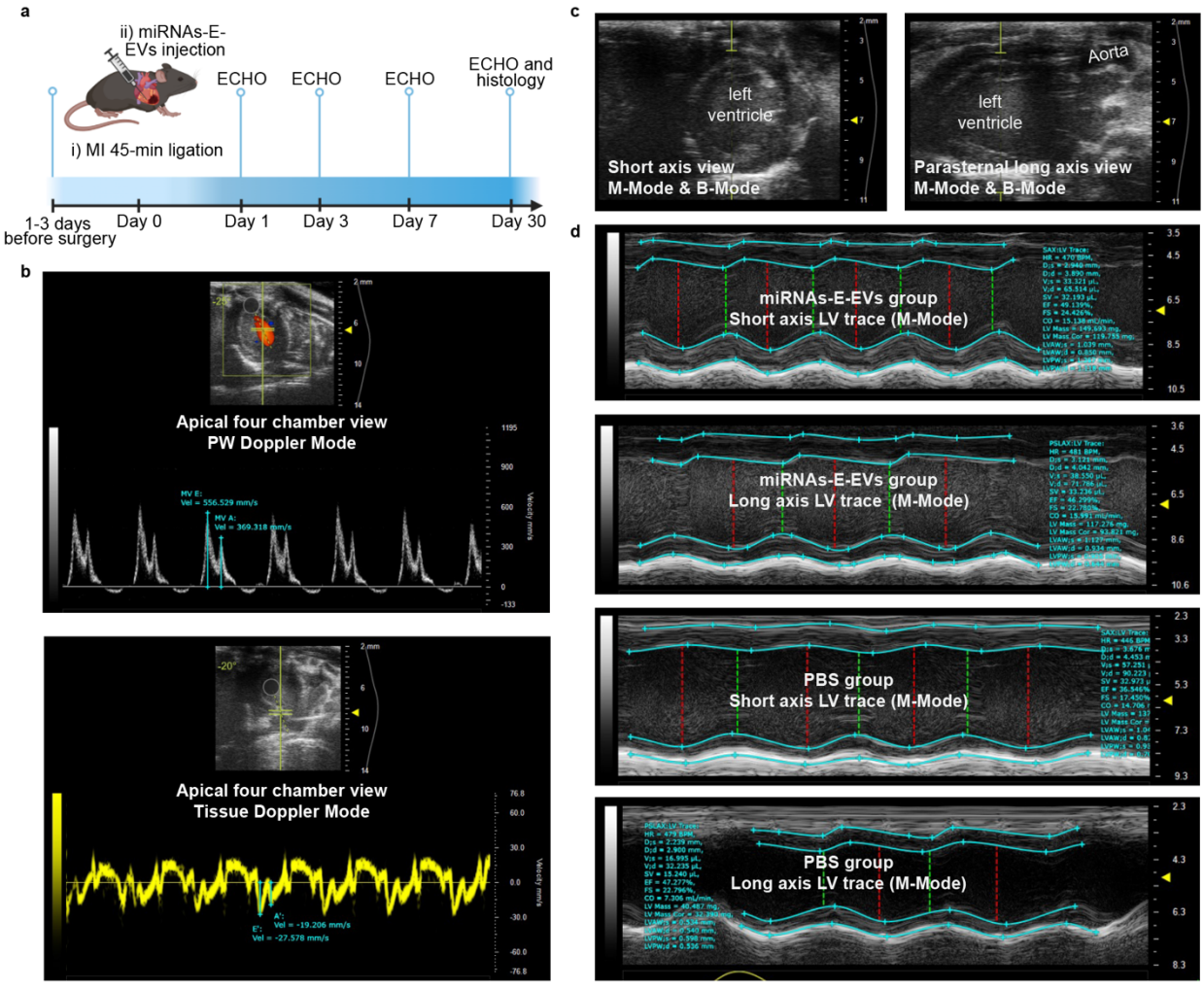

Figure 3-14. Evaluation of cardiac functions using echocardiography. a. Timeline of the experiment. Echocardiography studies were performed before the MI surgery and 1, 3, 7, 30 days after MI. Injections of therapeutical EVs or PBS (negative control) were performed after 45-min ligation. **b.** Top: representative image shows the apical four-chamber view and E/A assessment under PW Doppler Mode; bottom: representative image shows the apical four-chamber view and A'/E' assessment under Tissue Doppler Mode. **c.** Left: representative image shows the short axis view; right, representative image shows the parasternal long axis view. **d.** Representative images show the LV trace of the M-mode echo.

We found that miRNAs-E-EVs treatments repaired the cardiac functions in three days, while PBS control mice took seven days to recover. The miRNAs-E-EVs treatment mice showed gradually improved left-ventricular functions in terms of EF, FS, and CO post-MI. On day 3, miRNAs-E-EVs treatment mice had no significantly different EF, FS, and CO values compared to healthy mice without MI surgery **(Fig. 3-15).** For the E/A, A'/E' assessment, day 7 miRNAs-E-EVs treatment mice showed similar ratios to the pre-surgery mice while PBS treated mice showed large individual variations. Besides, miRNAs-E-EVs treated MI mice showed better growth compared to the PBS-treated MI mice regarding the body weight, heart weight, and tibia length measured three days after MI and injection.

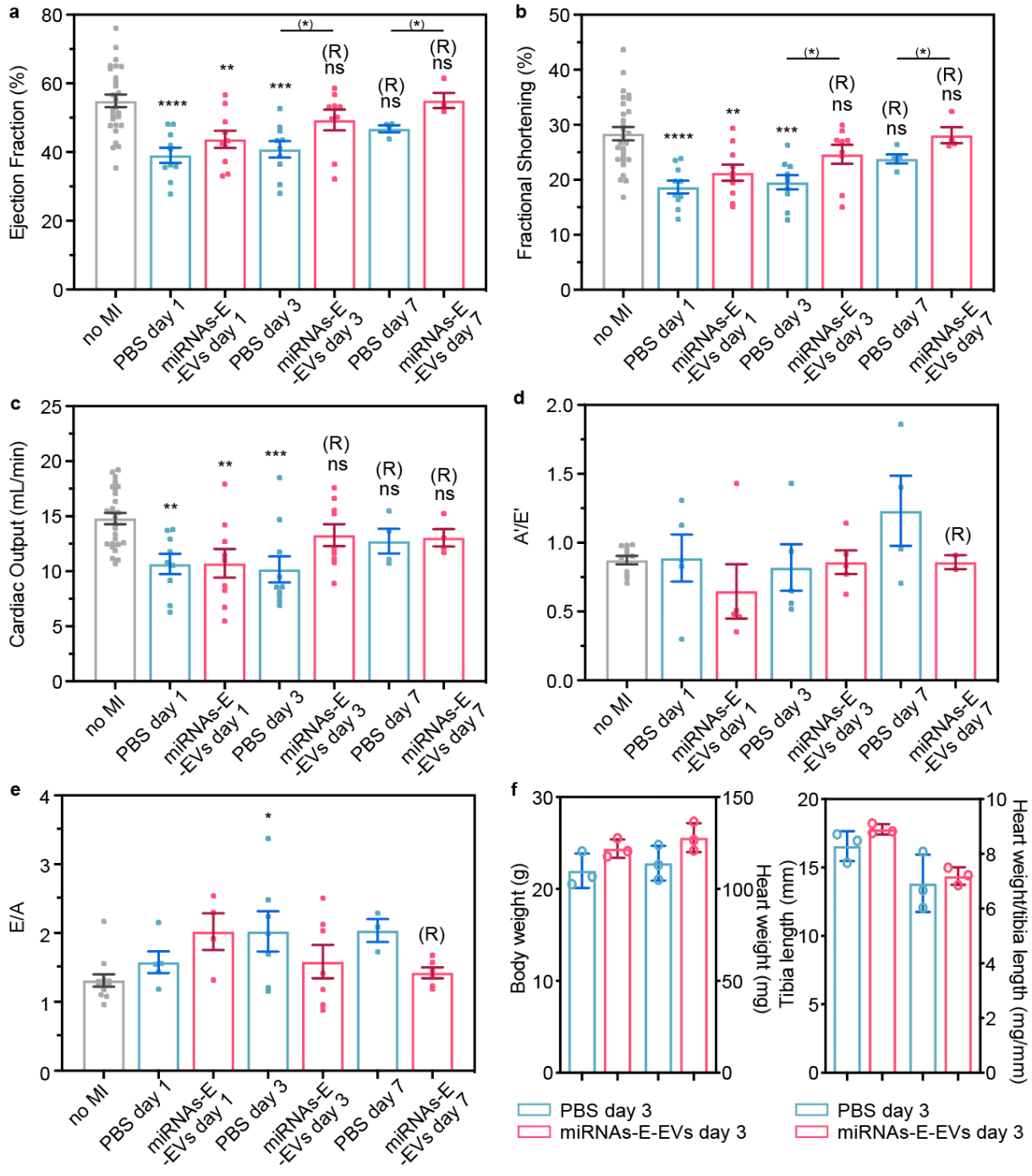

Figure 3-15. Injection of miRNAs-E-EVs improves cardiac functions in MI-mice. a-c. EF, FS, and CO show that miRNAs-E-EVs recovered (indicated by R in the bar chat) the heart systolic and diastolic function in three days; no significant difference to the value from healthy mice ('No MI' included both mice without MI measured along with MI-mice at different growth time or the

Figure 3-15, continued. experimental mice measured before their MI surgery). It took 7 days for PBS control mice to recover their EF, FS, and CO. Statistical analysis was performed either using ANOVA tests with Dunnett's correction for multiple comparison with a single control (the 'no MI' group) or unpaired two-tailed t-tests, indicated using '(*)'. Each bar chart shows the mean value ± S.E.M and individual results; each mouse generated a value from long-axis M-mode and a value short-axis M-mode, (n=28 for no MI; n = 10 for day 1, 3; n = 4 for day 7). R for recovered; * for $P < 0.05$; **$P < 0.01$, ***$P < 0.001$, ****$P < 0.0001$ and ns for not significant or $p \geq 0.05$. **d-e.** A'/E' and E/A assessment of the heart systolic and diastolic functions shows recovered (indicated by R in the bar chat) value in miRNAs-E-EVs treatment 7 days post-MI. **f.** MI mice with miRNAs-E-EVs treatment shows better growth compared to the PBS-treated MI mice.

We also evaluated the heart strain, a measurement of the extent of heart deformation during pumping and relaxing cycles, using B-mode images and studied the time-to-peak and heart regional synchronicity. Strain at a particular point along the endocardium can be calculated as a percentage describing the deformation at two cardiac cycles. For example, the distance between a point and a secondary point inside the myocardium (outside of the endocardium) is measured at the baseline timepoint in the cardiac cycle (i.e., the R-wave), and this distance is compared to the distance between the same two points at another instant in the cardiac cycle. The difference between the two distances (i.e., deformation) can be represented as a percentage (i.e., strain) of the original distance. Due to the dynamic nature of the heart, strain can be measured in three different planes (i.e., circumferential, radial, longitudinal). Based on the direction of deformity that is detected, radial strain was measured from both short-axis and long-axis B-Mode images, circumferential strain was measured from short-axis images, and longitudinal strain was measured from long-axis images. We then assessed the synchronicity between regions of the heart using

time-to-peak analysis in strain curves, where the time from the R-wave (baseline) to the maximum peak was determined in six segments of the left ventricular (LV) wall. Phase, a calculation based on the entire cardiac cycle rather than just the maximum strain point (as is used in time-to-peak analysis), was also calculated as a percentage, where the times of each segmental sinusoid (deconstructed via Fourier Transformation) reaches their peak are compared to the peak of the average sinusoid component of all the left ventricular segments.

The miRNAs-E-EVs treatments of MI mouse showed great synchronicity between regions of the MI heart **(Fig. 3-16)**, while PBS-injected control mouse demonstrated certain degree of desynchronization post-MI. Besides, miRNAs-E-EVs has helped maintain the time-to-peak value of the strain; there is no obvious changes of the time-to-peak in circumferential, radial, longitudinal strain curves along the endocardium comparing the pre-surgery (healthy) mouse and the MI mouse treated by miRNAs-E-EVs. However, PBS-treated MI mice showed prolonged time-to-peak in short-axis circumferential and radial strain curves along the endocardium.

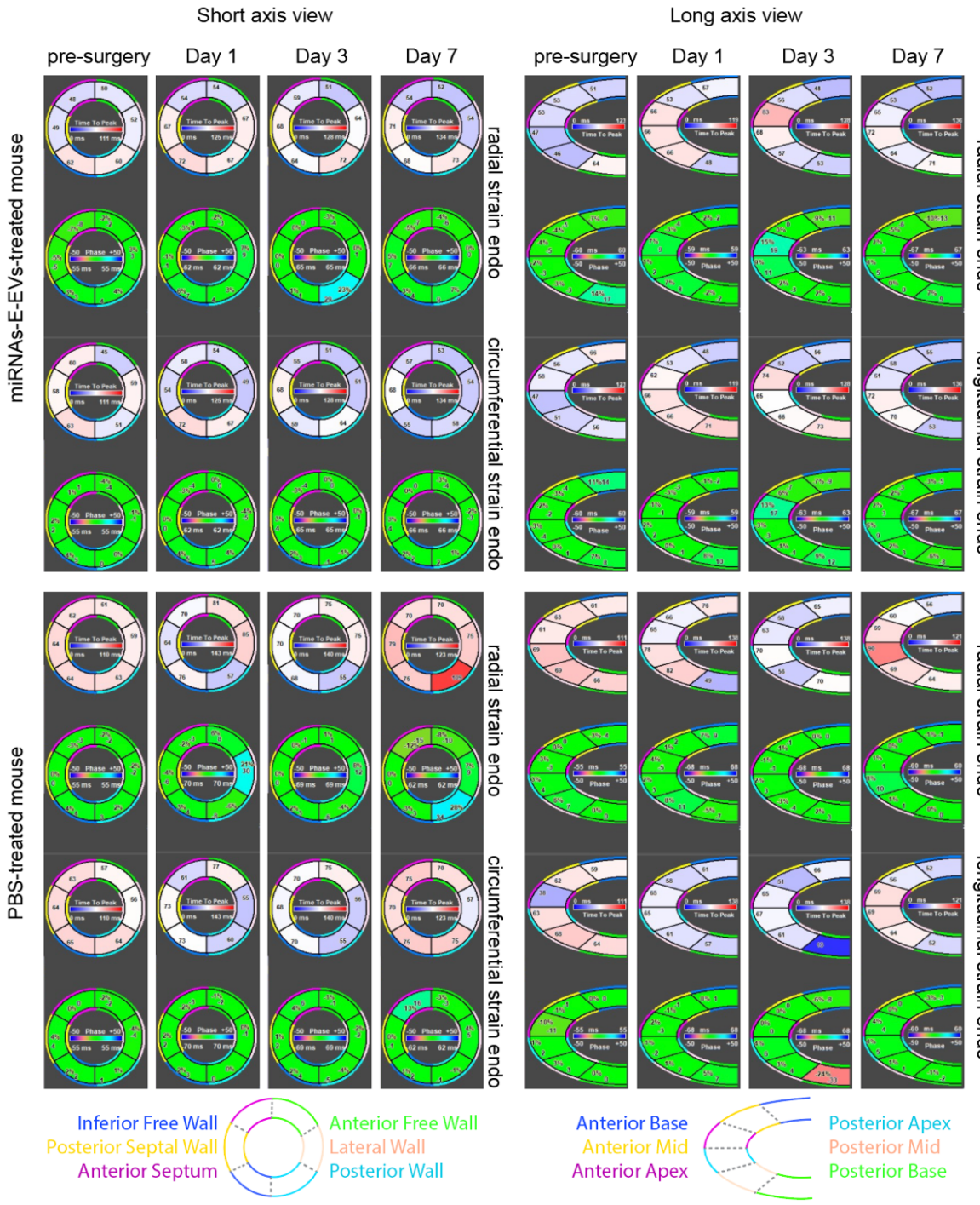

Figure 3-16. Time-to-peak analysis and heart regional synchronicity. Treatment with miRNAs-E-EVs in MI-mice maintained heart synchronicity and time-to-peak while PBS control showed asynchronism and prolonged time-to-peak in short-axis radial and circumferential stain along endocardium.

Electrocardiogram (ECG) was also recorded during the echocardiography. Similar to the echo data, the ECG and corresponding spectrogram also showed that miRNAs-E-EVs treatment was able to recovery the heart rhythm and electrical activity in three days back to pre-surgery healthy level **(Fig. 3-17).** We also analyzed the R wave deflections in the ECG QRS complex **(Fig. 3-18)** and found that a PBS-treated mice showed diminished rise rate (only ~50% retention) post-MI compared to pre-surgery healthy level, while miRNAs-E-EVs treatment maintained both the rise rates (97% retention on day 2; 94% retention on day 3) and fall rates rates (101% retention on day 2; 99% retention on day 3).

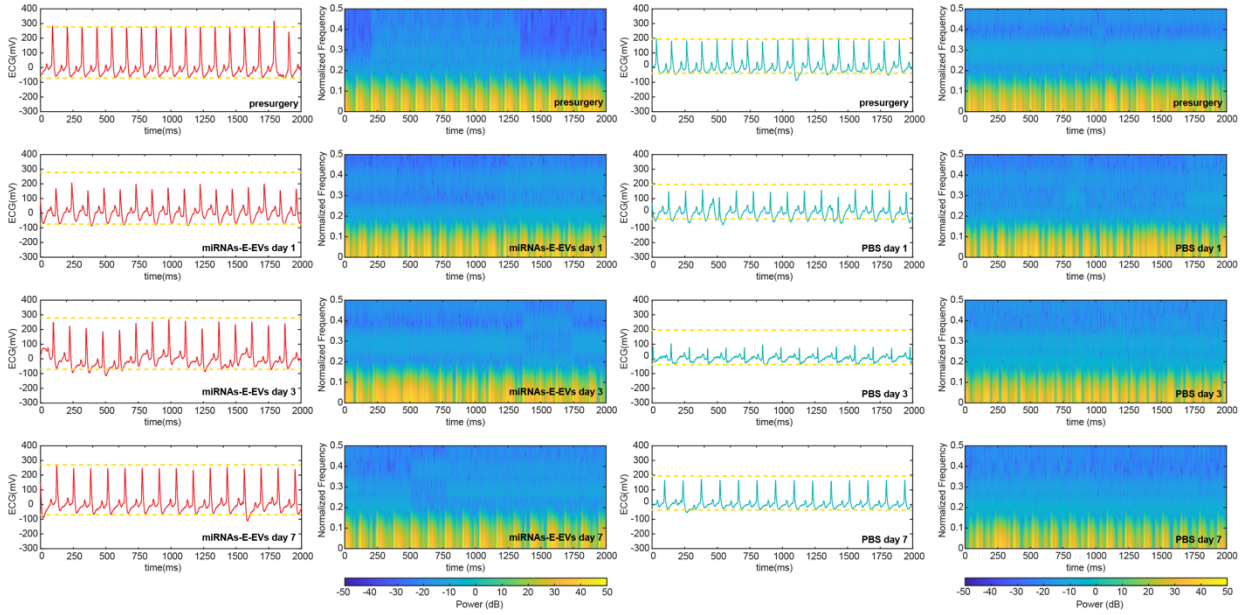

Figure 3-17. Representative ECG and spectrogram of the MI mice. Left ECG and spectrogram, a MI mouse with miRNAs-E-EVs treatment demonstrated recovered ECG post MI; Right ECG and spectrogram, a representative MI mouse with PBS treatment demonstrated approximately recovered ECG post MI.

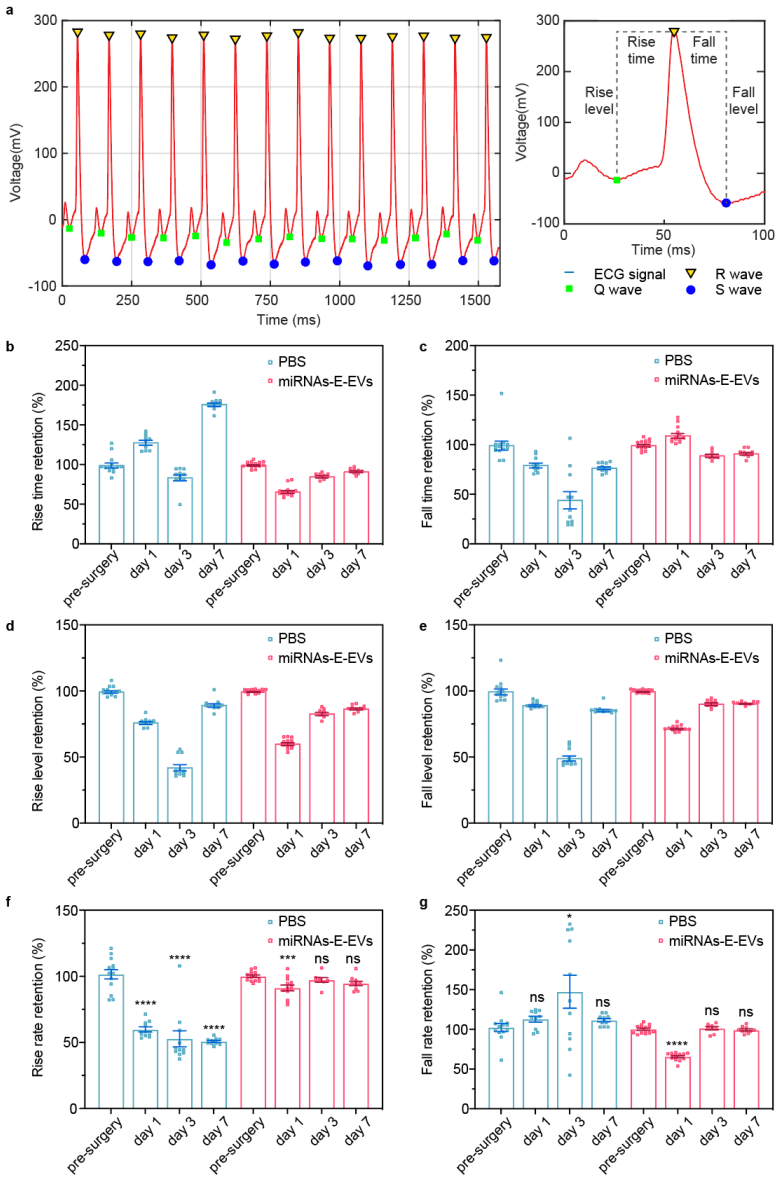

Figure 3-18. Analysis of ECG signals and QRS complex. a. Representative ECG shows the example of Q, R, S waves. **b.** Rise time measured from the Q-to-R rise in ECG signals and retention is normalized to pre-surgery health mice rise time. PBS-treated MI mice shows prolonged rise time. **c.** Fall time retention obtained from the R-to-S fall in ECG signals. **d.** Rise level retention calculated from the Q-to-R rise in ECG signals. **e.** Fall level retention calculated from the R-to-S fall in ECG signals. **f.** Rise rate retention calculated from Q-to-R rise in ECG signals. PBS-treated MI mice shows only 50% retention of the pre-surgery (healthy) rate while miRNAs-E-EVs kept

Figure 3-18, continued. the rise rate of the heart post-MI. **g.** Fall rate retention calculated from R-to-S fall in ECG signals. All statistical analysis was performed using ANOVA tests with Dunnett's correction for multiple comparison with a single control (pre-surgery). Results are measured on the same mouse at different time points (day 1, 3, 7 after MI). Each bar chart shows individual data points and the mean value ± S.E.M of multiple measurements in an ECG ($n > 8$). *$P < 0.05$, **$P < 0.01$, ***$P < 0.001$, and ns for not significant or $p \geq 0.05$.

After 30 days survival post-MI, phenotypic characterization of the heart was conducted via histological analyses (**Fig. 3-19).** The hearts were harvested and fixed in 10% formalin, embedded in paraffin, sliced into horizontal cross-section slices (5 µm thickness; 500 µm steps), and stained with Haematoxylin and eosin (H&E) and Masson's trichrome (MTC) stainings. The extent of cardiac fibrosis was quantified by blinded researchers and calculated using the area of positive MTC staining region (blue) as a proportion of the total tissue section area.

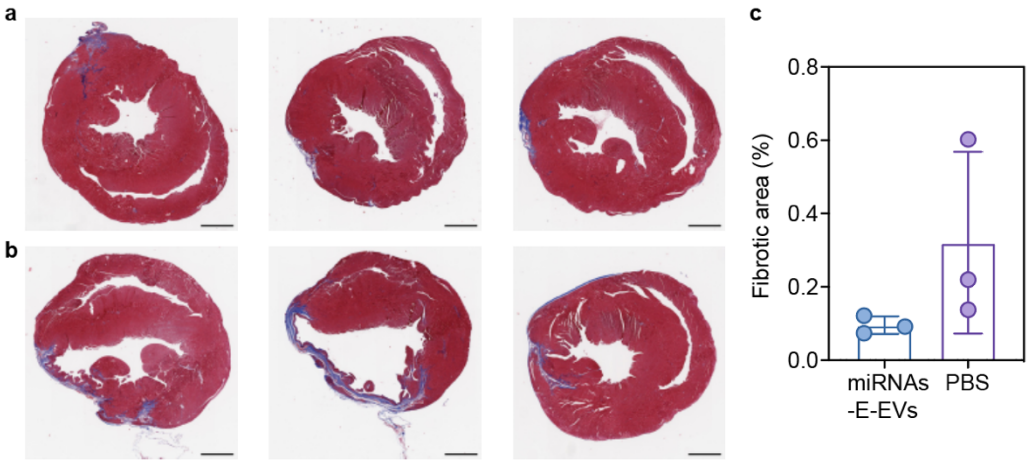

Figure 3-19. Treatment of miRNAs-E-EVs shows reduced fibrosis post-MI. a. Representative images of the Masson's trichrome staining of heart 30 days after MI and injection of miRNAs-E-EVs. Scale bar, 1 mm. **b.** Representative images of the Masson's trichrome staining of the infarcted heart 30 days after MI and injection of PBS negative control. Scale bar, 1 mm. **c.** Summary of the

Figure 3-19, continued. percentage of fibrotic area (blue region in the trichrome staining). Treatment of miRNAs-E-EVs shows reduced fibrosis post-MI.

3.3 Discussion and Outlook

We investigated the bioelectrical stimulation on exosomal production, and we revealed that exposing cells to alternating electrical stimulation stimulates their generation without detriment to cell viability. Using the bioelectrical stimulation generated EVs as carriers for microRNAs, we delivered two therapeutical microRNAs for cardiac tissue repair, which speed up the function recovery in myocardial infarction mice. Altogether, our prove-of-concept work represents a system for producing EVs using electrical stimulation for *in vivo* tissue repair.

With the acute exosomal amplification in HeLa cells, we hope to further scale up the production to produce sufficient homogeneous quantities of bioelectrical stimulation-generated EVs for clinical related translation. For better translate exosome therapy into clinical practice, a simultaneous microRNA loading during the electrical stimulation is preferred instead of post-isolation loading. Besides, extending the practice of bioelectrical exosomal production in other cell types, especially in electrical excitable cells like neurons and cardiomyocytes, would bridge the exosome field and the bioelectronic field, and may benefit the studies of biomodulation to yield a understanding of the electrical-induced cellular dynamics from subcellular or molecular level.

3.4 Experimental

3.4.1 Device Fabrication

Device design was performed in AutoCAD software. Electrodes had a width of 10 μm with 40 μm spacing between the two interdigitated electrode comb. Interdigitated gold electrodes were fabricated using photolithography on #1.5 glass (0.17-mm thickness) substrates (Ted Pella Inc., ClariTex coverglass for super mega slides, 64 mm x 50mm). First, the thin glass was cleaned with acetone and IPA in the ultrasonic bath (72 kHz), soaked in DI water in sequential order, and dried using nitrogen gas. HMDS vapor priming was then implemented on the glass slide using the YES-58TA system to facilitate the adhesion. Then the glass substrate was bonded onto a silicon carry wafer slide (55mm x 70 mm) utilizing AZ2070 photoresist to prevent the thermal expansion of glass during baking processes. This step is critical to avoid the detaching of cured photoresist on the glass due to uneven mechanical strains during baking. The photoresist was selected as an easily solvent-removable, clean-room accessible, and thickness-controllable adhesive. In contrast, conventional adhesives, such as crystalbond^{TM}, are hard to apply and remove, and the thickness is hard to control. AZ2020 photoresist was spin-coated on the glass and soft baked at 110 °C for 2 min. After exposure using a Heidelberg direct writer (MLA150, 375 nm laser, 190 mJ/cm^2, defocus +1), the photoresist was baked at 110°C for 2 min and developed using AZ 300MIF for 60 s. After DI water rinsing and O_2 descum, 5 nm chromium and 100 nm gold were evaporated on the patterned surface using an electron-beam evaporator (Angstrom EvoVac Electron Beam Evaporator). Lastly, the resist was stripped in remover PG at 80°C for 6 h, during which the glass substrate bonded by AZ2070 also detached from the silicon wafer. In sequential order, the patterned gold@glass was cleaned using acetone, IPA, N2 gas, DI water, and N2 gas. A schematic of the fabrication process is shown in **Fig. 3-2**.

3.4.2 Device Chamber and Wiring

A mixture of 10:1 PDMS to curing agent was poured onto a homemade **polyacrylic** plastic mold cut by laser cutter and glued using dichloromethane. The PDMS in mode was left to cure for 2 h at 80 °C after degassing in a vacuum desiccator. Once the PDMS is fully cured, the PDMS layer is peeled off. The device is cut with a blade and bonded onto the patterned glass after oxygen plasma treatment (200W, 2 min).

A large pad connected to the comb-shape single-channel electrode allowed for manual connection to jumper wires. Jumper wires were connected to the pads via soldering, and the connections and excess connecting traces were insulated using silicone glue (Kwik-Sil, World Precision Instruments). Devices were sterilized with 70% ethanol and ultraviolet light and washed three times with PBS before the cell culture.

3.4.3 Cell Culture

HeLa were cultured in high glucose Dulbecco's Modified Eagle Medium (DMEM) supplemented with 10% FBS, 100 U/ml penicillin G, 100 mg/ml streptomycin sulfate, and 2 mM glutamine. All cultures were maintained at 37°C, 5% CO_2, and 100% humidity. Prior to electrical stimulation and quantification experiments, the culture media was changed to DMEM media constructed with 10% exosome depleted FBS (System Biosciences LLC, EXOFBS50A1).

3.4.4 Transfection

The plasmid used for transfection was the pCMV-Sport6-CD63-pHluorin plasmid, a gift from DM Pegtel (Addgene # 130901). The plasmid was amplified in Escherichia coli DH5a and was isolated and purified using the ZymoPURE DNA Plasmid Isolation Kit. DNA purity and

integrity were determined spectroscopically. The DNA (100 ng/μL) was stored at -20°C for future usage.

Plasmid transfections were performed using Fugene HD transfection reagent according to the manual on cells at 30–50% confluency. Fugene HD and pCMV-Sport6-CD63-pHluorin DNA (3:1) were added into Opti-MEM™ (FISHER SCIENTIFIC COMPANY LLC, 31985070) reduced serum medium and incubator at room temperature for 15 min before adding to cell culture. Cells were stimulated and imaged using TIRF after 48-72 h transfection.

3.4.5 Bioelectrical Stimulation

Cells were seeded on the sterilized devices and cultured for 24 hours before electrical stimulation. Interdigitate electrode devices were connected to a potentiostat (SP-200, BioLogic), and biphasic voltage waveforms of various amplitudes of voltage, frequencies, and duration were delivered using the EC-Lab® Express (v.5.56) program. The electric potential was reported as the potential between the two individual interdigitated combs. To reuse the stimulation devices, 0.25% trypsin-0.02% EDTA (Sigma-Aldrich, 59428C), 10% sodium dodecyl sulfate (SDS) solution (Invitrogen™, 15553027), acetone, IPA, ethanol, UV, PBS washing were sequentially applied for 30 min to clean the gold electrode surface and sterilize the device.

3.4.6 Electrochemistry Characterizations

Cyclic voltammetry (CV) and impedance measurements were evaluated with or without cell cultures on the devices using a potentiostat (SP-200, BioLogic) controlled by EC-Lab® Express (v.5.56). For the measurement, a pair of interdigitated gold electrodes on silicon substrate was connected as the working electrode, a platinum wire was connected as a counter electrode,

and a Ag/AgCl (1 M) electrode was connected as a reference electrode. CV was performed within -1V to 1V voltage window with a scan rate of 100 mV/s, and potentiostatic electrochemical impedance spectroscopy (PEIS) measurements were performed from 1Hz to 1000 kHz frequency range.

3.4.7 COMSOL Simulation of Electrostatic Potential

The device structure constructed using AutoCAD was imported into COMSOL Multiphysics software (version 5.6) for performing finite element simulations of electrostatic potential between the interdigitated combs. The potential between the interdigitated electrodes was set to ± 1 V.

3.4.8 Real-Time Monitoring of Exosomal Secretion

The transfected cells expressing pHluorin-tagged CD63 were cultured on interdigitated gold electrodes on glass substrates to enable fluorescent imaging. The two individual combs were connected to electrical inputs for bioelectrical stimulations while simultaneous time-lapse Total Internal Reflection Fluorescence (TIRF) imaging. Imaging was performed using 488 nm laser setup (power = < 25% or < 2.5 mW to minimize photobleaching) on the Oxford Nanoimager (ONI) with a 100× (1.4NA) oil immersion super apochromatic objective (Olympus) and an ORCA- Flash 4.0 V3 sCMOS camera (Hamamatsu Photonics). The ONI images field of view is 50µm x 80µm and 0.117 µm pixel size. During all imaging and bioelectrical stimulation experiments, the temperature was controlled to 37°C, and Tyrode's solution (2 mM $CaCl_2$, 2.5 mM KCl, 119 mM NaCl, 2 mM $MgCl_2$, 30 mM glucose; pH 7.4) buffered with 25 mM HEPES was used as media in

the stimulation PDMS chamber. Time-lapse images were captured at a frame rate of 10 frames per second (fps) before and during the electrical stimulation.

3.4.9 Exosome Secretion Image Analysis

Time-dependent exosome secretion were analyzed at selected regions of interest (ROIs) with a burst fluorescent intensity. To see the exosomal production characteristic, we get the maximum intensity projection from the image stack using ImageJ, Z Project function. Bleach correction was conducted using exponential fit. Representative pHluorin intensity profiles were taken from 9 pixel x 9 pixel square (1.05 μm x 1.05 μm field of view). 3D project function (color code: mpl-inferno; projection method: brightest point; axis of rotation: y-axis; initial angle: 90; total rotation and increment: 0). Fusion activity was defined as the number of events over a time-lapse experiment, which varied between experiments but was typically between 50 s to 100 s. $N \geq 5$ cells were imaged per condition in different imaging windows. Data shown are representative experiments replicated in independent experiments.

3.4.10 EVs Isolation

EVs were purified from cell culture supernatant after 24-h culture with or without bioelectrical stimulation. The supernatant was centrifuged at 2,000 g for 10 min to remove cellular debris. The supernatant was transferred to a new tube, and total exosome isolation reagent (Invitrogen™, 4478359) was added 1:2 (v/v) to the cell-free culture media. After vertexing and storing under 4 °C overnight, the EVs were collected by centrifuging at 11,200 g for 1 h. EVs are contained in the pellet at the bottom of the tube. After aspirating and discarding the supernatant,

the EVs pellet was resuspended in 20-100 µl PBS for downstream analysis. The isolated EVs were kept at 4°C for 1 week or at -20°C for long-term storage.

3.4.11 EVs Electron Microscopy Characterization

Isolated EVs were fixed with 2% paraformaldehyde PBS solution for 1 h and then transferred to lacey carbon support film with ultrathin carbon film (Ted Pella. Inc., # 01825). Afterward, the adsorbed EVs were stained with uranyl acetate (2%) for 30 s, and samples were washed carefully with 100 µL distilled water. After air drying, the EVs were imaged with a transmission electron microscope (TEM, FEI Tecnai G2 Spirit) under 120 kV.

3.4.12 EVs Super-Resolution dSTORM

We conducted dSTORM imaging to validate the presence of known EV membrane markers (e.g., the tetraspanins CD63, CD9, and CD81). Sample preparation was performed following the manufacturer's instructions using the EV Profiler Kit (Oxford Nanoimaging Inc.; product EV-MAN-1.0), which includes reagents for EVs capturing/immobilization, fixation, blocking, washing, dSTORM imaging buffers, and validated antibodies with dSTORM-compatible fluorophores for EVs labeling (i.e., anti-CD9-CF®488, anti-CD81-CF®647, and anti-CD63-CF®568 in 10 µg/ml working solution). Briefly, a 2.5 µl EV sample was added to a 3.5 µl blocking solution and mixed gently without introducing bubbles. After 5 mins incubation at room temperature, 3 µl of mixed antibodies (1 µl of each marker, ~ 1 µg/ml final labeling concentration) was added to the EV solution, followed by gently mixing and incubating overnight at 4˚C. The next day, after capture chip surface preparation, EV capture was performed immediately by incubating the antibody labeled EVs onto the capture chip for 15 mins at room temperature (which

was done without exposing the chip to light). The chip lanes were washed with 100 µl wash buffer; then, 50 µl of fixation solution was added to each lane for 10 minutes and washed with 100 µl wash buffer. Next, dSTORM imaging buffer was added, then the chip lanes were immediately sealed with an adhesive strip to avoid liquid evaporation.

For three-color dSTORM acquisition, the Nanoimager S (Oxford Nanoimaging Inc.) camera was calibrated using 100 nm Tetraspek microspheres (Invitrogen T7279) diluted in PBS. Calibration beads were viewed under the Nanoimager using a 405/473/561/640 nm laser configuration with the 100× oil-objective lens. Images were taken using the NimOS software with 10 ms per frame and 5000 frames per channel. EVs from the HCT116 human colorectal cell line (2.1 × 1011 per ml), validated for tetraspanin expression, were used as a standard positive control.

The super-resolution dSTORM image was processed using the ONI image analysis cloud platform CODI (alto.codi.bio) for drift correction, filtering, and counting. The image frames were first filtered according to the laser sequence in which the localization was detected. Then the standard deviation of the fitted point spread (sigma) was set to 300 nm, and the localization precision was set to 10-30 nm. EVs were reconstructed by setting the length of the merged three-color clusters to be less than 2000 nm to filter out large aggregates. Representative $CD9^+$, $CD81^+$, and $CD63^+$ triple-positive EVs images (pseudo-colored in blue for CD9, green for CD63, and red for CD81) were shown and analyzed for shapes, sizes, and marker distributions.

3.4.13 MicroRNA Loading

Therapeutics microRNA-199a (mmu-miR-199a-3p, Applied Biological Materials Inc., MCM01432) and microRNA-210 (mmu-miR-210, Applied Biological Materials Inc., MCM01489) were co-loading (1:1) into bioelectrical stimulation-generated EV carriers using Exo-Fect™

siRNA/miRNA transfection kit (System Biosciences, LLC, EXFT200A-1) according to manufacturer's instructions. Successful loading was verified by culturing non-fluorescent HeLa cells with EVs loaded with Cy5-labeled control siRNA and measuring the percentage of fluorescent cells.

3.4.14 Animal

Wild-type C57BI6 mice (6-8 weeks of age, male, weight > 20 g) were obtained from Charles River Laboratories and housed in the animal facility of the University of Illinois at Chicago. The animal room was maintained at a humidity of 40–60% and a temperature of 18–23 °C under a 12-h-light/12-h-dark cycle. The animals were allowed free access to food and water. All the procedures were approved by the Ethics / Animal Care Committee of the University of Illinois at Chicago.

3.4.15 Mice Acute Myocardial Infarction (AMI) Model

Prior to surgery, mice were be weighed and given a subcutaneous injection of Buprenorphine SR LAB (1.0 mg/kg). Anesthesia will be introduced using 1.5-3% isoflurane inhalation in a closed chamber. Aseptic procedures will be used for all surgery and instruments will be sterilized with a hot bead sterilizer between mice. Depth of anesthesia monitoring will be carried out by assessing reluctance to move via lack of response to a toe-pinch. Surgical anesthesia will be maintained using 2% isoflurane delivered through a vaporizer with air connected in series to rodent ventilator. Chest will be shaved, or hair removed via Nair® depilating agent. Skin is then scrubbed with betadine solution + 70% isopropyl alcohol three times followed by sterile saline. A left thoracotomy was performed via the fourth intercostal space to expose the heart. The left

anterior descending coronary artery (LAD) was identified and temporally ligated. Ligation was released after 45 minutes, and the reperfusion phase started. Then EVs loaded with miR-199a-3p and miR-210 were suspended in 200 µl of PBS and delivered by four intramyocardial injections in four locations (10 µL each) to peri-infarct area within 5 minutes after reperfusion into each mouse. In this experimental setting, the delivery of the EVs directly following MI surgery avoids a second surgery, which would importantly increase animal mortality. PBS was used as a negative control. The lungs were hyperinflated by increasing positive end-expiratory pressure and the thoracotomy site was closed. The animals were observed and studied for four weeks post-surgery. All these surgical procedures were performed in the University of Illinois at Chicago Cardiovascular Research Core. Phenotypic characterization for MI mice was conducted via echocardiography and histology.

3.4.16 Echocardiography

We conducted pre-surgery echo, and on day 1 (24 hours after surgery), day 3, day 7, and day 30 using a 550Hz transducer (VisualSonics Inc.) and the Vevo 2100 Imaging System (VisualSonics Inc.).

To prepare the mouse for echocardiography, a mouse was first anaesthetized in a knock down box using 3% isofluorane. The hair on the ventral side was removed using a depilatory cream (Nair®) and cleaned with Kimwipes® wipers prior to imaging. After applying a small amount of electrode gel (Parker Laboratories, Inc.) to the copper leads on the heated (37°C) operation platform (VisualSonics, Inc.), the prepared mouse was positioned onto the platform with ventral side up and the paws were taped to the copper leads to provide the electrocardiogram (ECG). Respiratory waveform and respiratory rate were monitored simultaneously and all heart rates for

mice were maintained over 400 bpm (beats per minute). A layer of pre-warmed ultrasound gel (Parker Laboratories, Inc.) was added onto the mouse chest before imaging.

To identify the anatomical structures and evaluate the heart functions, we collected parasternal long axis view (PLAX) and parasternal short axis view (PSAX) using both brightness mode (B-mode) setting and motion mode (M-mode) setting. Besides, we collected Pulsed-Wave (PW) Doppler Mode and Tissue Doppler Mode waveforms to assess mitral valve flow and annulus in the apical four chamber view, where we measured the E, A, E', and A' waves to evaluate the systolic and diastolic function and myocardium health. Color Doppler Mode was applied for quick visualization of blood flow.

Evaluation of regional cardiac function including the ejection fraction (EF), fraction shortening (FS), cardiac output (CO), E/A, E'/A', and strain were analyzed using the Vevo LAB software (VisualSonics Inc., v.5.7.0).

3.4.17 Histological Analyses

Day 3 and day 30 mice were fully anesthetized. The excised hearts were collected, briefly washed in PBS, weighted, cut in half, fixed in 10% formalin at room temperature, embedded in paraffin, sliced into horizontal 5 μm sections per 500 μm step, and further processed for histology. Haematoxylin and eosin (H&E) and Masson's trichrome (MTC) staining were performed according to standard protocol and analyzed for morphology. The extent of cardiac fibrosis was measured on 20X magnification images by blinded researchers and quantified by calculating the area of positive MTC staining region (blue) as a proportion of the total field of view. In all quantifications of images, we considered, for each animal, at least 5 sectors of the heart sections.

3.5 Bibliography

1. Cocucci, E. & Meldolesi, J. Ectosomes and exosomes: shedding the confusion between extracellular vesicles. *Trends Cell Biol.* **25**, 364–372 (2015).
2. Pegtel, D. M. & Gould, S. J. Exosomes. *Annu. Rev. Biochem.* **88**, 487–514 (2019).
3. Alenquer, M. & Amorim, M. Exosome biogenesis, regulation, and function in viral infection. *VIRUSES-BASEL* **7**, 5066–5083 (2015).
4. Kalluri, R. & LeBleu, V. S. The biology, function, and biomedical applications of exosomes. *Science* **367**, eaau6977 (2020).
5. Frühbeis, C., Fröhlich, D., Kuo, W. P. & Krämer-Albers, E.-M. Extracellular vesicles as mediators of neuron-glia communication. *Front. Cell. Neurosci.* **7**, (2013).
6. Blanchette, C. R. & Rodal, A. A. Mechanisms for biogenesis and release of neuronal extracellular vesicles. *Curr. Opin. Neurobiol.* **63**, 104–110 (2020).
7. Puig, B., Brenna, S. & Magnus, T. Molecular communication of a dying neuron in Stroke. *Int. J. Mol. Sci.* **19**, 2834 (2018).
8. Budnik, V., Ruiz-Cañada, C. & Wendler, F. Extracellular vesicles round off communication in the nervous system. *Nat. Rev. Neurosci.* **17**, 160–172 (2016).
9. Schnatz, A., Müller, C., Brahmer, A. & Krämer-Albers, E. Extracellular vesicles in neural cell interaction and CNS homeostasis. *FASEB BioAdvances* **3**, 577–592 (2021).
10. Song, L., Tian, X. & Schekman, R. Extracellular vesicles from neurons promote neural induction of stem cells through cyclin D1. *J. Cell Biol.* **220**, e202101075 (2021).
11. Fowler, C. D. NeuroEVs: characterizing extracellular vesicles generated in the neural domain. *J. Neurosci.* **39**, 9262–9268 (2019).
12. Xiao, J. *et al.* Cardiac progenitor cell-derived exosomes prevent cardiomyocytes apoptosis through exosomal miR-21 by targeting PDCD4. *Cell Death Dis.* **7**, (2016).
13. Feng, Y., Huang, W., Wani, M., Yu, X. & Ashraf, M. Ischemic preconditioning potentiates the protective effect of stem cells through secretion of exosomes by targeting Mecp2 via miR-22. *PLOS ONE* **9**, (2014).
14. Mayourian, J. *et al.* Exosomal microRNA-21-5p mediates mesenchymal stem cell paracrine effects on human cardiac tissue contractility. *Circ. Res.* **122**, 933–944 (2018).
15. Chung, I.-M., Rajakumar, G., Venkidasamy, B., Subramanian, U. & Thiruvengadam, M. Exosomes: current use and future applications. *Clin. Chim. Acta* **500**, 226–232 (2020).
16. Gao, L. *et al.* Exosomes secreted by hiPSC-derived cardiac cells improve recovery from myocardial infarction in swine. *Sci. Transl. Med.* **12**, eaay1318 (2020).
17. Gao, J., Wang, S. & Wang, Z. High yield, scalable and remotely drug-loaded neutrophil-derived extracellular vesicles (EVs) for anti-inflammation therapy. *BIOMATERIALS* **135**, 62–73 (2017).
18. Shetgaonkar, G. G. *et al. Drug Deliv. Transl. Res.* **12**, 1047–1079 (2022).
19. Ohno, S. & Kuroda, M. Exosome-mediated targeted delivery of miRNAs. in *Lentiviral Vectors and Exosomes as Gene and Protein Delivery Tools* (ed. Federico, M.) vol. 1448 261–270 (Springer New York, 2016).
20. Lee, K., Yi, Y. & Yu, Y. Remote control of t cell activation using magnetic janus particles. *Angew. Chem. Int. Ed.* **55**, 7384–7387 (2016).
21. Möller, A. & Lobb, R. J. The evolving translational potential of small extracellular vesicles in cancer. *Nat. Rev. Cancer* **20**, 697–709 (2020).

22. Zhang, X. *et al.* Engineered extracellular vesicles for cancer therapy. *Adv. Mater.* **33**, 2005709 (2021).
23. Herrmann, I. K., Wood, M. J. A. & Fuhrmann, G. Extracellular vesicles as a next-generation drug delivery platform. *Nat. Nanotechnol.* **16**, 748–759 (2021).
24. Lee, J.-H. *et al.* Emerging biogenesis technologies of extracellular vesicles for tissue regenerative therapeutics. *J. Tissue Eng.* **12**, 204173142110190 (2021).
25. Meng, W. *et al.* Prospects and challenges of extracellular vesicle-based drug delivery system: considering cell source. *Drug Deliv.* **27**, 585–598 (2020).
26. Sun, L. *et al.* Serum deprivation elevates the levels of microvesicles with different size distributions and selectively enriched proteins in human myeloma cells *in vitro*. *ACTA Pharmacol. Sin.* **35**, 381–393 (2014).
27. Burnley-Hall, N., Willis, G., Davis, J., Rees, D. & James, P. Nitrite-derived nitric oxide reduces hypoxia-inducible factor 1 alpha-mediated extracellular vesicle production by endothelial cells. *NITRIC OXIDE-Biol. Chem.* **63**, 1–12 (2017).
28. King, H., Michael, M. & Gleadle, J. Hypoxic enhancement of exosome release by breast cancer cells. *BMC CANCER* **12**, (2012).
29. Yang, Z. *et al.* Large-scale generation of functional mRNA-encapsulating exosomes via cellular nanoporation. *Nat. Biomed. Eng.* **4**, 69–83 (2020).
30. Najrana, T. *et al.* Mechanical stretch regulates the expression of specific miRNA in extracellular vesicles released from lung epithelial cells. *J. Cell. Physiol.* **235**, 8210–8223 (2020).
31. Ambattu, L. A. *et al.* High frequency acoustic cell stimulation promotes exosome generation regulated by a calcium-dependent mechanism. *Commun. Biol.* **3**, 553 (2020).
32. Kumar, R. *et al.* Fibroblast growth factor 2-mediated regulation of neuronal exosome release depends on VAMP3/cellubrevin in Hippocampal neurons. *Adv. Sci.* **7**, 1902372 (2020).
33. Headland, S., Jones, H., D'Sa, A., Perretti, M. & Norling, L. Cutting-edge analysis of extracellular microparticles using ImageStream(X) imaging flow cytometry. *Sci. Rep.* **4**, (2014).
34. Savina, A., Furlan, M., Vidal, M. & Colombo, M. Exosome release is regulated by a calcium-dependent mechanism in K562 cells. *J. Biol. Chem.* **278**, 20083–20090 (2003).
35. Hsu, C. *et al.* Regulation of exosome secretion by Rab35 and its GTPase-activating proteins TBC1D10A-C. *J. Cell Biol.* **189**, 223–232 (2010).
36. Ostrowski, M. *et al.* Rab27a and Rab27b control different steps of the exosome secretion pathway. *Nat. Cell Biol.* **12**, 19-U61 (2010).
37. Trajkovic, K. *et al.* Ceramide triggers budding of exosome vesicles into multivesicular Endosomes. *Science* **319**, 1244–1247 (2008).
38. Sinha, S. *et al.* Cortactin promotes exosome secretion by controlling branched actin dynamics. *J. Cell Biol.* **214**, 197–213 (2016).
39. Kojima, R. *et al.* Designer exosomes produced by implanted cells intracerebrally deliver therapeutic cargo for Parkinson's disease treatment. *Nat. Commun.* **9**, 1305 (2018).
40. Shyong, Y., Chang, K. & Lin, F. Calcium phosphate particles stimulate exosome secretion from phagocytes for the enhancement of drug delivery. *Colloids Surf. B-Biointerfaces* **171**, 391–397 (2018).
41. Messenger, S., Woo, S., Sun, Z. & Martin, T. A Ca^{2+}-stimulated exosome release pathway in cancer cells is regulated by Munc13-4. *J. Cell Biol.* **217**, 2877–2890 (2018).

42. Bebelman, M., Bebelman, M., van Niel, G., Pegtel, M. & Verweij, F. Real-time imaging assay of multivesicular body-PM fusion to quantify exosome release from single cells. *Protoc. Exch.* (2018).
43. Verweij, F. J. *et al.* Quantifying exosome secretion from single cells reveals a modulatory role for GPCR signaling. *J. Cell Biol.* **217**, 1129–1142 (2018).
49. Eschenhagen, T. *et al.* Cardiomyocyte regeneration a consensus statement. *Circulation* **136**, 680–686 (2017).
50. Porrello, E. *et al.* transient regenerative potential of the neonatal mouse heart. *Science* **331**, 1078–1080 (2011).
51. Jopling, C. *et al.* Zebrafish heart regeneration occurs by cardiomyocyte dedifferentiation and proliferation. *Nature* **464**, 606-U168 (2010).
44. Eulalio, A. *et al.* Functional screening identifies miRNAs inducing cardiac regeneration. *Nature* **492**, 376-+ (2012).
45. Aguirre, A. *et al. In vivo* activation of a conserved microrna program induces mammalian heart regeneration. *Cell Stem Cell* **15**, 589–604 (2014).
46. Diez-Cunado, M. *et al.* miRNAs that induce human cardiomyocyte proliferation converge on the hippo pathway. *Cell Rep.* **23**, 2168–2174 (2018).
50. Giacca, M. & Zacchigna, S. Harnessing the microRNA pathway for cardiac regeneration. *J. Mol. Cell. Cardiol.* **89**, 68–74 (2015).
51. Liu, B. *et al.* Cell type–specific microRNA therapies for myocardial infarction. *Sci. Transl. Med.* **13**, eabd0914 (2021).
52. Chen, M.-H. *et al.* MicroRNA-199a regulates myocardial fibrosis in rats by targeting SFRP5. *Eur. Rev. Med. Pharmacol. Sci.* **23**, 3976–3983 (2019).
53. Li, Z. *et al.* miR-199a impairs autophagy and induces cardiac hypertrophy through mTOR activation. *CELL DEATH Differ.* **24**, 1205–1213 (2017).
54. Tao, Y. *et al.* miR-199a-3p promotes cardiomyocyte proliferation by inhibiting Cd151 expression. *Biochem. Biophys. Res. Commun.* **516**, 28–36 (2019).
55. Li, Z. *et al.* miR-199-sponge transgenic mice develop physiological cardiac hypertrophy. *Cardiovasc. Res.* **110**, 258–267 (2016).
56. el Azzouzi, H. *et al.* The hypoxia-inducible microrna cluster mir-199a similar to 214 targets myocardial PPAR delta and impairs mitochondrial fatty acid oxidation. *CELL Metab.* **18**, 341–354 (2013).
57. Torrini, C. *et al.* Common regulatory pathways mediate activity of micrornas inducing cardiomyocyte proliferation. *Cell Rep.* **27**, 2759-2771.e5 (2019).
58. Joris, V. *et al.* MicroRNA-199a-3p and microRNA-199a-5p take part to a redundant network of regulation of the NOS (NO synthase)/NO pathway in the endothelium. *Arterioscler. Thromb. Vasc. Biol.* **38**, 2345–2357 (2018).
59. Fan, Z. *et al.* MicroRNA-210 promotes angiogenesis in acute myocardial infarction. *Mol. Med. Rep.* (2018).
60. Wang, N. *et al.* Mesenchymal stem cells-derived extracellular vesicles, via miR-210, improve infarcted cardiac function by promotion of angiogenesis. *Biochim. Biophys. Acta BBA - Mol. Basis Dis.* **1863**, 2085–2092 (2017).

Chapter 4. Single-Cell Single-Molecule Interrogation of T Cell Biochemical Sensitivity

4.1 Introduction

4.1.1 T Cell Biology

T cells, a type of leukocyte, orchestrate the adaptive immune response against infection and cancer. The T-cell receptors (TCRs) recognize antigenic peptides presented on major histocompatibility complexes (pMHCs) on antigen-presenting cells (APCs) and trigger T-cell signaling and subsequent immune responses[1,2]. A TCR consists of a variable TCRαβ heterodimer and a nonvariable transmembrane signal transduction CD3 complex. T cells can also be transduced with genetically engineered chimeric antigen receptors (CARs) to recognize tumor-associated antigens (e.g., CD19) on cancer cells. A CAR consists of an extracellular single-chain antibody fragment (scFv) antigen binding domain, a transmembrane region, and intracellular signaling domains. Upon antigen recognition by the TCRs or CARs, T cells proliferate, differentiate, and execute effector functions, including cytokine secretion and lysing of target cells[1,2]. So far, T-cell biology, and the ability to leverage the unique physical properties of antigen recognition by TCRs/CARs, have underpinned many immunotherapies for cancer and infection treatments and transplant rejection prevention[3–7]. Thus, understanding T-cell function and developing APCs for specific immunological functions is critical for advancing immunotherapy applications.

4.1.2 Usages of Synthetic Antigen-Presenting Systems

The development of synthetic antigen-presenting systems that interrogate specific T-cell signaling and function is critical for systematically understanding the immune cell biology and advancing immunotherapy applications[6]. Previous studies have used various synthetic antigen-

presenting systems with controllable design parameters (surface modification, porosity, therapeutic cargoes, etc.) to study TCR molecular structures, conformation, nano-organization, kinetics, segregation, and catch bonds during TCR recognition and signaling[8]. Synthetic APCs can also be produced on a large scale, circumventing the need to harvest and culture dendritic cells and reducing the cost, time, and donor-donor variance[9] associated with T-cell expansion and the study of adoptive immunotherapy[10,11]. For example, at the ensemble level, commercially available Dynabeads are widely used in T-cell expansion, isolation, and cytokine production[12], and recently developed synthetic scaffolds have enabled the expansion and manufacture of T cells with high efficiency[13–15]. Furthermore, controllable design parameters of synthetic materials allow the investigation of ligand-receptor interactions for quantifying the impact of various biochemical signals on T-cell immunity. At the single-cell level, synthetic Janus particles with spatially distributed ligands have been used to control membrane dynamics, clustering of intracellular proteins, and calcium signaling in T cells[16,17].

While existing synthetic material approaches to T-cell research focus on the ensemble or single-cell level, the next wave of refinements in our understanding of immune cell biology is likely to come from data at the nanometer scale and single-molecule level. Previous studies suggested that TCR-pMHC recognition is exceptionally specific, and a thorough understanding of TCR or CAR recognition at the single-molecule level is expected to facilitate vaccine development and cellular immunotherapy[18–20]. However, the single-molecule single-cell study of TCR or CAR recognition requires precise manipulation of the synthetic material, a nano-engineering capability beyond the scope of the current synthetic APS toolkit. Besides, although studies (without reaching single-molecule resolution) suggested that the recognition sensitivity of TCRs is greater than that of CARs[21–23], CAR recognition is still much less studied using synthetic APS compared to

intensive research in TCRs. Single-molecule resolution should provide critical insight into the CAR recognition process.

4.1.3 Hexapod bAPS for Investigating T Cell Biochemical Sensitivity

T-cell research using antigen-presenting systems at the ensemble level or the single-cell level can provide complementary insight into T-cell activation and signaling. However, synthetic material toolkits that probe T cells at both levels are lacking, although they would be necessary for advancing basic immunology and immunotherapy. Here, we develop a biomimetic antigen-presenting system (bAPS) using bifunctional hexapod heterostructures (*i.e.*, hematite core and nanoscale silica branches) for single-cell single-molecule stimulation (Chapter 4) and ensemble modulation of T-cell signaling (Chapter 5).

In proof-of-principle studies, we apply the hexapod heterostructure-based bAPS to interrogate the signaling and biochemical sensitivity of T cells. The silica branches on the hexapod allow bioconjugation of ligands and spatial confinement of bAPS/T-cell contact interfaces. The bAPS can be manipulated using a glass micropipette (via the hexapod branches) for single-cell-level modulation with single-molecule resolution (function 1: probing T cell biochemical sensitivity, Chapter 4).

In this chapter, we report single-molecule resolution of T-cell sensing/activation by a single agonist peptide-major histocompatibility complex; distinct T-cell receptor (TCR) responses to discriminate structurally similar peptides that differ by just one amino acid; and the superior sensitivity of TCR antigen recognition compared to chimeric antigen receptors (CARs). The multimodal hexapod bAPS presents unexplored, nanotechnology-based biointerface tools for investigating recognition, signaling, and the biochemical sensitivity of T cells and beyond.

4.2 Results and Discussion

4.2.1 Hexapod Heterostructure Design and Synthesis

To develop a synthetic material system that can modulate individual T cells with molecular precision (aimed function 1), we developed the bifunctional biomimetic hexapod heterostructures (i.e., bAPS). We demonstrated how hexapod-based bAPS could achieve controllable single-cell, single-molecule biochemical interrogation of T-cell signaling (**Fig. 4-1**).

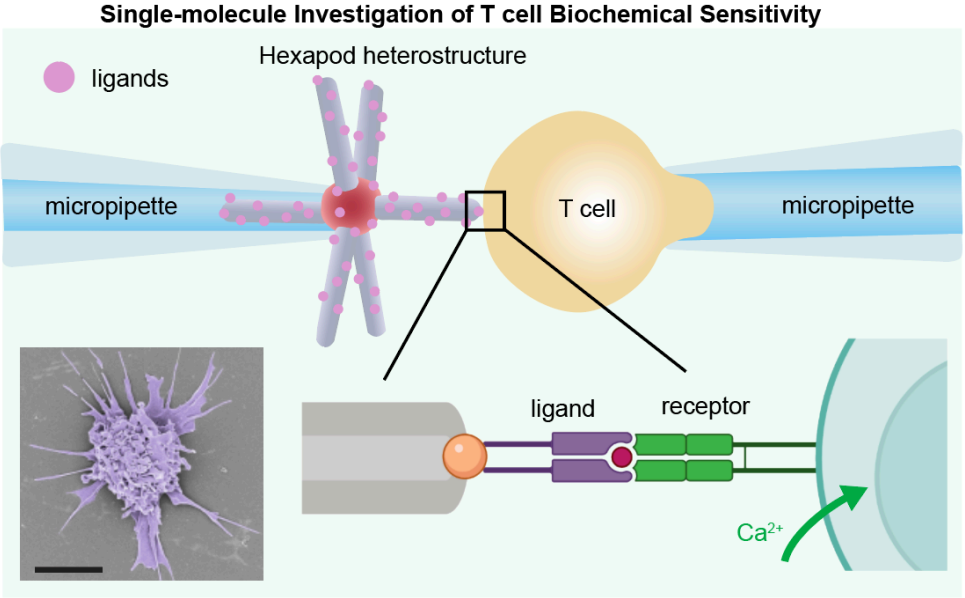

Figure 4-1. Hexapod-enabled single-molecule interrogation of T-cell biochemical sensitivity. The single-cell to single-particle molecular level biochemical interrogation system. The unique hexapod structure enables single-particle manipulation using an open-orifice aspiring micropipette. Spatial confinement provided by the nanoscale branch allows molecular-level contact with a single aspectant micropipette-held T-cell. Insert, a scanning electron microscope (SEM) image of a dendritic cell showing structural similarity with the biomimetic hexapods. Scale bar, 5 μm.

We selected □-Fe_2O_3 or hematite, a weakly magnetic material (**Table 4-1**), as the hexapod building block.

Table 4-1. Representative magnetic iron oxides

Material	Chemical Formula	Magnetic susceptibility[24] ($10^{-8}m^3kg^{-1}$)	Synthesis	Structure	Ref.
Lepidocrocite	γ-FeO·OH	70	ethylene glycol (EG) mediated solution method	nanoflakes	25
Ilmenite	$FeTiO_3$	200	Sol-gel method	Nanoparticles, not stable	26
Hematite	**α-Fe_2O_3**	**60**	**Easy, sol-gel method**	**Cubic particles, uniform, dispersed**	27
Goethite	α-FeO·OH	70	Hydrothermal	Nanorods	28
Maghemite	γ-Fe_2O_3	40,000	Polyol-Mediated Process	Nanoflowers	29
Magnetite	Fe_3O_4	50,000	Precipitation	Nanoparticles, aggregates, may not be uniform, stable	30

Hematite was synthesized into submicron scale cubes (a typical length: ~ 860 nm), enabling the formation of nanoscale silica branches (diameter: ~ 50 - 500 nm; length: ~ 1 - 3 μm) on each face to form hexapod heterostructures (**Fig. 4-2**). To grow the branches, we first dispersed the hematite microcubes in viscous polymer liquid (10% wt./v. polyvinylpyrrolidone or PVP in 1-pentanol)[31]. Following the introduction of the silica precursor (tetraethoxysilane or TEOS) and condensation catalyst (NH_4OH), emulsion droplets formed on the faces of the hematite by phase separation. Silica condensation is initiated in the water phase emulsion droplets, producing six evenly distributed nanoscale silica branches around (a typical diameter: 400 nm) the hematite core (**Fig. 4-3 and Fig. 4-4**). The hexapods remained stable in PBS or culture medium for more than 24 h (**Fig. 4-5**), which allowed enough time for our aimed immunobiology applications.

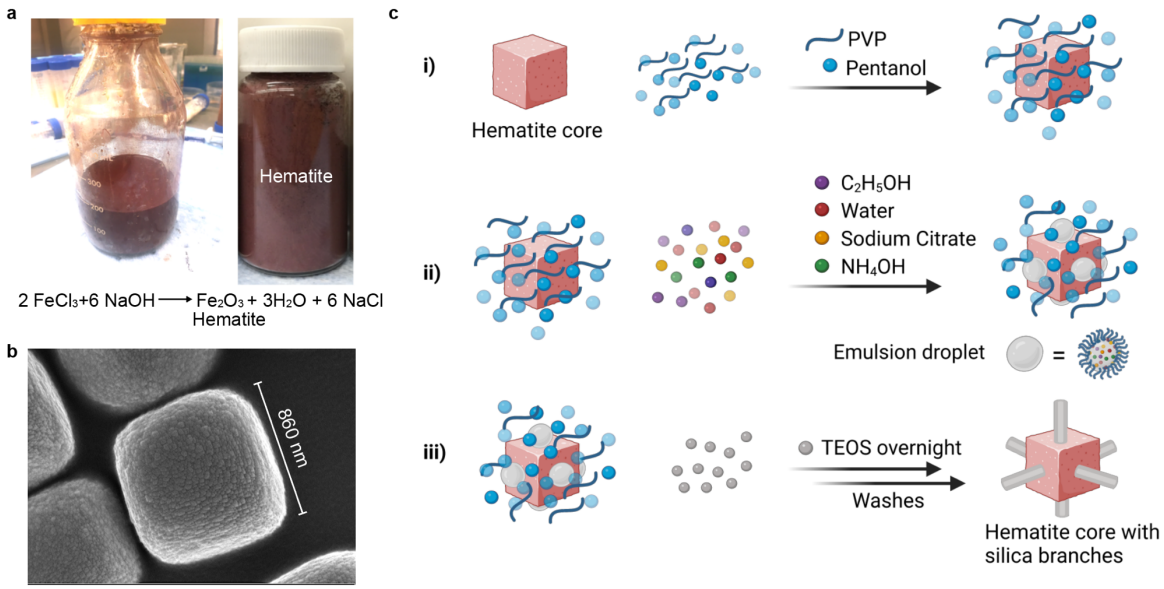

Figure 4-2. Hexapod synthesis. a. Hematite cores are synthesized via ferric hydroxide gel condensation. **b.** The hematite is a cubic hexahedron. **c.** The synthesis of hexapod: i) hematite cores are dispersed in PVP pentanol solution. The viscous solution helps evenly distribute the branches by preventing precipitation and hematite aggregation. ii) water forms emulsion droplets on the hematite surface. PVP and citrate help the oil/water phase separation. iii) silica branches grow via tetraethoxysilane (TEOS) condensation from six emulsion droplets, one branch forms on each facet of the cubic hematite core. TEOS is the silica precursor, NH_4OH is the catalyst for TEOS condensation, and the addition of C_2H_5OH forms a homogeneous solution in the droplets.

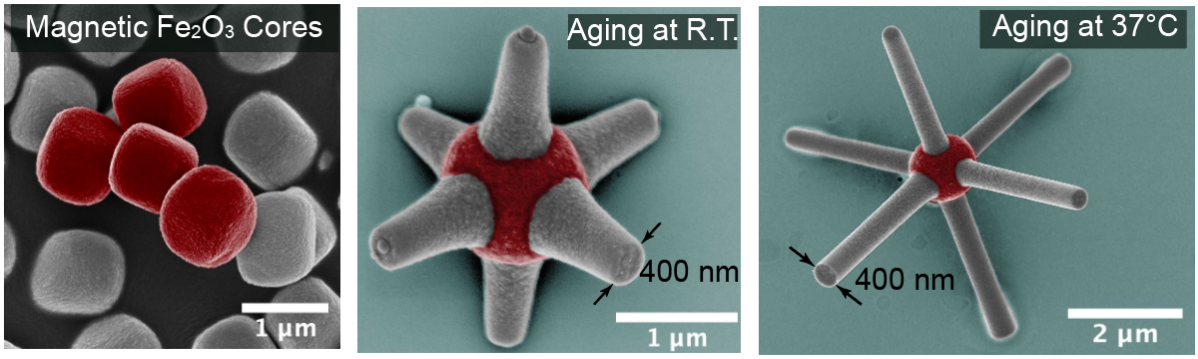

Figure 4-3. Synthesized hexapods. Left, SEM image showing the synthesized hematite microcubes. **Middle and right,** Synthesized hexapods have a symmetrical structure with six branches on each face of the hematite cubes. Branch length can be tuned during synthesis by aging under different temperatures. The branch diameter is 400 nm.

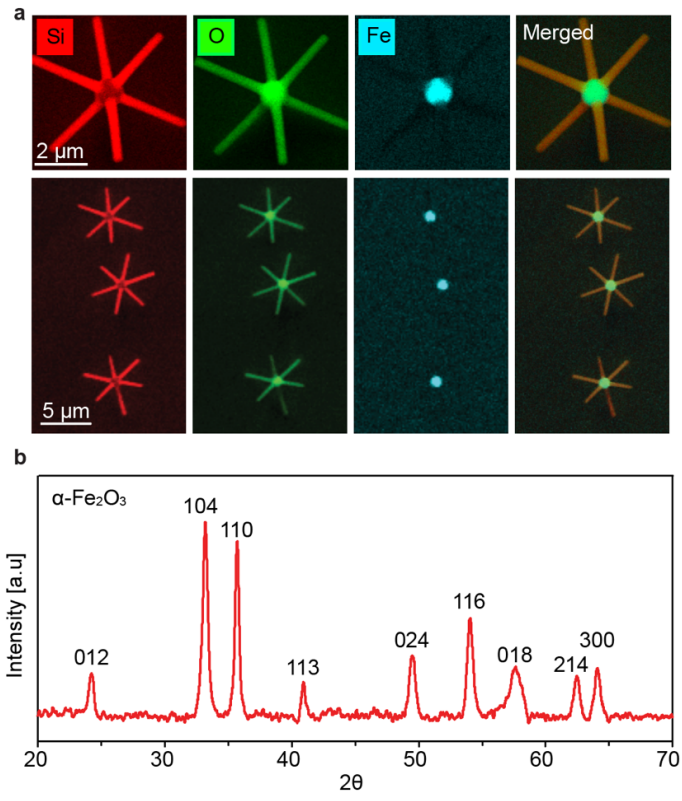

Figure 4-4. Hexapod composition characterization. a. Energy-dispersive spectroscopy (EDS) element mapping shows the hexapods branches are characterized with silicon (Si, red) and oxygen

(O, green), while the cores are characterized with iron (Fe, blue) and oxygen (O, green). Thus, hexapods are made of silica branches and an iron oxide core. Scale bar, 2µm (top) and 5 µm (bottom). **b.** The powder X-ray diffraction (pXRD) shows that the hexapods are made of α-Fe2O3 or hematite. The branches are amorphous silica and show no peaks in the pXRD.

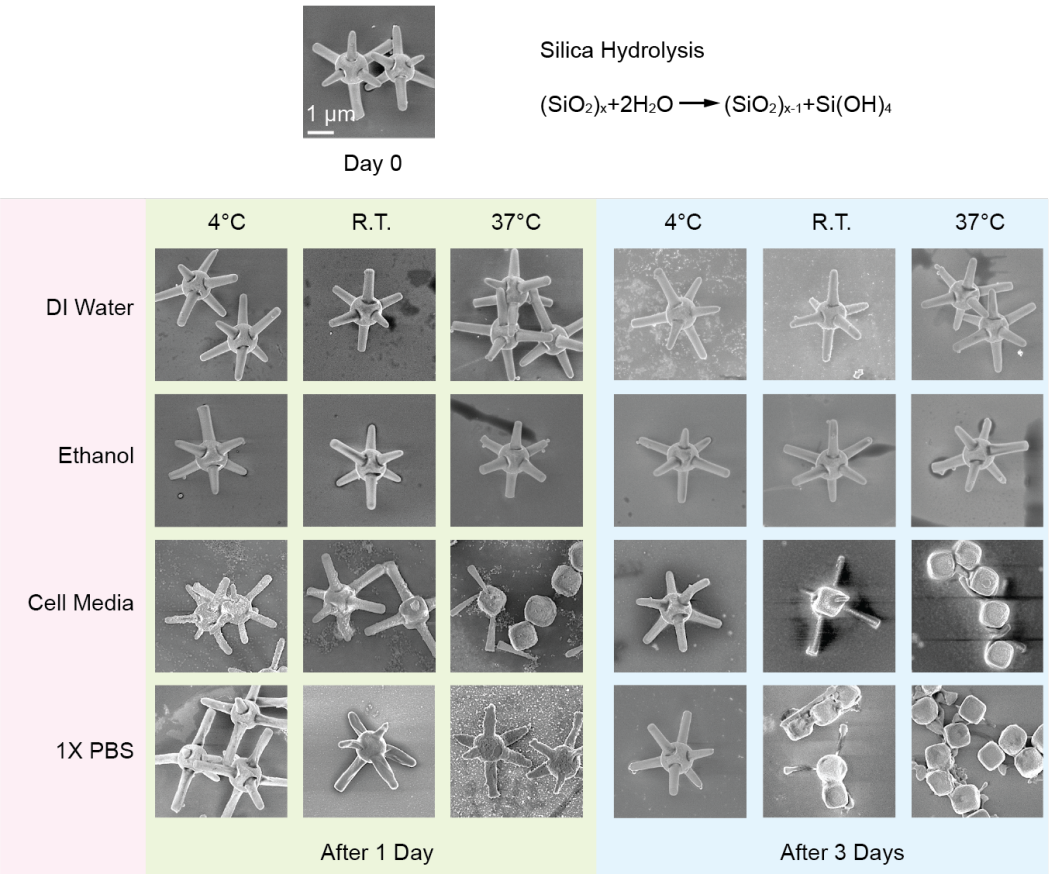

Figure 4-5. Hexapod stability. We dispersed hexapods in DI water, ethanol, cell culture media, and 1X PBS, respectively, and stored them at four °C, room temperature (R.T.), and 37 °C before being examined by a scanning electron microscope (SEM). SEM images show that hexapods were well-preserved in DI water and ethanol but started degradation after one day in cell media and PBS. After three days, the silica branches completely degraded in 37 °C media and PBS. We thus stored

Figure 4-5, continued. the hexapods in ethanol, and after surface modification in PBS, we used the hexapod bAPS within 24 hours for our immunobiological experiments. Scale bar, 1μm.

4.2.2 Hexapod Biochemical Surface Design, Modifications, and Quantifications

To investigate single molecule-induced biochemical signaling in individual T cells, we conjugated stimulatory ligands (*e.g.*, pMHCs, anti-CD3 antibodies[32], CD19 molecules) and non-stimulatory ligands/proteins (e.g., null pMHCs, bovine serum albumin or BSA, and isotype antibodies) to the hexapod via streptavidin-biotin interactions (**Fig. 4-6 and Table 4-2**). Basically, pMHC (negative control: non-stimulatory peptide-bound MHC) and anti-CD3 (negative control: IgG isotype) were used to trigger TCR responses; CD19 (negative control: BSA) was used to stimulate the constructed CD19-targeting CAR-T cells. Our data showed that ligands were evenly distributed across the hexapod surfaces, and these modified hexapods were well dispersed in PBS (**Fig. 4-7 and Fig. 4-8**).

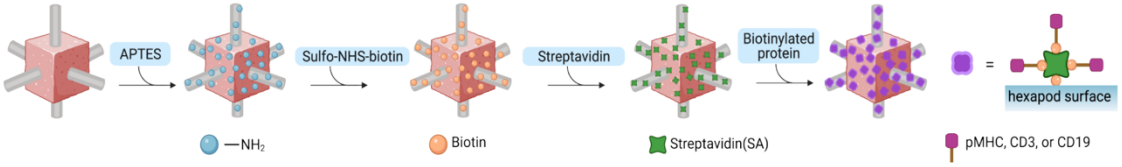

Figure 4-6. Biochemistry surface modification steps.

Table 4-2. Molecular designs on the nanostructured hexapod surfaces in this work

Hexapod modification	Interfaced cell	Experiment	Result
CD19	PE-antiCD19	Quantification of surface protein density	Only one molecule at the silica branch tip
Empty	Primary 5C.C7 $CD4^+$ T cells	Biochemical single-cell single-molecule micropipette experiments	Poking for force is not inducing calcium signals

Table 4-2, continued.

Hexapod modification	Interfaced cell	Experiment	Result
pMHC (p=MCC)	Primary 5C.C7 $CD4^+$ T cells	Biochemical single-cell single-molecule micropipette experiments	Single pMHC induces calcium signal
pMHC (P=MCC, 102S, or null)	Primary 5C.C7 $CD4^+$ T cells	Biochemical single-cell single-molecule micropipette experiments	T cell discriminates closely related peptides that only differ by one amino acid in the short sequence
pMHC (P=OVA, G4, or null)	Primary OT1 $CD8^+$ T cells	Biochemical single-cell single-molecule micropipette experiments	
antiCD3 or CD19	CAR T cells	Biochemical single-cell single-molecule micropipette experiments	TCR transduction is more efficient than that of CAR
antiCD3 or CD19	T or CAR T cells	Biointerface SEM imaging	Tight hexapod/cell biointerfaces
CD19	CAR T cells	Biointerface confocal imaging	
pMHC (p=MCC)	Primary 5C.C7 $CD4^+$ T cells	Tracking analysis	No aggregration; hexapods and hexapod-bound cells perform directed motion in rorating magnetic field
pMHC (p=OVA or MCC)	Primary 5C.C7 $CD4^+$ or OT1 $CD8^+$ T cells	Biophysical rotation experiments	Primary T cell activation and cytokine production are amplified by rotation (torques or forces)
antiCD3 or CD19	CAR T cells	Biophysical rotation experiments	CAR T cell activation and cytokine production are amplified by rotation (torques or forces)
antiCD3 and anti-CD28	T cell blasts (day 6-10)	Biophysical rotation experiments	T cell blasts activation and cytokine production are amplified by rotation (torques or forces)
pMHC (p = null) or BSA or isotype	T or CAR T cells	Biochemical single-cell single-molecule micropipette experiments and biophysical rotation experiments	Negative controls

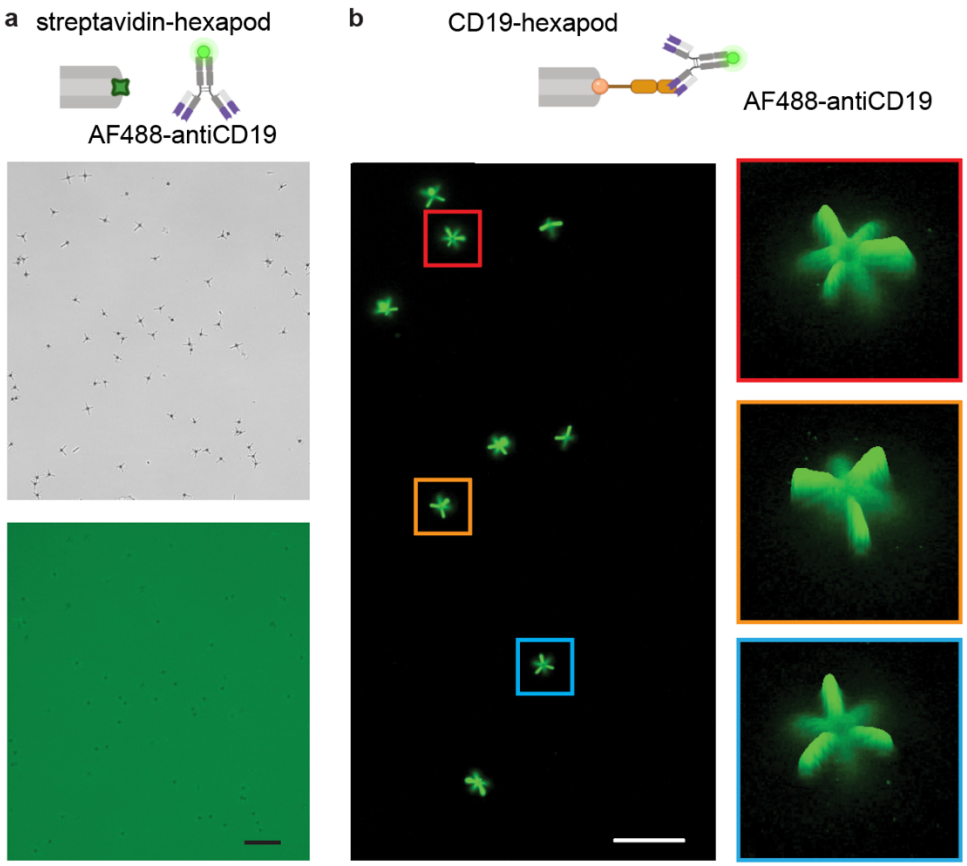

Figure 4-7. Hexapod heterostructure protein modifications. a. There are no fluorescence signals when labelling streptavidin (SA)-hexapods using AF488-antiCD19. SA-hexapods are negative controls. The microscopy picture shows that hexapods have good dispersion and distribution in PBS after protein modification. Scale bar, 20 µm. **b.** CD19-hexapods were labelled with fluorescence using AF488-antiCD19. Fluorescent image and 3D zoom-in views show that CD19 is evenly distributed on the hexapods. Scale bar, 20 µm.

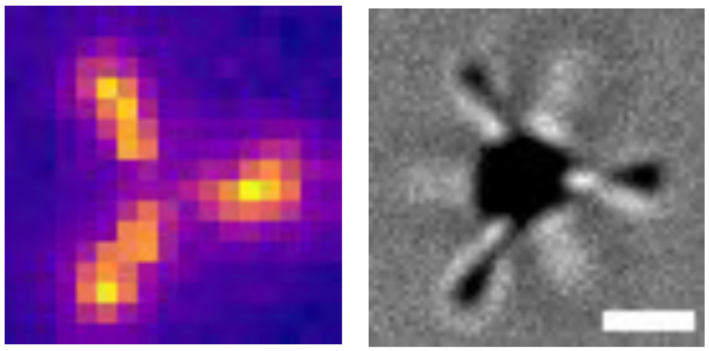

Figure 4-8. Representative images of PE-anti-CD19-labelled CD19-hexapod. Left: fluorescent channel; right: brightfield image. Scale bar, 1μm.

To quantify the coating density on hexapods, we labeled CD19-modified with PE-anti-CD19 antibody. Using commercially available PE calibration beads (Quantibrite^{TM}) that have four fluorescence intensity levels as standard curves, we quantified the coating density on CD19-hexapods to be 7.54 molecules/μm^2 and 7.87 molecules/μm^2 by microscopy (**Fig. 4-9**) and flow cytometry (**Fig. 4-10**), respectively. The nanoscale branch tips (r ~ 200 nm) of hexapod heterostructures spatially confine the hexapod/cell interface to 0.13 μm^2. On average, this area harbors a single ligand molecule. The conjugation dosage was kept the same in all ligand modifications.

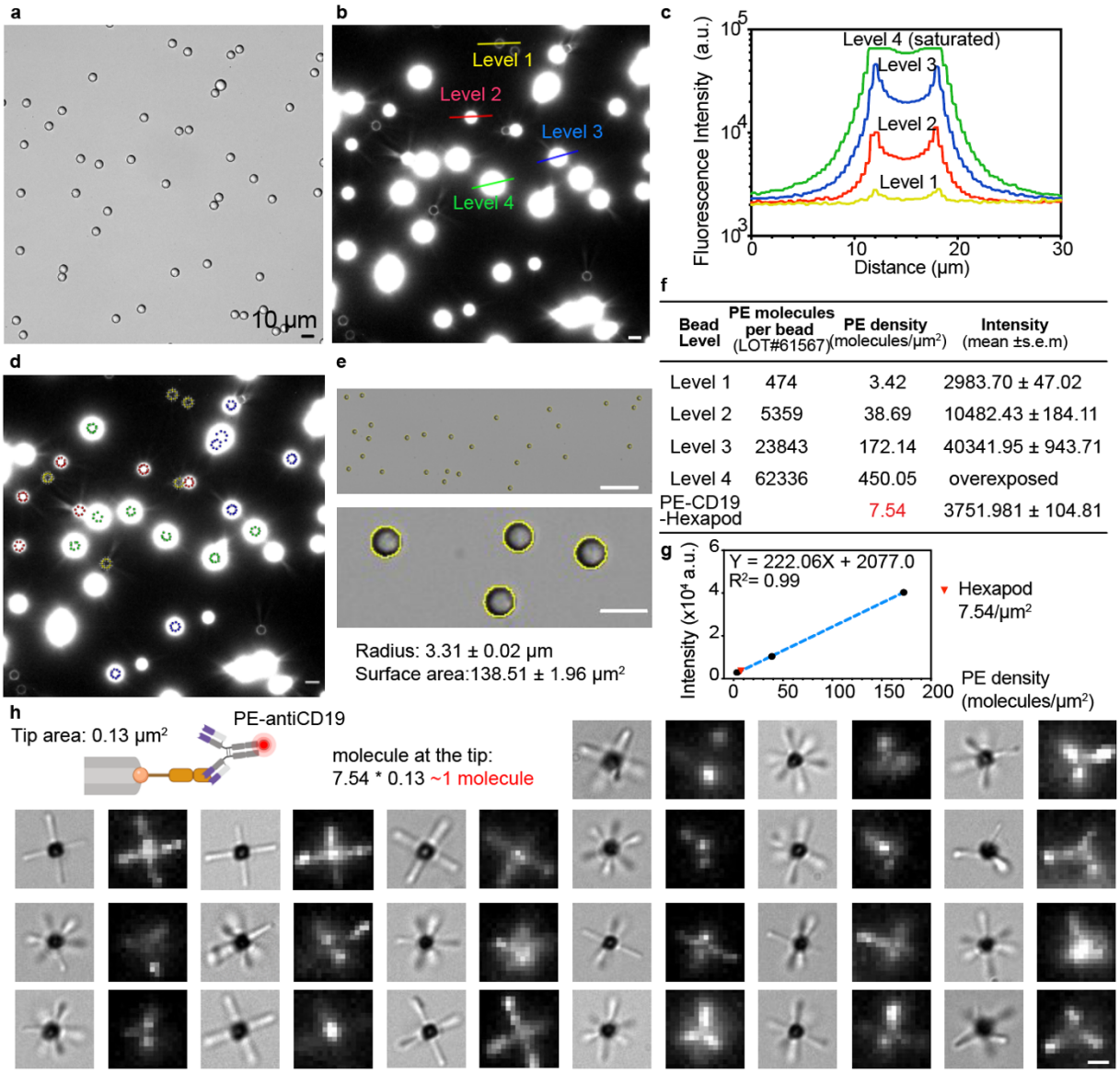

Figure 4-9. Optical microscopic quantification of surface molecule densities. a. Image showing the uniformly dispersed BD Quantibrite™ PE calibration beads. Scale bars, 10 µm. **b.** PE fluorescent of the Quantibrite™ PE calibration beads. Scale bars, 10 µm. **c.** Four fluorescence intensity levels measured from lines in **b** (yellow, level 1; red, level 2; blue, level 3; green, level 4). The bead edges (PE bead surface) show the highest intensity in each bead. **d.** The surface PE intensities of BD Quantibrite™ PE beads were measured. Regions of interest (ROIs) of the four levels were indicated in circles (yellow, level 1; red, level 2; blue, level 3; green, level 4). Scale

Figure 4-9, continued. bars, 10 μm. **e.** Image showing the uniform size of BD Quantibrite™ PE calibration beads (r = 3.31 μm). Scale bars, 50 μm (top) and 10 μm (bottom). **f.** PE molecule and corresponding density levels. **g.** PE coating density on the hexapod is calculated to be 7.54 molecules/μm^2. On the 0.13 μm^2 tip (diameter = 400 nm), there is one CD19 molecule. Black, PE standard beads; blue dash line, standard curve. **h.** The characterization labeling (schematics) and representative images of the PE-labelled CD19-hexapod. The PE intensities of PE-labelled CD19-hexapods were measured, and these hexapods were calculated to have a coating density of 7.54 molecules/μm^2. On the 0.13 μm^2 (r= 400 nm) tip, there is only one molecule. Scale bar, 1μm.

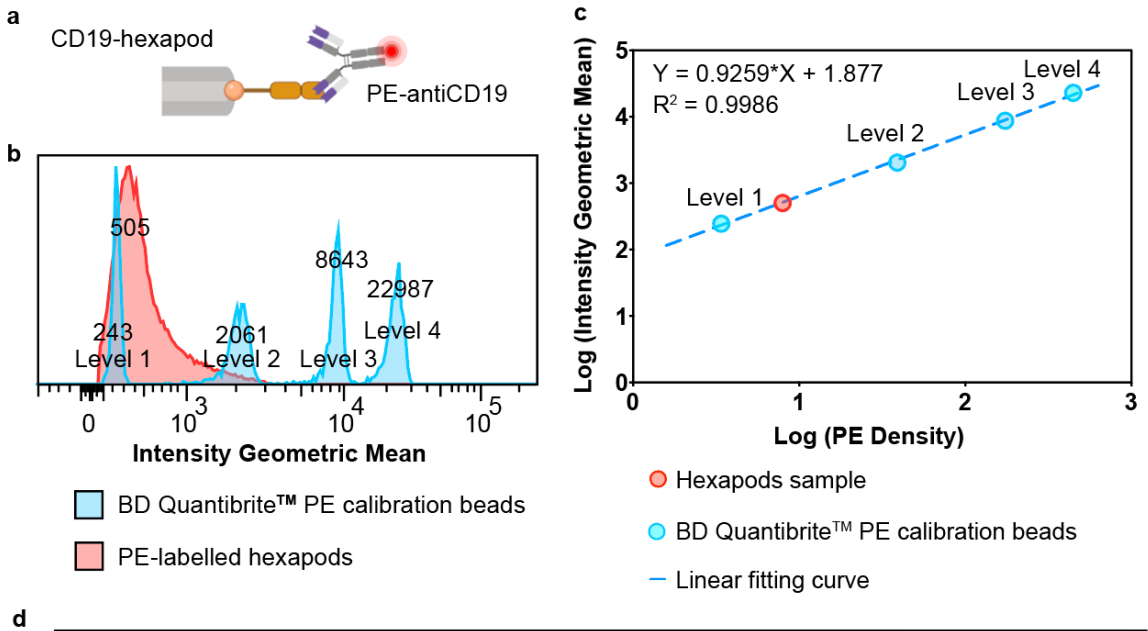

d

Material	Method	Calculated PE molecules density (molecules/μm²)	Estimated contact area between material and T cell (μm²)	Molecule amount at the T cell/material interface
PE-antiCD19 -labelled CD19-Hexapods	Flow cytometry	7.87	0.13	**1.02**
	Optical microscope	7.54		**0.98**

Figure 4-10. Flow cytometry quantification of surface molecule densities. a. Schematic showing the PE-labelled CD19-hexapod. **b.** Flow cytometry intensity of PE-antiCD19 labelled

Figure 4-10, continued. CD19-hexapods and BD Quantibrite™ PE calibration beads. **c.** CD19 (PE staining) density standard curve. **d.** Calculated hexapod surface CD19 density and corresponding molecule amount.

4.2.3 Single-Molecule Probing of TCR Signaling and Biochemical Sensitivity

The symmetrical structure of hexapod heterostructures enables micropipette operation for single-cell, single-molecule biochemical studies with a single silica branch (#1) fitting into the micropipette orifice, another four lateral branches (#2 - #5) prevent indrawing, and the last branch (#6) is available for single-molecule probing. To precisely position the hexapod heterostructures for formation of a bAPS/T cell contact interface, we applied a micromanipulator system in which one open-orifice aspiring micropipette holds a pMHC-coated hexapod and another holds a primary T cell (**Fig. 4-11**). T cells were labeled with a calcium indicator (Calbryte 520 AM) to monitor real-time Ca^{2+} signaling triggered by a single pMHC molecule (**Fig. 4-12a**). Notably, calcium fluxes in primary 5C.C7 $CD4^+$ T cells were observed upon contact with an I-E^k MHC loaded with MCC (MCC-MHC), an agonist for the 5C.C7 TCR (**Fig. 4-12b)**. Hexapod tips without pMHC did not induce any calcium signal changes, indicating that the calcium flux is specific to the TCR/pMHC interaction (not from any biophysical poking force, **Fig. 4-12c).**

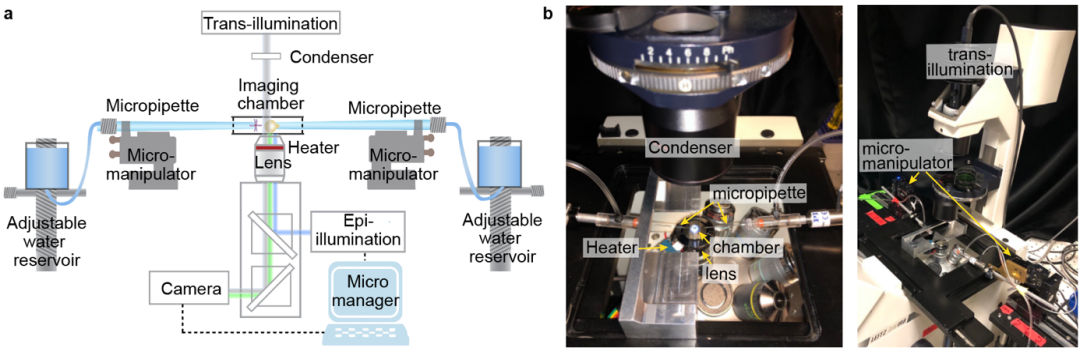

Figure 4-11. Micropipette experimental setup. a. Schematic showing the micropipette experimental setup. **b.** Pictures showing the micropipette experimental setup.

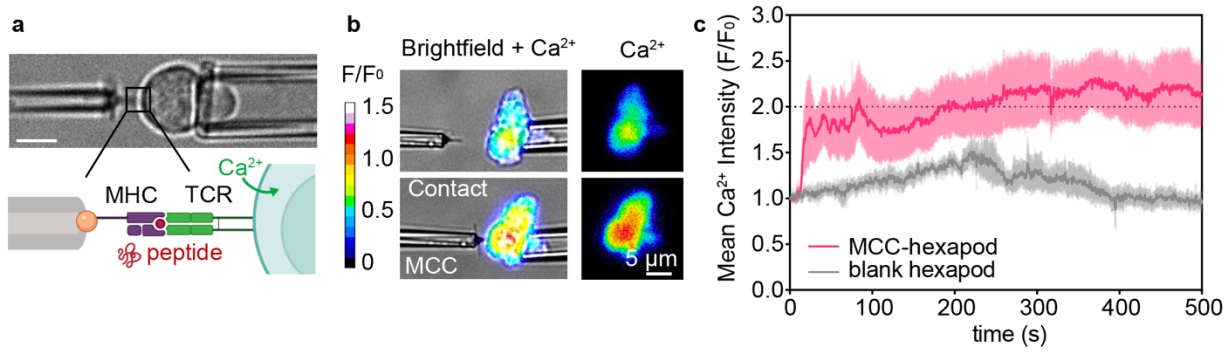

Figure 4-12. Micropipette experiments and investigation of T-cell calcium signalling. a. Top: representative picture of the experimental setup. A pMHC-coated hexapod aspirated by a pipette is in contact with a T cell held stationary by an opposing pipette. The position of the hexapod was controlled by a micromanipulator. Calcium signaling in the T-cell was observed. Scale bar, 5 µm. Bottom: schematic showing a close-up look at the pMHC molecule contacting the T-cell membrane. **b.** Calcium flux was observed in a single primary 5C.C7 $CD4^+$ T cell upon contacting a pMHC (peptide = MCC) on a hexapod tip, indicating T cell biochemical sensitivity reaches single-molecule level. **c.** The absence of pMHC causes no calcium signal changes, hence calcium flux is specific to the TCR/pMHC interaction (not from biophysical poking force).

Single amino acid alterations in the short peptide sequence (8-16 amino acids) induced distinct calcium profiles in the interfaced T cell, indicating that TCR can differentiate peptides with only one amino acid difference. For example, the weak agonist G4-MHC-hexapod induced diminished calcium flux in OT-1 $CD8^+$ T cells compared to the agonist OVA-MHC-hexapod (**Fig. 4-13 and Fig. 4-14**); G4 and OVA sequences differ by just one amino acid. Similarly, the weak agonist 102S-MHC-bound hexapod induced delayed calcium flux with diminished intensity than the agonist MCC-MHC-bound hexapod in 5C.C7 $CD4^+$ T cells (**Fig. 4-15**). We further tested the specificity of TCR recognition using non-stimulatory peptide (*e.g.*, human CLIP 87-101 peptide)-presented MHC-hexapods as negative controls (null) for mouse T cells, and these null pMHC-

hexapods did not elicit calcium fluxes in T cells (**Figs. 4-13, 4-14, 4-15**). Therefore, TCR discriminates self and foreign peptides with a biochemical sensitivity down to one amino acid level. TCR/pMHC recognition is exceptionally specific, as single-residue alterations on antigenic peptides can induce significantly different T-cell responses. These observations align well with previous studies[18,33–35].

As the first synthetic material system to probe the single-molecule TCR activation and the different T-cell responses induced by single-residue alterations in antigenic peptides, the hexapod-based bAPS represents a new route to single molecule-level studies of signaling and functions in immune cells (see **Table 4-3** for other systems), and with further development may be utilized to screen for effective T-cell molecular stimulators.

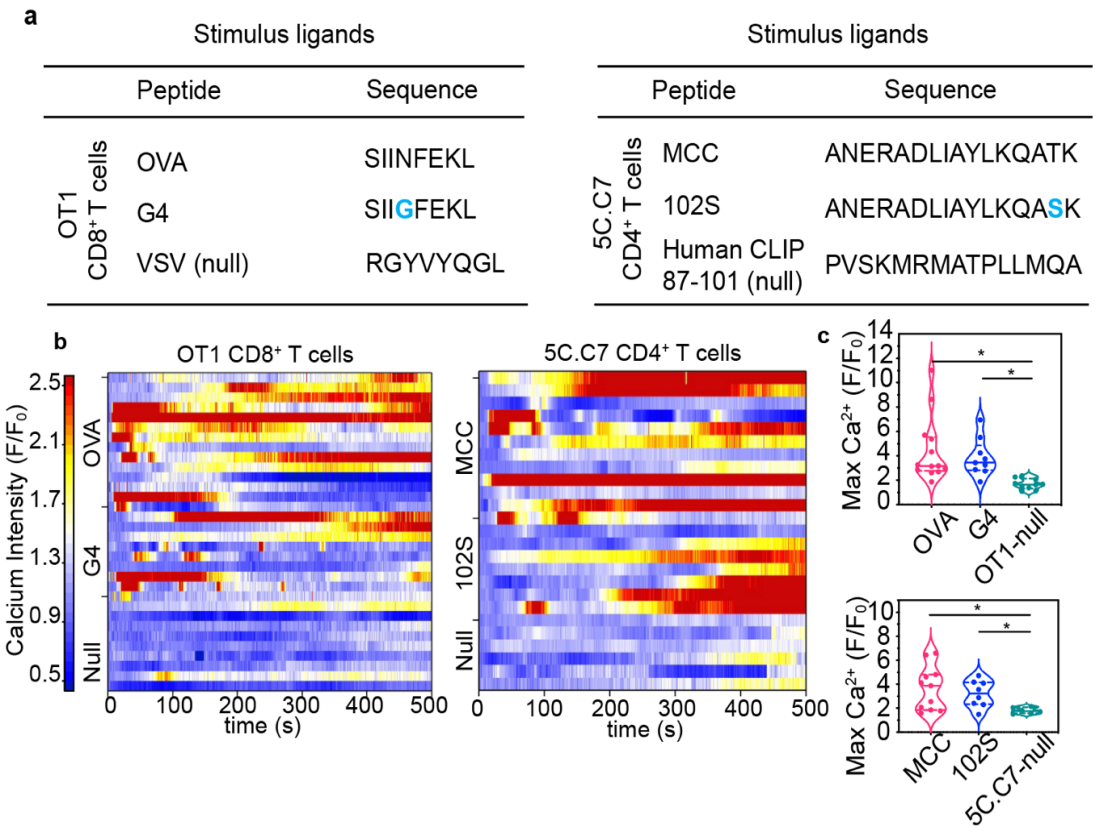

Figure 4-13. Calcium signals upon contacting various pMHC-hexapods. a. Peptide stimulus ligands associated with MHC used in this work. Various pMHC agonists for both 5C.C7 CD4$^+$

cells and OT-1 CD8$^+$ cells were modified onto the hexapods. Non-stimulatory peptides (null) were used as negative controls. **b.** Individual calcium intensity (F/F_0) profiles of a pMHC-hexapod stimulated T cells. **c.** Maximum calcium intensity (F/F_0) of each pMHC-hexapod stimulated T cell. One-way Brown-Forsythe and Welch's ANOVA test with Dunnett's T3 multiple comparisons was performed (* for $P < 0.05$; $N \geq 6$).

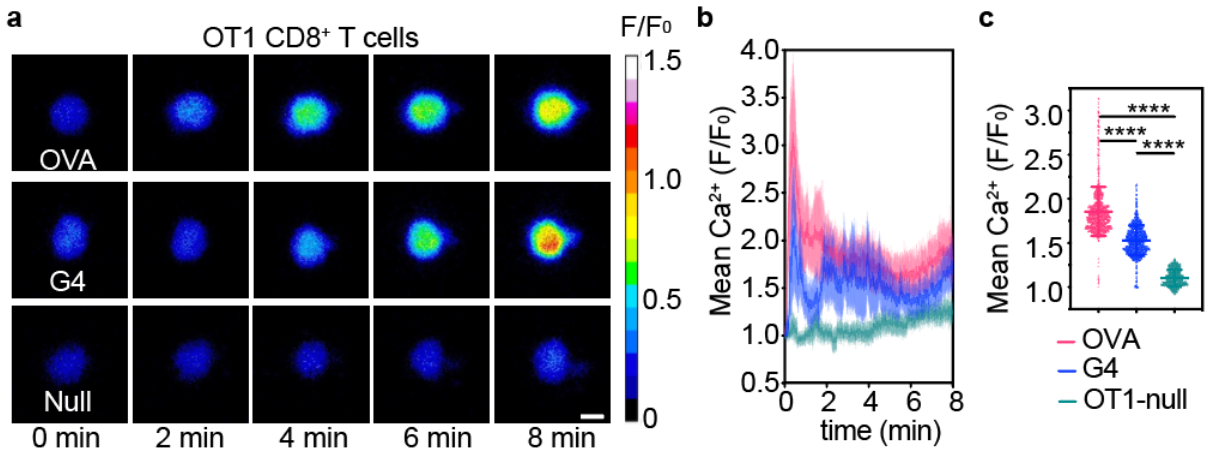

Figure 4-14. Primary OT1 CD8$^+$ T cell calcium signals. a. Representative images of the time-lapse calcium signal intensity (F/F_0) of OT1 CD8$^+$ T cells stimulated using an OVA-MHC-hexapod, a G4-MHC-hexapod, and a non-stimulatory peptide (null)-modified hexapod as the negative control. Scale bar, 5 µm. **b.** Distinct calcium profiles (mean $F/F_0 \pm$ standard error of mean or S.E.M) were observed upon stimulation with an OVA- (N = 13), G4- (N = 9), or null- (N = 10) MHC-hexapod. OVA and G4 have only one amino acid difference in their sequence, confirming the amino-acid level biochemical sensitivity of T cells. **c.** Calcium intensity value at each time point (2 frames per second or N = 960) of pMHC-hexapod stimulated OT1 CD8$^+$ T-cell. Lines, mean $F/F_0 \pm$ SD. Statistical analysis was performed with the unpaired two-tailed t-test. ****, $P < 0.0001$.

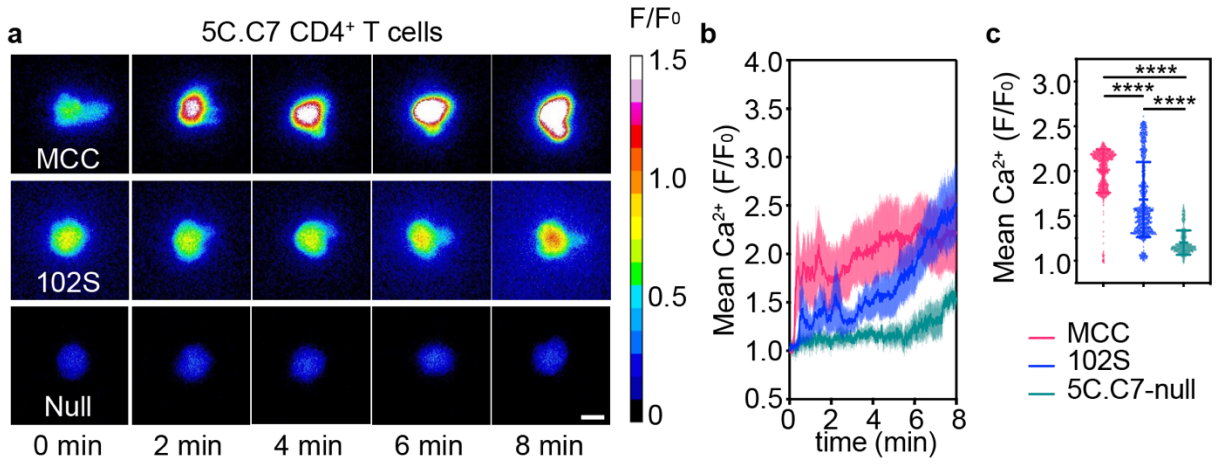

Figure 4-15. Primary 5C.C7 CD4$^+$ T cell calcium signals. a. Representative images of the time-lapse calcium signal intensity (F/F_0) of 5C.C7 CD4$^+$ T cells stimulated using an MCC-MHC-hexapod, a 102S-MHC-hexapod, and a non-stimulatory peptide(null)-modified hexapod for negative controls. Scale bar, 5 µm. **b.** Distinct calcium profiles (mean F/F_0 ± standard error of mean or S.E.M) were observed when stimulating with an MCC- (N = 11), 102S- (N = 8), and null- (N = 6) MHC-hexapod, respectively. MCC and 102S have only one amino acid difference in the sequence. Thus, T-cell has a biochemical sensitivity down to amino acid level. **c.** Calcium intensity value at each time point (2 frames per second or N=960) of pMHC-hexapod stimulated 5C.C7 CD4$^+$ T-cell. Lines, mean F/F_0 ± SD. Statistical analysis was performed using unpaired two-tailed t-test. **** for $P < 0.0001$.

Table 4-3. Representative artificial antigen-presenting systems

Material	Contact area (µm^2)	Molecule # at the contact	Study	Ref.
Hexapod	0.13	1	Immune cell biochemical sensitivity	Our work
Mesoporous silica microrods (MSRs)	N.A. (Size = ~70 µm × 5 µm)	N.A.	human T-cell expansion	14

Table 4-3, continued.

Material	Contact area (μm^2)	Molecule # at the contact	Study	Ref.
Magnetic particles	N.A. (Diameter = 50 nm; 300 nm; 600nm)	N.A. (Density = ~1000, ~250, ~1250 pMHC-Ig/μm^2)	Investigate ligand density in enriching T cells	36
Janus particles	2.27 (calculated from Diameter = 1.7)	N.A.	Modulating T-cell Activation	17
Iron–dextran nanoparticles	N.A. (Diameter = 100 nm)	N.A. (Density = ~96 pMHC-Ig/μm^2 and ~92 anti-CD28/μm^2)	Magnetic field-induced T-cell receptor clustering enhances T-cell activation	37
Janus particles	0.11	180-224	Clustering ligands to enhance stimulation	38
Silanized beads on a micropipette -aspirated red blood cell	1-4	5-7	The kinetics of two-dimensional TCR and pMHC interactions determine T-cell responsiveness	33
Dynabeads® Human T-Activator CD3/CD28	N.A.	N.A.	*Ex vivo* T-cell isolation, activation, and expansion	Gibco™
HLA-Ig–coated aAPCs	N.A. (10^7 beads/ml)	N.A. (Final peptide concentration of 30 μg/ml)	*Ex vivo* expansion of antigen-specific cytotoxic T cells	39

4.2.4 Application of Hexapod bAPS to Explore CAR Biochemical Sensitivity

Unlike TCRs (**Fig. 4-16a**), CARs are synthetic chimeric membrane receptor proteins that consist of an extracellular single-chain antibody fragment (scFv), an extracellular hinge, a transmembrane region, co-stimulatory CD28 or 4-1BB, and intracellular CD3ζ signaling domains (**Fig. 4-16b**)[40,41]. CAR-transduced T cells have achieved remarkable success in treating

relapsed/refractory B-cell malignancies with high levels of $CD19^+$ tumor cells; however, much remains to be uncovered in CAR recognition and signaling studies.

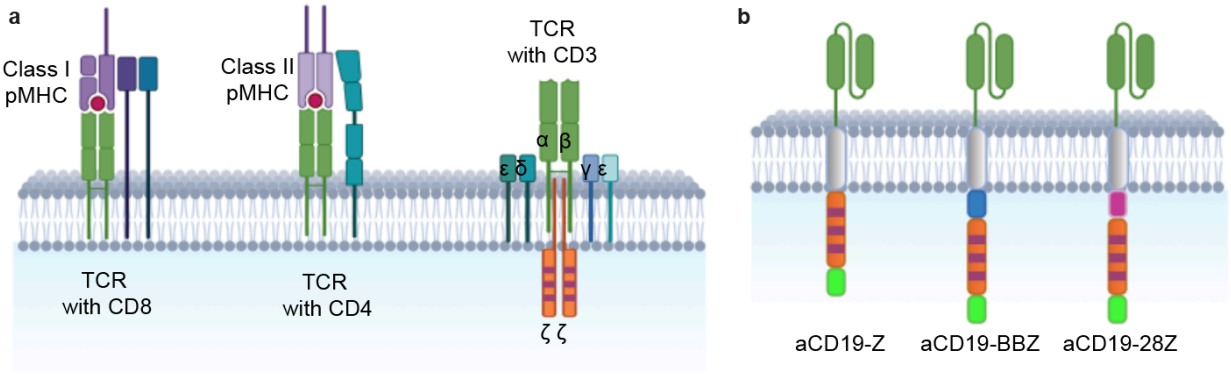

Figure 4-16. Receptors and CAR T-cell construction. a. A TCR comprises a variable TCRαβ antigen-binding domain and three nonvariable transmembrane signal transduction CD3 domains (CD3γε, CD3δε, and CD3ζζ). The activation of T cells to recognize and kill pathogen-infected cells is driven by the interaction between pMHCs and TCRs. **b**. A CAR is a human-made chimeric membrane protein that consists of an extracellular single-chain antibody fragment (scFv), an extracellular hinge, a transmembrane region, co-stimulatory CD28 or 4-1BB, and intracellular CD3ζ signaling domains.

Hexapod-enabled single-cell and single-molecule biochemical interrogation can serve as a biomolecule screening platform to test the sensitivity of T cells to various target ligands. Here, we employ the hexapod bAPS to biochemically investigate the sensitivity of CD19 CARs. We constructed CD19-targeting CAR T cells, which co-express endogenous TCRs and anti-CD19 CARs, from E6-1 Jurkat T cells (**Fig. 4-17**). Hexapods bound to anti-CD3 antibodies or the CD19 extracellular domain were used to investigate TCR and CAR signaling, respectively. The $CD19^+$ NALM-6 B-cell precursor leukemia cell line was used as a positive control.

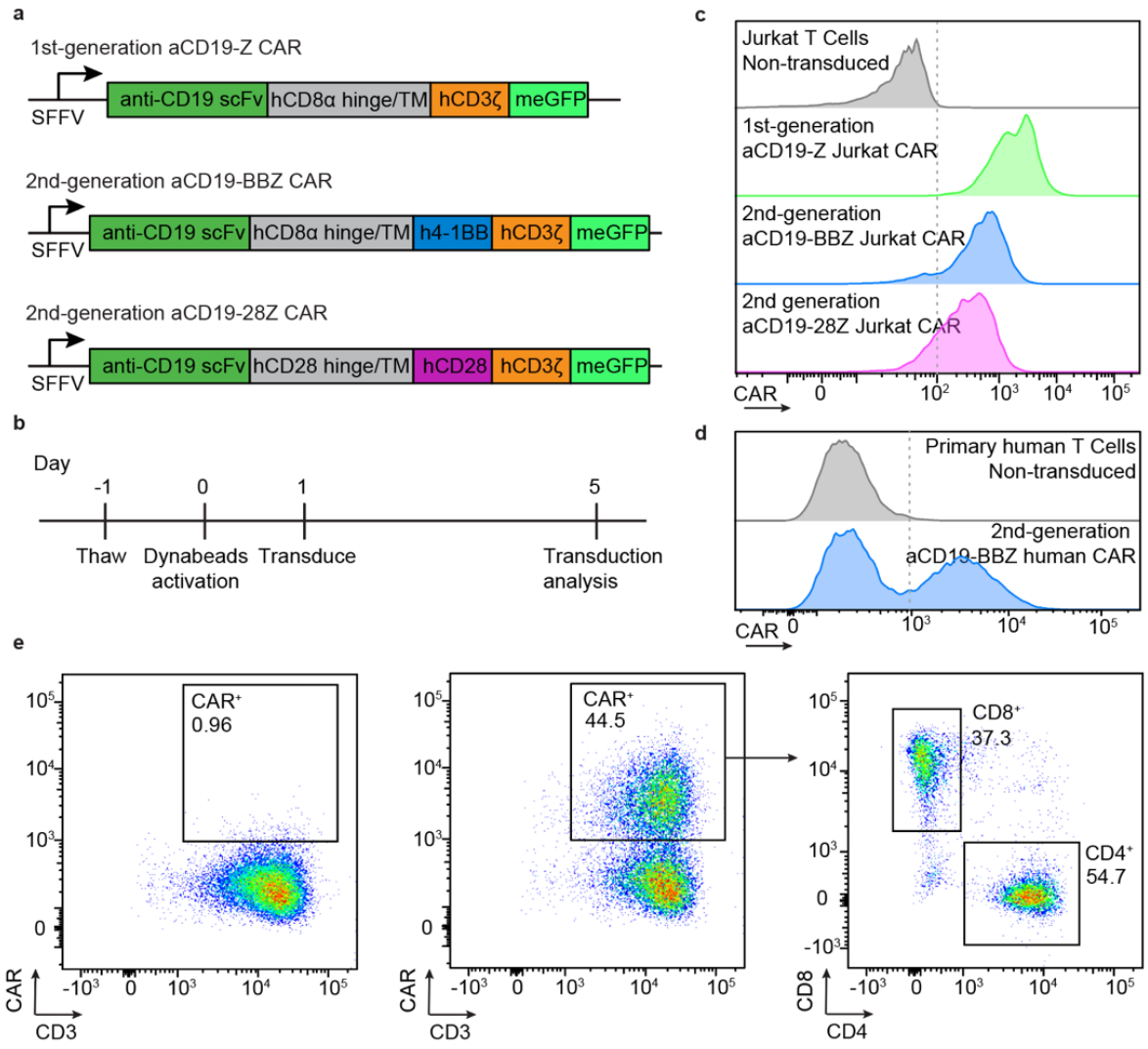

Figure 4-17. CAR T cell construction. a. Diagram depicting CAR construction. Each CAR contains a C-terminal meGFP to track CAR expression. CAR transcription is directed by a spleen focus-forming virus (SFFV) promoter. **b.** Diagram depicting the construction and transduction analysis of CAR T cells. **c.** Flow cytometry GFP expression shows the successful construction of anti-CD19 Jurkat CAR T cells. **d.** Flow cytometry GFP expression shows the successful construction of 41BB anti-CD19 human primary CAR T cells. **e.** CD3, CD4, and CD8 in 41BB anti-CD19 human primary CAR T cells.

By observing calcium in CAR T cells, we found a single TCR-targeting anti-CD3-hexapod induced strong calcium signaling in CAR T cells. In sharp contrast, a single CAR-targeting CD19-hexapod induced negligible calcium signaling (**Fig. 4-18**). The results from bAPS are in line with previous findings that TCR signal transduction is more sensitive than CAR signal transduction[21–23], providing insight into the curative deficiencies and limited efficacy of CAR T-cell therapies in treating tumors with diminished antigen expression. On the other hand, a $CD19^+$ NALM-6 cells induced saturated calcium signals in the contact CAR T cell (**Fig. 4-19**). NALM-6 cells and CAR T cells formed immunological synapses, indicating the recruitment of a high density of CAR receptors to the contact interface (**Fig. 4-20ab)**. We estimated that there were ≥ 27,015 CD19 molecules at the immunological synapses from the CAR T cell/NALM-6 contact area approximated from the confocal image (~77.49 μm^2; **Fig. 4-20c**) and the NALM-6 CD19 density (quantified from flow cytometry as ~ 349 CD19 molecules/μm^2; **Fig. 4-21**). Therefore, CAR T-cell signaling strength is highly dependent on tumor-antigen density. Our results indicated that TCRs are significantly more sensitive than CARs. These results may facilitate the rational design of next-generation high-sensitivity CARs against solid tumors, which are often characterized by antigen downregulation and loss[42,43].

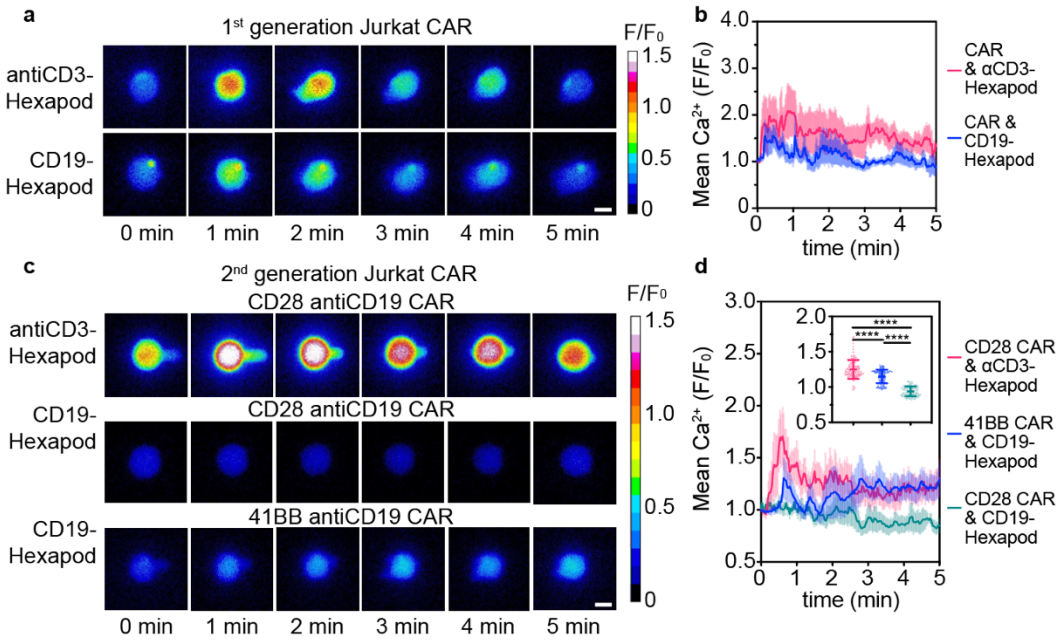

Figure 4-18. CAR T cell calcium response upon hexapod biochemical stimulation. a. Representative images of the induced calcium fluxes in 1st generation Jurkat T cells using antiCD3-hexapod or CD19-hexapod, respectively. Scale bar, 5µm. **b.** Calcium profiles (mean $F/F_0 \pm$ S.E.M, N = 5) show that antiCD3-hexapod induced stronger calcium than CD19-hexapod in 1st generation Jurkat T cells, indicating TCR transduction has higher efficiency than CAR transduction. **c.** Representative images of the induced calcium fluxes in 2nd generation Jurkat T cells using antiCD3-hexapod or CD19-hexapod, respectively. Scale bar, 5µm**. d.** Calcium profiles (mean F/F_0 ± S.E.M; N= 4 to 9) show that anti-CD3-hexapod induced a stronger calcium flux than the CD19-hexapod in 2nd generation Jurkat T cells, indicating TCR transduction has higher efficiency than CAR transduction. Insert in **d:** Mean calcium intensity value in hexapod bAPS stimulated 2nd CAR T cells at each time point (0.5 frames per second or N = 150). Lines, mean $F/F_0 \pm$ SD. Statistical analysis was performed with the unpaired two-tailed t-test. ****, $P < 0.0001$.

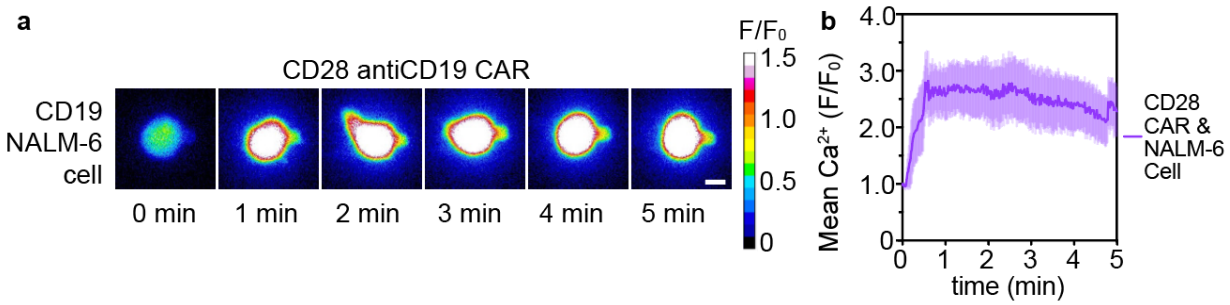

Figure 4-19. NALM-6 cell induced saturated calcium signals in CAR T cells. a. Representative images of induced calcium fluxes in 2nd generation Jurkat T cells using a NALM-6 cell. Scale bar, 5µm. **b.** Calcium profile (mean $F/F_0 \pm$ S.E.M, N = 6) of NALM-6 cell-induced calcium. NALM-6 cells serve as a positive control.

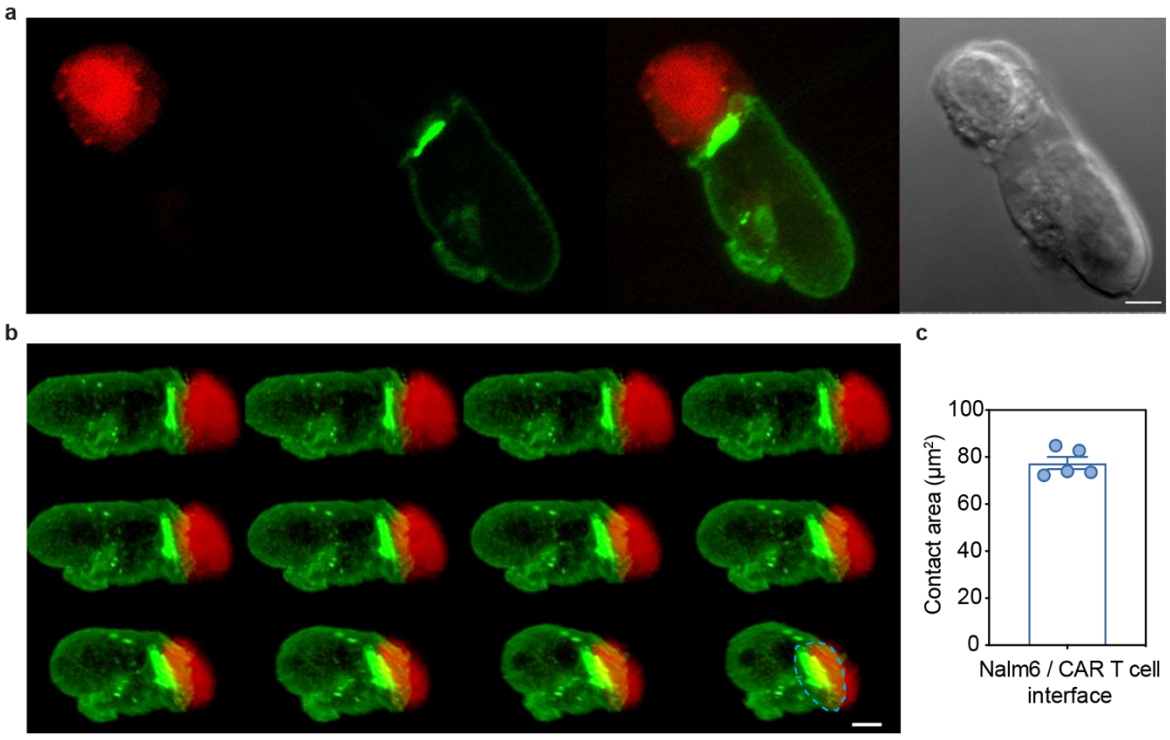

Figure 4-20. Nalm-6/CAR T-cell interface. a. A representative confocal image of the immunological synapses formed between an aCD19-28z-meGFP CAR Jurkat-cell (green) and a mCherry-labelled NALM-6 (red). Scale bar, 5µm. **b.** 3D montages of the bull's-eye shape

Figure 4-20, continued. immunological synapse between a mCherry-NALM-6 (red) and an aCD19-28z-meGFP CAR Jurkat-cell (green). Scale bar, 5 μm. Blue dashed line indicates the contact area between the NALM-6 cell and the CAR T-cell. **c.** The contact area between the NALM-6 cell and the CAR T-cell in b was measured. Five individual measurements and mean ± s.e.m (77.49 ± 2.63 μm^2) were presented on the bar chart.

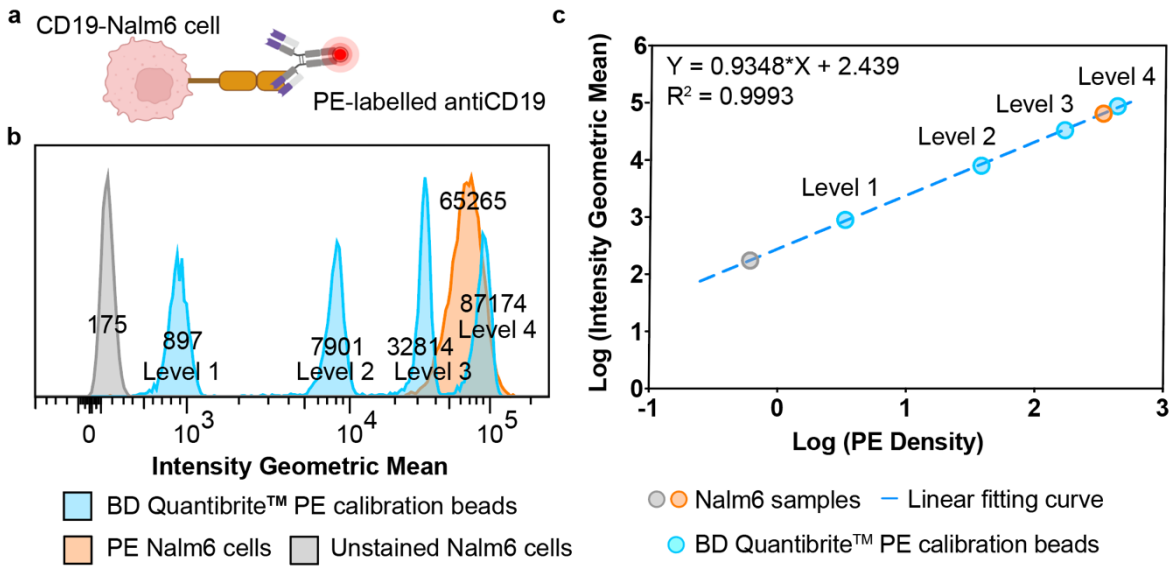

d

Material	Calculated PE molecules density (molecules/μm²)	Estimated contact area between material and T cell (μm²)	Molecule amount at the T cell/material interface
Nalm6-PEantiCD19	348.62	77.49	27014.56
Unstained Nalm 6	0.62	N.A.	N.A.

Figure 4-21. Quantification of surface CD19 density of NALM-6 cells. a. Schematic showing the characterization labeling on NALM-6 cells. **b.** Flow cytometry intensity of unstained NALM-6 cells, PE-antiCD19-labelled NALM-6 cells, and BD Quantibrite™ PE calibration beads. **c.** NALM-6 CD19 (PE staining) standard curve. **d.** Calculated NALM-6 CD19 density and corresponding molecule amount at the contact (i.e., CAR/NALM-6 interface).

4.3 Conclusion

Existing synthetic materials approaches to T-cell research generally focus on ensembles or individual cells. However, the subsequent major advances in our understanding of immune cell biology are likely to come from data obtained at the molecular and nanometer scales. Studies of TCR and CAR recognition at the single-molecule level require precise manipulation of the biointerfaces, which is beyond the capabilities of most synthetic tools. It is essential to introduce new modulation approaches to study T cells with single-molecule resolution.

In this collaborative work, we develop a bi-functional hematite-silica hexapod heterostructure for biomimetic antigen-presenting to address the single-molecule challenge. Nanostructured silica branches on the hexapod allow bioconjugation of ligands and spatial confinement of the biointerfaces. In proof-of-principle studies, we apply the hexapod heterostructures to interrogate the signaling and biochemical sensitivity of T cells. The bifunctional biomimetic hexapod heterostructures were positioned using an open-orifice aspiring micropipette to contact a T cell with spatially confined a single molecule for single-cell biochemical sensitivity investigation.

We investigated T-cell responses in a spectrum of spatial-temporal biochemical studies. Using the micropipette single cell-signaling assay, we demonstrated with a single-molecule resolution that TCRs can detect a single pMHC ligand and discriminate between closely related peptides with only one amino acid difference in the short peptide sequence. We also showed that single TCR signal transduction sensitivity is significantly better than that of a single CAR, indicating that the engineering of high-sensitivity or large-density CARs will be critically important in treating cancer relapses and solid tumors, two great challenges in the CAR-T-cell cancer immunotherapy field. This novel material-based biochemical and biophysical investigative

approach provides insights into T-cell and CAR T-cell sensitivities, which may facilitate the future development of cancer immunotherapies and rational vaccine design.

4.4 Experimental

4.4.1 Hexapod Synthesis

Hexapods were synthesized following a two-step process[1], which includes core synthesis via ferric hydroxide gel condensation and silica branch growth via hydrolysis and condensation from six emulsion droplets, one on each face of the cubic hematite core. Firstly, hematite cubic cores were prepared by thoroughly mixing 10 mL DI water, 100 mL 2M $FeCl_3$ solution, and 90 mL 6M sodium hydroxide solution. The mixture was aged in a 100°C oven for eight days in a sealed Pyrex bottle, and as-synthesized hematite cubes were washed three times using ethanol by sedimentation and resuspension before drying at 60°C. For the growth of silica branches, 1 mL anhydrous ethanol, 200 μL DI water, 200 μL hematite cube water suspension (1.6 wt%), 100 μL 0.18 M sodium citrate aqueous solution, 200 μL ammonia (28 wt% in water) and 100 μL TEOS were introduced in sequence into 10 mL 1-pentanol PVP (1.0 g, M.W. 40000) solution. All ingredients were mixed by stirring or shaking by hand, and the mixture was aged in a sealed bottle for 12 h. Then, reddish powders were washed three times using ethanol and collected by centrifugation at 1500 rpm for 5 min. A stock solution of hexapods was prepared by adding 1 mL ethanol to the above sedimentation (~ 6×10^8 particles/mL). The hexapods can be stored in ethanol at 4°C for a few months. Hexapod synthesis steps are shown in **Fig. 4-2**.

4.4.2 Hexapod Surface Functionalization

Hexapods (150 μL from stock solution) were incubated with 6% (v/v) (3-aminopropyl) triethoxysilane (APTES) in ethanol for 30 min for amino group modification. For biotinylation, washed hexapods were re-dispersed in 450 μL 0.1 M sodium bicarbonate ($NaHCO_3$, pH=8.2) buffer solution and 50 μL 0.01 M sulfobiotin-NHS (freshly prepared in DI water, Calbiochem®, 203118) was added to make a 1 mM biotin coating environment. Biotinylation was conducted at room temperature for 30 min, and the hexapods were washed in PBS three times. The washed hexapods were collected using centrifugation and re-dispersed in 400 μL PBS. Then streptavidin (2 g/L) was added to the biotinylated hexapods 1:1 (v/v) for 30 min at 4°C. Streptavidin-modified hexapods were then blocked with 1% bovine serum albumin (BSA) before incubation with biotinylated peptide-loaded major histocompatibility complex (pMHC) monomers. Hexapods were centrifuged at 1500 rpm and washed in PBS three times between each step. After the last wash, the modified hexapods were stored at 4°C before use. The functionalization steps are shown in Fig. 4-6.

4.4.3 Biotinylated Molecules (pMHCs, CD19, antiCD3)

Biotinylated pMHC monomers were generated by the NIH Tetramer Core Facility. Biotinylated class-I H-$2K^b$ MHC was complexed with SIINFEKL (OVA), SIIGFEKL (G4), or RGYVYQGL (VSV, null) peptide. Biotinylated class-II IE^k MHC was covalently complexed with ANERADLIAYLKQATK (MCC), ANERADLIAYLKQASK (102S), or PVSKMRMATPLLMQA (human CLIP 87-101, null) peptide. The biotinylated pMHC monomers and biotinylated human CD19 (ACROBiosystems, CD9-H82E9) were aliquoted and stored at -80°C, and a fresh aliquot was used in each experiment. Biotin anti-mouse CD3ε (clone: 145-2C11,

BioLegend, 100304), biotin Armenian hamster IgG isotype (clone: HTK888, BioLegend, 400904), biotin anti-mouse CD28 (clone: 37.51, BioLegend, 102104), biotin Syrian hamster IgG isotype (clone: SHG-1, BioLegend, 402004), biotin anti-human CD3 (clone: OKT3, BioLegend, 317320), biotin mouse IgG2a, κ isotype (clone: MOPC-173, BioLegend, 400204) and biotinylated BSA (BioVision, 7097-5) were stored at 4^{o}C prior to use.

For surface functionalization, biotinylated pMHC monomer (class I peptide-H-2K^{b}, 0.2mg/mL; class II peptide-I-E^{k}, 0.18mg/mL), biotinylated CD19 (ACROBiosystems, 20□g/mL), biotinylated anti-mouse CD3ε (BioLegend, 20□g/mL) and biotinylated anti-mouse CD28 (BioLegend, 5□g/mL) antibodies, or biotinylated anti-human CD3 (BioLegend, 20□g/mL) were added to streptavidin-modified hexapods. For co-coating with both anti-CD3 and anti-CD28, the molar ratio was controlled to 2:1 (anti-CD3:anti-CD28).

4.4.4 Surface Protein Quantification

Hexapod surface protein modification was verified with AF488-anti-CD19 and PE-antiCD19 (**Fig. 4-7 and Fig. 4-8**). For quantification, PE anti-human CD19 antibody (HIB19, Biolegend, 302207) was used to label CD19-hexapod and NALM-6 cells. NALM-6 cells were cultured in RPMI 1640 with 10% fetal bovine serum (X&Y Cell Culture, FBS-500), and CD19-hexapods were stored in 1X PBS prior to PE labeling. PE-anti-CD19 labeling was performed under 37°C for 30 min. Surface protein density was quantified using BD Quantibrite^{TM} PE beads (BD, 340495, LOT 61567) with four PE density levels as references. BD Quantibrite^{TM} PE beads were reconstituted using 0.5 mL 1X PBS with sodium azide plus 0.5% BSA. Optical imaging (Nikon eclipse Ti2 inverted microscope, 60× oil immersion objective, N.A. 1.40, PCO.PANDA SCMOS camera, **Fig. 4-9**) and flow cytometry (**Fig. 4-10**) were independently performed to quantify the

fluorescence levels on PE-anti-CD19-labeled CD19-hexapods and NALM-6 cells. The BD Quantibrite™ PE beads were used with PE-labeled hexapod-CD19 bAPS and NALM-6 cells in their optimized instrument settings.

4.4.5 Mice

The 5C.C7 T-cell receptor (TCR) transgenic RAG2 knockout mice with a B10.A background were a generous gift from the National Institute of Allergy and Infectious Diseases (NIAID). The CD45.1 homozygous OT-1 TCR transgenic Tcra-V2 and Tcrb-V5 insert mice with a C57BL/6 background were a generous gift from Dr. Melody Swartz Lab (Pritzker School of Molecular Engineering, University of Chicago). All the mice were bred and maintained in the Animal Facility of the University of Chicago with an animal protocol approved by the Institutional Animal Care and Use Committee of the University of Chicago. Aged 6-8 weeks mice were used in this study. Animals of both sexes were used, and the influence of sex was not considered in the data analysis.

4.4.6 Mouse T Cells Preparation and Isolation

To obtain mouse T cells, 5C.C7 or OT1 mouse spleen was harvested and run through a 70 mm cell strainer with warm complete medium, which is RPMI 1640 with L-glutamine medium (Cytiva, SH30027.01) containing 10% fetal bovine serum (X&Y Cell Culture, FBS-500) and supplemented to a final concentration with 1% Penicillin/Streptomycin (Life Technologies, 15140122_3683884612) and 50 μM β-mercaptoethanol (Sigma-Aldrich, M3148).

Splenocytes were resuspended in 5 mL of RBC Lysis Buffer (Life Technologies, 00-4300-54) for 5 min, washed three times, and resuspended in 5 mL of complete medium. 10 μM MCC

peptide (amino acids 88–103, ANERADLIAYLKQATK) or 10 nM OVA peptide (amino acids 257-264, SIINFEKL) was added to stimulate T-cell proliferation on day 0, and 100 U/mL recombinant mouse IL-2 (Sigma-Aldrich, I0523) was added the following day. Naïve T cells were used for cell surface markers test and cytokine production evaluation; Day 6-10 blasting T cells were used for cytokines and calcium tests. Live T-cell suspensions were separated from the dead cells using Ficoll-Paque Plus density gradient media (GE Healthcare, 17-1440-02) density gradient centrifugation (centrifuged at 2000 rpm for 10 min at 4°C, acc/dec: SLOW/SLOW). $CD4^+/CD8^+$ T cells were then harvested by negative selection with the MojoSort™ Mouse $CD4^+/CD8^+$ T-cell Isolation Kits (Biolegend, 480033, 480035). After three washes, cells were resuspended in complete medium for use.

4.4.7 2D Fluorescent Micropipette Assays

A single-cell micropipette setup was used to investigate the biochemical impact of single hexapod stimulation on an individual cell, with calcium signaling as readout. The micropipette apparatuses were constructed using a Leica DM IRB inverted microscope placed on an anti-vibration table (Newport) equipped with manometer systems to apply suction pressure through glass pipettes (**Fig. 4-11**). Two opposing micropipettes mounted to two identical piezoelectric micromanipulators (Sensapex) were used to capture and control the contact between a hexapod and a cell. A sample chamber of the desired size was prepared by cutting coverslips. The temperature of the sample chamber (37°C) was maintained by an objective heater (Bioptechs). To avoid medium evaporation during heating, the chamber was sealed with mineral oil (Sigma, M8410) on both sides.

For real-time calcium imaging, the sample was illuminated by sequentially triggered exposure to 470 ± 25 nm cyan light or 550 ± 20 nm green light (Spectra X, Lumencor) and a white LED light (TLED+, Sutter Instrument). Triggering of light channels and data acquisition were performed with analog modulation using μManager software[44]. Time-lapse calcium images were acquired through a 100× objective by an Andor iXon Ultra EMCCD camera. Signals from calcium dyes were collected at intervals of 500 ms for up to 10-20 min and postprocessed with Fiji software (v.2.3.0) and MATLAB (R2020b).

4.4.8 Single-cell Calcium Imaging

For calcium signaling experiments, ~10^6 cells were incubated with 10 μM calcium indicator ($CD4^+$, $CD8^+$ T cells: Calbryte™ 520 AM [AAT Bioquest, 20650]; CAR T cells: Calbryte™ 590 AM [AAT Bioquest, 20700]) for 1 h in HHBS buffer (Hanks Buffer with 20 mM Hepes) at 37°C / 5% CO_2 and then incubated at room temperature for 30 min. All imaging experiments were performed in the presence of 2 mM probenecid (Thermo Fisher Scientific, P36400). After incubation, T cells were washed three times with HHBS, resuspended in minimal imaging media (MIM: colorless RPMI with 5% FBS and 10 mM HEPES), incubated in MIM for 10 min at 37°C, and then transferred to the micropipette sample chamber before data collection. T cells (2 μL) and hexapods (2 μL) were added to MIM (600 μL) in the cell chamber.

4.4.9 CAR-T Cells

CAR Construction: From N-terminus to C-terminus, the anti-CD19 CAR consists of an extracellular FMC63-based scFv, CD8α hinge and transmembrane region, 4-1BB and CD3ζ intracellular domains, and monomeric enhanced green fluorescent protein (meGFP). The C-

terminal meGFP was included to track CAR transduction efficiency and expression. The hinge, transmembrane region, and intracellular domains were designed identically to the clinical CAR construct used in tisagenlecleucel. The anti-CD19 CAR was cloned onto a pHR vector backbone under the control of the spleen focus-forming virus (SFFV) promoter (**Fig. 4-16 and Fig. 4-17**).

Lentiviral Production: Plasmids carrying a human CAR were cloned onto the pHR vector backbone. Transfer plasmids were transfected into the Lenti-X 293T packaging cell line (Takara, 632180) for lentiviral production. Lenti-X 293T-cell lines were routinely cultured in DMEM and 10% fetal bovine serum (X&Y Cell Culture, FBS-500).

In brief, packaging cells were grown overnight and transfected the following day via Lipofectamine 3000 (Invitrogen, L3000001). For lentiviral production, transfer plasmids (0.95 μg, containing the CAR on the pHR vector backbone), packaging plasmids (0.72 μg, psPAX2), and envelope plasmids (0.22 μg, pMD2.G) were co-transfected into Lenti-X 293T cells. After 72 hours, the viral supernatant was concentrated by ultracentrifugation and stored at -80°C until transduction.

CAR-Cell Line and Primary CAR T-cell Preparation: Concentrated lentiviruses were used to transduce E6-1 Jurkat cells or primary human peripheral blood mononuclear cells (PBMCs) from a donor. E6-1 Jurkat cells were routinely cultured in RPMI-1640 (Gibco, 11875093) supplemented with 10% fetal bovine serum (X&Y Cell Culture, FBS-500). Primary PBMCs were routinely cultured in T-cell medium (RPMI supplemented with 10% FBS, 1% Pen/Strep, 2 mM L-glutamine, 50 mM 2-mercaptoethanol, 50 U/mL IL-2). Prior to transduction, Jurkat cells or PBMCs were activated for 24 hours with Dynabeads™ Human T-Activator CD3/CD28 (Gibco, 11161D).

During transduction, lentiviruses were added to cells along with protamine sulfate (Millipore Sigma, P3369-10G) to a final concentration of 10 μg/mL. Jurkat cells were transduced

with a multiplicity of infection of 1, while primary cells were transduced with a multiplicity of infection of 5. Cells were spinoculated at 800 × g for 60 minutes at room temperature. Then, cells were grown for 72-96 hours before analysis of transduction efficiency by flow cytometry. Cells were stained for CD3 (BV421), CD4 (BV510), and CD8 (PerCP/Cy5.5) (**Fig. 4-17**).

4.5 Bibliography

1. Neal, L. R. *et al.* The basics of artificial antigen presenting cells in t cell-based cancer immunotherapies. *J. Immunol. Res. Ther.* 2, 68–79 (2017).
2. Alam, S. M. *et al.* T-cell-receptor affinity and thymocyte positive selection. *Nature* 381, 616–620 (1996).
3. Artzy-Schnirman, A. *et al.* Artificial antigen presenting cells for detection and desensitization of autoreactive t cells associated with type 1 diabetes. *Nano Lett.* **22**, 4376–4382 (2022).
4. Karlsson, A. C., Humbert, M. & Buggert, M. The known unknowns of T cell immunity to COVID-19. *Sci. Immunol.* 5, eabe8063 (2020).
5. Rurik, J. G. *et al.* CAR T cells produced *in vivo* to treat cardiac injury. *Science* 375, 91–96 (2022).
6. Seo, D. *et al.* A Mechanogenetic toolkit for interrogating cell signaling in space and time. *Cell* 165, 1507–1518 (2016).
7. Super, M. *et al.* Biomaterial vaccines capturing pathogen-associated molecular patterns protect against bacterial infections and septic shock. *Nat. Biomed. Eng.* 6, 8–18 (2022).
8. van der Merwe, P. A. & Dushek, O. Mechanisms for T cell receptor triggering. *Nat. Rev. Immunol.* 11, 47–55 (2011).
9. Kobayashi, E. *et al.* Rapid cloning of antigen-specific T-cell receptors by leveraging the cis activation of T cells. *Nat. Biomed. Eng.* (2022).
10. Steenblock, E. R. & Fahmy, T. M. A comprehensive platform for *ex vivo* T-cell expansion based on biodegradable polymeric artificial antigen-presenting cells. *Mol. Ther.* 16, 765–772 (2008).
11. Wang, C., Sun, W., Ye, Y., Bomba, H. N. & Gu, Z. Bioengineering of artificial antigen presenting cells and lymphoid organs. *Theranostics* 7, 3504–3516 (2017).
12. Neurauter, A. A. *et al.* Cell isolation and expansion using dynabeads ®. in *Cell Separation* (eds. Kumar, A., Galaev, I. Y. & Mattiasson, B.) vol. 106 41–73 (Springer Berlin Heidelberg, 2008).
13. Agarwalla, P. *et al.* Bioinstructive implantable scaffolds for rapid *in vivo* manufacture and release of CAR-T cells. *Nat. Biotechnol.* (2022).
14. Cheung, A. S., Zhang, D. K. Y., Koshy, S. T. & Mooney, D. J. Scaffolds that mimic antigen-presenting cells enable *ex vivo* expansion of primary T cells. *Nat. Biotechnol.* 36, 160–169 (2018).
15. Zhang, D. K. Y., Cheung, A. S. & Mooney, D. J. Activation and expansion of human T cells using artificial antigen-presenting cell scaffolds. *Nat. Protoc.* 15, 773–798 (2020).
16. Gao, Y. & Yu, Y. How half-coated janus particles enter cells. *J. Am. Chem. Soc.* 135, 19091–19094 (2013).
17. Chen, B. *et al.* Janus particles as artificial antigen-presenting cells for T cell activation. *ACS Appl. Mater. Interfaces* 6, 18435–18439 (2014).
18. Huang, J. *et al.* A single peptide-major histocompatibility complex ligand triggers digital cytokine secretion in CD4(+) T cells. *Immunity* 39, 846–857 (2013).
19. Irvine, D. J., Purbhoo, M. A., Krogsgaard, M. & Davis, M. M. Direct observation of ligand recognition by T cells. *Nature* 419, 845–849 (2002).
20. Purbhoo, M. A., Irvine, D. J., Huppa, J. B. & Davis, M. M. T cell killing does not require the formation of a stable mature immunological synapse. *Nat. Immunol.* 5, 524–530 (2004).

21. Gudipati, V. *et al.* Inefficient CAR-proximal signaling blunts antigen sensitivity. *Nat. Immunol.* 21, 848–856 (2020).
22. Salter, A. I. *et al.* Comparative analysis of TCR and CAR signaling informs CAR designs with superior antigen sensitivity and *in vivo* function. *Sci. Signal.* 14, eabe2606 (2021).
23. Hu, Y. *et al.* Antigen multimers: Specific, sensitive, precise, and multifunctional high-avidity CAR-staining reagents. *Matter* 4, 3917–3940 (2021).
24. van Dam, R. L. *et al.* Spatial variability of magnetic soil properties. in (eds. Harmon, R. S., Broach, J. T. & Holloway, Jr., J. H.) 665 (2004).
25. Jia, Y. *et al.* Facile one-pot synthesis of lepidocrocite (γ-FeOOH) nanoflakes for water treatment. *New J. Chem.* 37, 2551 (2013).
26. Raghavender, A. T. *et al.* Nano-ilmenite $FeTiO_3$: synthesis and characterization. *J. Magn. Magn. Mater.* 331, 129–132 (2013).
27. Rossi, L. *et al.* Cubic crystals from cubic colloids. *Soft Matter* 7, 4139–4142 (2011).
28. Hinrichs, S. *et al.* Goethite nanorods: synthesis and investigation of the size effect on their orientation within a magnetic field by SAXS. *Nanomaterials* 10, 2526 (2020).
29. Gavilán, H. *et al.* Formation mechanism of maghemite nanoflowers synthesized by a polyol-mediated process. *ACS Omega* 2, 7172–7184 (2017).
30. Li, Q. *et al.* Correlation between particle size/domain structure and magnetic properties of highly crystalline Fe3O4 nanoparticles. *Sci. Rep.* 7, 9894 (2017).
31. Kim, J.-H., Hwang, H. J., Oh, J. S., Sacanna, S. & Yi, G.-R. monodisperse magnetic silica hexapods. *J. Am. Chem. Soc.* 140, 9230–9235 (2018).
32. Mahtabani, A. *et al.* On the silica surface modification and its effect on charge trapping and transport in pp-based dielectric nanocomposites. *ACS Appl. Polym. Mater.* 2, 3148–3160 (2020).
33. Huang, J. *et al.* The kinetics of two-dimensional TCR and pMHC interactions determine T-cell responsiveness. *Nature* 464, 932–936 (2010).
34. Sasmal, D. K. *et al.* TCR–pMHC bond conformation controls TCR ligand discrimination. *Cell. Mol. Immunol.* 17, 203–217 (2020).
35. Rosenberg, J., Cao, G., Borja-Prieto, F. & Huang, J. Lattice light-sheet microscopy multi-dimensional analyses (LAMDA) of t-cell receptor dynamics predict T-cell signaling states. *Cell Syst.* 10, 433-444.e5 (2020).
36. Hickey, J. W. *et al.* Efficient magnetic enrichment of antigen-specific T cells by engineering particle properties. *Biomaterials* 187, 105–116 (2018).
37. Perica, K. *et al.* Magnetic field-induced t cell receptor clustering by nanoparticles enhances t cell activation and stimulates antitumor activity. *ACS Nano* 8, 2252–2260 (2014).
38. Lee, K. & Yu, Y. Janus nanoparticles for T cell activation: clustering ligands to enhance stimulation. *J. Mater. Chem. B* 5, 4410–4415 (2017).
39. Oelke, M. *et al.* Ex vivo induction and expansion of antigen-specific cytotoxic T cells by HLA-Ig–coated artificial antigen-presenting cells. *Nat. Med.* 9, 619–625 (2003).
40. June, C. H., O'Connor, R. S., Kawalekar, O. U., Ghassemi, S. & Milone, M. C. CAR T cell immunotherapy for human cancer. *Science* vol. 359 1361–1365 (2018).
41. Weinkove, R., George, P., Dasyam, N. & McLellan, A. D. Selecting costimulatory domains for chimeric antigen receptors: functional and clinical considerations. *Clin. Transl. Immunol.* 8, e1049 (2019).
42. Hou, A. J., Chen, L. C. & Chen, Y. Y. Navigating CAR-T cells through the solid-tumour microenvironment. *Nat. Rev. Drug Discov.* 20, 531–550 (2021).

43. Marofi, F. *et al.* CAR T cells in solid tumors: challenges and opportunities. *Stem Cell Res. Ther.* 12, 81 (2021).
44. Edelstein, A. D. *et al.* Advanced methods of microscope control using μManager software. *J. Biol. Methods* 1, e10 (2014).

Chapter 5. Hexapod bAPS-Based Interrogation of T cell Biophysical Sensitivity

5.1 Introduction

5.1.1 Magnetic Materials as Magneto-Mechanical Transducers

As a magnetic field signaling receiver and convertor, magnetic materials can transform the external energy of the magnetic field into mechanical energy. In static magnetic fields, often generated via permanent magnets (e.g., NdFeB), a field with gradients from about 1 to 100 T/m can be produced. Dynamic magnetic fields of different oscillation modes can be produced with electromagnets. Depending on the field strength, oscillating frequencies, and directions, magnetic materials can rotate and move accordingly. The overall magnetic moment **m**, contributed via the individual atomic magnetic moment, is the intrinsic parameter for magnetic materials to generate forces. It can be defined as $m = M_s V$, where M_s is the particle magnetization under magnetic saturation and V is the particle volume. The strength of M_s is proportional to the magnetic susceptibility χ and the magnetic field strength H, and in the material, the magnetic induction $B = \mu_0(H + M_s)$, where μ_0 is the vacuum permeability. In a dilute material aqueous suspension solution, B can be simplified as $B = \mu_0 H$. In a uniform magnetic field, a torque $\boldsymbol{\tau}$ that acts on the material will align the magnetic moment m with the field direction: $\boldsymbol{\tau} = mB = \mu_0 M_s V H$. The corresponding magnetic field energy $U = -(mB)$, and the magnetic gradients generate forces $\boldsymbol{F} = -\boldsymbol{\nabla U} = \boldsymbol{\nabla}(m \cdot B) = \mu_0 V M_s(\nabla H)$**.** Herein, the field exerts a torque to rotate the materials such that the magnetic moment is parallel to the applied field direction and produces a translational force to attract the materials toward the regions with stronger field strength.

The magnetic force magnitudes can be characterized based on the steady-state motion of the particle. At the steady state, the magnetic force is balanced by and can be approximated to the

fluid dragging force. For magnetic particles moving in an aqueous medium within a magnetic gradient, the velocity, $\boldsymbol{v}$, is in the range of ~10^{-6} m/s and the dimension, L, of the particle is in the range of ~10^{-6} m, while the viscosity, η, of the water at 25 °C is ~8.90×10^{-4} m^2s^{-1}. According to the Navier-Stokes equation, where the Reynolds number is defined as $Re = inertial\ forces/viscous\ forces = \eta L/v$, the inertial terms can be ignored because Re <<1 and viscous forces dominate in the magnetic materials aqueous solution. Therefore, the magnetic force can be approximated to the dragging force and solved by the Stokes drag equation, $\boldsymbol{F}_{stoke} = 6\pi\eta r_h \boldsymbol{v}$, where η is the solvent viscosity, r_h is the radius of magnetic materials and $\boldsymbol{v}$ is the particle moving speed.

The magnetism arises from the movement of electrons within the material. Each electron in the atom contributes to a magnetic moment given by the orbital and the spin moments: $\mu_{total} = \mu_{orbital} + \mu_{spin}$. In the crystal structure, the magnetic moment in a solid is mainly due to the spin moments of unpaired electrons: $\mu_{spin} = g_s \times \mu_B \times S \approx \mu_B$. The spin g-factor is $g_s \approx 2$, S is the spin of the electron, +1/2 or −1/2, and μ_B is the Bohr magneton (9.274×10^{-24} J/T). For an ion with n unpaired electrons, the total magnetic moment due to the spin contribution is given by $\mu = \sqrt{n(n+2)}\ \mu_B$. For example, in the case of Fe^{3+}, with five unpaired electrons, the estimated value of 5.9 μB is similar to the observed value.

Element composition, doping ratio, cation distribution, and material structure play critical roles in magnetic properties. Some elements such as iron demonstrate a high χ and exhibit strong magnetization in the presence of an applied field. Their magnetization can also be further enhanced by doping ions such as Zn, Co, and Mn, introducing more unpaired electrons or reducing off-site magnetic spins[1]. The magnetic properties are also size-dependent, and generally, for small particles, the saturation magnetization (M_s) is positively correlated with their size. According to the

magnetic domain theory, first proposed by Pierre-Ernest Weiss in 1906, the particle will be in the single domain when its diameter is smaller than the critical diameter (D_c), where ferromagnetic coupling aligns spins of free electrons into one direction. The D_c is estimated to be $36\sqrt{AK}/\mu M_s^2$, where A is the exchange constant, K is the effective anisotropy constant which measures the energy per unit volume to flip magnetization direction, μ is the vacuum permeability, and M_s is the saturation magnetization[2]. For most magnetic materials, D_c ranges from 10 to 100 nanometers. As particle sizes increase and the diameter exceeds the D_c, there will be a decrease in the coercivity, H_c, due to the formed multi-domain structure in the bulk materials. The size-dependency of H_c has been demonstrated in different systems of magnetic NPs. For example, in $Co_{0.6}Fe_{2.4}O_4$ nanoparticles, the size increase from 10 to 20 nm leads to H_c change from 0 to 810 Oe[3]. Moreover, specific shapes can increase net magnetic magnetization. For instance, some cubic particles exhibit better magnetization properties than spherical ones of the same size, which results from the prevalent disordered spins at the corners of nanocubes, whereas the spins are broadly distributed at the surface of nanospheres[4].

Generally, the manipulation of mechano-sensitive biomolecules requires forces of piconewtons (pN). For example, the mechanosensitive channels in hair cells can be opened with a single force pulse of about 0.3 pN[5], and a force of ~10 pN is needed to activate a single PIEZO ion channel[6]. In summary, the geometry and configuration of the magnetic field and the intrinsic properties of magnetic materials have to be specially tailored to meet the desired regulation.

5.1.2 Magneto-Mechanical Transductions for Cell Fate Regulation

Mechanical signals are increasingly recognized as overarching regulators of cell behaviors. Magneto-mechanical forces at extra-, inter-, or intracellular levels allow for significant alteration

of the membrane potentials, therefore, driving the membrane potential with magnetic materials opens new opportunities to study cellular processes. As tiny non-invasive tools, magnetic materials can also be considered for various promising broad application potentials in cell therapy, neurobiology, and nanomedicine. Therefore, understanding how magneto-mechanical forces can remotely alter the cell machinery and specifically induce the required cellular responses can provide new routes for regulating cell fate.

The magneto-mechanical modulation techniques have advantages, including 'action at a distance', high spatial-temporal resolution, non-invasiveness, and the possibility of adjustable dosage. Moreover, magnetic fields are the only modality that can penetrate deep tissues without tissue heating and field attenuation, owing to the low magnetic susceptibility of biological matter. As such, magnetic materials are also suitable for interfacing at arbitrarily deep sites that existing methods have problems assessing. We anticipate that with improvements in areas like ease of experimental setup, its usage will become more prevalent.

Among many functional materials, magnetic materials transduce magnetic actuation to mechanical forces, which have great potential in various bioapplications because of the bio-mechano-sensation. Magnetic materials are excellent candidates for cell fate regulation, cancer therapies, and neurotherapeutics. Magnetic materials offer maneuverability through fine-tuned compositions and geometries to transduce remote magnetic fields into required localized forces on cells. The induced magneto-mechanical forces can be used to regulate specific cell fate and address demanding manipulations in cell cycle progression. So far, magnetic field-induced forces have been applied to induce mechanical stretch of ion channels to manipulate intracellular ion flux, deliver mechanical forces via surface receptors through the cell membrane to stimulate signaling

cascades, form biomolecule clusters to initiate apoptosis, and physically destruct cellular structure or intracellular organelles by oscillation.

5.1.3 Effects of Magneto-Mechanical Forces on Cells

Many studies have shown that various force inputs could initiate biochemical responses, such as the protein unfolding, clustering, and coordination of signaling cascades, and therefore, regulate pathways leading to gene expression, protein synthesis, remodeling of cellular structures, and even cellular phenotype changes. Although these efforts were fruitful, how a mechanical cue is sensed and computed at the molecular level into meaningful biological behaviors has long remained enigmatic.

So far, it is known that mechanical forces can be directly translated into biochemical signals via several mechanosensitive ion channels[7], which include but are not limited to the N-type Ca^{2+} channels, NOMPC, TREK-1, TRPV4, and PIEZO ones[8]. They cover a broad conductance spectrum, ranging from 3 nS (MscL ion channels) to tens of pS (ENaC ion channels). Probed by the patch-clamp technique, the sensitivities to mechanical forces of different ion channels are also of different values. For example, PIEZO 1/2 is highly sensitive and responsive to low-stress forces of pico-Newton (pN), while TWIK-1 is almost insensitive to mechanical forces.

Besides mechanosensitive ion channels, mechanical forces can also be sensed directly and transduced into biochemical signals via several mechanosensitive receptors, such as integrin, selectin, T-cell receptor, Wnt-Frizzled receptor, and PECAM-1. In addition, YAP and TAZ are also elucidated to serve as two highly related mechanosensitive transcriptional regulators, which read a broad range of mechanical cues, such as shear stress and extracellular matrix rigidity[9–12].

YAP/TAZ orchestrates the responses into cell-specific transcriptional programmes, which is critical for cell behavior and regeneration.

The effects of mechanical forces fall into three categories: (i) directly regulate the cellular ionic balance through stretch-induced ion channel activations; (ii) initiate signaling cascades through membrane proteins/receptor responses towards membrane tension or substrate stiffness; (iii) direct stimulate or destruct cellular structures or intracellular organelles through physical perturbation.

Remote regulations of cellular activities at the molecular level are of increasing interest in biomedical research. In addition to chemical, genes, and previously mentioned modulations, mechanical forces also play a pivotal role in regulating cell fate, which have prompted a rapid growth of mechanobiology. Magnetic-mechanical stimulations have been revealed to have vital impacts on cell activity modulation. Understanding how magneto-mechanical forces can remotely alter the cell machinery and specifically induce the required cellular responses can provide new routes for regulating cell fate. After tethering with specific biomolecules, magnetic materials can exert forces on targeted cellular compartments and manipulate mechanical microenvironments. So far, magnetic actuation has been applied to induce mechanical stretch of ion channels to control intracellular ion flux, deliver mechanical forces via surface receptors through the cell membrane to stimulate signaling cascades, form biomolecule clusters to initiate apoptosis, and destruct cellular structure by physical oscillation. Herein, magnetic-mechanical stimulations have been revealed to perform vital impacts on cell fate regulation.

In the past decade, several promising magneto-mechanical stimulation-based applications arose in stem-cell-based regenerative medicine and the modulation of other types of somatic cells. Early in 2010, El Haj and co-workers demonstrated that the actuation of magnetic nanoparticles

toward the potassium channel TREK-1 caused osteoprogenitor cell differentiation toward an osteogenic lineage[13]. In 2015, Rotherham and El Haj demonstrated 250 nm superparamagnetic iron oxide nanoparticles (SPION) that functionalized with anti-Frizzled antibodies could activate Wnt/β-catenin signaling of human mesenchymal stem cells through the Wnt Frizzled receptor[14]. More recently, Kang and co-workers reported that oscillating magnetic fields could regulate stem cell focal adhesions and differentiation *in vitro* and *in vivo* via SPION modified with Arg-Gly-Asp (RGD) peptide, which targeted αvβ3 integrin[15]. They also reported macrophage adhesion and polarization regulation with a similar system[16]. In 2016, Wang and co-workers demonstrated a force-induced gene transcription of a green fluorescent protein (GFP)-tagged bacterial-chromosome dihydrofolate reductase (DHFR) with RGD-coated magnetic beads[17]. They suggested that the applied local stresses at integrins were further propagated from the actin cytoskeleton to the linker of the nucleoskeleton and the cytoskeleton complex, and then, through lamina-chromatin interactions, the transmitted mechanical force directly deformed chromatin and upregulated the transcription.

Magnetic material-based mechanical stimulations are also a rising research field with great potential for cancer therapies. It can serve as a novel route to trigger downstream biochemical signals by producing oscillations, clustering membrane receptors, or targeting specific organelles to initiate programmed cell death. Respectively, scientists from the Argonne National Laboratory utilized the oscillations of iron-nickel magnetic microdiscs to transmit forces to destroy cancer cells[18]. They achieved around 90% cancer-cell destruction in *vitro* within ten minutes when applying a low-frequency alternating magnetic field of a few tens of hertz. Cheon *et al.* used death receptor 4 (DR4)-conjugated $Zn_{0.4}Fe_{2.6}O_4$ magnetic nanoparticles, which aggregate and form receptors clusters within a magnetic field, to promote apoptosis of DLD-1 colon cancer cells[19].

Breakage of organelles, for example, magneto-mechanical destruction of lysosomes, induces cancer cell death[20–22].

For acute and chronic neural stimulation with magneto-mechanical forces, Dr. Tay and colleagues have explored and discussed several possible modulation mechanisms via mechanosensitive ion channels[23–25]. So far, four mechanosensitive ion channels (PIEZO1, PIEZO2, TRPV4, and N-type Ca^{2+}) are activatable by acute magneto-mechanical stimulation in neural networks. In addition, Tay *et al.* also claimed that chronic modulations (over 4 days) could serve as a noninvasive neuromodulation tool for reducing endogenous ion channel expression in neural circuits, which, if true, can be adopted for treating diseases like hypersensitivity to pain or epilepsy where such mechanosensitive channels are usually overexpressed. In 2016, they found that magneto-mechanical forces, ranging from 0.1 nanonewtons (nN) to 1 nN, can trigger Ca^{2+} influx in cortical neural networks without any observable cytotoxicity. A 20% increment in Ca^{2+} fluorescence signals with a spatial resolution of 200 μm together with an increased frequency in calcium spiking were observed in the stimulated neural networks. Adding the ω-Conotoxin, an inhibitor of the mechano-sensitive N-type calcium channels, blocked the effects of nanomagnetic force stimulation, suggesting the role of N-type Ca^{2+} channels in mediating calcium influx in response to magnetic force. However, they could not rule out the involvement of other channel types that the nanomagnetic forces might stimulate at this stage. Later in 2017, Tay *et al.* applied a chronic stimulation on a fragile X syndrome (FXS) neural network model, where the above-mentioned magneto-mechanical forces could reduce the expression of N-type Ca^{2+} ion channels. By 2018, Tay *et al.* showed a significant increase in Ca^{2+} influx in the primary dorsal root ganglion (DRG) neurons upon acute magneto-mechanical treatment of 0.15 - 1 micron-newtons (μN) using a fabricated three-dimensional hydrogel that encapsulated superparamagnetic iron oxide

nanoparticles. Based on expression levels of mechanosensitive ion channels in DRG, pharmacological inhibiting experiments by testing with different neurotoxins, and electrophysiological measurements with micropillar substrate, they reasoned that endogenous PIEZO2 and TRPV4 channels are likely contributed the most to Ca^{2+} influx. Remarkably, they also showed that a chronic magneto-mechanical stimulation could reduce the expression of PIEZO2 channels, supporting their hypothesis that magnetic forces can mediate mechanosensitive ion channel equilibrium.

In summary, several exciting new avenues in biomedical research have already been opened, taking advantage of the application of magneto-mechanical forces in remote manipulation of specific cellular events with elegant precision *in vitro* and, more importantly, *in vivo.* So far, the magnetic field-induced biomechanical forces have provided scientists with powerful tools to investigate cell mechanical properties, activate mechanosensitive ion channels, probe the mechanisms governing ion channel activity, construct 'biochips' for cell assays, develop new therapies for diseases, and elucidate signaling pathways that lead to activities such as apoptosis, the production of proteins and stress responses. To a large extent, the potential for magnetic actuation in investigations of cellular or subcellular mechanical properties and remote manipulations of specific physiological processes is still tremendous. And future clinical treatments of diseases with magneto-mechanical stimulation methods are certainly within the realm of possibility.

5.1.4 Hexapod bAPS for Investigating T Cell Biophysical Sensitivity

Mechanical signals, such as shear stress, contact tension, and substrate stiffness, have been shown to contribute to the leukocyte adhesion cascade and regulate T-cell signaling and

proliferation[26–28]. Although these findings were reported in immobilized T cells, likely, mechanical cues are also associated with function and activation in floating T cells.

T cells in the circulatory system are essential to protect the body against infections. These T cells are naturally suspension cells (i.e., non-adherent T cells). For example, more than 10^9/L (20 - 45% of white blood cells)[29] suspension T cells are found in human peripheral blood. However, the impact of mechanical forces on the activation of suspension T cells is unclear and still underappreciated.

Developing a mechanical force toolkit to investigate T-cell mechanosensing is challenging due to the suspension or free-floating nature of T cells. Existing methods to study T cell mechanosensing require immobilization of T cells onto a pre-coated substrate by membrane tethering or using an open-orifice micropipette via suction forces (**Table 5-1**)[28,30–34], the process of which may change both the cytoskeleton network and the physiological conditions, causing further stress or mechanical loading to the T cells. Several studies have used magnetic microrobots or particles to move single cells in PBS without fixation or immobilization to a substrate. While responses (calcium signaling, in particular) in individual suspension cells can be observed using fluorescent imaging, the mechanosensitive responses are not yet quantified. Magnetic particles have also been used to create an oscillatory environment that enhances T-cell activation[35]. However, due to the severe cell aggregation induced by the strong magnetic particles in that study, the evaluation of force on individual cells was almost impossible as aggregation will cause non-trivial and complicated forces. New modulation modes are required to physiologically study nanoscale physical impacts with single-molecule resolution on suspension/floating T cells *in vitro*.

Table 5-1. T-cell mechanosensing and biophysical investigations

Method	Material	Forces (pN)	Study	On floating T cells	Ref.
Hematite hexapod APS	pMHC- or protein-coated hematite hexapods	pN torques on micron hexapods	Immune cell biophysical sensitivity	Yes	Our work
AFM cantilever	pMHC- or anti-CD3-coated cantilever	180-250 pN range of forces	T-cell activation requires force generation	No	33
Optical Tweezers	antibody-coated or pMHC-coated beads (1 μm)	a tangential force (50 pN)	The αβ T-cell receptor is an anisotropic mechanosensor	No	31
Magnetic Janus Particles	Silica microparticles with nickel coating on one hemisphere	N.A.	Remote control of T-cell activation	Yes	36
Shear flow	microfluidic channel	8-25 pN	Practical label-free CD^{4+} T-cell counting of HIV-infected subjects	No	32
Fluorescence Biomembrane Force Probe	pMHC- or antibody-coupled glass bead attached to a micropipette-aspirated red blood cell	5-20 pN	Dynamic catch bonds between TCR and agonist pMHC triggers T-cell signaling	No	34
Molecular tension probes	DNA	4.7-19 pN	LFA-1/ICAM-1 forces fine-tune TCR-triggered T-cell activation	No	37
A genetically encoded tension sensor (GETS)	β2-integrins	1-6 pN	Intramolecular tension during T-cell migration	No	38

Table 5-1, continued.

Method	Material	Forces (pN)	Study	On floating T cells	Ref.
Magnetic oscillatory forces	Encapsulated alginate polymer and magnetic nanoparticles	N.A. (Cannot quantify forces because sever aggregation)	Oscilatory microenviroment amplied T-cell activation	Yes	35

Given that T cells are floating in the ensemble state, we then introduce a different mechanical manipulation mode, *i.e.*, enabling torque on floating T cells through the weak magnetic property of the hexapod biomimetic antigen-presenting system (bAPS, **Fig. 5-1**). The engineered synthetic hexapod heterostructures resemble immune-activating cells, such as dendritic cells (DCs) and B cells, in terms of functionality, morphological features, binding specificity, and length scale. Besides, hexapods are proposed to magneto-mechanically stimulate cells in a wireless and controllable way. Unlike Fe_3O_4 nanoparticles—magnetite nanoparticles with superparamagnetic behavior routinely used for single-cell biochemical and biophysical activation[36,39,40]—the weak magnetic properties of □-Fe_2O_3 (hematite) cause less particle aggregation and cell clustering in magnetic fields.

This chapter reports that magnetic field-induced piconewton·micrometer-level torques on the hematite hexapods amplify immune responses in suspension T and CAR-T cells. The multimodal hexapod bAPS presents unexplored, nanotechnology-based biointerface tools for investigating recognition, signaling, and the biophysical or mechanical sensitivity of T cells and beyond.

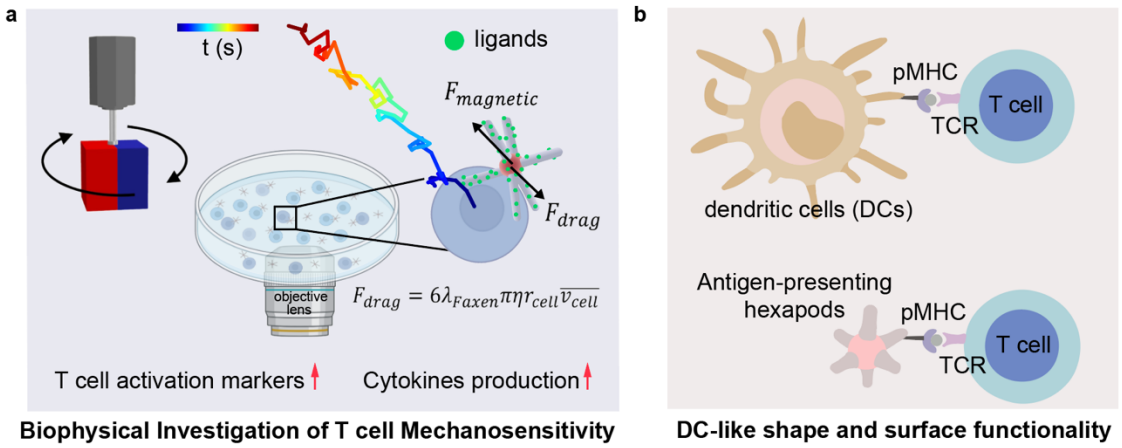

Figure 5-1. The hexapod bAPS for investigating T cell biophysical sensitivity. a. Hematite hexapods can be used for biophysical interrogation of the impact of force on floating T cells. The weak magnetic property of hematite enables rotational motion within a rotating magnetic field with minimal particle aggregation. Magnetic torques and dragging forces can be calculated to quantify the forces. **b.** The biomimetic hexapod heterostructures resemble immune-activating cells, such as dendritic cells (DCs) and B cells, in terms of functionality, morphological features, binding specificity, and length scale.

5.2 Results and Discussion

5.2.1 Magnetic Hexapod bAPS Rotation Study in Rotating Magnetic Field

The hematite core of the hexapod is weakly magnetic and can generate exogenous forces within a magnetic field. To study the movement of the hexapod in a rotating magnetic field, we placed the hexapods in PBS solution in a cell culture dish on a microscopic lens and placed a rotating magnet nearby (**Fig. 5-2**). The rotating magnetic field strength (2.3 to 5.22 mT) was calculated based on our experimental setup (**Fig. 5-2 and Fig. 5-3**) using a mathematical model[41]. We tracked the moving trajectories of hexapods. Each hematite hexapod rotated synchronously in the rotating magnetic field without apparent aggregation (**Fig. 5-4**). Upon co-culture anti-CD3-

hexapods or CD19-hexapods with T cells or CAR-T cells, respectively, hexapods fastened to the cells and formed tight attachments (**Fig. 5-5**).

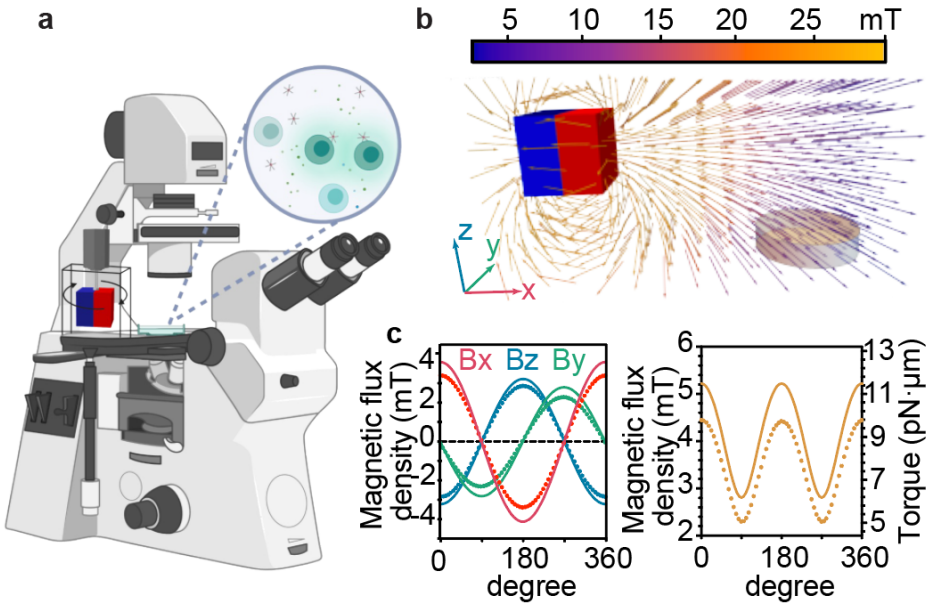

Figure 5-2. Magnetic hexapod-enabled torques on floating T cells. a. Schematic showing the experimental setup for force quantification. The hexapods are in a cell culture dish at (80 mm, 0, -37.3 mm) relative to a 2.54-cm cube neodymium (N52) permanent magnet. **b.** Calculated magnetic field vectors showing the strength and direction of the field. **c.** Measured (dots) and calculated (lines) magnetic flux density (field strength) around a hexapod position (center of the cell dish on the lens). Field strength ranges from 2.30 to 5.22 mT, corresponding to 5.06 to 11.48 pN·μm torques on a hexapod.

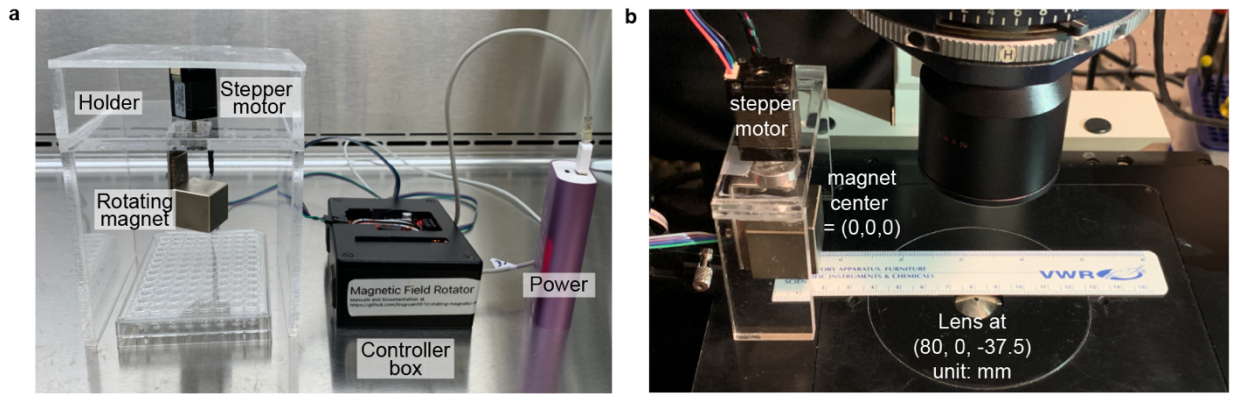

Figure 5-3. Rotating magnetic field device. a. A picture shows the magnetic field generator and control device. The rotator box contains a Metro M0 microcontroller, a real-time clock, an SD card for log file storage, and a stepper motor controller. **b.** A picture shows the experimental setup for tracking the hexapod moving using imaging. The hexapods were put in PBS solution in a cell culture dish and imaged at the microscopic lens position (x = 80 mm, y = 0 mm, z = -37.3 mm).

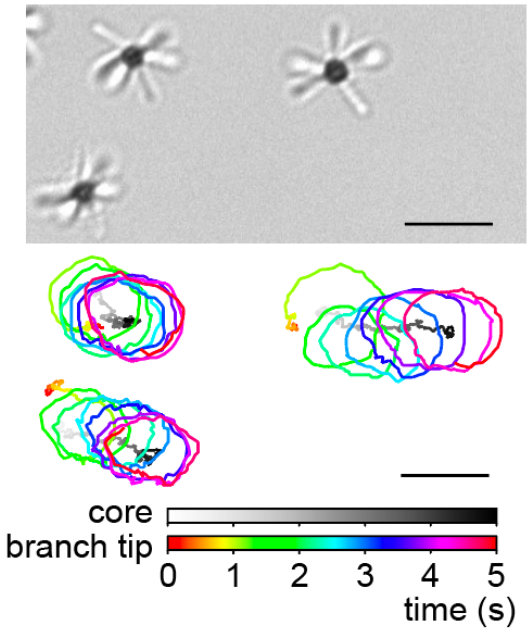

Figure 5-4. Hexapods rotate without aggregation. A representative image of dispersed hexapods (top) and real-time tracking of single hexapods (bottom) showed periodic rotational motion. The

Figure 5-4, continued. greyscale bar and the rainbow-color bar represent the positions of the hematite core and a hexapod branch tip, respectively. Scale bar, 5 µm.

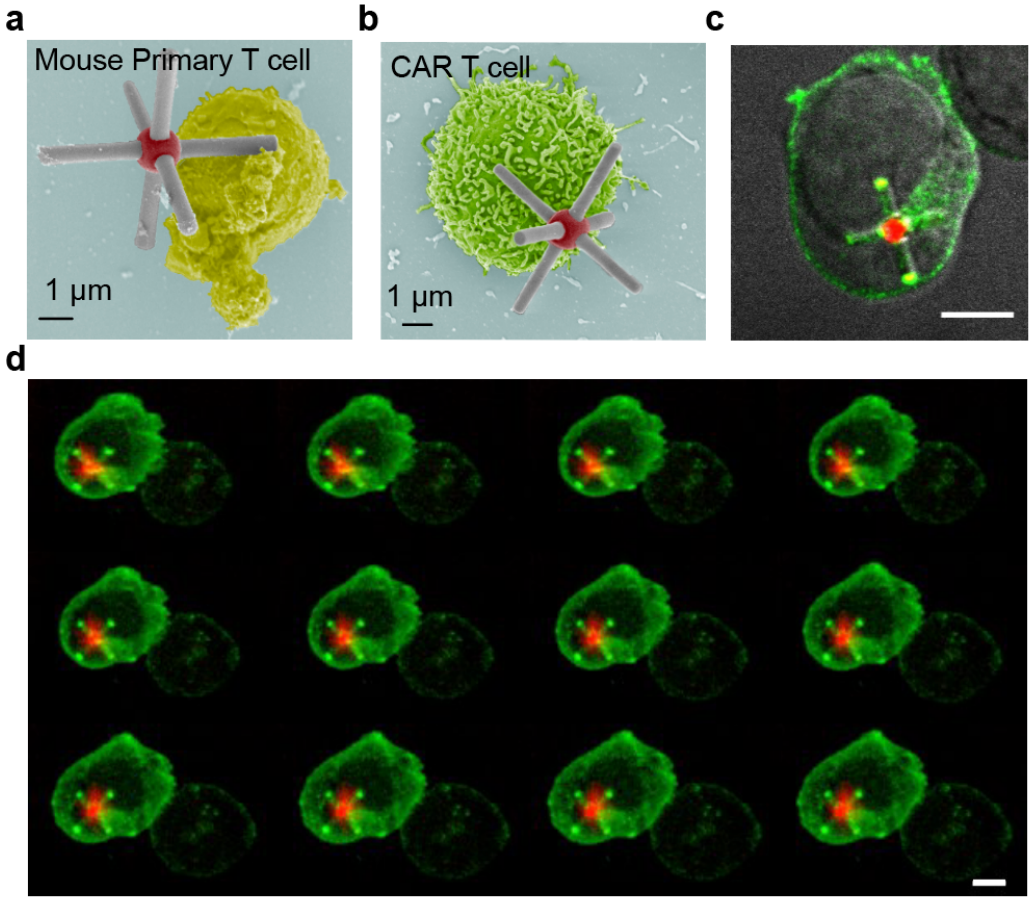

Figure 5-5. Hexapod/CAR T-cell interface. a. representative SEM image showing the tight interaction between an anti-CD3-hexapod and a primary mouse T-cell. Scale bars, 1 µm. **b.** representative SEM image showing the tight interaction between a CD19-hexapod and a CAR T-cell. Scale bars, 1 µm. **c.** representative confocal image showing a tight interface between an aCD19-28z-meGFP CAR Jurkat-cell (green) and an APC-streptavidin-labelled CD19-hexapod (red). Scale bar, 5 µm. **d.** 3D montages show the localized supramolecular activation cluster onto a CD19-hexapod (red, APC-streptavidin). Synapse formation was induced at the hexapod-cell interface. Scale bar, 5 µm.

5.2.2 Magnetic Hexapod-Induced Floating T cell Movement

The tight hexapod/cell junctions allowed the rotating hexapods to drive the movement of the cells (**Fig. 5-6ab**). For a moving trajectory analysis of the hexapod or the hexapod-bound cell at different time points, we used mean-square displacement (MSD) analysis. MSD is a statistical mechanics approach to quantifying transportation and diffusion of an object and characterizing properties such as diffusion coefficients, diffusion mode, and velocity for directed motion. We found that the free-standing T cells remained at rest with relatively minimal movement, undergoing Brownian motion or normal diffusion (MSD $\propto D \cdot t^{\alpha}$, $\alpha = 1$). In contrast, hexapod-bound cells showed hexapod-directed motion (MSD $\propto D \cdot t^{\alpha}$, $\alpha>1$, classic super diffusion due to active transport), having ~ 250-fold mean squared displacement (MSD) **(Fig. 5-6c)** compared to the hexapod-free cells.

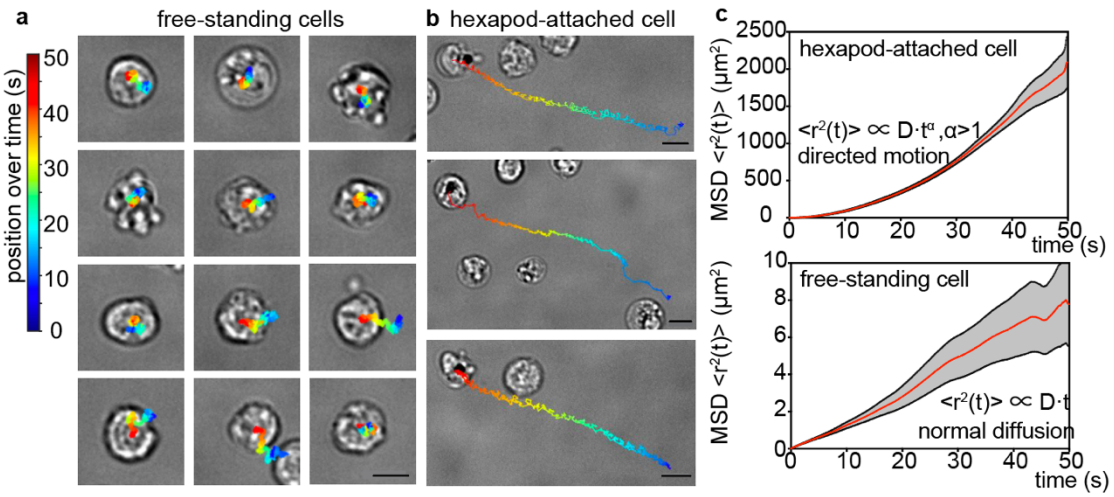

Figure 5-6. Analyses of motions in a rotating magnetic field. **a.** Moving trajectories of free-standing 5C.C7 CD4^{+} T cells in a rotating magnetic field. Scale bar, 5 μm. **b.** Moving trajectories of hexapod-bound T cells (hexapod, MCC-MHC-hexapod; T-cell, 5C.C7 CD4^{+} T cells) in a rotating magnetic field. Scale bar, 5 μm. **c.** Hexapod-bound cells (super diffusion or directed motion) have a >250-fold mean squared displacement (MSD) compared to hexapod-free cells

Figure 5-6, continued. (normal diffusion or Brownian motion). Hexapod, MCC-MHC-hexapod; T-cell, 5C.C7 $CD4^+$ T cells.

We estimated the diffusion coefficient, D, from the MSD (based on a 2-D diffusion estimation) and calculated the speed of floating T cells with or without hexapod attachment. Hexapod-bound T cells showed significantly higher diffusion coefficients and velocity compared to hexapod-free T cells **(Fig. 5-7)**. Hexapod-bound cells also displayed turbulent motion (**Fig. 5-8**), attributed to the highly variable magnetic driving force acting on the hexapods. Based on their trajectory, we calculated that a full rotation of hexapod-bound cells took 1.2 seconds (i.e., 50 rpm) (**Fig. 5-8)**. This cell rotational speed is the same as the rotating magnetic field, indicating synchronized rotation without time delays.

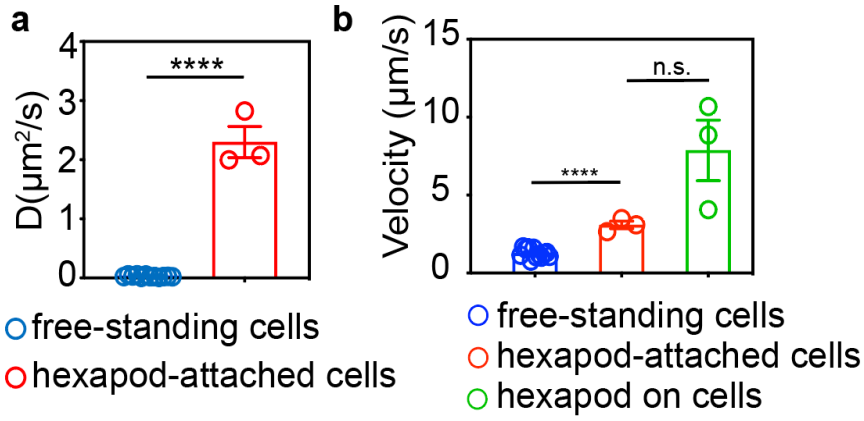

Figure 5-7. The diffusion coefficient and velocity calculated from moving trajectories. Calculated diffusion coefficient of hexapod-bound T cells and free-standing T cells. **b.** The calculated velocities from the trajectories.

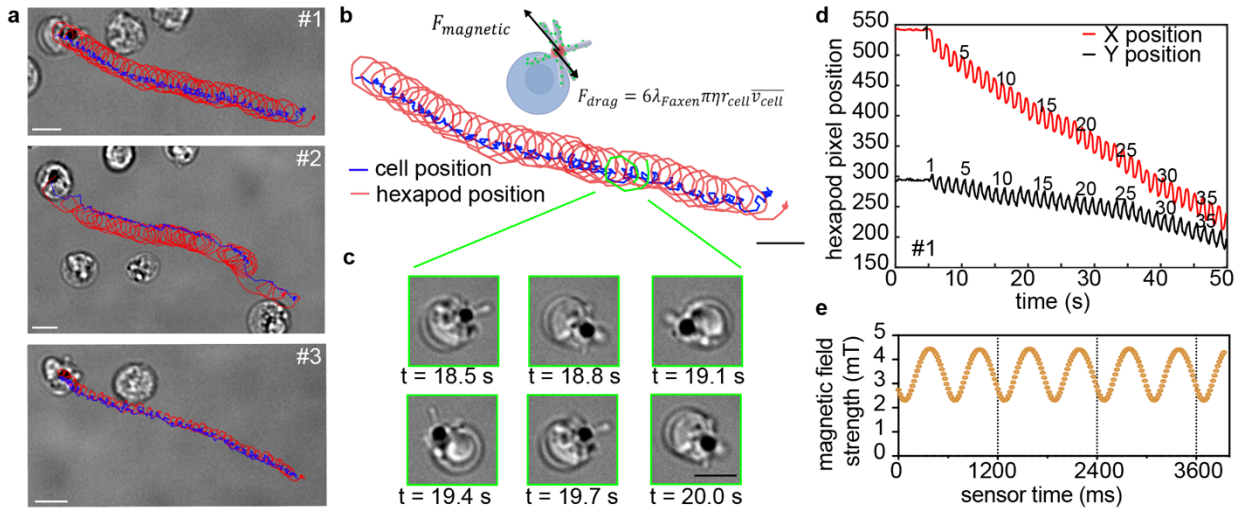

Figure 5-8. Analyses of movement of hexapod-bound T cells in a rotating magnetic field. a. The tracking trajectories of three representative hexapod-bound cells (red, hexapod core time-lapse position; blue, cell center time-lapse position). Scale bar, 5 μm. **b.** The tracking trajectory of #1 hexapod-bound T cell. Scale bar, 5 μm. **c.** Time-lapse pictures showing the positions of a hexapod-bound T cell at several time points (green trajectory in **b**). Each round rotation took 1.2 s, corresponding to 50 rpm. Scale bar, 5 μm. **d.** The time-lapse pixel position of the #1 hexapod-bound cell clearly shows the hexapod-bound cell rotated 38 rounds in 45 seconds (~a rotation speed of 50 rpm). Besides, the rotational and translational movement is constant (i.e., no acceleration). **e.** The measured magnetic field strength using a magnetometer indicates a rotation of 1200 ms per round, corresponding to 50 rpm.

5.2.3 Determination of Forces on Hexapod-Bound Floating T Cells

The exact determination of instantaneous forces acting on the magnetic hexapods is non-trivial due to the complicated relationship between the geometrical and magnetic torques[42], the ever-changing orientation of magnetic moment within the magnetic domain[43], and the ever-changing fluidic friction or dragging force acts on the moving cells[44]. However, the lack of linear

acceleration suggests that hexapod-bound cells are in quasi-equilibrium, achieving a balance between the magnetic and hydrodynamic or frictional forces. We approximate torque ($\tau = m \times B$) acting on the hexapod by classically defining the magnetic moment of the particle $m = I_0 V$, where the spontaneous magnetization per unit volume $I_0 = 2.2\times10^3$ A·m^{-1} for hematite[45] and the volume of hematite core $V \sim 1\ \mu m^3$. Therefore, in the magnetic fields used in the experiments (B ~ 2.30 mT to 5.22 mT), torque $\tau = m \times B = 5.06$ to $11.48\ pN \cdot \mu m$ on the hexapod. We also calculated the dragging force on hexapod-bound cells based on the Stokes' drag equation[44], $F_{drag} = 6\lambda_{Faxen}\pi\eta r_{cell}\overline{v_{cell}}$, where λ_{Faxen} is the Faxen's Law coefficient = 2.29, η is the dynamic viscosity = 6.90×10^{-4} Pa·s (water, 37 °C), r_p is the radius of T cell = 3.43 ± 0.10 μm, and $\overline{v_{cell}}$ is the velocity of hexapod-bound T cell. The dragging force F_{drag} on hexapod-bound T cells is estimated to be from 0.31 ± 0.04 pN to 0.80 ± 0.34 pN (mean ± std.), calculated based on the velocity of cells (3.08 ± 0.42 μm/s to 7.87 ± 3.42 μm/s, obtained from cell tracking the cell center and the hexapods on the T cell, respectively). Thus, the sub-piconewton dragging forces are less than a tenth of the magnitude of torques. As a result, dragging forces are negligible compared to torques and the cells are mainly experiencing the torques.

5.2.4 Hexapod-Based Studies of Exogenous Forces on Floating T cells and CAR-T cells

Having demonstrated that the hexapods can drive the T-cell movement through magnetic torques, we next investigated how the exogenous forces impact signaling in floating T cells and CAR T cells in a representative physiological environment. Hexapods were functionalized with stimulatory pMHC (e.g., agonist OVA-MHC) or non-stimulatory negative control molecules and co-cultured with primary mouse transgenic T cells in the absence and presence of rotating magnetic fields. We calculated the magnetic field in our rotation biophysical stimulation experiment (**Fig.**

5-9). The magnetic field strength of 2.13 to 3.07 mT corresponded to a torque of 4.69 to 6.75 pN·μm on the hexapod hematite core (**Fig. 5-10)**.

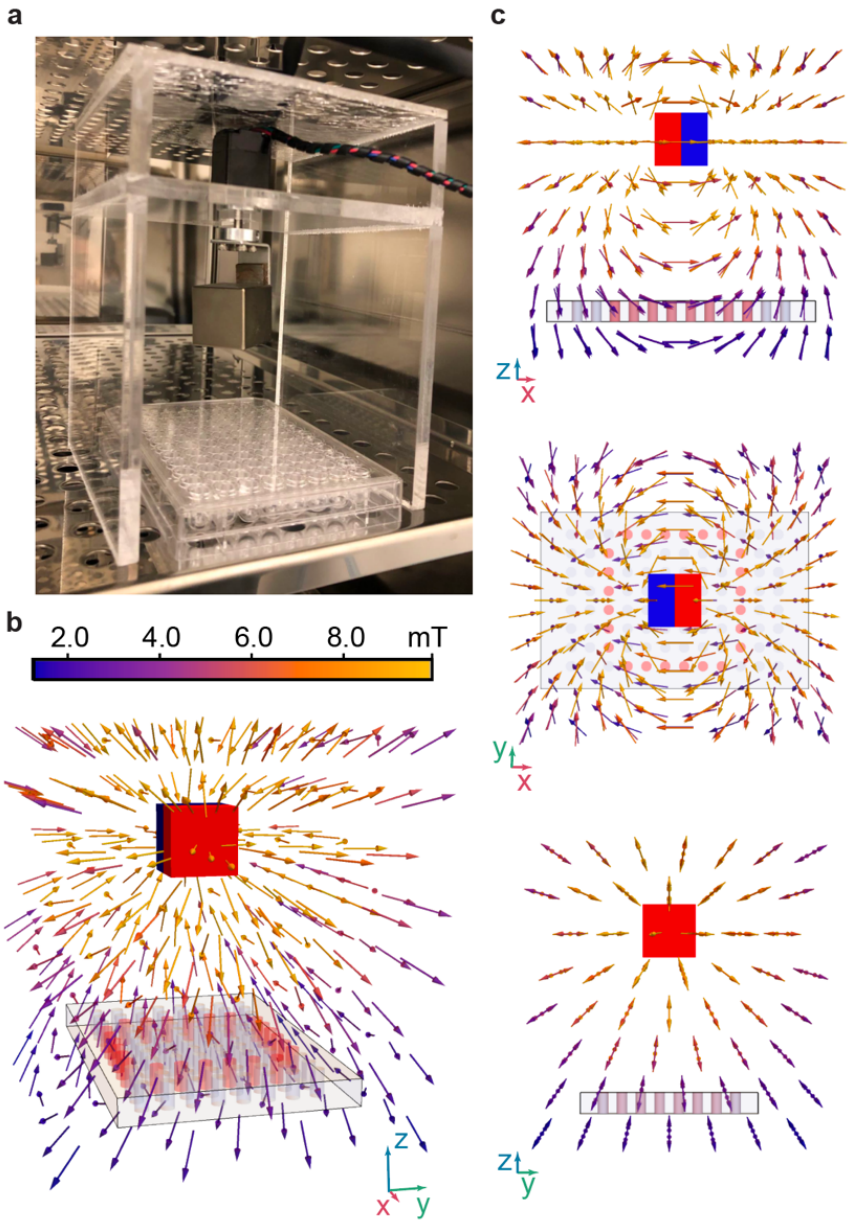

Figure 5-9. The magnetic field of the rotation biophysical stimulation experiment. a. A picture of the experimental setup. **b.** Illustration of the magnetic field vectors in the rotation biophysical stimulation experiment. **c.** Side, top, and front view of the magnetic field vectors in the rotation biophysical stimulation experiment.

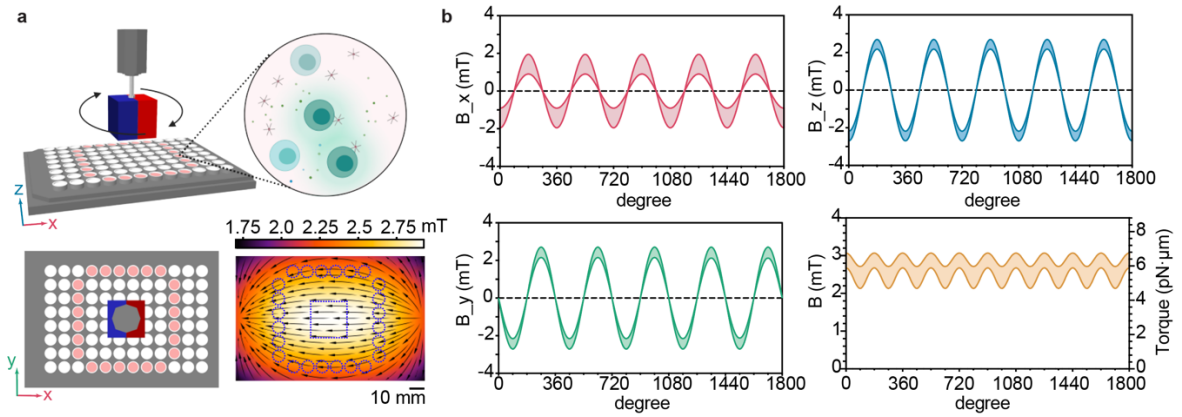

Figure 5-10. The magnetic field strength of the rotation biophysical stimulation experiment. **a.** Schematic showing the experimental setup for T-cell stimulation using the rotating hexapod bAPS. Cells were cultured in a 96-well plate. The magnetic field at the plane of the 96-well plate was calculated and illustrated (color, magnetic flux density; arrows, vectors in the x-y plane). **b.** the calculated magnetic field strength in cell culture wells. The total magnetic field ranges from 2.13 to 3.07 mT, calculated using the position of the wells with cells (x-axis, rotation degree), corresponding to torques of 4.69 to 6.75 pN·μm ($\boldsymbol{\tau} = \boldsymbol{m} \times \boldsymbol{B}, \boldsymbol{m} = \boldsymbol{I_0}\,\boldsymbol{V}$, the spontaneous magnetization per unit volume $\boldsymbol{I_0} = \boldsymbol{2.2}\times10^3$ A·m^{-1} and the volume of hematite core V ~ 1 μm^3).

After a 24-hour incubation, agonist pMHC-functionalized hexapods upregulated expression of CD69 (an early activation marker) and CD25 (a late activation marker) and elevated cytokine production in both CD8$^+$ OT-1 T cells and CD4$^+$ 5C.C7 T cells **(Figs. 5-11, 5-12, and 5-13).** Notably, the rotating magnetic field further upregulated both CD69 and CD25 expression in pMHC-bound cells compared to non-rotating pMHC-bound cells **(Figs. 5-11, 5-12, and 5-13).** Rotating hexapod stimulation also further significantly increased IL-2, TNF-α, and IFN-□ cytokine production **(Fig. 5-12 and 5-13).** Stimulation with pMHC-functionalized hexapods and the rotating magnetic field did not affect cell viability (**Fig. 5-14**). These results demonstrate that

TCRs are mechanosensitive, and hexapod-based rotational motion can amplify T-cell activation and cytokine production.

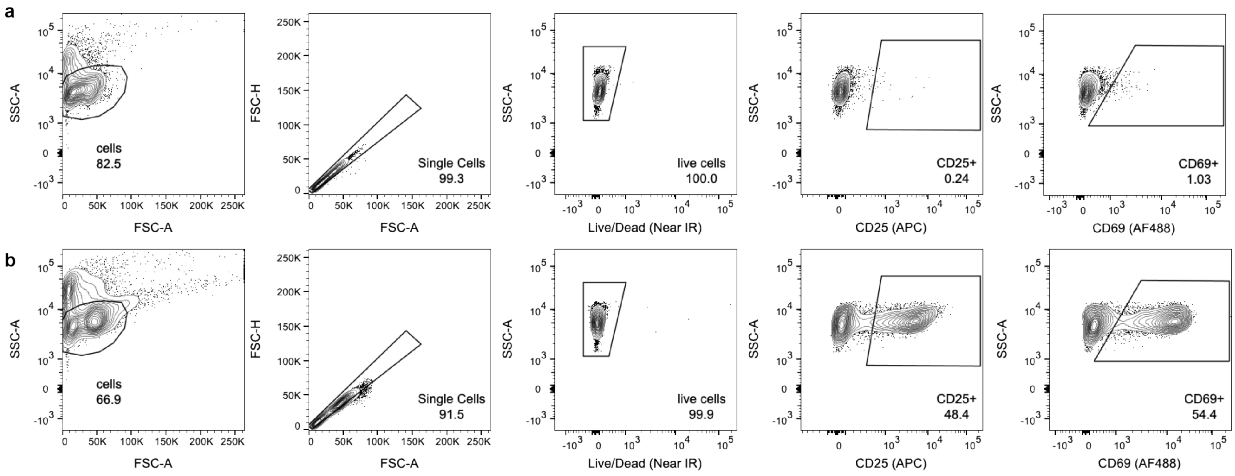

Figure 5-11. Gating strategy for CD25 and CD69 expression. Representative flow plots depicting the gating strategy for CD25 and CD69. OT1 CD8+ T cells were stimulated using pMHC-hexapods loaded with null-peptide (a, biological control) or OVA-peptide (b, experimental condition). Both hexapods were subject to magnetic rotation.

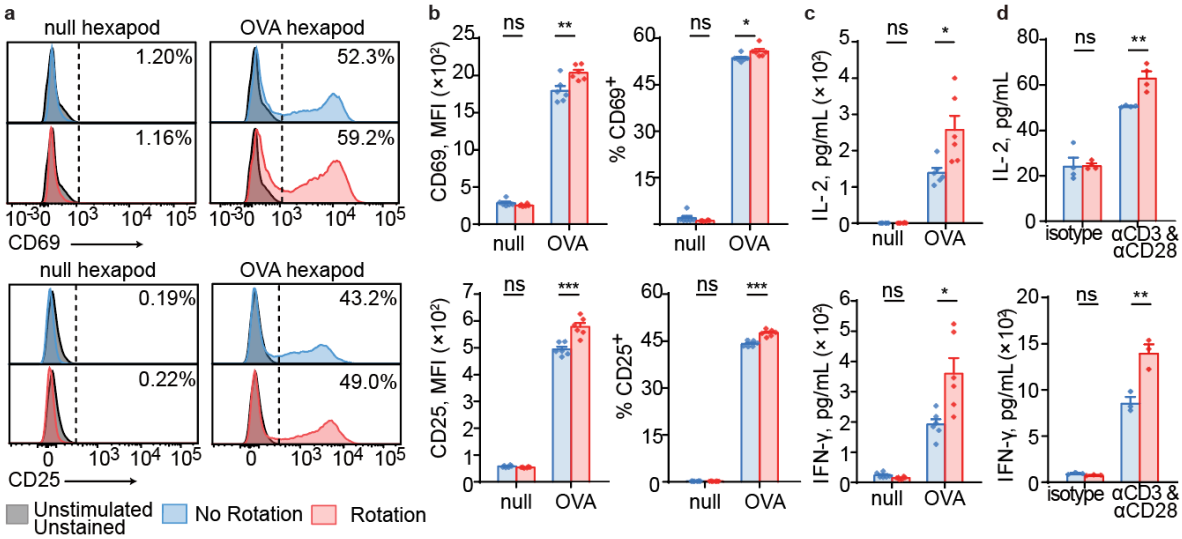

Figure 5-12. Hexapod APS amplified OT1 CD8⁺ T cell activation. a. Histograms showing representative CD69 (top) and CD25 (bottom) expression in primary OT-1 CD8⁺ T cells

Figure 5-12, continued. (sextuplicate independent experiments were performed). Unstimulated cells are shown in grey and used for gating. Filled plots indicate co-cultured cells with (red) or without (blue) rotation. **b.** Bar graphs of sextuple data depicting CD69 or CD25 mean fluorescence intensity (MFI) and the percentage of $CD69^+$ or $CD25^+$ cells. CD69 and CD25 expression levels were significantly amplified by magnetic rotation (i.e., biophysical forces). **c.** IL-2 and IFN-γ secretion was significantly amplified in hexapod-bAPS rotation-stimulated naïve primary mouse CD8+ T cells compared to static hexapod-bAPS-stimulated counterparts. **d.** IL-2 and IFN-γ secretion was significantly amplified in hexapod-bAPS rotation-stimulated Day 6-10 blast $CD8^+$ T cells compared to static hexapod bAPS-stimulated counterparts. Statistical analysis was performed using unpaired two-tailed t-tests. Results show individual replicates and the mean value ± S.E.M of multiple independent measurements (n = 6 for **b** and n = 3 or 4 for **c**). *P < 0.05, **P < 0.01, ***P < 0.001, and ns for not significant or p ≥ 0.05.

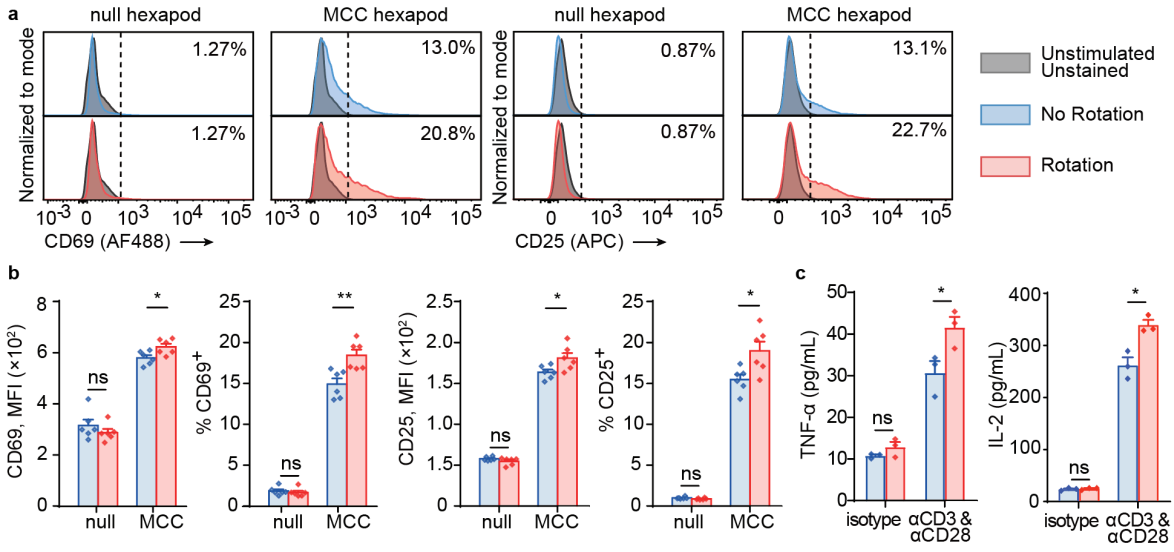

Figure 5-13. Hexapod APS amplified 5C.C7 $CD4^+$ T cell activation. a. Representative histograms from sextuplicate independent staining experiments of primary naïve 5C.C7 $CD4^+$ T cells. The staining of the unstained unstimulated cells is shown in gray and used for gating. Filled

Figure 5-13, continued. plots indicate co-cultured cells with (red) or without (blue) rotation. Left, CD69; right, CD25. **b.** Bar graphs of sextuple data depicting CD69 or CD25 MFI and the percentage of CD69 or CD25 positive cells. The expression level of CD69 and CD25 were significantly amplified by magnetic rotation (i.e., biophysical forces) in naïve 5C.C7 $CD4^+$ T cells. **c.** The secretion of TNF-α and IL-2 in Day 6-10 $CD4^+$ T cell blasts was measured using an enzyme-linked immunosorbent assay (ELISA). Rotation boosted cytokine production significantly compared to static hexapod (no rotation) groups. Statistical analysis was performed using unpaired two-tailed t-tests. Results show individual replicates and the mean value ± S.E.M of multiple independent measurements (n = 6 for **b** and n = 3 for **c**). *P < 0.05, **P < 0.01, and ns for not significant or p ≥ 0.05.

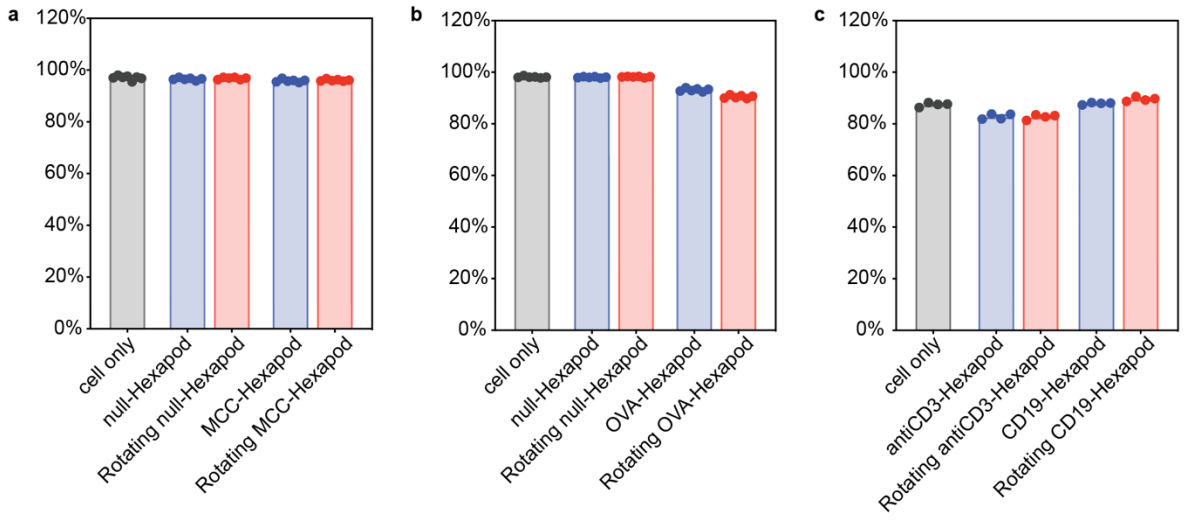

Figure 5-14. Rotating hexapod APS demonstrated good cell viability. a. Cell viability of primary 5C.C7 $CD4^+$ T cells. **b.** Cell viability of primary OT1 $CD8^+$ T cells. **c.** Cell viability of primary 41BB CAR T cells.

We further tested the impact of the hexapod rotation in CAR T-cell activation. Anti-human-CD3-hexapods and CD19-hexapods were, respectively, incubated with 4-1BB CAR-transduced

primary human T cells for 24 hours with or without rotating magnetic fields. Importantly, rotating magnetic fields further promoted IL-2 and IFN-□ cytokines production in 4-1BB CAR-transduced primary human T cells incubated with either anti-CD3-hexapods or CD19-hexapods (**Fig. 5-15**), indicating that both TCR and CAR are mechanosensitive receptors **(Fig. 5-16).**

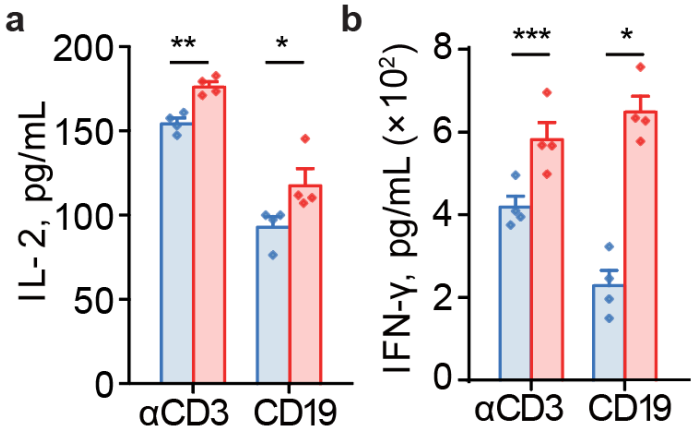

Figure 5-15. Hexapod APS amplified CAR-T cell activation. a. IL-2 and **b.** IFN-γ secretion was significantly increased in rotating anti-CD3- and rotating CD19-hexapods-treated 41BB CAR T cells compared to static groups, indicating that both the TCR and anti-CD19 CAR are mechanosensitive receptors responsive to hexapod-induced forces. All statistical analysis was performed using unpaired two-tailed t-tests. Results show individual replicates and the mean value ± S.E.M of multiple independent measurements (n = 4). *P < 0.05, **P < 0.01, and ***P < 0.001.

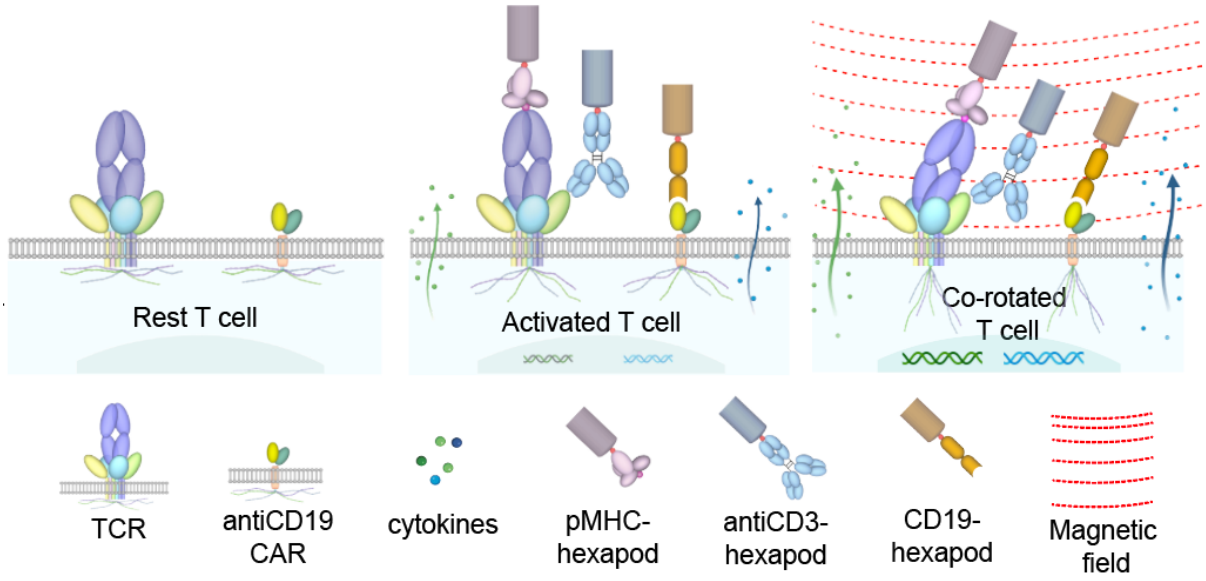

Figure 5-16. Schematic showing both TCRs and CARs are mechanosensitive receptors.

5.3 Conclusion

In this study, we developed a material-based bAPS to study the biochemical and biophysical impact on floating T cells. The bifunctional biomimetic hexapod heterostructures enabled physiologically relevant studies of T-cell biophysical sensitivity at the ensemble level (function 2).

Our results demonstrate the application of hexapod-bAPS in biophysical modulation studies in floating T and CAR-T cells. We showed that rotating hexapod-enabled exogenous forces can influence receptor activation dynamics, signal transduction, and cell fate of suspension cells. Hexapod-based rotational motion (i.e., mechanical forces) can amplify T-cell activation and facilitate quantification of cell surface and ensemble-level mechanosensitive responses. The data highlight that both the TCR and CAR on suspension cells are responsive to piconewton·micrometer level torque. Compared to other biophysical tools for studying mechanosensitivity (**Table 5-1**), the hexapod heterostructures allow the detection of mechanically

triggered T-cell signaling at the cellular ensemble level in floating T cells without the need for immobilization.

5.4 Experimental

5.4.1 Rotating Magnetic Field Device

An N52 Neodymium Permanent Magnet (1-inch cube) was attached to a home-built servo-based rotating system (parts obtained from electronics vendor Adafruit, **Fig. 5-3**). The rotational speed can be controlled from 20 rpm to 60 rpm. The portable devices can be positioned near the cell culture dishes and inside the CO_2 incubator or on the microscope. A three-axis magnetometer was connected to measure the real-time direction and strength of the rotating magnetic field as well as to calibrate the rotation speed. Logfiles and readouts are stored in an SD card. A detailed manual of the customized magnet rotator can be accessed via the link https://github.com/MagneticRotor/rotating-magnetic-field

5.4.2 Magnetic Field Calculations

Magnetic field $\vec{B}_0$ calculations for the cube magnet were performed using an analytical model[41]. Magnetization was chosen as 1480 mT, a reference value for the N52 magnet (1-inch cubic BX0X0X0-N52, K&J Magnetics). To generate the function of the rotating magnetic field $\vec{B}_{0,rot}(\vec{v},\theta)$, the z-axis rotation matrix $R_Z(\theta)$ was applied to the static field equation:

$$\vec{B}_0(\vec{v}) = \vec{B}_x(\vec{v}) + \vec{B}_y(\vec{v}) + \vec{B}_z(\vec{v}), where\ \vec{v} = \begin{bmatrix} x \\ y \\ z \end{bmatrix}$$

$$R_Z(\theta) = \begin{bmatrix} \cos\theta & -\sin\theta & 0 \\ \sin\theta & \cos\theta & 0 \\ 0 & 0 & 1 \end{bmatrix}$$

$$\vec{B}_{0,rot}(\vec{v},\theta) = R_Z(\theta)\,\vec{B}_0(R_Z(\theta)^{-1}\vec{v})$$

For all plotting, the starting point of rotation was chosen so that the magnetization vector is pointing along the x-axis. Calculation and visualization were performed in Wolfram Mathematica (13.0).

5.4.3 Confocal Microscopy of Immunological Synapses

We performed fixed samples imaging using an SP8 Leica Confocal system to capture CAR receptor interactions with the hexapod. A coverslip was coated with 0.01% [w/v] Poly-L-Lysine (Sigma, P8920) for 30 min at room temperature prior to sample loading for imaging. The effector cells, anti-CD19-28z-meGFP *CAR* (1M), were co-cultured with mCherry-labelled NALM-6 cells **(Fig. 4-20)** or APC-streptavidin-biotinylated-CD19-labelled hexapods **(Fig. 5-5)** at 1:1 ratio at 37°C / 5% CO_2 for 10 min, respectively. The samples were fixed using 2% PFA solution for 10 min. After washing with PBS twice, the suspension was added dropwise to the coated coverslip. After settling for 10 minutes, VectorShield™ mounting solution was dropped on the slide, and the slide was gently aligned. The VectorShield™ was smeared to cover the entire coverslip with the cells attached before sealing with nail polish and then imaging.

5.4.4 SEM Characterization of Hexapods and Cell/Hexapod Conjugates

A scanning electron microscope (SEM, Carl Zeiss, Germany, Merlin) was used to image the structures of synthesized hexapods and cell/hexapod conjugates. For hexapod characterization, diluted hexapods were dropped onto a piece of silicon wafer and coated with 8 nm platinum-palladium using a sputter coater (Ted Pella Cressington 208 HR) before imaging. For cell/hexapod conjugates characterization, T cells and anti-CD3/CD28 antibody-functionalized hexapods or

CAR T cells and CD19-functionalized hexapods were mixed and co-cultured on a 0.01% [w/v] Poly-L-Lysine (Sigma, P8920)-pretreated 1×1-cm Si chip for 30 minutes at 37°C/5% CO_2. T cells were then fixed in 4% paraformaldehyde (Electron Microscopy Sciences) and 0.4% glutaraldehyde (Sigma-Aldrich) in 0.2 M sodium cacodylate (Sigma-Aldrich) buffer (PH 7.2) overnight at 4°C. After fixation, samples were washed with distilled water, and then they were submerged into 30, 50, 70, 90, 95, and 100% ethanol solutions series sequentially to reduce the water content. The cell samples were dried with a critical point dryer (Leica EM CPD 300). Carbon dioxide (304.13 K, 73.8 bar) was injected into the system to exchange the ethanol at speed 1 for 16 cycles in a typical drying process. The cell samples were then coated with 8 nm Pt/Pd before SEM imaging. Images from the InLens detector were taken at various magnification levels with an accelerating voltage of 2.0 kV.

5.4.5 Rotation Tracking and Mean Squared Displacement (MSD) Analysis

To understand the hexapod's rotational dynamics of the hexapods, we recorded videos of the rotational motion with a Leica DM IRB inverted microscope equipped with a 100× oil immersion objective (numerical aperture = 1.40). Naïve CD4+ cells (3×10^6/mL) were cultured with MCC-MHC-hexapods (cell to hexapod ratio = 1:5). The rotating speed was set to 50 rpm, and an Andor iXon Ultra EMCCD camera was used for recording (10 frames/second or 100 ms per frame). The rotational motion was characterized by tracking the center point of the rotating hexapod iron oxide core and the end of one branch tip or tracking the center point of hexapod-bound T cells using ImageJ TrackMate. To estimate the MSD, tracking trajectories were analyzed with Matlab mdsanalyzer (https://github.com/tinevez/msdanalyzer). Diffusion coefficients were

calculated based on the first 20% of the MSD curve from the free 2-D diffusion (MSD = 4 Dt) equation.

5.4.6 Co-Cultures of Rotating Hexapods and T or CAR-T Cells

To study the impact of biophysical forces on floating primary T cells or CAR T cells, we set up the rotating magnet device on top of cell culture plates with the help of homebuilt acrylic holders. Each culture-containing well was the same distance from the magnet. Functionalized hexapods were mixed with T cells or CAR T cells (1.5×10^5 cells in 300 μL complete medium/well) with a hexapod to cell ratio of 10:1 and co-cultured for 24 h. For primary T-cell stimulation, anti-mouse-CD3-hexapods, null-hexapods, MCC-hexapods, and OVA-hexapods were used. For CAR T-cell stimulation, CD19-hexapod, BSA-hexapod, and anti-human-CD3-hexapod were used.

5.4.7 Cytokine ELISA

To measure cell cytokine secretion, supernatants were collected for enzyme-linked immunosorbent assay (ELISA). The supernatant was diluted 1:2 (IL-2) or 1:10 (IFN-γ) with PBS and analyzed using ELISA MAX™ Deluxe Set kits according to the manufacturer's instructions (human IL-2, [BioLegend, 431804]; human IFN-γ [BioLegend, 430104]; mouse IL-2, [BioLegend, 431004]; mouse IFN-γ [BioLegend, 430804]). ELISA plates (Nunc™ MaxiSorp™ ELISA Plates, BioLegend, 423501) were read in a Microplate Spectrophotometer (Epoch, BioTek). For each ELISA, an 8-point standard curve was generated ($R^2 > 0.99$). The raw data were transformed into pg/mL after fitting the standard curve.

5.4.8 Cell Surface Staining and Flow Cytometry

Following 24 hours of incubation, cell-hexapod pellets obtained by centrifugation were first washed with cold FACS buffer (PBS, 2% BSA, 0.05% sodium azide). Next, Fc receptors were blocked by incubation with Human TruStain FcX (BioLegend, 422302) or Mouse BD Fc Block (clone: 2.4G2, BD Pharmingen, 4182991) at 1:50 dilution for 15 minutes at 4°C. Then, cells were incubated for 30 minutes at 4°C in the dark with an antibody cocktail (staining solution). The staining solution for $CD4^+$ and $CD8^+$ T cells contained AlexaFluor 488 anti-mouse CD69 (clone: H1.2F3, BioLegend, 104516) and APC anti-mouse CD25 (clone PC61, BioLegend, 102012). Monoclonal antibodies were generally used according to manufacturer recommendations. After staining, cells were incubated briefly with a Live/Dead Fixable Near-IR Dead Cell Stain kit (Invitrogen, L34975), diluted 1:1000 in PBS, for 30 minutes at 4°C in the dark. Then, cells were washed three times in FACS buffer at 4°C before analysis by flow cytometry. 50,000 events were acquired on a BD LSRFortessa™ Cell Analyzer, and analysis was performed with the FlowJo software (v10.7.2, BD).

5.4.9 Quantification and Statistical Analysis

Statistical analyses were performed in GraphPad Prism (v.8.4.3) using unpaired two-tailed t-tests or ANOVA tests, as indicated in the figure legends. Data are presented as mean ± S.E.M.

5.5 Bibliography

1. Deng, H. *et al.* Monodisperse magnetic single-crystal ferrite microspheres. *Angew. Chem.* **117**, 2842–2845 (2005).
2. Wu, L., Mendoza-Garcia, A., Li, Q. & Sun, S. Organic phase syntheses of magnetic nanoparticles and their applications. *Chem. Rev.* **116**, 10473–10512 (2016).
3. Wu, L. *et al.* Monolayer assembly of ferrimagnetic $Co_xFe_{3-x}O_4$ nanocubes for magnetic recording. *Nano Lett.* **14**, 3395–3399 (2014).
4. Li, Q. *et al.* Correlation between particle size/domain structure and magnetic properties of highly crystalline Fe 3 O 4 nanoparticles. *Sci. Rep.* **7**, 9894 (2017).
5. Hudspeth, A. J. Making an effort to listen: mechanical amplification in the ear. *Neuron* **59**, 530–545 (2008).
6. Wu, J., Goyal, R. & Grandl, J. Localized force application reveals mechanically sensitive domains of Piezo1. *Nat. Commun.* **7**, 12939 (2016).
7. Kim, J. *et al.* Single-cell mechanogenetics using monovalent magnetoplasmonic nanoparticles. *Nat. Protoc.* **12**, 1871–1889 (2017).
8. Bavi, N. *et al.* Principles of mechanosensing at the membrane interface. in *The Biophysics of Cell Membranes* (eds. Epand, R. M. & Ruysschaert, J.-M.) vol. 19 85–119 (Springer Singapore, 2017).
9. Dupont, S. Role of YAP/TAZ in mechanotransduction. *Nature* **474**, (2011).
10. Brusatin, G., Panciera, T., Gandin, A., Citron, A. & Piccolo, S. Biomaterials and engineered microenvironments to control YAP/TAZ-dependent cell behaviour. *Nat. Mater.* (2018).
11. Azzolin, L. YAP/TAZ incorporation in the beta-catenin destruction complex orchestrates the Wnt response. *Cell* **158**, (2014).
12. Piccolo, S., Dupont, S. & Cordenonsi, M. The biology of YAP/TAZ: Hippo signaling and beyond. *Physiol. Rev.* **94**, 1287–1312 (2014).
13. Kanczler, J. M. *et al.* Controlled differentiation of human bone marrow stromal cells using magnetic nanoparticle technology. *Tissue Eng. Part A* **16**, 3241–3250 (2010).
14. Rotherham, M. & El Haj, A. J. Remote activation of the wnt/β-catenin signalling pathway using functionalised magnetic particles. *PLoS ONE* **10**, (2015).
15. Kang, H. *et al.* Remote control of multimodal nanoscale ligand oscillations regulates stem cell adhesion and differentiation. *ACS Nano* **11**, 9636–9649 (2017).
16. Kang, H. *et al.* Remote manipulation of ligand nano-oscillations regulates adhesion and polarization of macrophages *in vivo*. *Nano Lett.* **17**, 6415–6427 (2017).
17. Tajik, A. *et al.* Transcription upregulation via force-induced direct stretching of chromatin. *Nat. Mater.* **15**, 1287–1296 (2016).
18. Kim, D.-H. *et al.* Biofunctionalized magnetic-vortex microdiscs for targeted cancer-cell destruction. *Nat. Mater.* **9**, 165–171 (2010).
19. Cho, M. H. *et al.* A magnetic switch for the control of cell death signalling in *in vitro* and *in vivo* systems. *Nat. Mater.* **11**, 1038–1043 (2012).
20. Shen, Y. *et al.* Elongated nanoparticle aggregates in cancer cells for mechanical destruction with low frequency rotating magnetic field. *Theranostics* **7**, 1735–1748 (2017).
21. Domenech, M., Marrero-Berrios, I., Torres-Lugo, M. & Rinaldi, C. Lysosomal membrane permeabilization by targeted magnetic nanoparticles in alternating magnetic fields. *ACS Nano* **7**, 5091–5101 (2013).

22. Zhang, E. *et al.* Dynamic magnetic fields remote-control apoptosis via nanoparticle rotation. *ACS Nano* **8**, 3192–3201 (2014).
23. Tay, A., Sohrabi, A., Poole, K., Seidlits, S. & Carlo, D. D. A 3D magnetic hyaluronic acid hydrogel for magnetomechanical neuromodulation of primary dorsal root ganglion neurons. *Adv. Mater.* **30**, 1800927 (2018).
24. Tay, A., Kunze, A., Murray, C. & Di Carlo, D. Induction of calcium influx in cortical neural networks by nanomagnetic forces. *ACS Nano* **10**, 2331–2341 (2016).
25. Tay, A. & Di Carlo, D. Magnetic nanoparticle-based mechanical stimulation for restoration of mechano-sensitive ion channel equilibrium in neural networks. *Nano Lett.* **17**, 886–892 (2017).
26. Ley, K., Laudanna, C., Cybulsky, M. I. & Nourshargh, S. Getting to the site of inflammation: the leukocyte adhesion cascade updated. *Nat. Rev. Immunol.* **7**, 678–689 (2007).
27. Rossy, J., Laufer, J. M. & Legler, D. F. Role of mechanotransduction and tension in T cell function. *Front. Immunol.* **9**, 2638 (2018).
28. Zhu, C., Chen, W., Lou, J., Rittase, W. & Li, K. Mechanosensing through immunoreceptors. *Nat. Immunol.* **20**, 1269–1278 (2019).
29. Blumenreich, M. S. The white blood cell and differential count. in *Clinical Methods: The History, Physical, and Laboratory Examinations* (eds. Walker, H. K., Hall, W. D. & Hurst, J. W.) (Butterworths, 1990).
30. Harrison, D. L., Fang, Y. & Huang, J. T-cell mechanobiology: force sensation, potentiation, and translation. *Front. Phys.* **7**, 45 (2019).
31. Kim, S. T. *et al.* The αβ T cell receptor is an anisotropic mechanosensor. *J. Biol. Chem.* **284**, 31028–31037 (2009).
32. Cheng, X. *et al.* A microfluidic device for practical label-free $CD4^+$ T cell counting of HIV-infected subjects. *Lab Chip* **7**, 170–178 (2007).
33. Hu, K. H. & Butte, M. J. T cell activation requires force generation. *J. Cell Biol.* **213**, 535–542 (2016).
34. Liu, B., Chen, W., Evavold, B. D. & Zhu, C. Accumulation of dynamic catch bonds between tcr and agonist peptide-MHC triggers T cell signaling. *Cell* **157**, 357–368 (2014).
35. Majedi, F. S. *et al.* Augmentation of T-cell activation by oscillatory forces and engineered antigen-presenting cells. *Nano Lett.* **19**, 6945–6954 (2019).
36. Lee, K., Yi, Y. & Yu, Y. Remote control of t cell activation using magnetic janus particles. *Angew. Chem. Int. Ed.* **55**, 7384–7387 (2016).
37. Ma, V. P.-Y. *et al.* The magnitude of LFA-1/ICAM-1 forces fine-tune TCR-triggered T cell activation. *Sci. Adv.* **8**, eabg4485 (2022).
38. Nordenfelt, P., Elliott, H. L. & Springer, T. A. Coordinated integrin activation by actin-dependent force during T-cell migration. *Nat. Commun.* **7**, 13119 (2016).
39. Chen, B. *et al.* Janus particles as artificial antigen-presenting cells for t cell activation. *ACS Appl. Mater. Interfaces* **6**, 18435–18439 (2014).
40. Christiansen, M. G. & Anikeeva, P. Magnetic fields for modulating the nervous system. *Phys. Today* **74**, 28–34 (2021).
41. Engel-Herbert, R. & Hesjedal, T. Calculation of the magnetic stray field of a uniaxial magnetic domain. *J. Appl. Phys.* **97**, 074504 (2005).
42. Erokhin, S. & Berkov, D. Mechanical orientation of fine magnetic particles in powders by an external magnetic field: simulation‐based optimization. *Phys. Status Solidi B* **257**, 2000404 (2020).

43. Abrikosov, A. I., Sacanna, S., Philipse, A. P. & Linse, P. Self-assembly of spherical colloidal particles with off-centered magnetic dipoles. *Soft Matter* **9**, 8904 (2013).
44. Tanimoto, H., Sallé, J., Dodin, L. & Minc, N. Physical forces determining the persistency and centring precision of microtubule asters. *Nat. Phys.* **14**, 848–854 (2018).
45. Sacanna, S., Rossi, L. & Pine, D. J. Magnetic click colloidal assembly. *J. Am. Chem. Soc.* **134**, 6112–6115 (2012).

Chapter 6. Conclusion and Outlook

6.1 Conclusion

This thesis focuses on biointerfaces and material-enabled biophysical and biochemical modulations. Existing techniques for biointerfaces and recent advances were summarized in the introduction, including traditional metal-based electrodes, Si-based materials, and devices. These unique emerging platforms for bioelectric studies take advantage of their biocompatibility and physical properties (beyond the excellent electrical conductivity or semiconducting properties), introducing new functionalities to biointerfaces—for example, nano silicon-enabled light-controlled neuromodulations via photo-responses **(Chapter 1)**.

As a result of improvements in device designs, synthetic concepts, and fabrication, a wide range of new electronic systems can be developed for interfacing with various biological systems. To further interrogate bioelectrical activities and signaling with new synthetic concepts, I mainly focused on designing a micelle-enabled bottom-up fabrication route for producing carbon-based micro-supercapacitor-like devices, which were demonstrated to modulate bioelectrical activities from cellular lever to macroscopic tissues or organs (**Chapter 2**). Since biological systems are hierarchical and soft, we designed the carbon-based micro-supercapacitor with hierarchical porosity, reducing Young's modulus and helping efficient signal transductions across the interfaces.

We exploited the subcellular study by combining super-resolution imaging and electrical stimulation to study the natural cellular responses to electrical stimulation more closely. We found that external biophysical modulations play a crucial role in cell signaling by showing the real-time

exosome release upon electrical stimulation. We further demonstrated the scalable production of exosomes as therapeutical drug carriers and used the microRNA-loaded exosomes for myocardial infarction repair. Finally, the acute tissue repair we showed has promised future clinical applications of bioelectronics and exosomes (**Chapter 3**).

Beyond the bioelectrical stimulation, we also investigated biochemical and mechanical modulation. Considering the critical role of ligand-receptor interactions in immunobiology, we developed hexapod heterostructure bifunctional material platforms for single-cell single-molecule investigation of T cell biochemical sensitivity **(Chapter 4)** and ensemble-level investigation of biophysical (or mechanical) sensitivity physiologically **(Chapter 5).** We showed that T-cell sensing/activation could be achieved by a single agonist peptide-major histocompatibility complex, and T cells demonstrated distinct calcium responses upon contacting structurally similar peptides that differ by just one amino acid. We also confirmed the superior sensitivity of TCR antigen recognition compared to chimeric antigen receptors (CARs). Using the biophysical hexapod investigation, we reported that magnetic field-induced piconewton·micrometer-level torques on the hexapods could amplify immune responses in suspension T and CAR-T cells. Taken together, the multimodal hexapod bAPS presents new, nanotechnology-based biointerface tools for investigating recognition, signaling, and the biochemical/mechanical dual sensitivity of T cells and beyond.

6.2 Outlook

Cell signaling has been explored using a variety of materials and devices. But the exact underlying mechanisms that drive the induced responses remain largely unknown. Therefore, scientists and engineers have applied an interdisciplinary approach to designing synthetic

biointerfaces that disrupt the chemical and physical characteristics of the cellular microenvironment while providing controllable modulation. With synthetic materials in combination with biological ligands on the surface to mimic surface chemistries, with the design of microstructures and topography, and the physical function of the cellular microenvironment, strategies for enhancing a myriad of biomedical applications are highlighted in areas such as cell biology, immunobiology, and translation of cell therapeutics for clinical practice.

Nonetheless, because biological systems are complex, further research is required to answer the following questions that are not fully explained: What are molecular domains responsible for sensing external stimuli? How does the application of different functional biointerfaces specify the types of bio responses? What is the threshold for activation? These investigations will lay the root for biointerfaces with specificity. Even though questions remain over several mysteries, we cannot ignore the possibility of discovering new bioresponsive effects and applying the functional biointerfaces to more exciting applications.